Field Driven Vortex Domain Wall Motion in Magnetic Nanostructures

Dissertation

zur Erlangung des Doktorgrades
der Naturwissenschaften (Dr. rer. nat.)
der Fakultät für Physik
der Universität Regensburg

vorgelegt von

Tobias Weindler

aus Teublitz

im Jahre 2017

Promotionsgesuch eingereicht am: 27.10.2017
Die Arbeit wurde angeleitet von: Prof. Dr. Christian Back

Prüfungsausschuss:	Vorsitzender:	Prof. Dr. Gunnar Bali
	1. Gutachter:	Prof. Dr. Christian Back
	2. Gutachter:	Prof. Dr. Dieter Weiss
	weiterer Prüfer:	PD Dr. Jonathan Eroms

Contents

Chapter 1

Introduction

This thesis deals with the research area of domain walls (DW). In particular, the dynamics of field-driven vortex domain walls (VDW) in nano-stripes is investigated experimentally as well as by means of analytical calculations and micromagnetic simulations. But why should you do research in this small subarea of magnetism? It is important and interesting in both, the point of view of technological applications and the fundamental research of solid state physics. Concerning technological applications, novel storage and sensor devices relying on DWs and VDWs have been proposed respectively [1–3]. Compared to currently existing technologies, an enhanced performance is expected. For instance, the racetrack memory proposed in 2008 by S. S. P. Parkin [1] operates like a shift register [2] and should combine as non-volatile memory device the high performance and reliability of solid-state memories, and at the same time it has the low costs of disc-drive storages. In a racetrack memory the information is stored in a magnetic thin film stripe geometry where the in-plane magnetized domains represent the "0" and "1" bits. Reading the information can be realized by magnetic tunnel junction magnetoresisitive sensing devices [4], while the writing of bits is possible through different methods, for example, spin-momentum transfer torque (SST) [5, 6]. The shifting of the domains, which encode the digital information, is done also by spin-momentum transfer torque mediated by a spin-polarized electric current, which naturally arises when injecting an electric current into a magnetic material. How reliable and fast the domains can be shifted depends strongly on the dynamics of the DWs between domains with opposing magnetization direction. Aiming to build such storage media, a deep understanding of DW dynamics is a necessary prerequisite. Further proposed technological applications are magnetic sensors based on VCs and VDWs. Currently used micromagnetic sensors play a key role in a large variety of industry branches, for example, the automotive industry, where they are used for speed and position detection [3]. These sensors consist of a patterned magnetic element and a magnetoresistive sensor which utilizes effects, such as the giant magnetoresistance (GMR) [7–9], anisotropic magnetoresistance (AMR) [10] and tunnel magnetoresistance (TMR) [9, 11, 12]. However, actual sensors suffer from

a non-linear hysteresis curve and a high magnetic noise level. Micrometer-large ferromagnetic discs containing a magnetic vortex state are regarded as possible solution to avoid the latter mentioned limitation [3]. These sensors are proposed to operate with a higher linear regime and a magnetic noise level, which is an order of magnitude lower compared to actual used sensors. Therefore, a deep understanding of the complicated VC dynamics is necessary in order to build such a device. As it will become clear by the work done in this thesis, VDW are, besides the investigation of VCs in a disc [13–16], a possible way to tackle the investigation of VC dynamics. Of course, the investigation of DWs is important for basic research as well because on the one hand, side DW dynamics itself provides a huge variety of different aspects that can be discovered and which leads to a deeper understanding of DW and magnetization dynamics itself; on the other hand, it is a practical way to investigate certain basic material properties. Concerning the DW dynamics itself, examples are domain wall motion (DWM) at low and very high fields [17, 18] and by STT [19], DW depinning [20] and VC switching processes [21]. From the point of view of material properties, DW dynamics, especially the DWM of VDW, offers a convenient way to investigate magnetic damping mechanisms [22]. In the Landau-Lifshitz-Gilbert equation (LLG equation) [23–25] magnetic damping, and so the energy dissipation in the physical system, is parametrized by a scalar factor α. This implies that the energy dissipation is independent on the magnetic texture itself. However, an additional magnetic texture which depends on damping mechanism called non-local damping is proposed [26–28]. This additional damping enters respectively the LLG equation by an extra term proportional to a material parameter η, the spatial magnetic gradient and its time derivative. In order to catch effects of non-local damping, a fast moving magnetic texture is required, ideally accompanied with a strong magnetic gradient. Field driven VDWs in stripes provide such a toy model because they exhibit a natural given strong magnetic gradient due to the VC in the bulk and the half anti-vortices (HAVs) located at the edges. These three objects form together a VDW and strongly influence the dynamics of the DW. Because of their strong magnetic gradient, they are sensitive to non-local damping, and a possible effect should be, if large enough, measurable by DWM in the linear regime. A better overall understanding of the basic science of DWs has a retroactive effect on the earlier mentioned technological applications allowing to tailor the materials and magnetic systems to the respective requirements.

This thesis focuses on a special aspect of VDW dynamics arising in relatively wide stripes at fields above the Walker breakdown (WB) [29]. Differences for the breakdown mechanism of VDW with different chirality χ are evidenced by experimental data, analytical calculations and micromagnetic simulations. A new behaviour of VDWs with chirality $\chi = +1$ is discovered above the WB being causal for the mentioned different breakdown mechanism.

The thesis is organized as follows: In Ch. 2 the theoretical background for the investigation of DWM is set. Starting in Sec. 2.1 with the basic equation of magnetization dynamics (LLG eq.) and its basic properties, the considerations proceed to the reformulation of this equation into an equivalent force equation

in Sec. 2.2. This is the Thiele equation and a detailed derivation is provided. It is followed by a generalization of this equation which is introduced and discussed in the context of VDW motion in Sec. 2.3. The chapter ends with Sec. 2.4 and Sec. 2.5 where the theoretical background for the measurement techniques is provided. In Ch. 3 the experimental techniques and the way the acquired data were evaluated is presented. In Sec. 3.1 the sample design is explained, while Sec. 3.2-3.5 presents the measurement techniques superconducting quantum interference device (SQUID), time-resolved Kerr microscopy (TR-MOKE), full-film ferromagnetic resonance (full-film FMR) and wide-field Kerr microscopy (wide-field MOKE) which were utilized in this work. Subsequently the data evaluation of the obtained measurement and simulation data (Sec. 3.6 and Sec. 3.7) is described. In Ch. 4 the experimental results and the data from micromagnetic simulations are shown. Sec. 4.1 gives an overview of the results obtained from the sample characterization, while in Sec. 4.2 the chirality-dependent VDW dynamics is evidenced and discussed from different points of view. This thesis is closed by Ch. 4.2.12 and ends with the appendix .

Chapter 2

Theoretical Background

In this chapter the theoretical foundations for understanding and describing the DWM are laid. Beginning with the description of the basic equation of magnetization dynamics (LLG eq., Sec. 2.1), a conversion into a more suitable force equation with respect to DWM follows (Thiele eq., Sec. 2.2). Sec. 2.3 contains the detailed discussion of the dynamics of VDWs in the frame of the Thiele equation. The chapter is closed by the presentation of the theoretical background for the measurement methods of FMR and Kerr microscopy in Sec. 2.4 and Sec. 2.5, respectively. As starting point of the theoretical considerations, the LLG eq. and its basic properties are introduced in the subsequent section.

In order to provide the theoretical background for magnetization dynamics and domain wall motion in Ch. 2, many intermediate steps for calculations and derivations are given; this concerns especially Sec. 2.2. However, detailed calculations are hard to find in available literature except some PhD theses like Krüger's *Current-Driven Magnetization Dynamics* [30]; Nevertheless, they are helpful to get into the topic of domain wall motion from the theoretical point of view, and so the calculation steps that were carried out by myself will be marked with the footnote "[1]".

2.1 Landau-Lifshitz-Gilbert Equation

Aiming to describe magnetization dynamics from a theoretical point of view, an equation that describes the time evolution of the magnetization vector $\vec{M}$ under the influence of different interactions is required. Besides different approaches to differential equations [31], the most common one is the Landau-Lifschitz equation (LL equation), which was formulated in 1935 [23]. It was modified later on by Gilbert in 1955 in order to adjust it to a Lagrangian formalism and to convert it to friction like damping [24, 25]. The Landau-Lifshitz-Gilbert equation (LLG equation) reads

$$\frac{\mathrm{d}\vec{M}}{\mathrm{d}t} = -\gamma_0 \vec{M} \times \vec{H}_{\mathrm{eff}} + \frac{\alpha}{M_{\mathrm{s}}} \vec{M} \times \frac{\mathrm{d}\vec{M}}{\mathrm{d}t} \tag{2.1}$$

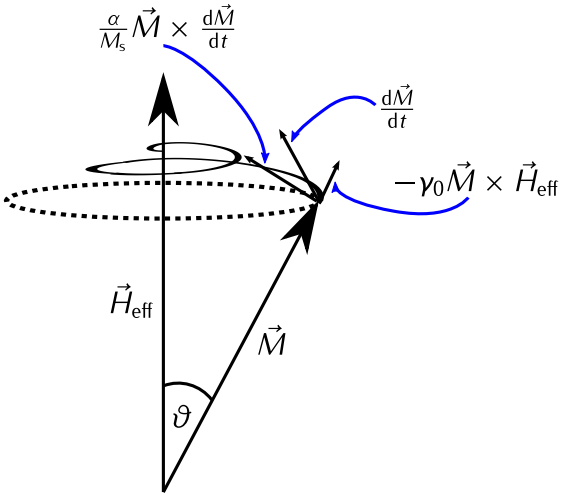

Figure 2.1. The sketch depicts the magnetization dynamics governed by the LLG equation. Having a magnetization $\vec{M}$ deflected by an angle ϑ from the effective field $\vec{H}_{\text{eff}}$, two different torques are present which sum up to the total changing rate $\frac{d\vec{M}}{dt}$. $-\gamma_0 \vec{M} \times \vec{H}_{\text{eff}}$ is the precessional torque causing a precession of $\vec{M}$ around the effective field $\vec{H}_{\text{eff}}$, while $\frac{\alpha}{M_s}\vec{M} \times \frac{d\vec{M}}{dt}$ (the damping term) is forcing the magnetization to align parallel to the effective field.

and states that the time change rate $\frac{d\vec{M}}{dt}$ of the magnetization $\vec{M}$ is governed by two terms, the precessional (first one) and the damping term (second one). The LLG eq. as well as the LL eq. can be derived from a phenomenological [23, 32] or quantum mechanics point of view [33]. The factor γ_0 is given by $-\mu_0\gamma$, where γ is the gyromagnetic ratio and μ_0 is the magnetic permeability of the vacuum. The effective field $\vec{H}_{\text{eff}}$ contained in the precessional term is determined by the variational derivative of the energy density $\mathcal{E}$ of the physical system with respect to $\vec{M}$ and given by [32]:

$$\vec{H}_{\text{eff}} = -\frac{1}{\mu_0}\frac{\delta \mathcal{E}}{\delta \vec{M}} \tag{2.2}$$

In the damping term, α is the Gilbert damping parameter, which is a material-dependent key number that quantifies the dissipation rate of energy in the system. Concerning the two terms describing the time evolution of $\vec{M}$, they can be understood in the following way: Neglecting the damping term, it is found that the time change rate of the magnetization is governed solely by the precessional term. This precessional term is very similar to the equation of the motion of a gyroscope. Having a torque acting on a spinning gyroscope, it starts to precess around its initial equilibrium position. In the same way it is the case for the magnetization; when an effective field, which can constitute out of an external field and different physical interactions, is acting on $\vec{M}$, the magnetization starts to precess around its equilibrium position.

This precessional motion would continue forever if the damping and energy dissipation were absent, respectively. However, from experimental results it is a well known fact that the magnetization aligns very fast along the effective field. To take this fact into account, a damping term has to be included. Such a damping term has to leave the length of the magnetization vector unchanged

because the conservation of saturation magnetization M_s is assumed. Due to this reason, it has to be perpendicular to the vector $\vec{M}$, and the only way to formulate the desired term is as it is done in Eq. (2.1). For the sake of completeness it should be noted, that the term $\vec{M} \times \frac{\mathrm{d}\vec{M}}{\mathrm{d}t}$ can be written as $\vec{M} \times \vec{M} \times \vec{H}_\mathrm{eff}$ as well - an equivalent notation used for example in the original work by Landau and Lifschitz [23]. Conservation of saturation magnetization with respect to time leads to interesting consequences for the terms contained in the LLG equation. This will be helpful later on when an equation for the description of DWM based on the LLG equation (see Sec. 2.2) is derived. Preservation of M_s can be demonstrated by multiplying all terms in the LLG eq. by $\vec{M}$ yielding[1] [32]:

$$\begin{aligned} \vec{M} \cdot \frac{\mathrm{d}\vec{M}}{\mathrm{d}t} &= \frac{1}{2}\frac{\mathrm{d}}{\mathrm{d}t}\left|\vec{M}\right|^2 \\ &= -\gamma_0 \underbrace{\vec{M} \cdot \left(\vec{M} \times \vec{H}_\mathrm{eff}\right)}_{=0} + \frac{\alpha}{M_\mathrm{s}} \underbrace{\vec{M} \cdot \left(\vec{M} \times \frac{\mathrm{d}\vec{M}}{\mathrm{d}t}\right)}_{=0} = 0 \end{aligned} \tag{2.3}$$

As result[1]

$$\frac{\mathrm{d}}{\mathrm{d}t}\left|M_\mathrm{s}\right| = 0 \tag{2.4}$$

the conservation of the saturation magnetization is obtained. Additionally, it can be concluded, due to the fact that the two terms on the right side are equal zero, that they are perpendicular to $\vec{M}$ [32].

$$\vec{M} \perp \vec{M} \times \vec{H}_\mathrm{eff} \perp \vec{M} \times \frac{\mathrm{d}\vec{M}}{\mathrm{d}t} \tag{2.5}$$

Furthermore, Eq. (2.3) states that the dot product of the magnetization with its own time change rate is zero. Because of this fact, $\vec{M}$ and $\frac{\mathrm{d}\vec{M}}{\mathrm{d}t}$ are perpendicular to each other[1].

$$\vec{M} \perp \frac{\mathrm{d}\vec{M}}{\mathrm{d}t} \tag{2.6}$$

However, since all vectors are perpendicular with respect to the magnetization vector, care should be taken to $\vec{M}$; but only $\vec{M}$, $\vec{M} \times \vec{H}_\mathrm{eff}$ and $\vec{M} \times \frac{\mathrm{d}\vec{M}}{\mathrm{d}t}$ are forming an orthogonal basis and are orthogonal regarding each other respectively [32]. Based on this prerequisites, the theoretical considerations evolve to the derivation of an equation which is more suitable for the description of DWM.

2.2 Thiele Equation

In this section the basic equation for the investigation of DWM, the Thiele equation, is derived. As a starting point, the basic idea behind the Thiele equation explained in Sec 2.2.1 and the conversion of the LLG eq. into an equivalent field eq. (Sec. 2.2.2) is demonstrated. These results lead to an effective force den-

[1] This calculation has been carried out by myself.

sity and force equation (Sec. 2.2.3), respectively, and they result in the Thiele equation discussed in Sec. 2.2.4.

2.2.1 Basic Idea

The basic idea behind the Thiele equation [34] is to consider the domain wall as a rigid magnetic particle which is not deforming while moving along the stripe with a constant velocity (steady-state motion). Having a rigid particle, the total force acting on the domain wall itself can be considered, so that it is possible to write an equation of motion for the case of steady-state motion as[1] [34, 35]:

$$\sum_x \vec{F}^x = 0 \tag{2.7}$$

Here, x stands for the different forces arising from the LLG equation. So it should be thought about the force acting on a magnetic texture under the influence of an external magnetic field. Starting with the force that acts on a magnetic dipole and extending it to the magnetization, the potential energy $E^x_{\mathrm{Pot},i}$ of a magnetic dipole (with magnetic moment $\vec{\mu}^i_{\mathrm{s}}$) in an external field $\vec{H}^x$ is given by[1] [36, 37]:

$$E^x_{\mathrm{Pot},i} = -\mu_0 \vec{\mu}^i_{\mathrm{s}} \cdot \vec{H}^x \tag{2.8}$$

Summing up over all magnetic moments in a volume V, whereby the assumption is taken that one magnetic moment covers a volume V_i, the corresponding energy density is obtained[1] [37, 38]

$$\mathcal{E}^x = \frac{\sum_i^N E^x_{\mathrm{Pot},i}}{\sum_i^N V_i} = -\mu_0 \frac{\sum_i^N \vec{\mu}^i_{\mathrm{s}}}{\sum_i^N V_i} \cdot \vec{H}^x = -\mu_0 \vec{M} \cdot \vec{H}^x \tag{2.9}$$

which is caused by the influence of a field $\vec{H}^x$. Here, the definition was used with the result that the magnetization is given by the total amount of magnetic moments per volume [38]. The total energy density $\mathcal{E}$ is obtained by summing over all fields $\vec{H}^x$ [1]:

$$\mathcal{E} = \sum_x \mathcal{E}^x = -\mu_0 \sum_x \vec{M} \cdot \vec{H}^x = -\mu_0 \vec{M} \cdot \sum_x \vec{H}^x = -\mu_0 \vec{M} \cdot \vec{H}_{\mathrm{eff}} \tag{2.10}$$

Here, the sum over the different field contributions $\vec{H}^x$ is denoted as the effective field $\vec{H}_{\mathrm{eff}}$ [32] (see Sec. 2.1). By integrating over the full volume V, the energy E

$$\begin{aligned} E &= \sum_x E^x = \sum_x \int_V \mathcal{E}^x \,\mathrm{d}V \\ &= \sum_x -\mu_0 \int_V \vec{M} \cdot \vec{H}^x \,\mathrm{d}V = -\mu_0 \int_V \vec{M} \cdot \sum_x \vec{H}^x \,\mathrm{d}V \end{aligned} \tag{2.11}$$

is found[1], which is equal to the Zeeman energy [36–38]. The force density is given by the derivation of the energy density with respect to the spatial components. Assuming the field $\vec{H}^x$ as spatially constant, it yields[1] [39, 40]:

$$\mathcal{E}^x = -\mu_0 \left(M_x H_x^x + M_y H_y^x + M_z H_z^x \right) \tag{2.12}$$

and the force density vector $\vec{f}^x$ originating from one certain field $\vec{H}^x$ reads[1] [34, 38, 41]

$$\begin{aligned} \vec{f}^x = -\vec{\nabla}\mathcal{E}^x &= \mu_0 \begin{pmatrix} \frac{\partial M_x}{\partial x} H_x^x & \frac{\partial M_y}{\partial x} H_y^x & \frac{\partial M_z}{\partial x} H_z^x \\ \frac{\partial M_x}{\partial y} H_x^x & \frac{\partial M_y}{\partial y} H_y^x & \frac{\partial M_z}{\partial y} H_z^x \\ \frac{\partial M_x}{\partial z} H_x^x & \frac{\partial M_y}{\partial z} H_y^x & \frac{\partial M_z}{\partial z} H_z^x \end{pmatrix} \\ &= \mu_0 \underbrace{\begin{pmatrix} \frac{\partial M_x}{\partial x} & \frac{\partial M_y}{\partial x} & \frac{\partial M_z}{\partial x} \\ \frac{\partial M_x}{\partial y} & \frac{\partial M_y}{\partial y} & \frac{\partial M_z}{\partial y} \\ \frac{\partial M_x}{\partial z} & \frac{\partial M_y}{\partial z} & \frac{\partial M_z}{\partial z} \end{pmatrix}}_{=J_{\vec{M}}^{\mathrm{T}}} \begin{pmatrix} H_x^x \\ H_y^x \\ H_z^x \end{pmatrix} \\ &= \mu_0 J_{\vec{M}}^{\mathrm{T}} \vec{H}^x = \mu_0 \left(\frac{\partial \vec{M}}{\partial \vec{R}} \right)^{\mathrm{T}} \vec{H}^x \end{aligned} \tag{2.13}$$

whereby the matrix which contains the spatial derivatives is identified as the transposed Jacobian matrix $J_{\vec{M}}^{\mathrm{T}}$ [41, 42] of the magnetization $\vec{M}$. Additionally, it is possible to write the transposed Jacobian matrix $J_{\vec{M}}^{\mathrm{T}}$ in symbolic notation $\left(\frac{\partial \vec{M}}{\partial \vec{R}}\right)^{\mathrm{T}}$, which will be utilized in the following considerations. Then, the total force $\vec{F}$ is found by summing over all fields x [1].

$$\begin{aligned} \vec{F} = -\vec{\nabla}E = -\sum_x \left(\vec{\nabla} E^x \right) &= -\sum_x \int_V \left(\vec{\nabla}\mathcal{E}^x \right) \mathrm{d}V \\ = \sum_x \mu_0 \int_V \left(\frac{\partial \vec{M}}{\partial \vec{R}} \right)^T \cdot \vec{H}^x \,\mathrm{d}V &= \mu_0 \int_V \left(\frac{\partial \vec{M}}{\partial \vec{R}} \right)^T \cdot \sum_x \vec{H}^x \,\mathrm{d}V \end{aligned} \tag{2.14}$$

Neglecting the integration over the volume yields the force densities[1] [34].

$$\vec{f}^x = \mu_0 \left(\frac{\partial \vec{M}}{\partial \vec{R}} \right)^{\mathrm{T}} \cdot \vec{H}^x \tag{2.15}$$

$$\vec{f} = \sum_x \vec{f}^x = \mu_0 \sum_x \left(\frac{\partial \vec{M}}{\partial \vec{R}} \right)^{\mathrm{T}} \cdot \vec{H}^x = \mu_0 \left(\frac{\partial \vec{M}}{\partial \vec{R}} \right)^{\mathrm{T}} \cdot \sum_x \vec{H}^x \tag{2.16}$$

Therefore, the question arises what the fields are contributing to $\vec{H}_{\mathrm{eff}}$ and how they are including the dynamics given by the basic equation of magnetization dynamics (LLG eq.). Finding the answer to this question is the task of the next section.

2.2.2 Equivalent Field Equation

The latter question gets a first answer by calculating the force in an alternative manner. Another way is to start from the expression of the energy, applying the nabla operator and using the chain rule in combination with the variation derivative of the energy density concerning the magnetization vector $\vec{M}$ [1] [32, 38, 43].

$$\begin{aligned}\vec{F} = -\vec{\nabla}E = -\int_V \left(\vec{\nabla}\mathcal{E}\right) \mathrm{d}V = -\int_V \frac{\delta\mathcal{E}}{\delta\vec{M}}\frac{\partial\vec{M}}{\partial\vec{R}}\,\mathrm{d}V \\ = \mu_0 \int_V \vec{H}_{\mathrm{eff}}^{\mathrm{T}}\frac{\partial\vec{M}}{\partial\vec{R}}\,\mathrm{d}V = \mu_0\int_V \left(\frac{\partial\vec{M}}{\partial\vec{R}}\right)^{\mathrm{T}}\cdot\vec{H}_{\mathrm{eff}}\,\mathrm{d}V\end{aligned} \tag{2.17}$$

Since the total energy density of the system is under consideration, the variational term gives $-\mu_0\vec{H}_{\mathrm{eff}}$ [32], where the effective field $\vec{H}_{\mathrm{eff}}$ is the same as expressed in the sum in formula Eq. (2.10). This yields the equal expression for the sum over all forces, and one obtains [32]:

$$\vec{H}_{\mathrm{eff}} = \sum_x \vec{H}^x \tag{2.18}$$

Knowing now that the sum over all forces is given by the effective field H_{eff}, this knowledge can be used for resolving the LLG eq. with respect to H_{eff} by applying $\vec{M}\times$ to all terms in the LLG equation. Before doing this, a more intuitive access, concerning how to find the different field terms, should be given in the following. Considering the LLG eq. and thinking about the force that acts on the magnetization $\vec{M}$, the most obvious way is to consider the effective field entering the equation in the precessional term. H_{eff} is restricted to H_{ext} because, as it will become clear later on, only the external field H_{ext} is important for the DWM [34].

$$\vec{H}_{\mathrm{eff}} = \vec{H}_{\mathrm{ext}} = \vec{H} \tag{2.19}$$

At this stage it should be mentioned that the external field $\vec{H}_{\mathrm{ext}}$ will be denoted for simplicity in the following as $\vec{H}$. This field creates a force on the magnetization and is the origin for the motion of the DW. Thus, H is the equivalent field respecting the precessional term. The precessional term is again obtained by applying $-\gamma_0\vec{M}\times$ to H. Aiming to include the dynamics of the LLG in the fields, the question has to be asked whether there are fields associated with the time evolution and damping term or not. Denoting these terms as $\vec{H}^{\mathrm{g}}$ and $\vec{H}^{\alpha}$, they have to fulfill the condition[1]:

$$-\gamma_0\vec{M}\times\vec{H}^{\mathrm{g}} = \frac{\mathrm{d}\vec{M}}{\mathrm{d}t} \tag{2.20}$$

$$-\gamma_0\vec{M}\times\vec{H}^{\alpha} = \frac{\alpha}{M_{\mathrm{s}}}\vec{M}\times\frac{\mathrm{d}\vec{M}}{\mathrm{d}t} \tag{2.21}$$

Applying again $\vec{M}\times$ to both sides of Eq. (2.21) and (2.20), it is possible to resolve it with respect to the fields $\vec{H}^{\mathrm{g}}$ and $\vec{H}^{\alpha}$. First $\vec{H}^{\mathrm{g}}$ [1]:

$$-\gamma_0 \vec{M} \times \vec{M} \times \vec{H}^{\mathrm{g}} = \vec{M} \times \frac{\mathrm{d}\vec{M}}{\mathrm{d}t} \tag{2.22}$$

$$-\gamma_0 \left(\vec{M} \left(\vec{M} \cdot \vec{H}^{\mathrm{g}} \right) - \vec{H}^{\mathrm{g}} \left(\vec{M} \cdot \vec{M} \right) \right) = \vec{M} \times \frac{\mathrm{d}\vec{M}}{\mathrm{d}t} \tag{2.23}$$

$$\vec{H}^{\mathrm{g}} = \frac{1}{\gamma_0 M_{\mathrm{s}}^2} \vec{M} \times \frac{\mathrm{d}\vec{M}}{\mathrm{d}t} \tag{2.24}$$

Now $\vec{H}^{\alpha}$ [1]:

$$-\gamma_0 \vec{M} \times \vec{M} \times \vec{H}^{\alpha} = \frac{\alpha}{M_{\mathrm{s}}} \vec{M} \times \vec{M} \times \frac{\mathrm{d}\vec{M}}{\mathrm{d}t} \tag{2.25}$$

$$-\gamma_0 \left(\vec{M} \left(\vec{M} \cdot \vec{H}^{\alpha} \right) - \vec{H}^{\alpha} \left(\vec{M} \cdot \vec{M} \right) \right) = \frac{\alpha}{M_{\mathrm{s}}} \left(\vec{M} \left(\vec{M} \cdot \frac{\mathrm{d}\vec{M}}{\mathrm{d}t} \right) - \frac{\mathrm{d}\vec{M}}{\mathrm{d}t} \left(\vec{M} \cdot \vec{M} \right) \right) \tag{2.26}$$

$$-\vec{H}^{\alpha} = \frac{\alpha}{\gamma_0 M_{\mathrm{s}}} \frac{\mathrm{d}\vec{M}}{\mathrm{d}t} \tag{2.27}$$

And for completeness with the force [1]:

$$\vec{H}^{\mathrm{f}} = \vec{H} \tag{2.28}$$

Giving the field equation [1]:

$$\vec{H}^{\mathrm{g}} = \vec{H}^{\mathrm{f}} - \vec{H}^{\alpha} \tag{2.29}$$

Applying again $-\gamma_0 \vec{M}\times$, it returns to the LLG equation. As it can be seen, it is possible to transform the LLG eq. into an equivalent field equation and vice versa by multiplying the equations with $-\gamma_0 \vec{M}\times$ and $\vec{M}\times$, respectively. Knowing the result, a more formalistic and straight path can be taken by considering the LLG (in the version for small α), setting $\vec{H}_{\mathrm{eff}} = \vec{H}$

$$\frac{\mathrm{d}\vec{M}}{\mathrm{d}t} = -\gamma_0 \vec{M} \times \vec{H} + \frac{\alpha}{M_{\mathrm{s}}} \vec{M} \times \frac{\mathrm{d}\vec{M}}{\mathrm{d}t} \tag{2.30}$$

and dividing both sides by $-\gamma_0$. This yields[1] [34]

$$-\frac{1}{\gamma_0} \frac{\mathrm{d}\vec{M}}{\mathrm{d}t} = \vec{M} \times \vec{H} - \frac{\alpha}{\gamma_0 M_{\mathrm{s}}} \vec{M} \times \frac{\mathrm{d}\vec{M}}{\mathrm{d}t} \tag{2.31}$$

and it is possible to bring all terms to the left hand side. This results in an equation which states that the sum over all torques is zero[1] [34].

$$-\frac{1}{\gamma_0} \frac{\mathrm{d}\vec{M}}{\mathrm{d}t} - \vec{M} \times \vec{H} + \frac{\alpha}{\gamma_0 M_{\mathrm{s}}} \vec{M} \times \frac{\mathrm{d}\vec{M}}{\mathrm{d}t} = 0 \tag{2.32}$$

Applying again $\vec{M}\times$, it yields[1] [34]:

$$-\frac{1}{\gamma_0}\vec{M}\times\frac{\mathrm{d}\vec{M}}{\mathrm{d}t}-\vec{M}\times\vec{M}\times\vec{H}+\frac{\alpha}{\gamma_0 M_\mathrm{s}}\vec{M}\times\vec{M}\times\frac{\mathrm{d}\vec{M}}{\mathrm{d}t}=0 \tag{2.33}$$

$$-\frac{1}{\gamma_0 M_\mathrm{s}^2}\vec{M}\times\frac{\mathrm{d}\vec{M}}{\mathrm{d}t}-\vec{M}\underbrace{\frac{\left(\vec{M}\cdot\vec{H}\right)}{M_\mathrm{s}^2}}_{=\beta}+\vec{H}-\frac{\alpha}{\gamma_0 M_\mathrm{s}}\frac{\mathrm{d}\vec{M}}{\mathrm{d}t}=0 \tag{2.34}$$

Again, the same fields are gained as in the more intuitive approach discussed beforehand [34].

$$\vec{H}^\mathrm{g}+\vec{H}^\mathrm{m}+\vec{H}^\mathrm{f}+\vec{H}^\alpha=0 \tag{2.35}$$

As it can be seen, an additional term is arising from the precessional term of the LLG. This is the magnetization equivalent field $\vec{H}^\mathrm{m}$ as denoted in the same way by Thiele [34]. It will become clear that this term is unimportant because it vanishes in both when the force densities are calculated and the field equation is transformed back to the LLG equation. To conclude it, the equivalent field equation containing the fields is given by [34]:

$$\begin{aligned}
&\vec{H}^\mathrm{m}=-\beta\vec{M} && \text{(magnetization equivalent field)}\\
&\vec{H}^\mathrm{f}=\vec{H} && \text{(force term)}\\
&\vec{H}^\alpha=-\frac{\alpha}{\gamma_0 M_\mathrm{s}}\frac{\mathrm{d}\vec{M}}{\mathrm{d}t} && \text{(damping equivalent term)}\\
&\vec{H}^\mathrm{g}=-\frac{1}{\gamma_0 M_\mathrm{s}^2}\vec{M}\times\frac{\mathrm{d}\vec{M}}{\mathrm{d}t} && \text{(gyroscopic field)}
\end{aligned} \tag{2.36}$$

These fields are spatial orthogonal vectors because they are basically nothing else than the rotated vectors of the torque vectors in the LLG equation. It has been demonstrated previously that these torque vectors are orthogonal (see Sec. 2.1).

2.2.3 Effective Force Density and Force Equation

In the previous section the expressions for the fields which include the dynamics of the LLG eq. and act on the magnetization $\vec{M}$ have been obtained. Inserting these equations for the fields into the expression found for the force densities, it yields [1] [34]:

$$
\begin{aligned}
&\vec{f}^{\mathrm{m}} = -\mu_0 \left(\frac{\partial \vec{M}}{\partial \vec{r}}\right)^{\mathrm{T}} \vec{H}^{\mathrm{m}} = \mu_0 \beta \left(\frac{\partial \vec{M}}{\partial \vec{r}}\right)^{\mathrm{T}} \vec{M} \\
&\text{(magnetization equivalent force density)} \\
&\vec{f}^{\mathrm{f}} = -\mu_0 \left(\frac{\partial \vec{M}}{\partial \vec{r}}\right)^{\mathrm{T}} \vec{H}^{\mathrm{f}} = -\mu_0 \left(\frac{\partial \vec{M}}{\partial \vec{r}}\right)^{\mathrm{T}} \vec{H} \\
&\text{(force density)} \\
&\vec{f}^{\alpha} = -\mu_0 \left(\frac{\partial \vec{M}}{\partial \vec{r}}\right)^{\mathrm{T}} \vec{H}^{\alpha} = \frac{\mu_0 \alpha}{\gamma_0 M_{\mathrm{s}}} \left(\frac{\partial \vec{M}}{\partial \vec{r}}\right)^{\mathrm{T}} \left(\frac{\mathrm{d}\vec{M}}{\mathrm{d}t}\right) \\
&\text{(damping equivalent force density)} \\
&\vec{f}^{\mathrm{g}} = -\mu_0 \left(\frac{\partial \vec{M}}{\partial \vec{r}}\right)^{\mathrm{T}} \vec{H}^{\mathrm{g}} = \frac{\mu_0}{\gamma_0 M_{\mathrm{s}}^2} \left(\frac{\partial \vec{M}}{\partial \vec{r}}\right)^{\mathrm{T}} \left(\vec{M} \times \frac{\mathrm{d}\vec{M}}{\mathrm{d}t}\right) \\
&\text{(gyroscopic force density)}
\end{aligned}
\tag{2.37}
$$

It is worth noting that the expressions for the force densities are functions of the spatial coordinate which is represented by the vector $\vec{r}$, and additional, it functions of time t. The only exception with respect to the time dependence is the force density $\vec{f}^{\mathrm{f}}$, where by assumption the external field $\vec{H}_{\mathrm{ext}}$ is constant in time. The time dependence enters the mathematical expressions for the force densities by the time dependence of $\vec{M}$ and $\frac{\mathrm{d}\vec{M}}{\mathrm{d}t}$. The partial derivative of $\vec{M}$ with respect to $\vec{r}$ itself is independent on t, though the magnetization $\vec{M}$ is a function of t. This seems a bit strange, but it can be easily explained by the properties of the partial derivative. The explanation for this fact will be done, among other things, in the next section. Summarizing, it can be stated that you should denote consequently and more precisely the force densities $\vec{f}^{\mathrm{m}}(\vec{r},t)$, $\vec{f}^{\mathrm{f}}(\vec{r},t)$, $\vec{f}^{\alpha}(\vec{r},t)$ and $\vec{f}^{\mathrm{g}}(\vec{r},t)$ instead of $\vec{f}^{\mathrm{m}}$, $\vec{f}^{\mathrm{f}}$, $\vec{f}^{\alpha}$ and $\vec{f}^{\mathrm{g}}$. As explained, parts of the equations for the force densities are already independent on t. Striving for a force equation which describes the motion of a magnetic particle or a domain wall, which is moving with constant velocity, it is easy to assume that the forces acting are constant in time. Therefore, the question arises, whether it is possible to make the expressions for $\vec{f}$ time-independent or not. As it will be seen, the assumption of a magnetic texture moving with constant velocity, the steady-state approximation, is the key to this question. This special mobility regime of steady-state motion is investigated in detail in the next subsection, and important implications on the further analysis are found.

2.2.3.1 Steady-State Motion

The main goal Thiele was pursuing in his work was to find an equation that allows a more realistic prediction of the steady-state motion velocity of magnetic domains than in works done before [34]. The detailed considerations about the steady-state approximation following now may look a little bit too ornate, but a proper understanding of the mathematical treatment and implications of this

approximation is necessary to understand Thiele's analysis and the collective coordinate approach to DWM (see. Sec. 2.3.2). A key point in the derivation of the Thiele equation is the steady-state approximation, which is based on the following two assumptions:

- The structure of the domain wall is fixed during the uniform motion.
- The whole domain wall is moving with constant velocity $\vec{v}$.

These assumptions can be justified with a few easy physical considerations. Having a domain wall at rest at a certain time, the magnetic texture of the wall is given by the minimization of the total energy of the DW E_{tot} which is mainly governed by the competitive energy contributions of exchange and dipolar energy. Applying an external field $\vec{H}$, the magnetic texture of the wall will undergo a transition because E_{tot} is not in a minimum anymore. The wall will increase its velocity which opens a channel to dissipate energy that is brought to the system due to the Zeeman energy induced by the external field. This movement leads to non-zero terms of $\frac{\mathrm{d}\vec{M}}{\mathrm{d}t}$ and follows, as a result, generating additional torques on the magnetization of the wall. These torques acting on $\vec{M}$ lead to a change of the magnetization profile of the wall. This change in velocity and torque continues until the whole system reaches a new state, where total energy and torque are minimized. In this state the magnetic texture of the wall is fixed again, and the velocity $\vec{v}$ is constant. This is the situation which is denoted as stead-state motion. From the two assumptions justified now, another fact can be directly concluded:

- The magnetization $\vec{M}$ of the domain wall can be represented in relation to an arbitrary point within the wall.

Since the magnetic texture of the wall is fixed during steady-state motion with velocity $\vec{v}$, all points of the wall move with the same velocity in the same direction. This implies that it is possible to choose an arbitrary point within the wall to parametrize the magnetic profile of the wall in relation to this point. As a further consequence, the motion of the wall can be reduced solely to the motion of this single point.

- The motion of a domain wall can be reduced to the motion of a single point within the wall.

Such points can be chosen arbitrarily, but it is convenient to select points which are characteristic and outstanding with respect to their symmetry within the wall. As it can be seen later on, an advantageous choice can simplify the calculation of the magnetization-dependent terms appearing in the Thiele equation; for example, such characteristic points can be the middle of a Bloch wall [44] or the position of a vortex core within a VDW [30]. In these cases the magnetization can be represented via the distance r' with regard to this point. Applying now all assumptions, it will become clear that the consequent application of the steady-state approximation has an important impact on the further mathematical treatment of the problem. To gain deeper insight, it is convenient

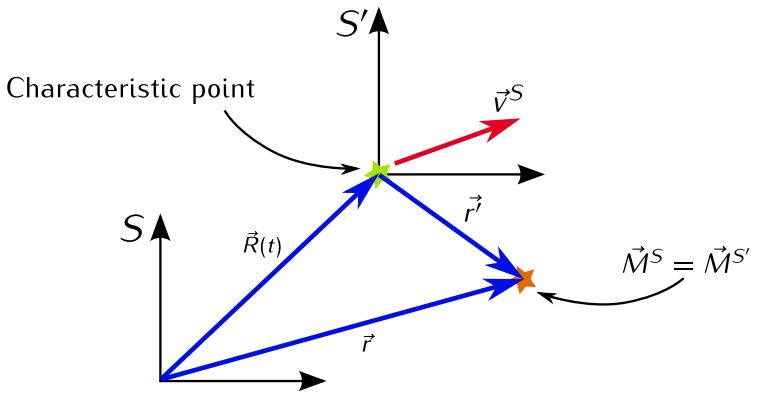

Figure 2.2. Sketch illustrating the geometric situation for the coordinate transformation from inertial system S to S' by Galilean transformation.

to start with a static case at time $t = t_0$, where the magnetization $\vec{M}$ at the point $\vec{r}$ is considered. Furthermore, the position of the characteristic point within the domain wall is chosen to be at $\vec{R}_0$. Having[1]

$$\vec{r} = \begin{pmatrix} x \\ y \\ z \end{pmatrix} \qquad \vec{R}_0 = \begin{pmatrix} X_0 \\ Y_0 \\ Z_0 \end{pmatrix} \qquad \vec{r'} = \begin{pmatrix} x' \\ y' \\ z' \end{pmatrix} \tag{2.38}$$

it is found for the distance $\vec{r'}$ between both points[1] [34, 35, 45] (see Fig. 2.2):

$$\vec{r'} = \vec{r} - \vec{R}_0 \tag{2.39}$$

$$\begin{pmatrix} x' \\ y' \\ z' \end{pmatrix} = \begin{pmatrix} x - X_0 \\ y - Y_0 \\ z - Z_0 \end{pmatrix} \tag{2.40}$$

From a more abstract point of view, $\vec{r'}$ is not solely the distance between the two points at position $\vec{r}$ and $\vec{R}_0$, it is the representation of $\vec{r}$ in a new coordinate system with its origin of ordinates at $\vec{R}_0$ additionally. What was found by the consequent application of the assumptions done before is nothing else than a change of coordinate system by a Galilean transformation [43, 46]. A Galilean transformation is one of the simplest transformations in physics, and, for example, it is used in classical mechanics to achieve the change from a coordinate system S to a new one S' which is shifted by a constant or time-dependent vector relative to the coordinate origin of the initial system S [43]. Like for every transformation, a change of variables is appearing which is based on a certain corresponding transformation rule. Regarding the Galilean transformation, it is the change from variable $\vec{r}$ (in S) to $\vec{r'}$ (in S') via the transformation rule $\vec{r'} = \vec{r} - \vec{R}_0$. Resulting from this, it is obtained for the magnetization in S and S' [1]

$$\vec{M}^S = \vec{M}^S(\vec{r}, \vec{R}_0) \qquad \text{and} \qquad \vec{M}^{S'} = \vec{M}^{S'}(\vec{r'}) \tag{2.41}$$

which yields that $\vec{M}^S$ is a function of both vectors while $\vec{M}^{S'}$ depends on $\vec{r'}$. In that which follows, it will be distinguished between the representation of

the magnetization $\vec{M}^S$ in the old and the magnetization $\vec{M}^{S'}$ in the new system. It is important to note that the values for $\vec{M}^S(\vec{r}, \vec{R}_0)$ and $\vec{M}^{S'}(\vec{r'})$ are the same because both are only two different representations of the magnetization $\vec{M}$ at a certain point. It can be obtained[1] [34]:

$$\vec{M}^S(\vec{r}, \vec{R}_0) = \vec{M}^{S'}(\vec{r'}) = \vec{M}^{S'}(\vec{r} - \vec{R}_0) \tag{2.42}$$

Going a step further and considering a DW which exhibits a steady-state motion with velocity $\dot{\vec{R}} = \vec{v}^S$ in the coordinate system S, a time-dependent vector $\vec{R}(t)$ for the position of the characteristic point is found and is given by[1] [34, 35]:

$$\vec{R}(t) = \vec{R}_0 + \dot{\vec{R}} \cdot t = \vec{R}_0 + \vec{v}^S \cdot t \tag{2.43}$$

Later on, when the considerations concerning the Galilean transformation are done, the velocity $\vec{v}^S$ will be set equal to $\vec{v}$, but for now lets keep the discrimination between the quantities in both coordinate systems. Talking about this kind of distinction, it should be noted that in principal it has to be written t and t' for the time in the coordinate system S and S', respectively. However, as usual for transformations of the Galilean type, the time in both systems is the same and it is common to set $t = t'$. Resulting from this, the time-dependent transformation rule for the Galilean transformation is given by[1] [34]

$$\vec{r'}(t) = \vec{r} - \vec{R}(t) \tag{2.44}$$

where the vector $\vec{r'}(t)$ is a function of t. Introducing the vectors $\vec{r'}(t)$, $\vec{R}(t)$, $\dot{\vec{R}}$ and $\vec{v}^S$ as[1]

$$\vec{r'} = \begin{pmatrix} x'(t) \\ y'(t) \\ z'(t) \end{pmatrix} \qquad \vec{R}(t) = \begin{pmatrix} X(t) \\ Y(t) \\ Z(t) \end{pmatrix} \qquad \dot{\vec{R}} = \begin{pmatrix} \dot{X} \\ \dot{Y} \\ \dot{Z} \end{pmatrix} \tag{2.45}$$

$$\vec{v}^S = \begin{pmatrix} v_x^S \\ v_y^S \\ v_z^S \end{pmatrix} \qquad \vec{v} = \begin{pmatrix} v_x \\ v_y \\ v_z \end{pmatrix} \tag{2.46}$$

it yields[1]:

$$\begin{pmatrix} X(t) \\ Y(t) \\ Z(t) \end{pmatrix} = \begin{pmatrix} X_0 + \dot{X} \cdot t \\ Y_0 + \dot{Y} \cdot t \\ Z_0 + \dot{Z} \cdot t \end{pmatrix} = \begin{pmatrix} X_0 + v_x^S \cdot t \\ Y_0 + v_x^S \cdot t \\ Z_0 + v_x^S \cdot t \end{pmatrix} \tag{2.47}$$

$$\begin{pmatrix} x'(t) \\ y'(t) \\ z'(t) \end{pmatrix} = \begin{pmatrix} x - X(t) \\ y - Y(t) \\ z - Z(t) \end{pmatrix} = \begin{pmatrix} x - X_0 - \dot{X} \cdot t \\ y - Y_0 - \dot{Y} \cdot t \\ z - Z_0 - \dot{Z} \cdot t \end{pmatrix} = \begin{pmatrix} x - X_0 - v_x^S \cdot t \\ y - Y_0 - v_y^S \cdot t \\ z - Z_0 - v_z^S \cdot t \end{pmatrix} \tag{2.48}$$

To clarify it, the assumption of a moving DW (or in general, a moving magnetic texture) with constant velocity leads to time dependencies for the vectors $\vec{R}(t)$ and $\vec{r'}(t)$. Since the magnetizations in both systems are functions of these vectors, they become time-dependent as well; but these time-dependencies leave

the conclusions done in the static case regarding the magnetizations $\vec{M}^S$ and $\vec{M}^{S'}$ in both systems unchanged. Again it is found for the dependencies of the magnetizations and the vectors[1]

$$\vec{M}^S(t) = \vec{M}^S(\vec{r}, \vec{R}(t)) \qquad \text{and} \qquad \vec{M}^{S'}(t) = \vec{M}^{S'}(\vec{r'}(t)) \tag{2.49}$$

which means that $\vec{M}^S$ is still a function of both vectors (but now with a time dependent $\vec{R}(t)$) while $\vec{M}^{S'}$ depends on $\vec{r'}(t)$. The same holds true for the statement that both values for the magnetizations $\vec{M}^S(\vec{r}, \vec{R}(t))$ and $\vec{M}^{S'}(\vec{r'}(t))$ are the same because, even when time dependent, they are only different representations of the magnetization at the same point[1].

$$\vec{M}^S(\vec{r}, \vec{R}(t)) = \vec{M}^{S'}(\vec{r'}(t)) = \vec{M}^{S'}(\vec{r} - \vec{R}(t)) \tag{2.50}$$

Founding on this prerequisites, it is possible to investigate the time derivative of the magnetizations in both coordinate systems, which will lead to a deeper insight of the effect of the steady-state approximation, and how this influences the further mathematical treatment of the problem. In a first step, the time derivative in both coordinate systems is performed, where it yields on the one hand side[1] [45]

$$\begin{aligned} \frac{\mathrm{d}\vec{M}^S(\vec{r}, \vec{R}(t))}{\mathrm{d}t} &= \frac{\partial \vec{M}^S(\vec{r}, \vec{R}(t))}{\partial \vec{r}} \underbrace{\frac{\partial \vec{r}}{\partial t}}_{=0} + \frac{\partial \vec{M}^S(\vec{r}, \vec{R}(t))}{\partial \vec{R}(t)} \underbrace{\frac{\partial \vec{R}(t)}{\partial t}}_{=\vec{v}^S} \\ &= \frac{\partial \vec{M}^S(\vec{r}, \vec{R}(t))}{\partial \vec{R}(t)} \vec{v}^S \end{aligned} \tag{2.51}$$

and on the other side[1]:

$$\begin{aligned} \frac{\mathrm{d}\vec{M}^{S'}(\vec{r'}(t))}{\mathrm{d}t} &= \frac{\partial \vec{M}^{S'}(\vec{r'}(t))}{\partial \vec{r'}(t)} \underbrace{\frac{\partial \vec{r'}(t)}{\partial t}}_{=\vec{v}^{S'}} \\ &= \frac{\partial \vec{M}^{S'}(\vec{r'}(t))}{\partial \vec{r'}(t)} \vec{v}^{S'} \end{aligned} \tag{2.52}$$

Here, the fact was utilized that the time evolution of the magnetization at a given point $\vec{r}$, which does not change in time, leads to $\frac{\partial \vec{r}}{\partial t} = 0$. At this stage of the consideration regarding the time change rate of the magnetization in the two frames, an important statement can already be concluded. While in the frame S the characteristic point at $\vec{R}(t)$ is moving with velocity $\vec{v}^S$, the motion in the new coordinate system S' is determined by the velocity of the point $\vec{r'}$; or in other words, while in S the observer is at rest, the characteristic point (and so the magnetic texture) is moving away from the point $\vec{r}$. In contradiction, in the moving frame S' it looks like the observer is sitting at the characteristic point, and now the point where $\frac{\mathrm{d}\vec{M}^{S'}}{\mathrm{d}t}$ has to be determined is moving away with velocity $\vec{v}^{S'}$. This means that by changing the coordinate system S to S', the motion is shifted from the characteristic point to the observer. The velocity $\vec{v}^{S'}$ can be determined in terms of $\vec{v}^S$ by exploiting the concrete expression for $\vec{r'}(t) = \vec{r} - \vec{R}(t)$, which follows the transformation rule of the Galilean transformation[1].

$$\frac{\partial \vec{r'}(t)}{\partial t} = \frac{\partial}{\partial t}\left(\vec{r} - \vec{R}(t)\right) = -\frac{\partial \vec{R}(t)}{\partial t} = -\dot{\vec{R}}(t) = -\vec{v}^{S} \tag{2.53}$$

This leads to[1] [34, 35]

$$\frac{\mathrm{d}\vec{M}^{S'}(\vec{r'}(t))}{\mathrm{d}t} = \frac{\partial \vec{M}^{S'}(\vec{r'}(t))}{\partial \vec{r'}(t)}\left(-\vec{v}^{S}\right) \tag{2.54}$$

and by comparison to the value of $\vec{v}^{S'}$ in terms of $\vec{v}^{S}$ [1] one gets:

$$\vec{v}^{S'} = -\vec{v}^{S} \tag{2.55}$$

Here, a second important impact of the change into the moving coordinate system was obtained. It has already been stated earlier that in S' the point, where the magnetization has to be investigated, is moving with velocity $\vec{v^{S'}}$. It becomes clear that in the moving frame S' it looks like the point $\vec{r'}(t)$ would move with the same velocity $\vec{v}^{S}$ as the characteristic point is moving in S; but in contradiction, $\vec{r'}(t)$ is moving in the opposite direction as the characteristic point, which is stated by the minus sign. As it will become more clear later on, the possibility to express $\vec{v}^{S'}$ in relation to $\vec{v}^{S}$ is very helpful for the further mathematical treatment. Continuing with the considerations, the identity of $\vec{M}^{S}(\vec{r},\vec{R}(t))$ and $\vec{M}^{S'}(\vec{r'}(t))$ will be exploited. The equality of both expressions also implies that the time derivative for both is the same. This yields[1]

$$\frac{\mathrm{d}\vec{M}^{S}(\vec{r},\vec{R}(t))}{\mathrm{d}t} = \frac{\mathrm{d}\vec{M}^{S'}(\vec{r'}(t))}{\mathrm{d}t} \tag{2.56}$$

and in combination with the preliminary work in this section it yields[1]:

$$\frac{\partial \vec{M}^{S}(\vec{r},\vec{R}(t))}{\partial \vec{R}(t)}\vec{v}^{S} = \frac{\partial \vec{M}^{S'}(\vec{r'}(t))}{\partial \vec{r'}(t)}\left(-\vec{v}^{S}\right) \tag{2.57}$$

What has been found so far is that the time derivative in the steady-state motion regime can be expressed as the product of the spatial gradient of the magnetization and the steady-state velocity. This holds true for both coordinate systems S and S' but in both cases the gradient are time dependent. Although, in the moving coordinate system S' - in this frame it has already been stated that the motion is shifted from the magnetic texture to the point $\vec{r'}(t)$ - the total derivative with respect to t is not purely given by the velocity. As it will be seen, a total decoupling of the spatial gradients from time t in the moving system S' can be achieved. This can be done by making a change of variables in S' from $\vec{r'}(t)$ to $\vec{r}$. For this task, $\vec{r}$ has to be expressed in terms of $\vec{r'}(t)$ what can be obtained by transponing the equation for the transformation rule[1]

$$\vec{r'}(t) = \vec{r} - \vec{R}(t) \qquad \rightarrow \qquad \vec{r} = \vec{r'}(t) + \vec{R}(t) \tag{2.58}$$

and by calculating the partial derivative of $\vec{r}$ with respect to $\vec{r'}(t)$; this yields the new partial derivative[1]:

$$\frac{\partial \vec{r}}{\partial \vec{r'}} = 1 \qquad \rightarrow \qquad \frac{\partial}{\partial \vec{r'}(t)} = \frac{\partial}{\partial \vec{r}} \tag{2.59}$$

It can be understood intuitively that both partial derivatives are the same. The reason for this is that both vectors describe the same point, and when the position of this point is changed by an infinitesimal span, then the effect on $\vec{r}$ and $\vec{r'}(t)$ has to be the same. Using this result, it yields[1]

$$\frac{\partial \vec{M}^S(\vec{r}, \vec{R}(t))}{\partial \vec{R}(t)} \vec{v}^S = \frac{\partial \vec{M}^{S'}(\vec{r'}(t))}{\partial \vec{r}} \left(-\vec{v}^S\right) \tag{2.60}$$

and it is obtained that the partial derivative of $\vec{M}^{S'}(\vec{r'}(t))$ considering the vector $\vec{r}$ is now independent on time. Although $\vec{M}^{S'}(\vec{r'}(t))$ is a function of t, it can be understood by the fact that $\vec{r'}(t))$ depends on two variables, namely $\vec{r}$ and $\vec{R}(t)$.

Applying the partial derivative with respect to $\vec{r}$, it has the same effect as when the other variable $\vec{R}(t)$ is regarded as constant and the derivative regarding $\vec{r}$ can be calculated.

Thus, only the time independent vector $\vec{r}$ is important for the calculation of the partial derivative and the spatial gradient in S' which becomes independent of t as well. This leads to the conclusion that in the moving coordinate system S', the spatial derivative is independent of time, and it is possible to shift the time dependence purely into the time change rate $\dot{\vec{R}}(t)$ of the position $\vec{R}(t)$, namely the velocity $\vec{v}^S$. Another interesting and useful outcome of the calculations becomes clear when the minus sign on the right hand side of the velocity it put in front of the partial derivative[1].

$$\frac{\partial \vec{M}^S(\vec{r}, \vec{R}(t))}{\partial \vec{R}(t)} \vec{v}^S = -\frac{\partial \vec{M}^{S'}(\vec{r'}(t))}{\partial \vec{r}} \vec{v}^S \tag{2.61}$$

Using the fact that $\vec{M}^S(\vec{r}, \vec{R}(t))$ and $\vec{M}^{S'}(\vec{r'}(t))$ are equal,

$$\frac{\partial \vec{M}^S(\vec{r}, \vec{R}(t))}{\partial \vec{R}(t)} \vec{v}^S = -\frac{\partial \vec{M}^S(\vec{r}, \vec{R}(t))}{\partial \vec{r}} \vec{v}^S \tag{2.62}$$

it becomes obvious that it is possible to perform the Galilean transformation from S to S' simply by replacing $\frac{\partial}{\partial \vec{R}(t)}$ by $-\frac{\partial}{\partial \vec{r}}$, yielding the following substitution relation[1] [45]

$$\frac{\partial}{\partial \vec{R}(t)} \quad \rightarrow \quad -\frac{\partial}{\partial \vec{r}} \tag{2.63}$$

or in component-wise representation[1] [45]:

$$\frac{\partial}{\partial X_i(t)} \quad \rightarrow \quad -\frac{\partial}{\partial x_i} \tag{2.64}$$

It should be noted that the substitution relation depends on the concrete form of the transformation relation which determines $\vec{r'}(t)$. The substitution relation which has been obtained is, of course, only valid for $\vec{r'}(t) = \vec{r} - \vec{R}(t)$. For Galilean transformations, which exhibit other forms, the corresponding substitution rule has to be determined anew. In fact, this relation is the most important in this section because it yields a deep insight into the physical nature of the steady-

state approximation and the Thiele equation, respectively. Interpreting this, it states that there is a connection between the change of $\vec{M}$ with respect to the position of the characteristic point and the change rate of $\vec{M}$ with respect to the point $\vec{r}$. Though the minus sign is neglected, this statement remains valid. This is striking because on the one side, the position vector of the characteristic point, which is determined by a collection of few singe coordinates, is considered, and on the other hand, a general vector $\vec{r}$ that can describe every point in the sample is dealt with. More precisely, the exchange rule obtained between $\frac{\partial}{\partial \vec{R}(t)}$ and $-\frac{\partial}{\partial \vec{r}}$ via Galilean transformation yields that it is possible to describe the motion of a magnetic texture in the frame of the steady-state approximation with a small set of collective coordinates. This fact is emphasized more in the so called collective coordinate approach (CCA) [45, 47], which is, by the inclusion of some other things, a generalization of Thiele's approach to DWM. This will be explained in more detail in Sec. 2.3.2.1. In the following, the distinction between quantities in the frame S and S' will be omitted respectively because $\vec{M}$ is the same in both frames. For now it will be used only $\vec{M}$ instead of $\vec{M}^S$ or $\vec{M}^{S'}$. With this framework, it is possible to obtain the single force density terms in the approximation for steady-state motion[1]:

$$
\begin{aligned}
&\vec{f}^{\mathrm{m}} = -\mu_0 \left(\frac{\partial \vec{M}}{\partial \vec{r}}\right)^{\mathrm{T}} \vec{H}^{\mathrm{m}} = \mu_0 \beta \left(\frac{\partial \vec{M}}{\partial \vec{r}}\right)^{\mathrm{T}} \vec{M} \\
&\text{(magnetization equivalent force density)} \\
&\vec{f}^{\mathrm{f}} = -\mu_0 \left(\frac{\partial \vec{M}}{\partial \vec{r}}\right)^{\mathrm{T}} \vec{H}^{\mathrm{f}} = -\mu_0 \left(\frac{\partial \vec{M}}{\partial \vec{r}}\right)^{\mathrm{T}} \vec{H}_{\mathrm{ext}} \\
&\text{(force density)} \\
&\vec{f}^{\alpha} = -\mu_0 \left(\frac{\partial \vec{M}}{\partial \vec{r}}\right)^{\mathrm{T}} \vec{H}^{\alpha} = \frac{\mu_0 \alpha}{\gamma_0 M_{\mathrm{s}}} \left(\frac{\partial \vec{M}}{\partial \vec{r}}\right)^{\mathrm{T}} \left(\frac{\partial \vec{M}}{\partial \vec{r}}\right) (-\vec{v}) \\
&\text{(damping equivalent force density)} \\
&\vec{f}^{\mathrm{g}} = -\mu_0 \left(\frac{\partial \vec{M}}{\partial \vec{r}}\right)^{\mathrm{T}} \vec{H}^{\mathrm{g}} = \frac{\mu_0}{\gamma_0 M_{\mathrm{s}}^2} \left(\frac{\partial \vec{M}}{\partial \vec{r}}\right)^{\mathrm{T}} \left(\vec{M} \times \left(\left(\frac{\partial \vec{M}}{\partial \vec{r}}\right) (-\vec{v})\right)\right) \\
&\text{(gyroscopioc force density)}
\end{aligned}
\tag{2.65}
$$

Evaluating these expressions for the force densities in more detail, the partial derivatives of $\vec{M}$ with respect to the vector $\vec{r}$ will be considered closely. In a first step, the total time differential for each component M_j (with $j = x, y, z$) of the magnetization $\vec{M}$ is taken, yielding in[1]:

$$\frac{\mathrm{d}\vec{M}}{\mathrm{d}t} = \begin{pmatrix} \frac{\mathrm{d}M_x}{\mathrm{d}t} \\ \frac{\mathrm{d}M_y}{\mathrm{d}t} \\ \frac{\mathrm{d}M_z}{\mathrm{d}t} \end{pmatrix} = \begin{pmatrix} \frac{\partial M_x}{\partial X}\frac{\partial X}{\partial t} + \frac{\partial M_x}{\partial Y}\frac{\partial Y}{\partial t} + \frac{\partial M_x}{\partial Z}\frac{\partial Z}{\partial t} \\ \frac{\partial M_y}{\partial X}\frac{\partial X}{\partial t} + \frac{\partial M_y}{\partial Y}\frac{\partial Y}{\partial t} + \frac{\partial M_y}{\partial Z}\frac{\partial Z}{\partial t} \\ \frac{\partial M_z}{\partial X}\frac{\partial X}{\partial t} + \frac{\partial M_z}{\partial Y}\frac{\partial Y}{\partial t} + \frac{\partial M_z}{\partial Z}\frac{\partial Z}{\partial t} \end{pmatrix} = \underbrace{\begin{pmatrix} \frac{\partial M_x}{\partial X} & \frac{\partial M_x}{\partial Y} & \frac{\partial M_x}{\partial Z} \\ \frac{\partial M_y}{\partial X} & \frac{\partial M_y}{\partial Y} & \frac{\partial M_y}{\partial Z} \\ \frac{\partial M_z}{\partial X} & \frac{\partial M_z}{\partial Y} & \frac{\partial M_z}{\partial Z} \end{pmatrix}}_{=\frac{\partial \vec{M}}{\partial \vec{R}(t)}} \begin{pmatrix} \frac{\partial X}{\partial t} \\ \frac{\partial Y}{\partial t} \\ \frac{\partial Z}{\partial t} \end{pmatrix} \tag{2.66}$$

Applying the substitution rule Eq. (2.63) (Eq. (2.64) respectively) derived in this section, the partial derivatives considering the position of the characteristic point can be expressed as partial derivatives with respect to the coordinates x_i (with $i = x, y, z$)[1].

$$\frac{\mathrm{d}\vec{M}}{\mathrm{d}t} = \underbrace{\begin{pmatrix} -\frac{\partial M_x}{\partial x} & -\frac{\partial M_x}{\partial y} & -\frac{\partial M_x}{\partial z} \\ -\frac{\partial M_y}{\partial x} & -\frac{\partial M_y}{\partial y} & -\frac{\partial M_y}{\partial z} \\ -\frac{\partial M_z}{\partial x} & -\frac{\partial M_z}{\partial y} & -\frac{\partial M_z}{\partial z} \end{pmatrix}}_{=-\frac{\partial \vec{M}}{\partial \vec{r}}} \underbrace{\begin{pmatrix} \frac{\partial X}{\partial t} \\ \frac{\partial Y}{\partial t} \\ \frac{\partial Z}{\partial t} \end{pmatrix}}_{=\vec{v}} \tag{2.67}$$

Shifting in a last step, the minus sign from the partial derivatives of M_j to the velocities, the expressions[1]

$$\frac{\mathrm{d}\vec{M}}{\mathrm{d}t} = \underbrace{\begin{pmatrix} \frac{\partial M_x}{\partial x} & \frac{\partial M_x}{\partial y} & \frac{\partial M_x}{\partial z} \\ \frac{\partial M_y}{\partial x} & \frac{\partial M_y}{\partial y} & \frac{\partial M_y}{\partial z} \\ \frac{\partial M_z}{\partial x} & \frac{\partial M_z}{\partial y} & \frac{\partial M_z}{\partial z} \end{pmatrix}}_{=\frac{\partial \vec{M}}{\partial \vec{r}}=J_{\vec{M}}} \underbrace{\begin{pmatrix} -v_x \\ -v_y \\ -v_z \end{pmatrix}}_{=-\vec{v}} \tag{2.68}$$

are found, and it can be recognized that the matrix given by $\frac{\partial \vec{M}}{\partial \vec{r}}$ is nothing else than the Jacobian matrix J of the magnetization $\vec{M}$. As a note, this matrix will be denoted in the following as $J_{\vec{M}}$. Resulting from this, it is possible to write the total time derivative of the magnetization in terms of the Jacobian matrix $J_{\vec{M}}$ and the (negative) velocity vector $\vec{v}$ [1].

$$\frac{\mathrm{d}\vec{M}}{\mathrm{d}t} = \left(\frac{\partial \vec{M}}{\partial \vec{r}}\right)(-\vec{v}) = J_{\vec{M}}(-\vec{v}) \tag{2.69}$$

Identifying $\frac{\partial \vec{M}}{\partial \vec{r}}$ as $J_{\vec{M}}$ is indeed very helpful to get a deeper insight into the terms appearing in the Thiele equation because it enables the application of methods of tensor calculus. Applying mathematical methods of tensor calculus will simplify the task of evaluating the expressions for $\vec{f}^{\mathrm{m}}$, $\vec{f}^{\mathrm{t}}$, $\vec{f}^{\alpha}$ and $\vec{f}^{\mathrm{g}}$. It will become clear later on that for the further mathematical treatment of the force density terms, it is convenient to express the Jacobian matrix of $\vec{M}$ in tensor notation which reads [41]:

$$J_{\vec{M}} = \sum_{ij} \frac{\partial M_j}{\partial x_i} \left(\vec{e}_j \otimes \vec{e}_i\right) \tag{2.70}$$

To understand this unfamiliar notation, a short introduction into tensor calculation with the outer product will be given in the appendix A1.

2.2.3.2 Magnetization Equivalent Term

The magnetization equivalent term for the force density is given by [34]

$$\vec{f}^{\mathrm{m}} = -\mu_0 \sum_{ij} \frac{\partial M_j}{\partial x_i} \left(\vec{e}_i \otimes \vec{e}_j\right) \cdot \vec{H}_j^{\mathrm{m}} \tag{2.71}$$

where $\vec{H}_{\mathrm{m}}$ is represented by [34]

$$\vec{H}^{\mathrm{m}} = -\beta \vec{M} = -\beta \sum_j \vec{M}_j \tag{2.72}$$

and $\vec{H}_j^{\mathrm{m}}$ can be written as $-\beta M_j \vec{e}_j$. Inserting this expression into the first one and applying component-wise notation[1]

$$\vec{f}^{\mathrm{m}} = \mu_0 \beta \sum_{ij} \frac{\partial M_j}{\partial x_i} M_j \left(\vec{e}_i \otimes \vec{e}_j\right) \cdot \vec{e}_j \tag{2.73}$$

it is obtained as formula which can be converted into the form[1]:

$$\vec{f}^{\mathrm{m}} = \frac{\mu_0 \beta}{2} \sum_i \left(\vec{e}_i \frac{\partial}{\partial x_i}\right) \left(\vec{M} \cdot \vec{M}\right) = 0 \tag{2.74}$$

Since $\vec{M} \cdot \vec{M} = M_{\mathrm{s}}^2$ and the saturation magnetization is assumed to be spatial constant [34], the partial derivatives of M_{s}^2 with respect to the coordinates x_i are equal zero. This leads to a vanishing magnetization equivalent force density $\vec{f}^{\mathrm{m}}$ [34].

2.2.3.3 Force Term

For the force density term arising from the external applied field, it yields [34]

$$\vec{f}^{\mathrm{f}} = -\mu_0 \sum_{ij} \frac{\partial M_j}{\partial x_i} \left(\vec{e}_i \otimes \vec{e}_j\right) \cdot \vec{H}_j^{\mathrm{f}} \quad , \tag{2.75}$$

where the corresponding field is given by the external field $\vec{H}_{\mathrm{ext}}$ itself [34]:

$$\vec{H}^{\mathrm{f}} = \vec{H}^{\mathrm{ext}} = \vec{H} = \sum_j \vec{H}_j \tag{2.76}$$

The components for the vector $\vec{H}^{\mathrm{f}}$ are found to be $\vec{H}_j^{\mathrm{f}} = \vec{H}_j = H_j \vec{e}_j$, which result in[1]

$$\vec{f}^{\mathrm{f}} = -\mu_0 \sum_{ij} \frac{\partial M_j}{\partial x_i} H_j \left(\vec{e}_i \otimes \vec{e}_j\right) \cdot \vec{e}_j \tag{2.77}$$

as a formula for the force density. Expressing the external field $\vec{H}$ via the variation derivative of the energy density $\mathcal{E}$ with respect to the magnetization $\vec{M}$, the term for $\vec{f}^{\,\mathrm{f}}$ reduces it to a very simple form[1].

$$\vec{f}^{\,\mathrm{f}} = \sum_i \frac{\partial \vec{M}}{\partial x_i} \cdot \frac{\delta \mathcal{E}}{\delta \vec{M}} \vec{e}_i = \sum_i \vec{e}_i \frac{\partial \mathcal{E}}{\partial x_i} = \vec{\nabla} \mathcal{E} \tag{2.78}$$

This result states that the force density is given by the gradient of the energy density of the physical system. However, since it is the goal to obtain an equivalent force density equation for the motion of a magnetic DW, the force vector $\vec{F}^{\mathrm{f}}$ from $\vec{f}^{\,\mathrm{f}}$ has to be calculated. This can be done by integrating over the whole volume V of the sample[1].

$$\vec{F}^{\,\mathrm{f}} = \sum_i \int_V \vec{e}_i \frac{\partial \mathcal{E}}{\partial x_i} \,\mathrm{d}V = \int_V \vec{\nabla} \mathcal{E} \,\mathrm{d}V \tag{2.79}$$

Since the order of taking the derivative and the integration does not matter (they are interchangeable), the energy density $\mathcal{E}$ is integrated over the volume V. This integral yields the total energy E of the system. What follows from this is the force vector which is given by [34, 45]:

$$\vec{F}^{\,\mathrm{f}} = \vec{\nabla} \int_V \mathcal{E} \,\mathrm{d}V = \vec{\nabla} E \tag{2.80}$$

For the sake of clarity, it should be mentioned that the energy E is equal to the potential U used later on in the considerations in Sec. 2.3.2.4.

2.2.3.4 Damping Equivalent Term

Viscosity, like dissipation, leads to a force density which acts on the VC as well. The density $\vec{f}^{\alpha}$ is [34]

$$\vec{f}^{\alpha} = -\mu_0 \sum_{ij} \frac{\partial M_j}{\partial x_i} (\vec{e}_i \otimes \vec{e}_j) \cdot \vec{H}_j^{\alpha} \tag{2.81}$$

where the field $\vec{H}^{\alpha}$, originating from the Gilbert damping term in the LLG eq., takes the form[1]:

$$\vec{H}^{\alpha} = -\frac{\alpha}{\gamma_0 M_\mathrm{s}} \sum_{jk} \frac{\partial M_j}{\partial x_k} (\vec{e}_j \otimes \vec{e}_k) \cdot (-v_k) \, \vec{e}_k \tag{2.82}$$

Writing $(-v_k)\,\vec{e}_k$ as $-\vec{v}_k$ and omitting the summation over the index j, the j-component for $\vec{H}^{\alpha}$ is gained [34].

$$\vec{H}_j^{\alpha} = -\frac{\alpha}{\gamma_0 M_\mathrm{s}} \sum_{k} \frac{\partial M_j}{\partial x_k} (\vec{e}_j \otimes \vec{e}_k) \cdot (-\vec{v}_k) \tag{2.83}$$

By inserting this result into Eq. (2.81), it yields the force density $\vec{f}^{\alpha}$ [34].

$$\vec{f}^{\alpha} = \frac{\alpha \mu_0}{\gamma_0 M_\mathrm{s}} \sum_{ijk} \frac{\partial M_j}{\partial x_i} \frac{\partial M_j}{\partial x_k} (\vec{e}_i \otimes \vec{e}_j) (\vec{e}_j \otimes \vec{e}_k) \cdot (-\vec{v}_k) \tag{2.84}$$

Applying tensor algebra by utilizing the relation $(\vec{e}_i \otimes \vec{e}_j)\,(\vec{e}_j \otimes \vec{e}_k) = \delta_{jj}\,(\vec{e}_i \otimes \vec{e}_k)$, writing δ_{jj} as $\vec{e}_j \cdot \vec{e}_j$ and assigning the base vectors $\vec{e}_j$ to the corresponding component of the magnetization[1], one gets

$$\vec{f}^{\alpha} = \frac{\alpha\mu_0}{\gamma_0 M_\mathrm{s}} \sum_{ijk} \left(\frac{\partial M_j}{\partial x_i} \vec{e}_j \right) \cdot \left(\frac{\partial M_j}{\partial x_k} \vec{e}_j \right) (\vec{e}_i \otimes \vec{e}_k) \cdot (-\vec{v}_k) \tag{2.85}$$

as the preliminary result. Then, summing over j, the full magnetization vectors $\vec{M}$ are recovered and the equation for the force density is given by[1]:

$$\vec{f}^{\alpha} = \frac{\alpha\mu_0}{\gamma_0 M_\mathrm{s}} \sum_{ik} \left(\frac{\partial \vec{M}}{\partial x_i} \right) \cdot \left(\frac{\partial \vec{M}}{\partial x_k} \right) (\vec{e}_i \otimes \vec{e}_k) \cdot (-\vec{v}_k) \tag{2.86}$$

Like before, the integration over V has to be carried out to obtain the force vector $\vec{F}^{\alpha}$ [45].

$$\vec{F}^{\alpha} = \sum_{ik} \underbrace{\frac{\alpha\mu_0}{\gamma_0 M_\mathrm{s}} \left\{ \int_V \left(\frac{\partial \vec{M}}{\partial x_i} \right) \cdot \left(\frac{\partial \vec{M}}{\partial x_k} \right) \mathrm{d}V \right\}}_{=\Gamma_{ik}} (\vec{e}_i \otimes \vec{e}_k) \cdot (-\vec{v}_k) \tag{2.87}$$

The integral over the spatial gradients of $\vec{M}$ plus prefactor are defined as the component ik of the damping tensor Γ in literature. Applying this definition, a rather compact form for the force vector $\vec{F}^{\alpha}$ is obtained [45].

$$\vec{F}^{\alpha} = \sum_{ik} \Gamma_{ik} \cdot (-\vec{v}_k) = -\Gamma \cdot \vec{v} \tag{2.88}$$

Thereby, the complete tensor Γ originates by summing over all components Γ_{ik} [45]

$$\Gamma = \sum_{ik} \frac{\alpha\mu_0}{\gamma_0 M_\mathrm{s}} \left\{ \int_V \left(\frac{\partial \vec{M}}{\partial x_i} \right) \cdot \left(\frac{\partial \vec{M}}{\partial x_k} \right) \mathrm{d}V \right\} (\vec{e}_i \otimes \vec{e}_k) \tag{2.89}$$

and it is worth mentioning that this is the representation for Γ in Cartesian coordinates. Strictly spoken, the magnetization $\vec{M} = \vec{M}(x, y, z)$ is a function of the three spatial coordinates x, y and z. As it becomes clear later on, due to symmetry reasons it is convenient to parametrize the magnetization in other coordinates, for example, spherical or cylindrical ones. Next, the reformulation of the tensor Γ in terms of arbitrary coordinates is performed. For this purpose, it is assumed that the magnetization is depending on a general set of the coordinates $x_{i'}$ and $x_{k'}$. It is important to mention that although, $x_{i'}$ and $x_{k'}$ are coordinates of the same coordinate system, mathematically they have to be treated as independent ones. Using Eq. (2.89) as starting point and taking the partial derivatives with respect to the new coordinates[1],

$$\Gamma = \int_V \left(\frac{\alpha\mu_0}{\gamma_0 M_\mathrm{s}} \sum_{\substack{ik \\ i'k'}} \left\{ \frac{\partial \vec{M}}{\partial x_{i'}} \frac{\partial x_{i'}}{\partial x_i} \right\} \cdot \left\{ \frac{\partial \vec{M}}{\partial x_{k'}} \frac{\partial x_{k'}}{\partial x_k} \right\} (\vec{e}_i \otimes \vec{e}_k) \right) \mathrm{d}V \tag{2.90}$$

is obtained. The partial derivatives of $\vec{M}$ with respect to $x_{i'}$ and $x_{k'}$ respectively, yield the associated basis vectors ($\vec{e}_{x_{i'}}$, $\vec{e}_{x_{k'}}$) in combination with a prefactor ($A_{x_{i'}}$, $A_{x_{k'}}$)[1].

$$\Gamma = \int_V \left(\frac{\alpha\mu_0}{\gamma_0 M_\mathrm{s}} \sum_{\substack{ik \\ i'k'}} \left\{ A_{i'} \vec{e}_{i'} \frac{\partial x_{i'}}{\partial x_i} \right\} \cdot \left\{ A_{k'} \vec{e}_{k'} \frac{\partial x_{k'}}{\partial x_k} \right\} (\vec{e}_i \otimes \vec{e}_k) \right) \mathrm{d}V \tag{2.91}$$

Combining $\vec{e}_{x_{i'}}$ and $\vec{e}_{x_{k'}}$ to $\delta_{i'k'}$, summing over i' and assigning the outer product to the corresponding partial derivatives, the expression[1]

$$\Gamma = \int_V \left(\frac{\alpha\mu_0}{\gamma_0 M_\mathrm{s}} \sum_{ikk'} \left\{ A_{k'} \vec{e}_i \frac{\partial x_{k'}}{\partial x_i} \right\} \otimes \left\{ A_{k'} \vec{e}_k \frac{\partial x_{k'}}{\partial x_k} \right\} \right) \mathrm{d}V \tag{2.92}$$

is gained. Carrying out the summation over i and k, it yields the nabla operator $\vec{\nabla}$ in Cartesian coordinates[1].

$$\Gamma = \sum_{k'} \frac{\alpha\mu_0}{\gamma_0 M_\mathrm{s}} \int_V \left(\left\{ A_{k'} \vec{\nabla} x_{k'} \right\} \otimes \left\{ A_{k'} \vec{\nabla} x_{k'} \right\} \right) \mathrm{d}V \tag{2.93}$$

The coefficients $A_{k'}$ are identified as the square root of the diagonal elements $g_{k'k'}$ of the metric tensor g in the corresponding coordinate system [41, 48]. Since dealing with Euclidean coordinate systems, where only the diagonal elements differ from zero [41], it is obtained for Γ [1]:

$$\begin{aligned} \Gamma &= \sum_{k'} \frac{\alpha\mu_0}{\gamma_0 M_\mathrm{s}} \int_V \left(\left\{ \sqrt{g_{k'k'}}\, \vec{\nabla} x_{k'} \right\} \otimes \left\{ \sqrt{g_{k'k'}}\, \vec{\nabla} x_{k'} \right\} \right) \mathrm{d}V \\ &= \sum_{k'} \frac{\alpha\mu_0}{\gamma_0 M_\mathrm{s}} \int_V g_{k'k'} \left(\left\{ \vec{\nabla} x_{k'} \right\} \otimes \left\{ \vec{\nabla} x_{k'} \right\} \right) \mathrm{d}V \end{aligned} \tag{2.94}$$

On base of this generalized formula, it is possible to formulate the equation for Γ in every desired coordinate system. The metric tensor itself results in Euclidean coordinate systems from $g = J^\mathrm{T} J$, where J and J^T are the Jacobian matrix and the transposed one respectively [41, 48]. Please note that the nabla operator $\vec{\nabla}$ is still in Cartesian coordinates requiring $x_{k'}$ to be a function of x, y and z. However, sometimes it is convenient for symmetry reasons to express the coordinates $x_{k'}$ as functions of curvilinear coordinates, e.g. cylindrical ones. In this case, the nabla operator and also the integration have to be performed in the corresponding coordinates. To conclude the general considerations concerning the damping dyadic, Γ will be calculated in spherical and cylindrical coordinates because they represent the most common curvilinear systems of coordinates. For spherical ones, the coefficients $A_{M_\mathrm{s}} = 1$, $A_\vartheta = M_\mathrm{s}$ and $A_\varphi = M_\mathrm{s} \sin(\varphi)$ are obtained[1] and result in[1] [34, 35]

$$\Gamma = \frac{\alpha\mu_0 M_\mathrm{s}}{\gamma_0} \int_V \left(\left\{ \vec{\nabla}\vartheta \right\} \otimes \left\{ \vec{\nabla}\vartheta \right\} + \sin^2(\vartheta) \left\{ \vec{\nabla}\varphi \right\} \otimes \left\{ \vec{\nabla}\varphi \right\} \right) \mathrm{d}V \tag{2.95}$$

for the damping tensor. Turning to cylindrical ones, $A_{M_\mathrm{s}} = 1$, $A_\varphi = M_\mathrm{s}$ and $A_z = 0$ is obtained, which yields[1]:

$$\Gamma = \frac{\alpha \mu_0 M_\mathrm{s}}{\gamma_0} \int\limits_V \left(\left\{ \vec{\nabla} \varphi \right\} \otimes \left\{ \vec{\nabla} \varphi \right\} \right) \mathrm{d}V \tag{2.96}$$

When comparing the expressions for Γ in both coordinate systems, it can be recognized that the latter one is a special case of the formulation in spherical coordinates; Γ in cylindrical coordinates arises when setting $\vartheta = \frac{\pi}{2} = const$ in the spherical coordinate system.

2.2.3.5 Gyroscopic Term

The last term that is going to be investigated is the gyroscopic force term, which originates from the precessional term in the LLG equation. Starting again with the formula for the force density vector $\vec{f}^{\mathrm{g}}$ [34]

$$\vec{f}^{\mathrm{g}} = -\mu_0 \sum_{ij} \frac{\partial M_j}{\partial x_i} \left(\vec{e}_i \otimes \vec{e}_j \right) \cdot \vec{H}_j^{\mathrm{g}} \tag{2.97}$$

and inserting the corresponding equivalent gyroscopic field $\vec{H}_j^{\mathrm{g}}$ into the equation, it reads [34]

$$\vec{H}_j^{\mathrm{g}} = -\frac{1}{\gamma_0 M_\mathrm{s}^2} \sum_{klm} M_k \frac{\partial M_l}{\partial x_m} \left(\vec{e}_l \otimes \vec{e}_m \right) \left(-\vec{v}_m \right) \delta_{lj} \epsilon_{klj} \tag{2.98}$$

and as result one gets[1]:

$$\vec{f}^{\mathrm{g}} = \frac{\mu_0}{\gamma_0 M_\mathrm{s}^2} \sum_{ijklm} \frac{\partial M_j}{\partial x_i} M_k \frac{\partial M_l}{\partial x_m} \left(\vec{e}_i \otimes \vec{e}_j \right) \left(\vec{e}_l \otimes \vec{e}_m \right) \left(-\vec{v}_m \right) \delta_{lj} \epsilon_{klj} \tag{2.99}$$

Using the relation $\left(\vec{e}_i \otimes \vec{e}_j \right) \left(\vec{e}_l \otimes \vec{e}_m \right) = \delta_{jl} \left(\vec{e}_i \otimes \vec{e}_m \right)$ for the next calculation steps and expressing the Levi-Civita symbol by an equivalent vector notation $\epsilon_{klj} = \{ (\vec{e}_k \times \vec{e}_l) \cdot \vec{e}_j \}$, it yields [34]

$$\vec{f}^{\mathrm{g}} = \frac{\mu_0}{\gamma_0 M_\mathrm{s}^2} \sum_{ijklm} \frac{\partial M_j}{\partial x_i} M_k \frac{\partial M_l}{\partial x_m} \left\{ (\vec{e}_k \times \vec{e}_l) \cdot \vec{e}_j \right\} \left(\vec{e}_i \otimes \vec{e}_m \right) \left(-\vec{v}_m \right) \tag{2.100}$$

as intermediate result. Expressing ϵ_{klj} by basis vectors allows you to assign the corresponding components to the associated vectors $\vec{e}_k$, $\vec{e}_l$ and $\vec{e}_j$. Summing over the indices i, j and k, the magnetization vector $\vec{M}$ is recovered and for $\vec{f}^{\mathrm{g}}$, which yields[1]:

$$\vec{f}^{\mathrm{g}} = \frac{\mu_0}{\gamma_0 M_\mathrm{s}^2} \sum_{im} \vec{M} \cdot \left\{ \left(\frac{\partial \vec{M}}{\partial x_i} \right) \times \left(\frac{\partial \vec{M}}{\partial x_m} \right) \right\} \left(\vec{e}_i \otimes \vec{e}_m \right) \left(\vec{v}_m \right) \tag{2.101}$$

Integrating over the total volume, V gains the vector of the gyroscopic force $\vec{F}^{\mathrm{g}}$ [45]

$$\vec{F}^{\mathrm{g}} = \sum_{im} \underbrace{\frac{\mu_0}{\gamma_0 M_{\mathrm{s}}^2} \int_V \vec{M} \cdot \left\{ \left(\frac{\partial \vec{M}}{\partial x_i} \right) \times \left(\frac{\partial \vec{M}}{\partial x_m} \right) \right\} \mathrm{d}V \, (\vec{e}_i \otimes \vec{e}_m)}_{=G_{im}} (\vec{v}_m) \tag{2.102}$$

where the volume integral over the magnetization vectors together with the prefactor are combined as the component G_{ij} of the gyroscopic tensor G. Based on this definition, the following compact notation for the vector of the gyroscopic force $\vec{F}^{\mathrm{g}}$ is gained [45].

$$\vec{F}^{\mathrm{g}} = \sum_{im} G_{im} \cdot \vec{v}_m = G \cdot \vec{v} \tag{2.103}$$

Thereby, the gyro tensor G, which reflects the action of the precession of magnetization, is given by [45, 47]:

$$G = \sum_{im} \frac{\mu_0}{\gamma_0 M_{\mathrm{s}}^2} \int_V \vec{M} \cdot \left\{ \left(\frac{\partial \vec{M}}{\partial x_i} \right) \times \left(\frac{\partial \vec{M}}{\partial x_m} \right) \right\} \mathrm{d}V \, (\vec{e}_i \otimes \vec{e}_m) \tag{2.104}$$

Basically, the final result for the gyro force is found by Eq. 2.104. However, it is possible to rewrite the expression for $\vec{F}^{\mathrm{g}}$ and G respectively by the use of some tensor algebra, which will lead to a deeper insight into the nature of this force. The gyroscopic tensor G is antisymmetric, and from tensor algebra it is known that you can address a vector to the corresponding tensor [48]. In the actual case, it is possible to rewrite G as $\vec{G}$ which transforms Eq. (2.103) into [34]:

$$\vec{F}^{\mathrm{g}} = \vec{G} \times \vec{v} = \sum_{ion} G_o v_n \epsilon_{oni} \vec{e}_i \tag{2.105}$$

$\vec{G}$ is the gyro vector and is calculated from the components G_{im} of the gyroscopic tensor G with the formula Eq. (2.104) [48].

$$\vec{G} = -\frac{1}{2} \sum_{oim} G_{im} \epsilon_{imo} \vec{e}_o \tag{2.106}$$

Inserting G_{im} into Eq. (2.106), it yields[1] [34]

$$\vec{G} = -\frac{\mu_0}{2\gamma_0 M_{\mathrm{s}}^2} \int_V \left(\sum_{\substack{oim \\ jkl}} \frac{\partial M_j}{\partial x_i} M_k \frac{\partial M_l}{\partial x_m} \epsilon_{ljk} \epsilon_{imo} \right) \mathrm{d}V \vec{e}_o \tag{2.107}$$

where the final result for $\vec{G}$ can be calculated by summing up over all indices. This mathematical subtlety gives a deeper insight into the nature of the gyro force term, although, the exact expression for the gyro vector is unknown so far. Being written as cross product of $\vec{G}$ and the velocity $\vec{v}$, the resulting vector $\vec{F}^{\mathrm{g}}$ is perpendicular to both, $\vec{G}$ and $\vec{v}$. This leads to a force and a motion respectively, which is perpendicular to the velocity direction and causes a sidewards motion. A result that also implies that one needs, at least, a two-dimensional model to describe the motion of DW correctly since a second spatial degree of freedom is necessary for the sidewards motion. Before the expression for the gyrovector will

be evaluated, a special notation of the product of the two Levi-Civita symbols should be mentioned. In Thiele's original work [34], another formulation is used, which can be understood by the framework done in appendix A2. Thiele notates $\epsilon_{ljk}\epsilon_{imo}$ in terms of the generalized Kronecker delta $\delta_{imo}^{ljk} = \delta_{imo}{}^{ljk}$ [48]. Applying this notation, $\vec{G}$ reads [34]:

$$\vec{G} = -\frac{\mu_0}{2\gamma_0 M_\mathrm{s}^2} \int\limits_V \left(\sum_{\substack{oim \\ jkl}} \frac{\partial M_j}{\partial x_i} M_k \frac{\partial M_l}{\partial x_m} \delta_{imo}{}^{ljk} \right) \mathrm{d}V \vec{e}_o \tag{2.108}$$

Proceeding to the evaluation of the gyro vector, it is helpful to recall an important assumption concerning the magnetization $\vec{M}$ which will simplify the summation over the six indices. In the whole thesis, it is assumed that the saturation magnetization M_s, or in other words the length of the magnetization vector $\vec{M}$, is spatial constant. Supposing now an orthogonal coordinate system, for instance spherical coordinates, where one coordinate is the length of the vector. When the infinitesimal contribution of the magnetization contained in an infinitesimal volume $\mathrm{d}V$ to the vector G is considered, the coordinate system is chosen to be locally $M_k = M_\mathrm{s}$ [30]. Strictly speaking, by integrating over the whole volume V, the local coordinate system is adjusted for every infinitesimal contribution to $\vec{G}$ in such a way that the coordinate M_k is parallel to the local magnetization vector $\vec{M}$. Additionally, the advantage of this special selection of coordinates arises from the conservation of saturation magnetization. Since the length of $\vec{M}$ does not change, spatial gradients can only differ from zero in the other two perpendicular directions. For G_0 the expression[1]

$$G_o = -\frac{\mu_0}{2\gamma_0 M_\mathrm{s}^2} \int\limits_V \left(\sum_{imjl} \frac{\partial M_j}{\partial x_i} M_\mathrm{s} \frac{\partial M_l}{\partial x_m} \epsilon_{ljM_\mathrm{s}} \epsilon_{imo} \right) \mathrm{d}V \tag{2.109}$$

is found as intermediate result. Summing over the other two indices (j and l) and using the antisymmetry of the expression, it is obtained[1]:

$$G_o = -\frac{\mu_0}{\gamma_0 M_\mathrm{s}} \int\limits_V \left(\sum_{im} \frac{\partial M_j}{\partial x_i} \frac{\partial M_l}{\partial x_m} \epsilon_{imo} \right) \mathrm{d}V \tag{2.110}$$

As before, the vector notation for the Levi-Civita symbol has been utilized and assigned to the gained basis vectors of the associated partial derivatives[1].

$$G_o = -\frac{\mu_0}{\gamma_0 M_\mathrm{s}} \int\limits_V \sum_{im} \left(\left\{ \vec{e}_i \frac{\partial M_j}{\partial x_i} \right\} \times \left\{ \vec{e}_m \frac{\partial M_l}{\partial x_m} \right\} \right) \cdot \vec{e}_o \, \mathrm{d}V \tag{2.111}$$

Inserting G_0 into $\vec{G}_0 = G_0 \vec{e}_0$ and summing o over the three spatial coordinates to obtain the expression for the gyro vector[1]

$$\vec{G} = \sum_o \vec{G}_o = -\frac{\mu_0}{\gamma_0 M_\mathrm{s}} \int\limits_V \left(\left\{ \vec{\nabla} M_j \right\} \times \left\{ \vec{\nabla} M_l \right\} \right) \mathrm{d}V \quad , \tag{2.112}$$

where M_j and M_l are the magnetization components perpendicular to the local M_s-direction. To round up the considerations, the expressions for the gyro tensor G and the corresponding vector $\vec{G}$ are converted to generalized coordinates. This generalization is achieved in the same way as for the conversion of

Γ to an arbitrary coordinate system. Starting from Eq. (2.104) for G_{im}, the assumption of $\vec{M}$ depends on a set of new coordinate, and taking the partial derivatives with respect to them, it leads to[1]

$$G_{im} = \sum_{i'm'} \frac{\mu_0}{\gamma_0 M_\mathrm{s}^2} \int_V \vec{M} \cdot \left\{ \left(A_{i'} \vec{e}_{i'} \frac{\partial x_{i'}}{\partial x_i} \right) \times \left(A_{m'} \vec{e}_{m'} \frac{\partial x_{m'}}{\partial x_m} \right) \right\} \mathrm{d}V \tag{2.113}$$

where the identities $\frac{\partial \vec{M}}{\partial x_{i'}} = A_{i'} \vec{e}_{i'}$ and $\frac{\partial \vec{M}}{\partial x_{m'}} = A_{m'} \vec{e}_{m'}$ have been already used. Identifying the coefficients as the square roots of the diagonal elements of the metric tensor g (see Sec. 2.2.3.4),

$$G_{im} = \sum_{i'm'} \frac{\mu_0}{\gamma_0 M_\mathrm{s}^2} \int_V \sqrt{g_{i'i'} g_{m'm'}} \vec{M} \cdot \left\{ \left(\frac{\partial \vec{x}_{i'}}{\partial x_i} \right) \times \left(\frac{\partial \vec{x}_{m'}}{\partial x_m} \right) \right\} \mathrm{d}V \tag{2.114}$$

is obtained[1] for G_{im} in generalized coordinates. Completing the considerations, $\vec{G}$ is transformed into the notation of generalized coordinates. Starting with the o-th component of the gyro vector, it is gained[1]:

$$G_0 = -\frac{\mu_0}{2\gamma_0 M_\mathrm{s}^2} \int_V \left(\sum_{\substack{im \\ i'km'}} \left\{ A_{i'} \frac{\partial x_{i'}}{\partial x_i} \right\} M_k \left\{ A_{m'} \frac{\partial x_{m'}}{\partial x_m} \right\} \epsilon_{i'm'k} \epsilon_{imo} \right) \mathrm{d}V \tag{2.115}$$

Choosing the local coordinate system as before, summing over the indices of the new coordinates and exploiting the antisymmetry of the gyro tensor, it results in[1]:

$$-\frac{\mu_0}{\gamma_0 M_\mathrm{s}} \int_V \left(\sum_{im} \left\{ A_{i'} \frac{\partial x_{i'}}{\partial x_i} \right\} \left\{ A_{m'} \frac{\partial x_{m'}}{\partial x_m} \right\} \epsilon_{imo} \right) \mathrm{d}V \tag{2.116}$$

In a last step, ϵ_{imo} is converted again into vector notation, and by summing over all indices[1]

$$\vec{G} = \sum_o \vec{G}_o = -\frac{\mu_0}{\gamma_0 M_\mathrm{s}} \int_V \left(\left\{ A_{i'} \vec{\nabla} x_{i'} \right\} \times \left\{ A_{m'} \vec{\nabla} x_{m'} \right\} \right) \mathrm{d}V \tag{2.117}$$

is found for the gyro vector in arbitrary coordinates. Again, as for the damping tensor Γ, the coefficients $A_{i'}$ and $A_{m'}$ are identified as the square root of the diagonal elements of the metric tensor. Writing $A_{i'}$ as $\sqrt{g_{i'i'}}$ and $A_{m'}$ as $\sqrt{g_{m'm'}}$ respectively, it yields for the gyrovector $\vec{G}$ [1]:

$$\begin{aligned} \vec{G} &= -\frac{\mu_0}{\gamma_0 M_\mathrm{s}} \int_V \left(\left\{ \sqrt{g_{i'i'}} \vec{\nabla} x_{i'} \right\} \times \left\{ \sqrt{g_{m'm'}} \vec{\nabla} x_{m'} \right\} \right) \mathrm{d}V \\ &= -\frac{\mu_0}{\gamma_0 M_\mathrm{s}} \int_V \left(\sqrt{g_{i'i'} g_{m'm'}} \left\{ \vec{\nabla} x_{i'} \right\} \times \left\{ \vec{\nabla} x_{m'} \right\} \right) \mathrm{d}V \end{aligned} \tag{2.118}$$

Please note that the spatial gradients are still formulated in Cartesian coordinates. In this case it is easier to calculate the gradients for symmetry reasons

in another coordinate system in which $\vec{\nabla}$ has to be converted. In spherical coordinates the two coordinates where the spatial gradients with respect to $\vec{M}$ differ from zero are ϑ and φ. By using the already calculated coefficients for both coordinates [34, 35],

$$\vec{G} = -\frac{\mu_0 M_\mathrm{s}}{\gamma_0} \int_V \sin(\vartheta) \left(\left\{ \vec{\nabla} \vartheta \right\} \times \left\{ \vec{\nabla} \varphi \right\} \right) \mathrm{d}V \tag{2.119}$$

is derived.

2.2.4 Thiele Equation

Summarizing the results of the evaluation of the force terms, the force equation can be written as[1] [35]

$$\vec{F}^\mathrm{f} + \vec{F}^\alpha + \vec{F}^\mathrm{g} = 0 \tag{2.120}$$

and reads with the explicit form of the force terms [45]

$$\vec{F} - \Gamma \cdot \vec{v} + G \cdot \vec{v} = 0 \tag{2.121}$$

which is the Thiele equation. Here, the force term $\vec{F}^\mathrm{f}$ originating from the external applied field $\vec{H}$ has been simply renamed to $\vec{F}$, because this is the standard labeling for the force term in the Thiele equation. As it was proven, the gyroforce term can be written as the cross product of the gyrovector $\vec{G}$ with the velocity vector $\vec{v}$ which gives another common notation of this equation [34, 35].

$$\vec{F} - \Gamma \cdot \vec{v} + \vec{G} \times \vec{v} = 0 \tag{2.122}$$

At this point, an important fact should be mentioned. Different sign conventions for the forces and the expressions of the tensors Γ and G are used in the literature. This comes mainly from four sources. First, it depends on whether one changes all terms in the LLG equation to the left or to the right side when calculating the effective force equation. The second source for different signs is due to a different sign convention in the steady-state motion ansatz for $\vec{M}$. As an example, in almost every text book or publication about the Thiele equation, the ansatz for the magnetization of a domain wall moving with constant velocity $\vec{v}$ is chosen to be $\vec{M}(\vec{r}) = \vec{M}(\vec{r}_0 - \vec{v}t)$. Applying the time derivative yields a minus sign for the velocity vector. However, a different convention can be found, for example, in the publication of Clarke et. al. [45], where the ansatz $\vec{M}(\vec{r}) = \vec{M}(\vec{r}_0, \vec{\xi}(t))$ is used ($\vec{\xi}$(t) is the position vector of the characteristic point in a generalized coordinates, see Sec. 2.3.2.1), leading to a lack of "-1" in every term where the time derivative of the magnetization enters the calculation. Another variation originates from the fact that it is possible to express the partial derivatives contained in the equation with respect to the position of the characteristic point or an arbitrary position (see Sec. 2.3.2.1). Further differences in the respective formulation of the Thiele equation can arise from the concrete definition of the damping tensor Γ. While Thiele defines in his original work Γ as negative, one can find Γ defined as a positive quantity, for instance, in [45]

Γ. As a final remark on the different notation that can be found in literature, it should be mentioned that different designations for the damping tensor can be found, while for the force and gyroscopic term the letter F and G is used respectively. The most common labeling for the damping tensor is D and Γ. In this thesis the notation Γ will be applied because the further analysis in this work concerning DWM is based on the collective coordinate approach of Clarke et. al [45]. where they denote the damping tensor in the same way.

2.3 Dynamics of Vortex Domain Walls

Based on the framework done in Sec. 2.2, the basics of VDW dynamics is investigated in Sec. 2.3. In a first step VDWs (Sec. 2.3.1) and their basic properties are described, and then it proceeds to the discussion of their dynamics described in the frame of the collective coordinate approach in Sec. 2.3.2.

2.3.1 Vortex Domain Walls

The information presented in this section are taken from the textbooks [37, 38, 49, 50]. If otherwise, it will be quoted accordingly. The magnetic structures under consideration in this thesis are vortex domain walls (VDWs). In this section a short overview will be given about how domain walls form, what different kinds are possible, and the properties of VDWs will be explained.

Due to energy minimization, domains and DWs form. Decaying into regions where the magnetization is aligned differently leads to the reduction of stray field and to the stray field energy of the magnetized sample correspondingly. These regions are called domains, and their existence leads directly to the existence of transient regions where the magnetization rotates between the magnetization direction in the adjacent domains; such transition regions are called domain walls, and their concrete shape depends strongly on the type of sample geometry under consideration. From an energetic point of view, decaying into domains reduces the stray field energy, but it costs energy to build up domain walls. Thus, the domain structure of a certain sample is governed by the balance between these two energy contributions. The size and type of a DW is governed and determined by the competitive interaction of the dipolar and exchange energy. While the dipolar interaction tries to align neighboring spins antiparallel, the exchange interaction favors a parallel orientation of the magnetization. As mentioned before, various numbers of different DW types are possible. In magnetic materials, Bloch [51] and Néel type walls [52] can form; Bloch walls are found in the bulk samples and Néel walls in a thin film geometry. The difference between both kinds of walls is the way the magnetization rotates between the adjacent domains. While the magnetization vector rotates in the plane of the DW in the Bloch wall, the vector rotates perpendicular to it in the case of a Néel wall. Another classification, or lets say an attribute one can address to a DW, is the angle of rotation between the neighbored domains. The most common types are the 90° and 180° DW, where, of course, other angles are possible as well. For 90° DWs, the magnetization in the adjacent domains is perpendicular to each other, while in the case of 180°, the spins are aligned anti-parallel.

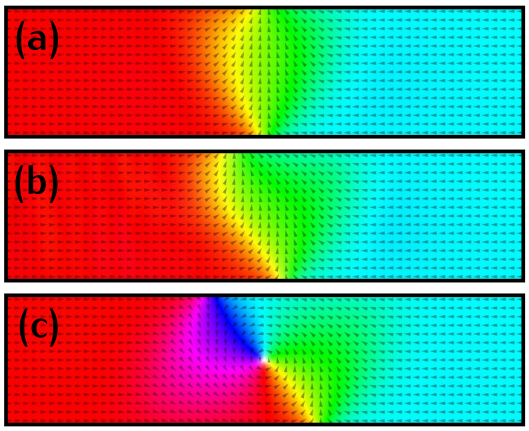

Figure 2.3. Three most common possible head-to-head DW configurations in magnetic stripes. (a) transverse wall, (b) asymmetric transverse wall and (c) VDW. Which type of DW is present depends strongly on the width w and thickness t of the stripe. While for relative thin stripes, transverse and asymmetric transverse walls are the favorable DW configuration, in thick stripes VDWs are the type of DW to be found.

The following considerations are restricted to 180° DWs. Regarding 180° DWs, one has to distinguish between two different sample geometries, namely nanowires and nanostrips. The classification into these two geometries is done by the aspect ratio $\frac{w}{t}$ of the width w and thickness (hight) t of the structure. Structures with $\frac{w}{t} \approx 1$ are called nanowires while geometries with an aspect ratio $\frac{w}{t} \gg 1$ are denoted as nanostrips [49]. Transverse and Bloch point walls are the favored DW structure in nanowires, while transverse, asymmetric transverse (ATV), vortex and a lot more types were found as possible magnetization structures in nanostripes, as it will be demonstrated [49, 53–55].

Since the type of samples investigated in this thesis corresponds to the situation of nanostripes described above, the further discussions will be restricted additionally to the geometry of nanostrips and the magnetic textures present in this case. Till proceeding to the discussion of types of DWs in nanostrips, another commonly used designation for 180° DWs in nanostrips should be mentioned. Depending on the magnetization direction in the domains on the left and right hand side of the DW, the terms head-to-head and tail-to-tail DW are often used. Head-to-head describes the case when the magnetization in both adjacent domains is pointing to each other, whereas tail-to-tail describes the situation when the magnetization is pointing away from each other. As mentioned earlier, different types of DWs are found to exist in the geometry of nanostripes (see Fig. 2.3). Which kind of head-to-head (or tail-to-tail) wall exists depends on the width and thickness of the stripe as wall as the exchange length λ. Transverse and VDWs where the first two types discovered by micromagnetic simulations [56]. Later on, a phase diagram was presented in [53] where in a small region of combinations for w and t, a modification of the TW, the asymmetric transverse wall, is forming.

In recent years micromagnetic studies have presented further extended phase diagrams, which predict rather complicated DW structures for rather thick and wide magnetic layers, for example, double or triple VDWs [54] or Landau DWs [55]. For experimental reasons, the further considerations focus on VDWs be-

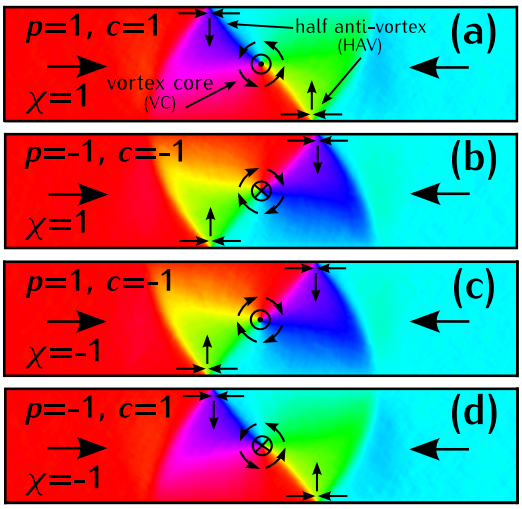

Figure 2.4. Pictures (a)-(d) display the four possible configurations of a VDW in magnetic stripes. The four configurations arise from the two configurations of the polarity p and circulation c, namely ± 1, resulting in VDWs with chirality $\chi = p \cdot c = \pm 1$. The magnetic structure of a VDW is made up of three different elementary topolgic defects. A VC within the stripe with an out-of-plane magnetization at its center and a curling magnetization around the VC. At the stripe edges the HAVs are located.

cause they are the favored kind of DW in the experimentally investigated samples.

VDWs are magnetic structures with a flux closed state and exhibiting a rich internal magnetic structure. This internal structure is made of three topological defects [57–59], namely a vortex core (VC) in the center and two half antivortices (HAVs) confined to the edges. For more information concerning the topological defect see Sec. 2.3.2. At the VC, which has its equilibrium position in the absence of an external applied field in the middle of the stripe, the magnetization curls clockwise or counter-clockwise and spirals out of plane towards the VC center. The VC is exchange dominated, and hence, the dimensions of this topological object are rather small and in the range of the exchange length λ. Typical values for the diameter between 10 up to 20 nm are found. The direction of the magnetization at the VC center can be described as the the polarity p. p is defined as $p = \frac{M_z}{|M_z|}$ and the quantity can take values $+1$ and -1. Around the vortex core, a region of in-plane curling magnetization forms. Depending on the sense of rotation (clockwise or counter-clockwise), the circulation c, a second important key quantity, can be addressed to the VDW. As for the polarity, c can take the values $+1$ (counterclockwise circulation of the magnetization around the VC) and -1 (clockwise circulation of the magnetization around the VC). Based on p and c the chirality $\chi = p \cdot c$ can be defined. The chirality χ has an important influence on the VDW dynamics as it will become clear later on. Following from this, it is obvious that four possible combinations for p and c are available that form two VDWs with chirality $\chi = +1$ and $\chi = -1$ each. In other words, VDWs exhibit a four times degenerated ground state.

At the edges, the two HAVs are located. Parallel to the stripe edges, the

magnetization points towards the HAV and then rotates sharply by 90° to the middle of the stripe at the position of the HAV (see Fig.2.4). This forms a radiating magnetic texture in the surroundings of the HAVs which evolves direct into the curling magnetization around the VC. Later on, it will be important for the calculation of the damping mechanism acting on the DW that, besides the VC and HAVs, a fourth magnetic texture can be identified. In the DW there are regions which can be described as Néel type walls. These walls are found to be at the connection line HAV-VC-HAV, and in addition, they are found where the in-plane curling magnetization encounters the magnetization in the adjacent domains. Straight Néel walls form at the connection line between the three topologically defects, while the walls emerging on the border of the DW are parabolic shaped. In the analytic model used later on, these Néel walls are treated more idealized [59]. As already mentioned, the term topological defects plays an important role in the treatment of DWs. Concerning topological defects, a topological charge q_t can be addressed to each of these substructures and the DW itself. A VC has a topological charge $q_\mathrm{t} = 1$, whereas, HAVs exhibit a fractional $q_\mathrm{t} = -\frac{1}{2}$ [59]. For the sake of completeness, besides VCs and HAVs other structures are possible. Furthermore, an anti vortex (AV) and half vortices (HVs) can be found. q_t for a AVC and HVs are $q_\mathrm{t} = -1$ and $q_\mathrm{t} = \frac{1}{2}$, respectively [58]. From an abstract mathematical point of view, the edge defects (HV and HAV) were discussed in [60, 61]. For a VDW the total topologic charge yields zero ($q_\mathrm{t} = 0$) [59], which is an important fact because it is a conserved quantity and influences the Walker breakdown mechanism.

Turning back to the behavior of a VDW under the action of an externally applied field, each of these single magnetic substructures in the VDW exhibit its own dynamics and influence greatly the overall dynamics of the DW itself. Four different mobility regimes are known for DWs. At very low fields below a the critical value H_p, the pinning field, no DWM occurs. This behavior is denoted as pinning and is caused by intrinsic or extrinsic defects, for example, dislocations, impurities or roughness at surface and edge. Overcoming this critical value, the linear mobility regime sets in, which is characterized by v being linear proportional to H and $\frac{1}{\alpha}$. This behavior is given in a field range between H_p and the critical field H_c, which is sometimes denoted as Walker field H_w. Reaching H_c is accompanied by a drop in velocity and displacement, respectively. This drop in velocity marks the third mobility regime. The steepness of this drop in velocity strongly depends on the width of the stripes. For very narrow stripes the drop in v is very sharp, while on the other side, for wide stripes a plateau region above H_c in the v-H-diagram can be observed. The reason why there is a different behavior observed for DWs in wide stripes will be clarified in this thesis by experimental data, theory and simulational results in Sec. 4.2. However, in general, the Walker breakdown in the case of VDW is caused by a polarity reversal of the VC. Applying an external field, the DW starts to move along the stripe, and additionally, the VC moves sidewards to one of the edges. This sidewards motion is due to the gyro force which is always perpendicular to the direction of motion of the VC. The gyro force $\vec{F}^\mathrm{g}$ is proportional to v and polarity p. Reaching a high enough field, the polarity reverses and leads to a reversal in direction of $\vec{F}^\mathrm{g}$ and hence a motion of the VC in reversed direction. Above the Walker field, this causes an oscillatory motion where the VC continuously travels across the

stripe and reverses its polarity p at each side.

Two different reversal mechanisms are known; there is either a reversal due to the collision of the VC with one of the HAVs and a subsequent reemission of the VC with opposite polarity, or a free reversal [62–64] due to the effect of the gyrofield. The latter one is well known and causal for the polarity reversal of VCs in discs [21]. Considering the reversal due to the collision with the HAVs, the VC (topological charge $q_\mathrm{t} = +1$) and the HAVs (topological charge $q_\mathrm{t} = -\frac{1}{2}$) combine; for a very short time, a half vortex (topological charge $q_\mathrm{t} = +\frac{1}{2}$) is formed until the VC is re-emitted. This reversal process and the following free reversal are an important example for the powerful concept of topological charge and its conservation respectively. Free reversals are happening as it follows: The gyro field deforms the VC with increasing velocity, so that close to the VC, a dip region (dynamic dip) with opposite p establishes. At a critical velocity, the VC is deformed that much that the VC region can be regarded as a hybridization of a VC with $p = +1$ and $p = -1$. Due to the strong magnetization gradient between the two VC, the exchange energy increases, and it becomes energetically more favorable for the dip region to split up into a vortex ($q_\mathrm{t} = +1$) and antivortex ($q_\mathrm{t} = -1$), whereby the antivortex ($q_\mathrm{t} = -1$) and the initial VC ($q_\mathrm{t} = +1$) annihilate. After this annihilation process which is accompanied by a strong emission of spin waves, a VC with reversed polarity remains and the reversal is finished.

Turning to the fourth mobility regime, at very high fields $H \gg H_\mathrm{c}$ a precessional motion sets in where the average velocity $< v >$ is directly proportional to the Gilbert damping parameter α.

As a last point, the motion of a VDW under the influence of an externally field will be described. Without the constriction of generality, a VDW with chirality $\chi = 1$ ($p = 1$, $c = 1$) under the action of an external applied field (being parallel to the longitudinal direction of the stripe) is considered. Taken only the external field $\vec{H}$ and the demagnetizing field $\vec{H}_\mathrm{dem}$ as constituents for the effective field $\vec{H}_\mathrm{eff}$ into account, the LLG eq. reads as following[1]:

$$\frac{\mathrm{d}\vec{M}}{\mathrm{d}t} = -\gamma_0 \vec{M} \times \left(\vec{H} + \vec{H}_\mathrm{dem}\right) + \frac{\alpha}{M_\mathrm{s}} \vec{M} \times \frac{\mathrm{d}\vec{M}}{\mathrm{d}t} \tag{2.123}$$

As it will become clear, the precessional and the damping term contribute to the total torque acting on the DW and moving it along the stripe in field direction. Interestingly, in the linear regime, the significant contribution to the forward motion originates from the two HAVs and not from the VC. The VC is dragged by the two HAVs along the stripe. In which way both terms in the LLG eq. cause a motion will be explained now and can be deduced from the LLG eq. written above.

Considering the leading HAV of the VDW, where it can be assumed in an idealized way that the magnetization is pointing in positive y-direction. From the precessional term, a torque $\frac{\mathrm{d}\vec{M}}{\mathrm{d}t}$ arises due to the external field, which forces the magnetization of the HAV slightly out of plane. This has two effects: On the one hand, this torque $\frac{\mathrm{d}\vec{M}}{\mathrm{d}t}$ enters the damping term and causes a torque parallel to the external field, which causes a motion along the stripe; on the

other hand, the out-of plane component of the magnetization in the HAV leads to a demagnetizing field $\vec{H}_{\mathrm{dem}}$ which is pointing in opposite direction to the z-component of $\vec{M}$. This demagnetizing field in turn is causing a torque on the in-plane magnetization in the HAV region, leading to a torque in stripe direction which originates from the precessional term. Again, the torque $\frac{\mathrm{d}\vec{M}}{\mathrm{d}t}$ due to $\vec{H}_{\mathrm{dem}}$ enters the damping term in the LLG eq. and causes a torque which counteracts the torque that forced the magnetization out of plane. When these torques cancel each other, then the DW reaches its steady state motion for a certain field strength of the external field. It should be noted that the consideration with respect to the leading HAV holds true for the trailing HAV and stays even valid for all other possible VDW configurations.

2.3.2 Vortex Domain Wall Motion in the Frame of the Collective Coordinate Approach

Having found the expressions for the three forces in the Thiele Equation which arise from the Landau-Lifshitz-Gilbert equation, the specific force terms $\vec{F}^{\mathrm{f}}$, $\vec{F}^{\alpha}$ and $\vec{F}^{\mathrm{g}}$ for the case of a VDW have to be determined. These prerequisites enable to investigate the internal dynamics of a VDW under the action of an external driving field H in detail. As publications [45, 47] are the theoretical basis for the investigations done hereinafter, the found expressions will be converted into the form used in the collective coordinate approach by Clarke and co-workers [45, 47]. Although it is done this way, it will always be tried to demonstrate the equivalence of the terms in the collective coordinate notation and, for example, the famous expressions of domain wall motion found by Walker [29].

Starting with the calculation of the force term $\vec{F}^{\mathrm{f}}$, which arises from the total energy in a stripe made out of Permalloy, the gyrovector $\vec{G}$ of a magnetic vortex will be calculated. The determination of $\vec{G}$ can be done in two different ways, namely by doing the calculation by hand based on symmetry considerations or, in a more elegant way, via the connection of G_{xy} to the gyrotensor G and the topological charge q_{t}. In Sec. 2.3.2.7 the analytical expression of a vortex in a disc is used as toy model to demonstrate the computation of the damping tensor Γ. Followed by this, for the determination of Γ a way more realistic model for a vortex domain wall, which incorporates not only the VC itself, but in addition, edge defects and internal Néel walls, which contribute to the viscous damping, is considered. With this result it is possible to write down the equation of a steady-state motion for the one and two dimensional case of a vortex domain wall. These equations in the frame of the collective coordinate approach are solved in Sec. 2.3.3; for both cases, important characteristics of this motion are derived.

This section introduces the generalization of Thiele's results [34], the so called Collective Coordinate Approach (CCA) [45, 47], and explains its general ideas and concepts in detail. Since the concepts, the CCA is based on, are partly abstract and hard to understand, they are illustrated by the example of head-to-head (or tail-to-tail) domain walls [56, 65]. In particular, the focus is set on vortex domain walls (VDWs) [49, 56] because this is the relevant case for

this thesis. Following this introduction, the analytic expressions of energy E, force $\vec{F}$, gyrotropic vector (or gyrovector) $\vec{G}$ and damping tensor Γ for a VDW are calculated (see Sec. 2.3.2.4-2.3.2.7). These calculations will be presented in detail to show on the one hand, how to apply the abstract concepts of the CCA for the determination of all relevant quantities appearing in the Thiele equation, and on the other hand, how to tackle these calculations the best way. As it will be demonstrated by the exploitation of symmetries of the DW, it is possible to simplify the mathematical task. Before starting to explain the CCA, a short historical overview of the investigation of VDW dynamics based on Thiele's analytical approach will be given. Since the formulation of the (most common) basic equation of magnetization dynamics in 1935 by Landau und Lifshitz [23], the Landau-Lifshitz equation (see Sec. 2.1), and its adoption to vicious friction by Gilbert [24, 25](the Landau-Lifshitz-Gilbert equation or LLG equation), it has become possible to predict the time evolution of magnetization in a huge variety of physical systems with all kinds of interaction mechanisms. However, magnetization, and so magnetization dynamics, is a collective phenomenon, and due to this reason its time evolution is hard to predict without numerical methods [66–68]. Exact analytical solutions are hard to obtain, in most cases they are only available in toy systems with reduced dimensions. Thus, in terms of DWM they are an example for cylindrical magnetic domains in films and platelets [69] or a one-dimensional 180° domain wall [29]. Determining such solutions is a tedious work, nevertheless, analytical solutions are always desirable.

In his groundbreaking publication about "Steady-State Motion of Magnetic Domains" from the year 1973 [34], A.A. Thiele found a new analytical approach to the calculation of the steady-state velocity of magnetic domains by rewriting the LLG equation into an equivalent force equation and by applying subsequently the "steady-state approximation". This leads, in the end, to two integrals which are simplifying the calculation of dynamic properties of magnetic domains. This has already been explained in Sec. 2.2 in detail. Thiele's equations opened a new way to examine theoretically the dynamic of magnetic domains. Since dealing with VDWs, the most interesting fact for this thesis is that the investigation of spin vortices based on the Thiele equation can be ascribed to the early 1980s [70]. In 1997 TV and VDWs as possible DW configurations in between head-to-head (or tail-to-tail) domains in thin magnetic magnetic strips [56] were discovered in micromagnetic simulations; these magnetic textures gained much attention very fast, since they are promissing candidates for technological applications. Not only since the proposal of the "Magnetic Domain-Wall Racetrack Memory" by S.S.P. Parkin in 2008 [1], these magnetic structures have already been regarded as a new basis to create novel data storage techniques since about 2000, for example, MRAM [71]. Around this time, the existence of magnetic vortex states in ferromagnetic nanodots made out of $Ni_{80}Fe_{20}$ and Co were proven with MFM techniques and Lorentz microscopy, respectively [72, 73]. In the same year, the structure of the VC itself was investigated experimentally with spin-polarized STM, and it was found to be consistent with results found by micromagnetic simulations [74]. In 2004 VDW and TW were proven to exist in ferromagnetic rings [65, 75] by both, simulations and experimentally. The DWs exhibit a rich internal structure and dynamics; these features greatly influence the motion of

the DW under the influence of an external applied field, which is especially true for VDWs [49, 56]. Complex internal DW structures are caused by the competitive action of local exchange and longe-range dipolar interaction on a submicron range, where both are of comparable strength [76, 77], for example, the Walker breakdown mechanism of a TV and VDW [49]; these origins are completely different compared to the one of a Bloch wall [29, 34, 44, 78]. These effects occurring in complex DW structures were barely captured in such models. Aiming at future technological applications, and in general for a better understanding of DWM, an advanced analytical model for the description of DW dynamics became necessary.

In the years 2005 to 2008, a group of authors (namely D.J. Clarke, O.A. Tretiakov, G.-W. Chern, Ya.B. Bazaliy, O. Tchernyshyov, H. Youk, K. Merit and B. Oppenheimer) investigated in a series of publications the structure and dynamics of DWs in magnetic nanostrips from different point of views [45, 47, 57–59]. Regarding the structure of DWs in flat nanomagnets (head-to-head and tail-to-tail walls), they found that such complex DWs (TV and VDWs) are composite objects out of a few elementary topological defects, namely V/AV and HV/HAV [57–59]. Remarkably this holds true for two extreme cases: the exchange-limit (thin and narrow stripes with $t \ll w \ll \frac{\lambda^2}{t} \ll w \log\left(\frac{w}{t}\right)$) [57] and magnetostatic-limit (thin and wide strips with $\lambda \ll t \ll w$ [58, 59]. Being valid in both limits, the statement about the composition of DW out of topological defects is also true in intermediate cases ($\lambda < t \ll w$) [59] which can be shown by calculating the magnetostatic limit via van den Bergs method [79] and by including exchange interaction pertubatively. This is an important result because this case reflects realistically the situation of DWM experiments in soft magnetic stripes and rings made out of $Ni_{80}Fe_{20}$ [22, 65]. To conclude it, "it appears that this general approach" of regarding DW as "composite objects may provide a basic model of complex magnetization dynamics in nanomagnets, by reducing it to the creation, propagation and annihilation of a few topological defects", as stated by O. Tchernyshyov and G.-W. Chern in [57]; or in other words, the motion of a DW is governed by the dynamic of its constituents. This fact has to be included into an analytical approach to DWM to get appropriate predictions. Based on their preliminary results in [57–59], the work of the aforementioned group of authors culminated in a new analytical approach to DWM [45, 47], which is a generalization of Thiele's DW analysis [34]. This is the Collective Coordinate Approach (CCA).

In the following section, the ideas and concepts of this model, which was first introduced in [47] and then explained in more detail in [45], are elucidated. Both publications considered a VDW as an illustrative example for the application of the CCA, and the theoretically predicted values, which resulted from this, for example the steady-state velocity below the walker field [45], were found to be in strikingly good agreement with experimental findings [17] and results from micromagnetic simulations [80]. This, in contrast, indicated that the CCA may possibly provide a fitting theoretical description for this work. Proceeding now to the introduction of the CCA, it should be emphasized that the described approach to DWM in the Sec. 2.3.2-2.3.3.2 is based on the publications of Tretiakov

et al. [47] and Clarke et al. [45]. Unfortunately, although trying to explain all concepts from scratch, it is sometimes inevitable to anticipate some of the results, which will be derived or calculated in subsequent sections later on. This already reflects the heuristic nature of some concepts and ideas of the CCA. By going through the explanation of the CCA, a good starting point for the discussion are the features which can be explained in a most general way and evolve to parts of the theory, which are best explained by a concrete example. Additionally, it is always tried to work out the differences and advantages compared to Thiele's analysis [34].

2.3.2.1 Generalization of Thiele's Analysis: Generalized Coordinates, Forces and Velocities

In view of Thiele's work, one difference, which is at the same time the most general feature of the CCA, is that in this generalized account to DWM, the spatial derivatives in connection to the vector $\vec{R}(t)$ are preserved. With this phenomenon, the CCA emphasizes strongly a property of "steady-state like" DWM as already pointed out in the section about the justification of steady-state motion (Sec 2.2.3.1); this kind of motion can be described by the position of a characteristic point within the DW. Here, the terminology "stead-state like" DWM is used because it should not be confused with the steady-state approximation. This has to be stated very clearly at this stage because the idea of characteristic points residing at a position $\vec{R}(t)$ is strongly connected to the steady-state motion, as it is described in Sec. 2.2.3.1. Assuming that the shape of a DW is fixed during steady-state motion, and thus the magnetization $\vec{M}$ can be parametrized by the distance $\vec{r'}$ in relation to the point $\vec{R}(t)$, which leads to the mathematical tool of Galilean transformation. An insight that enables it to be replaced in the steady-state motion regime the partial derivatives of $\vec{M}$ regarding the time dependent vector $\vec{R}(t)$ by ordinary (time independent) gradients (partial derivatives with respect to $\vec{r}$) of the magnetization via the substitution rule (see Sec. 2.2.3.1):

$$\frac{\partial}{\partial \vec{R}(t)} \qquad \rightarrow \qquad -\frac{\partial}{\partial \vec{r}} \tag{2.124}$$

As it will be seen later on, this idea of characteristic point is more general and not solely valid in the limit of stead-state motion with constant velocity $\vec{v}$. In fact, it can be applied to every kind of arbitrary DWM where it leads to the abstract concept of modes (see further down in the text) and enables to formulate a version of the Thiele equation [34], which is generalized to arbitrary motion of DWs.

Proceeding with the considerations concerning the fact that the CCA is writing the terms of the Thiele equation with partial derivatives $\frac{\partial}{\partial \vec{R}(t)}$. Before going into details, the findings for $\vec{F}^{\,\mathrm{f}}$, and G are reformulated by replacing $\frac{\partial}{\partial \vec{r}}$ by $-\frac{\partial}{\partial \vec{R}(t)}$ in the expressions for the force densities (Eq. (2.65)) in a first step. After that the calculations done in Sec. 2.2.3 have to be carried out again; but to shorten things, the outcome for the terms $\vec{F}^{\,\mathrm{f}}$, Γ and G, read[1]:

$$
\begin{aligned}
\vec{F}^{\mathrm{f}} &= -\vec{\nabla}_{\vec{R}} E = \sum_i -\frac{\partial E}{\partial X_i}\vec{e}_i \\
\Gamma &= \sum_{ik} \frac{\alpha\mu_0}{\gamma_0 M_{\mathrm{s}}} \left\{ \int_V \left(\frac{\partial \vec{M}}{\partial X_i}\right)\left(\frac{\partial \vec{M}}{\partial X_k}\right) \mathrm{d}V \right\} (\vec{e}_i \otimes \vec{e}_k) \\
G &= \sum_{im} \frac{\mu_0}{\gamma_0 M_{\mathrm{s}}^2} \int_V \vec{M} \cdot \left\{ \left(\frac{\partial \vec{M}}{\partial X_i}\right) \times \left(\frac{\partial \vec{M}}{\partial X_m}\right) \right\} \mathrm{d}V \, (\vec{e}_i \otimes \vec{e}_m)
\end{aligned}
\tag{2.125}
$$

Comparing this with the results obtained in Sec. 2.2.3, it can be recognized that, like before, the magnetization equivalent term $\vec{f}^{\mathrm{m}}$ vanishes, and all other terms keep their general form (with exception of the minus sign in $\vec{f}^{\mathrm{f}}$). Since nothing really changes, this might look like a nice playing around with the substitution rule $\frac{\partial}{\partial \vec{R}(t)} \rightarrow \frac{\partial}{\partial \vec{r}}$ at first sight. Thus, the reader might ask what the use of this way to write down the expressions appearing in the Thiele equation is. Since it is the strength of Thiele's approach that the calculation of the dynamic properties of a DW reduces to the determination of simple time-independent gradients of $\vec{M}$, and for sure, this advantage has to be utilized. Hence, the replacement $\frac{\partial}{\partial X_i} \rightarrow -\frac{\partial}{\partial x_i}$ will be carried out either way in the end, and the question arises why it is not done at the very beginning of the derivation.Basically, there are two main reasons.

In order to understand the first one, the origin of the substitution rule has to be recalled. Its derivation is based on the transformation rule of the Galilean transformation given by $\vec{r'} = \vec{r} - \vec{R}(t)$, which gives the connection between the representation of a vector in two coordinate systems S and S'; these origins of ordinates are shifted by a constant (or time-dependent) vector $\vec{R}(t)$. It has to be stated that replacing $\frac{\partial}{\partial X_i}$ by $-\frac{\partial}{\partial x_i}$ is only valid when $\vec{r'} = \vec{r} - \vec{R}(t)$ holds true; as it is the case, for example, for a Bloch wall in steady-state motion [29]. However, the transformation rule for the Galilean transformation does not have to look exactly like this, for instance, it can contain additional prefactors or rotations [43]. What may appear to be a mathematical subtlety has, indeed, an important practical relevance. As will be seen later in the calculation of the dissipation dyadic Γ for a VDW (see Sec. 2.3.2.8), DWs with a rich internal structure and dynamic may contain magnetic substructures, for these $\vec{r'} = \vec{r} - \vec{R}(t)$ is not valid. In the case of a VDW, such substructures are the DW-internal Néel walls [59] emanating from the VC. Aiming to grasp the dynamics of these magnetic substructures correctly, the transformation rule for the Galilean transformation has to be adapted, which consequently leads to another replacement rule. Striving for a generalization of Thiele's results, it is, indeed, useful to formulate $\vec{F}^{\mathrm{f}}$, Γ and G in terms of $\frac{\partial}{\partial \vec{R}(t)}$ instead of $\frac{\partial}{\partial \vec{r}}$; this may become clear by the given example related to a VDW. It is better to keep the equation generally as long as possible, determining the appropriate transformation rule, and apply the change to ordinary gradients only "short before" the actual calculation of the terms in the Thiele equation.

A second reason why it is favorable to keep $\frac{\partial}{\partial \vec{R}(t)}$ arises from the fact that due to the time-dependence of $\vec{R}(t)$, the quantities in the whole equation stay

time-dependent. This is leading to the point that up to this stage, the Thiele equation in the frame of the CCA is exact and is simple a reformulation of the LLG equation. In Thiele's scientific work [34], the equation of motion is already time-independent, due to the application of the steady-state approximation, and for this reason, it is only valid in this limit. In contradiction to this, the Thiele equation in the time-dependent version of the CCA containing partial derivatives $\frac{\partial \vec{M}}{R(t)}$ is universally valid and applicable to every kind of arbitrary DWM.

Summarizing the preliminary considerations, it can be stated that by the mere replacement of $\frac{\partial}{\partial \vec{r}}$ by $\frac{\partial}{\partial \vec{R}(t)}$ the valid scope of the equation is greatly expanded. Another level of generalization is achieved by replacing the vector $\frac{\partial}{\partial \vec{R}(t)}$ in Cartesian coordinates by a vector $\frac{\partial}{\partial \vec{xi}(t)}$ in generalized coordinates. Unfortunately, an exact mathematical proof that $\frac{\partial}{\partial \vec{R}(t)}$ can be replaced by $\frac{\partial}{\partial \vec{xi}(t)}$ cannot be provided because this is beyond the scope of this work. Nevertheless, it is at least vivid to explain why this is valid. Calculating the force terms appearing in the Thiele equation (Sec. 2.2.3.2-2.2.3.5), it has been demonstrated that the equations can be transformed straight forwardly from Cartesian to other generalized coordinate systems, e.g. curvilinear Euclidean systems as spherical or polar coordinates [39, 40]. This should make clear, at least, by feeling, that the equations can be written from the beginning in generalized coordinates. In other words, this is nothing else than another starting point. The derivation in Sec. 2.2.3.2-2.2.3.5 starts in Cartesian coordinates and transforms it to generalized ones, while the CCA enters the task at this stage and formulates everything in a generalized way with respect to coordinates.

Additionally, this leads, as a logical consequence, to generalized velocities $\dot{\vec{\xi}}(t)$ and forces $\vec{F}(t) = -\frac{\partial E}{\partial \vec{\xi}(t)}$. It should to be mentioned that the generalized coordinates ξ_i were labeled as x_i in the previous sections. Once validated this formulation of the equation, the calculation can be started in those coordinates which are simplifying the mathematical task. Afterwards, it is possible to transform all quantities back to those coordinate system in which the experimental values are measured, and therefore, the theoretical predictions have to be obtained. For example, measuring the steady-state velocity of a VDW along the stripe (x-direction), the dynamic properties are the best calculated in polar and spherical coordinates respectively due to the symmetry of the DW. Since in the wide-field Kerr microscopy measurements (see Sec. 3.5), the velocity in x-direction is determined, and the quantities found in curvilinear coordinates have to be transformed back to Cartesian ones in order to get theoretical predicted values for v_x. Ending up with the most general version of the Thiele equation, it yields[1] [45]:

$$\begin{aligned}
\vec{F}^{\,\mathrm{f}} &= -\vec{\nabla}_{\vec{\xi}} E = \sum_i -\frac{\partial E}{\partial \xi_i}\vec{e}_i \\
\Gamma &= \sum_{ik} \frac{\alpha \mu_0}{\gamma_0 M_\mathrm{s}} \left\{ \int_V \left(\frac{\partial \vec{M}}{\partial \xi_i}\right)\left(\frac{\partial \vec{M}}{\partial \xi_k}\right) \mathrm{d}V \right\} (\vec{e}_i \otimes \vec{e}_k) \\
G &= \sum_{im} \frac{\mu_0}{\gamma_0 M_\mathrm{s}^2} \int_V \vec{M} \cdot \left\{ \left(\frac{\partial \vec{M}}{\partial \xi_i}\right) \times \left(\frac{\partial \vec{M}}{\partial \xi_m}\right) \right\} \mathrm{d}V \, (\vec{e}_i \otimes \vec{e}_m)
\end{aligned} \tag{2.126}$$

Based on these equations, the quantities can be calculated in all kinds of arbitrary coordinate systems, including Cartesian ones, and the equations are easily applied for the theoretical description of a huge variety of moving magnetic structures appearing in different shaped structures, e.g. stripes [22], dots [72] and rings [65]. Of course, all quantities, for example, the energy E, have to be expressed as a measure of $\vec{\xi}(t)$.

Another fact which arises from dealing with generalized coordinates in combination with a spatial uniform saturation magnetization M_s has already been used in Sec. 2.2.3.2-2.2.3.5, but should be emphasized again because it can be overlooked in all the calculations. Assuming a spatially constant saturation magnetization ($\vec{\nabla}_{\vec{\xi}} \cdot \vec{M} = 0$ and $|\vec{M}| = M_\mathrm{s}$), the absolute value of $\vec{M}$ does not depend on the coordinates, and it is possible to express the magnetization vector $\vec{M}$ as $\vec{M}(\vec{R}(t)) = M_\mathrm{s}\vec{m}(\vec{R}(t))$ or $\vec{M}(\vec{\xi}(t)) = M_\mathrm{s}\vec{m}(\vec{\xi}(t))$, respectively. With $\vec{m} = \frac{\vec{M}}{|\vec{M}|} = \frac{\vec{M}}{M_\mathrm{s}}$ being the unit vector of the magnetization. This includes all coordinate systems which reflect this property of $\vec{M}$, e.g. spherical or polar coordinates, where one spatial coordinate is given and fixed by the saturation magnetization M_s. Parameterizing $\vec{M}$ in these kinds of coordinates, a factor M_s is obtained for every $\vec{M}$ or $\frac{\partial \vec{M}}{\partial \xi_i}$ contained in the equation for Γ and G. These additional prefactors can be written in front of the integrals. Based on these results, it is possible to express the equations Eq. (2.126) in terms of $\vec{m}(\vec{\xi}(t))$. They read[1] [45]:

$$\begin{aligned}
\vec{F}^{\,\mathrm{f}} &= -\vec{\nabla}_{\vec{\xi}} E = \sum_i -\frac{\partial E}{\partial \xi_i}\vec{e}_i \\
\Gamma &= \sum_{ik} \frac{\alpha \mu_0 M_\mathrm{s}}{\gamma_0} \left\{ \int_V \left(\frac{\partial \vec{m}}{\partial \xi_i}\right)\left(\frac{\partial \vec{m}}{\partial \xi_k}\right) \mathrm{d}V \right\} (\vec{e}_i \otimes \vec{e}_k) \\
G &= \sum_{im} \frac{\mu_0 M_\mathrm{s}}{\gamma_0} \int_V \vec{m} \cdot \left\{ \left(\frac{\partial \vec{m}}{\partial \xi_i}\right) \times \left(\frac{\partial \vec{m}}{\partial \xi_m}\right) \right\} \mathrm{d}V \, (\vec{e}_i \otimes \vec{e}_m)
\end{aligned} \tag{2.127}$$

Ending up with these equations, the considerations concerning the generalization of the Thiele equation can be concluded. In the next section it will be continued to elucidate further important aspects of the CCA and proceed with the discussion of some special quantities introduced by the CCA.

2.3.2.2 Special Physical Quantities used in the Collective Coordinate Approach

As mentioned at the end of the last section, it will be proceeded with the discussion of some special quantities introduced and utilized in the CCA. These physical quantities are the density of angular momentum J, the magnetic charge of the domain wall Q and the gyrotropic constant G_c. Please note, that the CCA denotes G_c as G. To avoid confusion with the notation of the gyroscopic tensor G in this work, the gyroscopic constant is written as G_c. Getting more and more into detail, the discussion arrives at ideas and concepts those reflect the heuristic nature of this approach to DWM. This heuristic approach will become very clear when discussing the quantities Q and especially G_c. Aiming to explain everything from scratch whenever possible, the start of the discussion is chosen to be

the consideration of the (absolute value) of the density of angular momentum J, which is a material property and the most generic physical quantity of the J, Q and G_c. Indeed, J is independent on the general shape of the sample and the DW type (magnetic texture) appearing. It can be understood in the following manner: The continuum limit for the magnetization is defined as [36–38],

$$\vec{M} = \frac{1}{V}\sum_{i=1}^{N}\vec{\mu}_\mathrm{s}^i = \frac{N}{V}\vec{\mu}_\mathrm{s} = n\vec{\mu}_\mathrm{s} = \gamma n\vec{s} = \gamma\vec{J} \tag{2.128}$$

and the factor $n\vec{s}$ can be regarded as $\vec{J}$, the vector of the density of angular momentum. Taking the absolute value on both sides, it yields[1]

$$M_\mathrm{s} = \gamma J \qquad \rightarrow \qquad J = \frac{M_\mathrm{s}}{\gamma} = \frac{\mu_0 M_\mathrm{s}}{\gamma_0} \tag{2.129}$$

with $|\vec{J}| = J$ and $\gamma_0 = \mu_0\gamma$. For a detailed explanation of all quantities see Sec. 2.1. Taking a close look on J reveals, that J is directly proportional to M_s and contains solely nature (μ_0) or material constants (γ_0) and by this it is a very general quantity that can be applied to every material. Please note that this statement about the generality of J, especially concerning the independency on the shape of the sample, holds true in the case of $Ni_{80}Fe_{20}$ only for samples with spatial dimensions larger than 10 nm. For $Ni_{80}Fe_{20}$ samples with thicknesses t of approximately 10 nm and smaller [81, 82], the saturation magnetization and the g-factor become a measure of t. But for almost realistic cases appearing in recent experimental studies, this limit will not fall below. Using J, the formulas for $\vec{F}^\mathrm{f}$, Γ and G_c as used in the CCA publicatios by Tretiakov et al. [47] and Clarke et al. [45] are finally obtained.

$$\begin{aligned}
\vec{F}^\mathrm{f} &= -\vec{\nabla}_{\vec{\xi}}E = \sum_i -\frac{\partial E}{\partial \xi_i}\vec{e}_i \\
\Gamma &= \sum_{ik}\alpha J\left\{\int_V\left(\frac{\partial\vec{m}}{\partial\xi_i}\right)\left(\frac{\partial\vec{m}}{\partial\xi_k}\right)\mathrm{d}V\right\}(\vec{e}_i\otimes\vec{e}_k) \\
G &= \sum_{im} J\int_V \vec{m}\cdot\left\{\left(\frac{\partial\vec{m}}{\partial\xi_i}\right)\times\left(\frac{\partial\vec{m}}{\partial\xi_m}\right)\right\}\mathrm{d}V\,(\vec{e}_i\otimes\vec{e}_m)
\end{aligned} \tag{2.130}$$

The discussion evolves now to the magnetic charge Q, a quantity which is in contradiction to J not completely independent on the magnetic structure in the regarded system or sample. Even when Q is not directly depending on the magnetic texture of the regarded DW itself, Q is determined by the magnetic state of the adjacent domains. Regarding in a first approximation a DW as a rigid magnetic particle, it is convenient to define the magnetic charge Q as used in the CCA in analogy to the electric charge of a particle. To avoid confusion, it should be pointed out that the magnetic charge Q is not exactly the same magnetic charge as it can be defined in micromagnetics as magnetic volume ($q_\mathrm{m,V}$) or surface charges ($q_\mathrm{m,S}$) [36, 38]. As will be see later on (see Eq. (2.150)), Q is connected to them, but not exactly equal! Q itself can be derived in two different ways: Both methods utilize the coefficient comparison between Zeeman energy E_Zee of a DW in a magnetic field and the potential

energy E_c of a charged particle in an electrical field, assuming in addition that $\vec{E}$ and $\vec{H}_{ext}$ are spatially homogeneous. Strictly speaking, the energy released when moving the DW (magnetic particle) and the particle possessing an electric charge by a distance X in the corresponding fields are compared. While the first way presented will only make intuitively clear, that the magnetic structure of the DW does not count, the second way which is based on the already mentioned magnetic charges ($q_{m,V}$, $q_{m,S}$) and Gauss's theorem [39], will provide a mathematically exact proof for this.

Concerning recent experimental [22, 83] and theoretical [26] results about field driven DWM, the most common DW type regarded are head-to-head (tail-to-tail) walls in thin magnetic samples. For this reason, and since such a case is treated in this thesis (namely VDWs), the considerations are confined to head-to-head (tail-to-tail) walls in the following. Nevertheless, the methods presented for the determination of Q can also be applied to other cases.

Starting with the first way of determing Q as it was used by Clarke et al. in [45]. Since comparing electrostatic and Zeeman energy, the Coulomb force $\vec{F}_c$ acting on a particle with charge q in a homogenous electrical field $\vec{E}$ (with $\vec{\nabla} \cdot \vec{E} = 0$), is given by [36, 84]:

$$\vec{F}_c = q\vec{E} \tag{2.131}$$

The energy needed to shift this particle about a distance X in this field is calculated by the line integral [43]

$$E = -\int_C \vec{F} \cdot \mathrm{d}\vec{r} \tag{2.132}$$

over the force. Assuming in analogy to the situation of the DW in an external magnetic field $\vec{H}_{ext}$ pointing along the stripe (x-direction), $\vec{E} = (E, 0, 0)$ and $\mathrm{d}\vec{r} = (\mathrm{d}r, 0, 0)$ is chosen to be parallel to x. Yielding an electrostatic energy E_c [36]

$$E_C = -q\int_C \vec{E} \cdot d\vec{r} = -qE\int_{r=0}^{X} dr = -qEX \tag{2.133}$$

(with $|\vec{E}| = E$) and comparing this to the Zeeman energy [38].

$$E_{Zee} = -\mu_0 \int_V \vec{M} \cdot \vec{H} dV \tag{2.134}$$

More precisely, the Zeeman energy released by the shift of the DW by a distance X is given through the comparison of the total Zeeman energy of the system before ($E_{Zee,tot}$) and after the shift ($E'_{Zee,tot}$). Without loss of generality, a head-to-head DW is considered. This DW is accompanied by two adjacent domains in a thin magnetic stripe with crossection A, given by the product of strip width w and thickness t. The change in Zeeman energy ΔE_{Zee} after a shift of X is determinded by changing the length of the domains 1 (left side of the DW) and 2 (right side of the DW). Moving the DW about X along the stripe alters the length of domain 1 from L_1 to $L'_1 = L_1 + X$ and domain 2 from L_2 to $L'_2 = L_2 - X$. Dealing solely with the magnetization in the domains, which is

spatially homogeneous, and the volume integral reduces to the multiplication of $-\mu_0\vec{M}\cdot\vec{H}$ by the Volume V [1].

$$\begin{aligned} E_{\mathrm{Zee}} &= -\mu_0 \int_V \vec{M}\cdot\vec{H}dV \\ &= -\mu_0\vec{M}\cdot\vec{H}\int_V dV \\ &= -\mu_0\vec{M}\cdot\vec{H}V \end{aligned} \tag{2.135}$$

To ensure that solely the spatial uniform magnetization of the domains are considered, l_{DW}, the length of the area which contains the DW, is chosen sufficent large enough to avoid an integration over its diverging magnetization with $\vec{\nabla}\cdot\vec{M}\neq 0$. Having $\vec{H}$ and $\vec{M}$ being parallel (domain 1 with $\vec{M}_1=(M_{\mathrm{s}},0,0)$) and antiparallel (domain 2 with $\vec{M}_2=(-M_{\mathrm{s}},0,0)$) to each other, the total Zeemann energy before and after the displacement of the DW is obtained[1]:

$$\begin{aligned} E_{\mathrm{Zee,tot}} = E_{\mathrm{Zee},1} + E_{\mathrm{Zee},2} &= -\mu_0 H M_{\mathrm{s}} wtL_1 + \mu_0 H M_{\mathrm{s}} wtL_2 \\ &= -\mu_0 H M_{\mathrm{s}} wt\,(L_1 - L_2) \\ E'_{\mathrm{Zee,tot}} = E'_{\mathrm{Zee},1} + E'_{\mathrm{Zee},2} &= -\mu_0 H M_{\mathrm{s}} wt\,(L_1 + X) + \mu_0 H M_{\mathrm{s}} wt\,(L_2 - X) \\ &= -\mu_0 H M_{\mathrm{s}} wt\,(L_1 - L_2) - \mu_0 H M_{\mathrm{s}} wt\,(2X) \end{aligned} \tag{2.136}$$

Here, the total Zeeman energies consist of the energy from domain 1 and 2, where the prime denotes the situation after the shift. Taking the difference between both values, it is found for the released Zeeman energy ΔE_{Zee} [1] [45]

$$E_{\mathrm{Zee,re}} = E_{\mathrm{Zee,tot}} - E'_{\mathrm{Zee,tot}} = -2\mu_0 H M_{\mathrm{s}} wtX \tag{2.137}$$

and by comparison with the electrostatic energy it is possible to define the magnetic charge Q for a head-to-head wall as [45]

$$Q = 2\mu_0 wtM_{\mathrm{s}} \tag{2.138}$$

and obtaining for the Zeeman energy expressed by Q [45, 47]:

$$E_{\mathrm{Zee,re}} = -QHX \tag{2.139}$$

Tail-to-tail walls lead to the same term, but with opposite sign, as can be easily checked. Defining the released energy as $E_{\mathrm{Zee,re}} = E_{\mathrm{Zee,tot}} - E'_{\mathrm{Zee,tot}}$ has been chosen in this way to get the right sign (minus) for the energy and the direction of the acting force on the DW. This force can be calculated by [43].

$$\vec{F}_{\mathrm{Zee}} = -\vec{\nabla}E_{\mathrm{Zee,re}} = \begin{pmatrix} QH \\ 0 \\ 0 \end{pmatrix} \tag{2.140}$$

yielding a positive value as expected, since applying an external field in (positive) x-direction, the DW should move in the same positive direction as well!

As became clear by determining Q for a head-to-head wall, it is intuitively plausible that the magnetic charge - defined on base of Zeeman energy - depends

only on the magnetic state of the domains. But it is possible to prove exactly by calculating the force and energy acting on the DW in terms of magnetic volume and surface charges (not to be confused with Q!). These magnetic charges are defined as [36, 38]

$$q_{\mathrm{m,V}} = \int_V \rho_{\mathrm{m}}\,\mathrm{d}V \qquad \text{and} \qquad q_{\mathrm{m,S}} = \int_A \sigma_{\mathrm{m}}\,\mathrm{d}A \tag{2.141}$$

where ρ_{m} and σ_{m} are the corresponding magnetic volume and surface charge densities. These densities are defined as [36, 38]

$$\rho_{\mathrm{m}} = -\vec{\nabla}\cdot\vec{M} \qquad \text{and} \qquad \sigma_{\mathrm{m}} = \vec{M}\cdot\vec{n} \tag{2.142}$$

and are connected to each other by Gauss's theorem [39]

$$\int_V \left(-\vec{\nabla}\cdot\vec{M}\right)\,\mathrm{d}V = \oint_S \vec{M}\cdot\vec{n}\,\mathrm{d}A \qquad , \tag{2.143}$$

where $\vec{n} = \vec{e}_n$ is the unit vector of the surface normal of A. Aiming to calculate Q in terms of these magnetic charges, an equation for E_{Zee} which incorporates them has to be found. For this purpose the derivative of E_{Zee} with respect to all spatial directions is taken, or in other words, the force acting on the DW is calculated by applying $-\vec{\nabla}$ to E_{Zee}. Finding[1]

$$\begin{aligned}
\vec{F}_{\mathrm{Zee}} = -\vec{\nabla}E_{\mathrm{Zee}} &= -\mu_0 \int_V \left\{\left(-\vec{\nabla}\cdot\vec{M}\right)\vec{H} - \vec{M}\left(\vec{\nabla}\cdot\vec{H}\right)\right\}\,dV \\
&= -\mu_0 \int_V \left(-\vec{\nabla}\cdot\vec{M}\right)\vec{H}\,dV \\
&= -\mu_0\vec{H}\int_V \underbrace{\left(-\vec{\nabla}\cdot\vec{M}\right)}_{\rho_{\mathrm{m}}}\,dV \\
&= -\mu_0 q_{\mathrm{m,V}}\vec{H}
\end{aligned} \tag{2.144}$$

which is an expression for the force in terms of the magnetic volume charge density. So far it has been demonstrated, that $\vec{F}_{\mathrm{Zee}}$ (and so E_{Zee}) is a measure of $q_{\mathrm{m,V}}$. Applying Gauss's theorem clearifies the picture and it becomes obvious, that Q is indeed independent of the magnetic texture of the DW. Replacing the volume integral by the integration of $\vec{M}\cdot\vec{n}$ over the enveloping surface around the DW,

$$\begin{aligned}
\vec{F}_{\mathrm{Zee}} &= -\mu_0\vec{H}\oint_S \underbrace{\vec{M}\cdot\vec{n}}_{\sigma_{\mathrm{m}}}\,dA \\
&= -\mu_0 q_{\mathrm{m,S}}\vec{H}
\end{aligned} \tag{2.145}$$

is found[1] and since A can be chosen arbitrarily, a rectangle is set as enveloping surface with surfaces parallel to the stripe at infinity and the intersecting ones in a large enough distance from the DW, so that $\vec{\nabla}\cdot\vec{M} = 0$ yields. By this, the integration reduces to an integral over the cross section $A = w\cdot t$ of the stripe and the quantity $\sigma_{\mathrm{m}} = \vec{M}\cdot\vec{n}$ is constant over the cross sectional area. Having[1]

$$\vec{F}_{\mathrm{Zee}} = -\mu_0 \sigma_{\mathrm{m}} \, (2A) \, \vec{H}_{\mathrm{ext}} \tag{2.146}$$

it is possible either to conclude directly by comparing $\vec{F}_{\mathrm{Zee}}$ and $\vec{F}_{\mathrm{c}}$ that the magnetic charge Q is given by $-2\mu_0\sigma_{\mathrm{m}}A$, or, based on previous considerations, regarding the energies E_{Zee} and E_{c}, respectively. Performing the path integral of $\vec{F}_{\mathrm{Zee}}$ over $\mathrm{d}\vec{r}$ (again it holds $\vec{H} \parallel \mathrm{d}\vec{r} \parallel \vec{e}_x$), one obtains[1]

$$\begin{aligned} E_{\mathrm{Zee}} = -\int_C \vec{F}_{\mathrm{Zee}} \cdot \mathrm{d}\vec{r} &= 2\mu_0\sigma_{\mathrm{m}} A \int_C \vec{H} \cdot \mathrm{d}\vec{r} \\ &= 2\mu_0\sigma_{\mathrm{m}} AH \int_{r=0}^{X} \mathrm{d}r \\ &= 2\mu_0\sigma_{\mathrm{m}} AHX \end{aligned} \tag{2.147}$$

and in a last step $\sigma_{\mathrm{m}} = \vec{M} \cdot \vec{n}$ has to be determinded. The surface normals are pointing always outwards of the volume V which is enclosed by the surface A, meaning that in the regarded case $\vec{M}$ and $\vec{n}$ are antiparallel on both surfaces on the lefthand an righthand side of the DW. Being antiparallel yields for σ_{m} [1]

$$\sigma_{\mathrm{m}} = -M_{\mathrm{s}} \tag{2.148}$$

and for E_{Zee} the expression[1]

$$\begin{aligned} E_{\mathrm{Zee}} &= -2\mu_0 M_{\mathrm{s}} AHX \\ &= -2\mu_0 wtM_{\mathrm{s}} HX \\ &= -QHX \end{aligned} \tag{2.149}$$

which contains the magnetic charge Q, is obtained. Thereby, the magnetic charge Q is given by the following relations[1] [45]:

$$Q = 2\mu_0 wtM_{\mathrm{s}} = -2\mu_0 A\sigma_{\mathrm{m}} = -\mu_0 q_{\mathrm{m,S}} \tag{2.150}$$

Proven that Q is really independent of the magnetic structure of the DW and solely the magnetic state of the adjacent domains counts, few additional remarks about the quantity Q as it is introduced by the CCA have to be done. As already mentioned, Q is not exactly the same magnetic charge as it is introduced in micromagnetics, but connected to it as can be seen in Eq. (2.150). Becoming already clear by the way Q has been defined based on Zeeman energy, the magnetic charge Q is a useful measure to set the equations for the energy of a DW in dependence of the spatial coordinates of characteristic points (for example the position of the VC). Talking about the energy of the DW, it should be noted in advance, that the energies will be denoted as $U(\vec{\xi}(t))$, with U being the free energy. For example, speaking about the dependence of U with respect to spatial coordinates of characteristic points, the energy E_{Zee} which helped to define the magnetic charge Q, is nothing else than $U(X)$, the component of the free energy U which depends on the x-position of the VC (characteristic point) (see Sec. 2.3.2.4). This energy $U(X)$ is a measure how much Zeeman energy is released when the dW moves along the stripe and yields in addition the force (by $-\frac{\partial U(X)}{\partial X}$), which acts on the DW and pushes it in longitudinal direction (see

Sec. 2.3.2.5).

As third and last quantity the gyrotropic constant G_c which is the most non generic one is discussed. This constant appears as preafactor in front of the gyrotropic tensor or the gyrovector $\vec{G}$ and is determinded by the magnetic structure of the DW itself. G_c itself is always proportional to J, what can be seen by looking at the formula for the gyrotropic tensor G in Eq. (2.130), which contains J as prefactor. The integral in Eq. (2.130) yields a proportionality factor depending on the magnetic structure of the DW. Without proof, the gyrotropic tensor G can always be written in the form [45]

$$G = G_c \epsilon \tag{2.151}$$

where ϵ is the Levi-Civita tensor. For the special case of a VDW the expressions can be modified to [45]

$$G = pG_c \epsilon \tag{2.152}$$

with p being the polarity of the VC and, as it will be explained in Sec. 2.3.2.6, G_c having the value [45, 47]:

$$G_c = 2\pi Jt \tag{2.153}$$

From a physically point of view, the vector $\vec{G}$ can be interpreted as the macrospin of the magnetic particle. Recalling assumptions which are the starting point for the derivation of the Thiele eq., the basic idea was to consider the DW as rigid particle moving under the influence of an external field. Since considering a magnetic texture which consists out of a large number of magnetic moments (spins), it has to enter somehow the Thiele equations. The way the magnetic moments entering the equations is via the gyroscopic tensor or alternatively in the reformulation as gyro vector $\vec{G}$. This rounds off the considerations of the physical quantities. Before proceeding to the last point of the discussion concerning the CCA, the Thiele equation will be expressed in the form as used by the authors of the CCA. It reads in general [45]

$$\vec{F} - \Gamma \dot{\vec{\xi}} + G_c \epsilon \dot{\vec{\xi}} = 0 \tag{2.154}$$

or for a VDW [45]:

$$\vec{F} - \Gamma \dot{\vec{\xi}} + pG_c \epsilon \dot{\vec{\xi}} = 0 \tag{2.155}$$

What has been obtained now is a generalized version of the Thiele equation, which is formally exact, since it is just a reformulation of the LLG equation in terms of forces. This equation can only be solved with numerical methods, but since aiming to determine analytical solutions for DWM, Eq. (2.154) (or Eq. (2.155) in the case of a VDW) it needs to be reduced to a set of coupled equations of motion. These equations describe the time evolution of the position of a few characteristic points within the DW. Since this is the strength and big advantage of Thiele's approach to DWM, reduction to a few coordinates has to be performed, which will lead then to a simplification of the mathematical task. For this aim the authors of the CCA introduce the concept of soft and hard

modes, which will be discussed in the next section.

2.3.2.3 Concept of Modes

The discussion finally arrived at a point where a concept utilized in the CCA will be elucidated, which is the most difficult to explain from scratch by basic physical principles. To understand the origin of the idea of modes as used by the CCA, an intuitive account is chosen to approach the concept from two different directions. In a first account a descriptive approach of the motion of a VDW is given. Within this description the terms "modes" and "characteristic times" are introduced. Following, the problem is addressed by energetic considerations. As mentioned, these modes are the best understood, when deeper knowledge about DWM is given. Following now, a description of the dynamic behaviour of a VDW under the influence of an external magnetic field $\vec{H}_{\mathrm{ext}}$ will be given. Thereby different field ranges and dynamics regimes are discussed.

A VW is composed out of three elementary topological defects, namely the VC in the bulk and two HAVs located at the stripe edges. These objects are relative stable and rigid objects when considering moderate magnetic fields smaller than approximately 2.5 mT [18]. In this case it is possible to regard them as coupled together, forming in this way a DW. Applying an external field below the critical Walker field H_{c} (sometimes denoted as H_{w}), the DW starts to move along the stripe. But in fact, and here a deeper knowledge about the internal dynamic of such kind of wall is required, the VC starts to move in x- and y-direction, while the HAVs adjust their motion in longitudinal direction adiabatically. What is meant by "adjust adiabatically"? To clearify, the fact has to be realized, that every motion is taking place on some characteristic time scale τ, depending on the specific kind of motion considered. Concerning the linear steady-state motion, the dynamics of the VC and the two HAVs are taking place on different τ's, whereby the τ for the HAVs is much shorter than for the VC. This means, the time which is needed for the HAV to adjust to the motion of the VC is so short, that it can not "be seen" moving. This is the meaning of the phrase "adjust adiabatically".

It can be also understood by the example of a spring pendulum. As already mentioned, the elementary topological defects can be regarded as coupled together. Thinking about a spring which can be moved at the upper end (where the VC is sitting) and a particle with mass m at the lower end (where one of the HAVs is located). May the spring have a spring constant D and including friction by the damping constant γ_{osc}, the whole system has an oscillation period T, which is equal to the characteristic time τ for the HAVs. Exciting now the whole system with a low excitiation frequency far away from the resonance frequency, the spring, synonymous for the interaction between VC and HAV, is behaving like a rigid (hard) connection. This is the case where the mass or HAV respectively adjusts adiabatically and therefore this kind of mode is called a "hard mode". As should become clear upon this picture, hard modes are non dynamic, their dynamic is governed by another mode. Going now to higher external fields exceeding the critical Walker field, the VC collides with one of the HAVs confined at the edges and is reemitted into the stripe with opposite polarity p [47, 49, 85]. Due to this polarity reversal, the VC moves across the stripe

in y-direction until it hits the second HAV at the opposite edge. Again, the VC is reemitted accompanied by a polarity reversal, moving back to the first edge and the process starts from the beginning. By this, the VC has an oscillatory motion in transversal direction, resulting in a lower net velocity in longitudinal direction, the so called Walker breakdown. This oscillatory behaviour is connected with a characteristic time T_{trans} which it takes the VC to cross the stripe on its way from one HAV to the opposite one. T_{trans} is remarkably independent of the stripe width w and in good approximation solely a function of the external field, proportional to $\frac{1}{H}$ (will be shown in Sec. 2.3.3.2). Cranking the field up, the transition time T_{trans} becomes shorter. Returning to the picture of the spring pendulum, in the case of the oscillatory motion of the VDW above H_{c}, the mass m (HAV) connected to the spring is now excited by a frequency with a shorter period T. Going to even higher fields the excitation frequency is altered and it becomes possible, that the resonance frequency of the driven harmonic oscillator is matched (or being at least very close to it). In this situation, the spring between the upper end (VC) and the lower one (HAV) cannot be regarded anymore as rigid. Indeed, the mass (HAV) attached to the spring can not follow directly (adiabatically) the motion of the upper end (VC) and the mass (HAV) moves with a phase shift compared to the motion of the upper end of the spring (VC). Due to this, the spring gets stretched and compressed and behaves like an elastic (soft) connection. This is the case that is denoted as a "soft mode" and where another motion gets excited, or in other words, becomes "visible". Becoming "visibel" can be understood as becoming dynamic.

In the previous example the case has been discussed, what is happening when very high fields above the critical Walker field H_{c} are reached. With T_{trans} becoming shorter, the overall dynamics of the DW, governed by the oscillatory motion of the VC, is becoming that fast, that the HAVs can not adapt adiabatically. From this fact one can conclude, that the time T_{trans} is the critical time which determines in the field regime above H_{c} whether a mode is soft or hard. In contradiction to this, the key number for the steady-state motion regime below the Walker breakdown is the time τ_1 which the VC needs to approach its steady-state velocity. Summing up it can be concluded, that there is a critical time T - depending strongly on the field regime considered - which serves as a distinctive criteria for modes being particularly soft or hard. These considerations can serve as the basis for an intuitive account to modes as used in the CCA, leading to a model which is based on an inductive argumentation.

Indeed, it turns out, that this concept of modes is generic and can be applied to all kinds of DWM. To conclude, it has been found that the DW internal dynamics under the influence of an external field $\vec{H}_{\text{ext}}$ can be decomposed into so called modes. These modes, where one can distinguish between hard and soft ones, are connected to coordinates of characteristic points. Having a soft mode implies, that the corresponding coordinate has to be regarded as dynamical, while coordinates connected with a hard mode are non dynamical and adjust adiabatically. Which modes are particularly soft or hard for a given dynamic regime (or field) depends on a characteristic time T which governs the overall motion of the DW in the field regime considered. Finding the appropriate time T, which most likely may vary between different dynamic regimes, is a tricky task and crucial for the correct description of the DW dynamics. Having T, the

following exemplary scheme is obtained [45, 47],

$$\underbrace{\tau_0 > \tau_1}_{\text{soft}} > T > \underbrace{\tau_2 > \tau_3 > \cdots}_{\text{hard}} \tag{2.156}$$

where modes having $\tau > T$ are soft and modes with $\tau < T$ are hard. This perspective on DWM is quite interesting, but how can it help to reduce the exact (generalized) Thiele equation to a set of coupled differential equations for a few coordinates of characteristic points?

In order to understand this question, the solution is to strive for an energetic consideration of the modes. To do this, it has to be recalled that the drift motion of DWs under the influence of an external field $\vec{H}_{\text{ext}}$ is determinded by the dissipation rate of the Zeeman energy. At this point it can be stated: Evidently, only those modes which dissipate most of the Zeeman energy are relevant to the drift motion of the DW. To dissipate much Zeeman energy, the modes have to be active long enough. Long enough means in this case relative to a characteristic time scale T on which the overall dynamics of the DW happens. This leads to the conclusion, that only those modes are relevant for the motion of the DW, whose time scales τ are larger than t, which applies for soft modes. On the other hand, hard modes, which are only extremely shortly active in comparison to the entire dynamic, dissipate very little energy and are therefore negligible. Since with every mode a coordinate is connected, the classification into soft and hard modes tells which coordinates have to be taken into account and so, this concept of modes is beneficial to reduce the mathematical task to solve a set of differential equations. Understanding what is meant by the term modes and what central role they are playing in the CCA, the discussion evolves to some of the fundamental aspects of this concept.

First of all it will be considered how to determine which modes are soft or hard. As powerful as this concept may be, it is useless without concrete values for T and τ's, by which one can make the distinction of modes. So, how to obtain the values? Unfortunately, the Thiele equation has to be solved for a different amount of coordinates taken into account (for example one-mode or two-mode approximation and so on), and obtain upon these results the value for the corresponding τ's. This will is done in Sec. 2.3.3.1-2.3.3.2. In order to anticipate the coming sections, is yields for example in the case of a VDW for the y-coordinate the following time dependence[1] [47]:

$$Y(t, H, w, c, p) = \frac{(c \cdot g(w) - p)\, G_{\text{c}} Q H}{k\Gamma_{\text{XX}}} \left(1 - e^{-\frac{k\Gamma_{\text{XX}}}{G_{\text{c}}^2 + \det\Gamma} t}\right) \tag{2.157}$$

where the appearing quantities will be explained in the corresponding sections. This result follows from a two-mode approximation (including X and Y position of the VC), and can be interpreted as the pre-factor in front of t in the exponent as the inverse characteristic time for the motion in y-direction. This time constant is given by the relation[1] [47]

$$\tau_1 = \frac{G_{\text{c}}^2 + \det\Gamma}{k\Gamma_{\text{XX}}} \tag{2.158}$$

and will be denoted in the following as τ_1. τ_1 can be interpreted as the time

constant for the approach of the VC to its equilibrium position in y-direction under the influence of an external applied field. Two important things have been found by this example, which will be emphasized again below. First, the characteristic times τ are decay constants for the motion of the associated coordinate, and second, these are decay constants for motion under an external magnetic field. They should not be confused with decay constants which describe the motion after the field is turned off. Understanding now the quantity τ, what about T, the time which determines the time scale on which the overall DW dynamic (in a certain regime) happens?

Choosing the appropriate time T is a matter of some physical intuition and again, knowledge about the DW dynamics is beneficial. In general T can either be a characteristic time τ itself, or the time scale of some feature of the DW dynamics. As for example, lets consider the steady-state motion at very weak applied fields below the critical Walker field H_c. Here, only the motion in x-direction is relevant and the following situation regarding T holds true: The dominant dynamics in this case is the motion in longitudinal direction which exhibits a characteristic time $\tau_0 = \infty$ (see Sec. 2.3.3.1), while the motion in y-direction is only relevant at the very first time after the external field $\vec{H}$ is applied. Approaching its equilibrium position in transverse displacement with a characteristic time constant τ_1, and regarding long pulse times t_p, the motion connected with τ_1 (and all higher modes with $\tau_n < \tau_1$) can be neglected, since $\tau_1 \ll t_\mathrm{p}$ is given. In this case it is possible to choose $T = \tau_1$ or somewhere in between τ_0 and τ_1 as distinctive criterion for which modes in particular are soft or hard. Steady-state motion is one example where it is suitable to choose a characteristic time τ_n as T. But T can also be some other characteristic time, as illustrated by the dynamics above the critical Walker field. For the oscillatory regime above the Walker breakdown, the superordinate dynamics is governed by the transition time T_trans, which the VC needs to get from one HAV to the other [45, 47].

$$T_\mathrm{trans} = \frac{\pi}{\mu_0 \gamma H} = \frac{\pi}{\gamma_0 H} \tag{2.159}$$

Here, T should be chosen to be equal to T_trans. Remarkably, the transition time for the VC is independent of the stripe width w and indirectly proportional to the external driving field H, as already stated by Clarke et al. in [45]. Calculating concrete numbers for T_trans, it is obtained that T_trans is smaller than τ_0 and τ_1, but larger than τ_2, the time constant for the motion of the HAVs. Based on the concept of soft and hard modes, it yields, that a two-mode approximation is a sufficient starting point to describe the oscillatory motion above H_c which is accompanied by a sharp drop in net velocity in longitudinal direction. Due to the dependence of T_trans on H, the transition time, and as a consequence of this the time T as well, becomes shorter by increasing the field $\vec{H}_\mathrm{ext}$. Going to higher fields, it is possible that T_trans becomes shorter than τ_2 and the mode for the HAVs becomes soft with the two-mode approximation being no langer valid, and giving rise to DW oscillations. Concerning $Ni_{80}Fe_{20}$, one of the prototypical materials for the investigation of DWM in all kinds of geometries, it is found that the difference between the values of τ_1 and τ_2 is large enough for the two-mode approximation being applicable up to fields of $\mu_0 H = 3.5$ mT. Above these fields

the eigendynamics of the two HAVs has to be included in order to get a suitable description of the DWM.

Another fact which becomes clear by looking at the discussion about how to find the matching T for a certain regime is, that T is no hard criteria. It is not a hard criteria in two different ways: First, the classification in hard and soft modes based on T gives a good starting point which modes (coordinates of characteristic points, respectively) should be taken into account. But nevertheless, more coordinates can be included, enhancing, under some circumstances, the description of the DW dynamics. As for example, for the low field mobility range of the DW discussed before, the x-coordinate (mode τ_0) is sufficient, what yields the steady-state velocity which is reached very fast by the DW. As a consequence, it yields a good description of the DWM at very low external fields. But nevertheless, it does not capture accurately the y-motion of the VC at the very beginning of the motion. Even T as classification criteria states, that the lowest mode with τ_0 is sufficient on this regime, a better description of the DWM is achieved by a two-mode approximation, which takes the two in-plane coordinates (X,Y) into account.

The second point concerning the fact, that the classification in soft and hard modes is no hard criterium is, that the transition between two dynamic regimes, where for example in one regime a mode τ_n is inactive (hard) and in the other one is active (soft), is fluent. Or in other words, the softening of a mode is a continuous process. It is not the case, that a mode is hard, respectively not active, and after increasing the external applied field it becomes suddenly soft and active. This can be understood again in the frame of the spring model utilized to explain the interactions between the VC and the HAVs. A hard mode was present when being in a far off resonant state and soft mode appeared by hitting the resonance. But this is only a part of the truth. As known from classical physics, the excitation does not solely happen exactly at the resonance point. It oscillates in a more or less broad frequency range of the excitation frequency around ω_0. Material constants determine the width of the frequency range, and so it can happen, that even T being larger than a certain decay time τ_n of a mode, and regarding the actual classification not important, it already influences the dynamics of the DW. This reflects the earlier mentioned fact, that the dynamics of a magnetic texture exhibits infinitely many modes and for an absolutely correct description all modes have to be taken into consideration. However, it turns out, that the theoretical description of the DWM by a few coordinates provides very good results. Assuming the characteristic times τ_n differ strongly enough from each other, relatively large field ranges are obtained for which a certain approximation (for example one- or two-mode approximation) is valid.

To round off the contemplations on the modes, the example of a 180° DW as discussed by Walker on the basis of a Bloch wall [29] will be revisited. Now the problem will be considered from the point of view of modes. In [29] a two-mode approximation was utilized (without knowing the terminology) to tackle the problem. Basically the DWM of this wall type exhibits in the one-dimensional case three degrees of freedom, namely the position q, the angle φ and the domain

wall width Δ. In general a system of three coupled differential equations would arise, but for moderate fields, the domain wall width Δ, which is a measure of φ, adjusts very fast (adiabatically) to the variation of φ. The reason for this is, that the characteristic decay time τ_Δ is much smaller than for the quantity φ, namely τ_φ. Thinking about the appropriate time T, it is obtained that it is similar to the case of a VDW in the oscillatory regime ($H > H_c$). While for a VDW an oscillatory motion of the VC from one HAV to the other is observed, in the case of a Bloch wall a starting of oscillations of the magnetization around the external field appears. The period time T_{oscil} of this oscillations is a good measure for T in a broad field range. Choosing $T = T_{\text{oscil}}$ yields, that a two-mode approximation is sufficient for the description of the DW dynamics in the steady-state motion and in the oscillatory regime above H_c. Calculating T and the characteristic times for q, φ and Δ it holds, that the value of T is between τ_φ and τ_Δ, while τ_q for the motion in longitudinal direction yields the highest value. Writing all decay times into the scheme for the classification into soft and hard modes, the following inequality [45]

$$\infty = \tau_q > \tau_\varphi > T \gg \tau_\Delta \tag{2.160}$$

is obtained, which is valid up to high fields in the oscillatory regime.

2.3.2.4 Energies

For the calculation of the forces acting on the VDW, the free energy $U(X, Y)$ the VC possesses under the action of an external applied field has to be known. In the following the considerations concerning the energy are restricted to the energy of the VC, since in the regarded cases in this thesis solely the dynamics of the VC is important. Of course, when investigating for example very high external fields, the dynamic of the HAVs becomes important and their energy has to be included in U. In the following, symmetries of the sample geometry are exploited to find the corresponding energies. Thereby the energy $U(X, Y)$ can be decomposed in one part which depends only on the longitudinal coordinate X of the VC and one depening only on Y. The energy reads[1]

$$U(X, Y) = U(X) + U(Y) \tag{2.161}$$

and in a first step the X-dependence of the free energy will be discussed. Imagine a head-to-head DW in a stripe that is displaced one time by X and the other time by $-X$, than $U(-X) = -U(X)$ is found for the behaviour of the energy which tells that $U(X)$ central symmetric with respect to X. This implies that a series expansion of $U(X)$ contains in general only terms with odd symmetry in X. In fact, only the term proportinal to X is physical meaningful and given by the Zeeman energy. Its value has been derived in the section about the special physical quantities of the CCA (see Sec. 2.3.2.2). To determine the Y-dependent contributions to the free energy, the underlying symmetries of the system are utilized. In the absence of an external field the sytem possesses a pure reflectional symmetry leading to $U(Y) = U(-Y)$.

In terms of a Taylor series, the expansion of $U(Y)$ contains solely terms with even powers in Y. However, a magnetic field breaks this reflectional symmetry due to the chiral magnetic structure of the VDW. The curling magnetization

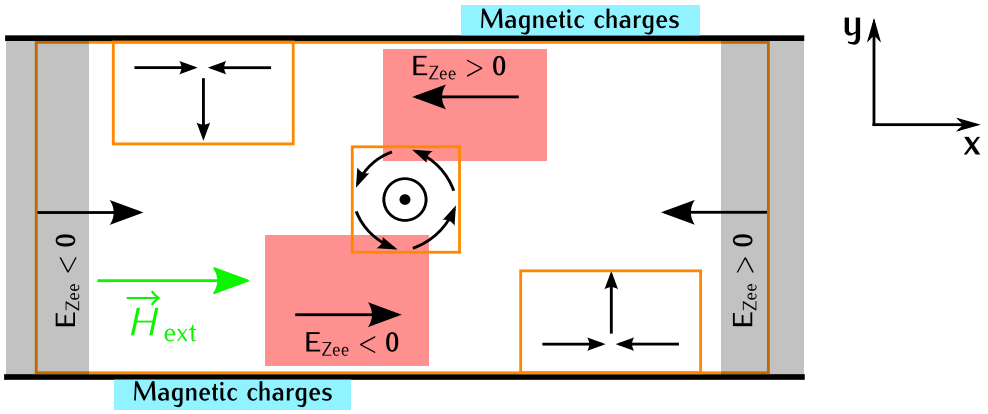

Figure 2.5. Schematic representation of a VDW with chirality $\chi = 1$ ($p = 1$, $c = 1$) and the resulting energies. In the case of an externally applied field H pointing in positive X-direction (from left to right), the areas (red) with positive and negative Zeeman energies (proportional to Y-position of the VC) built up above and below the VC, respectively. The magnetic charges at the stripe edges (indicated with light blue) create stray fields and cause the energy contributions proportional to Y^2. The energy contribution depending on the longitudinal position X of the DW originates from the domains at the left and the right side of the VDW. In the left domain the magnetization is aligned parallel with respect to H, in the right one antiparallel, respectively and one gains areas with negative and positive Zeeman energies (grey areas).

causes a Zeeman barrier which favors (depening on c) the motion of the VC to one stripe edge and hinders it with respect to the opposing one. This induces a slight point reflection symmetry in Y, allowing terms with odd power in the series expansion. In this case higher orders Y are possible due to the nonlinearity of the potential $U(Y)$, but for the purpose of linearization the considerations are restricted to Y^2 as highest order. The total free energy $U(X, Y)$ than is found to be [45, 47]

$$U(X,Y) = -QHX - rcQHY + \frac{k}{2}Y^2 + \mathcal{O}(X^2) + \mathcal{O}(Y^3) \tag{2.162}$$

where the first term is the Zeeman energy. The second term represents the Zeeman barrier in Y-direction which is parametrized by the numerically calculated factor r being of the order of 1. k as prefactor in the quadratic term is the constant characterizing the restoring force which tries to keep the VDW in the middle of the stripe. Based on these prerequisites, the discussion now moves on to the calculation of the forces acting on a VC under the action of an applied field.

2.3.2.5 Force Term

The forces acting on the VC are governed in the two-dimensional case by the energy $U(X, Y)$ obtained in the preceding section. Applying the partial derivatives of $U(X, Y)$ with respect to the spatial coordinates of the VC, the force vector $\vec{F}^{\mathrm{f}}$ is obtained[1]:

$$\vec{F}^{\,\mathrm{f}} = -\vec{\nabla}_{\vec{\xi}} U(X,Y) = \begin{pmatrix} F_X \\ F_Y \\ F_Z \end{pmatrix} = \begin{pmatrix} QH \\ rcQH - kY \\ 0 \end{pmatrix} \tag{2.163}$$

2.3.2.6 Gyrovector

For the calculation of the gyrovector of a VDW, solely the VC itself is considered, whereby the magnetization $\vec{M}$ is parametrized in spherical coordinates M_s, φ and ϑ. As demonstrated in Sec. 2.2.3.5, the gyrovector in these coordinates reads[1] [34]

$$\vec{G} = -\frac{\mu_0 M_\mathrm{s}}{\gamma_0} \int\limits_V \sin(\vartheta) \left(\left\{ \vec{\nabla}\vartheta \right\} \times \left\{ \vec{\nabla}\varphi \right\} \right) \mathrm{d}V \tag{2.164}$$

and due to symmetry, it is convenient to calculate the spatial gradients in polar coordinates ρ, β and z. Usually, the angle is denoted as φ, but since the azimuthal angle for the parametrization of $\vec{M}$ is labled in the same way, a change in labeling for this variable to β is done to avoid confusion. Considering only the region close to the VC, the magnetization posesses a radial symmetry, where φ depends only on β and the angle ϑ is purely a function of ρ. With this underlying symmetry, the cross product of the spatial gradients for φ and ϑ reduces to[1]

$$\vec{\nabla}\vartheta \times \vec{\nabla}\varphi = \frac{1}{\rho} \frac{\partial \vartheta}{\partial \rho} \frac{\partial \varphi}{\partial \beta} \vec{e}_z \tag{2.165}$$

where the relation $\vec{e}_\rho \times \vec{e}_\beta = \vec{e}_z$ is additionally exploited. Inserting this in Eq. (2.164) and integrating over the full volume in polar coordinates, it yields[1]

$$\vec{G} = -\frac{\mu_0 M_\mathrm{s}}{\gamma_0} \vec{e}_z \int\limits_{z=0}^{t} \mathrm{d}z \int\limits_{\beta=0}^{2\pi} \frac{\partial \varphi}{\partial \beta} \mathrm{d}\beta \int\limits_{\rho=0}^{\infty} \sin(\vartheta) \frac{\partial \vartheta}{\partial \rho} \mathrm{d}\rho \tag{2.166}$$

and by using the parametrization of φ in dependency on β, which is given by [30, 45]

$$\varphi = n\beta + c\frac{\pi}{2} \qquad \rightarrow \qquad \frac{\partial \varphi}{\partial \beta} = n \tag{2.167}$$

is obtained. The partial derivative of φ with respect to β is the winding number n of the vortex. For the sake of completeness it should be mentioned, that the the factor c contained in the formula for φ is the circulation of the vortex, which is beside the polarity p the second key parameter to characterize a magnetic vortex. Making a change of variables to convert the integration over ρ into an integral over ϑ, the expression for $\vec{G}$ is given by[1]

$$\vec{G} = -\frac{\mu_0 M_\mathrm{s}}{\gamma_0} \vec{e}_z \int\limits_{z=0}^{t} \mathrm{d}z \int\limits_{\beta=0}^{2\pi} n \, \mathrm{d}\beta \int\limits_{\vartheta=(1-p)\frac{\pi}{2}}^{\frac{\pi}{2}} \sin(\vartheta) \, \mathrm{d}\vartheta \tag{2.168}$$

and reduces finally to[1]:

$$\vec{G} = -\frac{2\pi\mu_0 M_\mathrm{s} n t}{\gamma_0}\vec{e}_z \cos((1-p)\frac{\pi}{2}) \tag{2.169}$$

Discussing the two cases for the possible values of p, it holds[1]

$$\cos\left((1-p)\,\frac{\pi}{2}\right) = \begin{cases} p=1 & \rightarrow \cos(0) = 1 = p \\ p=-1 & \rightarrow \cos(\pi) = -1 = p \end{cases} \tag{2.170}$$

that the cosine term always yields the polarity p. The case distinctions is leading to the final result for the gyrovector $\vec{G}$ of a vortex core in a disc, those formula also holds true for a VDW [30, 45].

$$\vec{G} = -\frac{2\pi\mu_0 M_\mathrm{s} n t p}{\gamma_0}\vec{e}_z \tag{2.171}$$

In principle, the task of calculating the gyrovector is finished, but since there is a second more abstract method in determining $\vec{G}$, the second calculation method should be presented additionally. Turning to the expression of the component G_{xy} of gyrotensor, given by Eq. (2.104) [45, 47]

$$G_{xy} = \frac{\mu_0}{\gamma_0 M_\mathrm{s}^2}\int_V \vec{M}\cdot\left\{\left(\frac{\partial\vec{M}}{\partial x}\right)\times\left(\frac{\partial\vec{M}}{\partial y}\right)\right\}\mathrm{d}V \tag{2.172}$$

and comparing it with the expression of the topological charge q_t. Dealing with a magnetic texture only varying in the x-y-plane, it becomes clear from the general formula for G, that only the component G_{xy} has to be taken into account. The topological charge of a magnetic texture as for example a skyrmion or a vortex, is calculated from [45, 86]

$$q_\mathrm{t} = \frac{1}{4\pi M_\mathrm{s}^3}\int_A \vec{M}\cdot\left\{\left(\frac{\partial\vec{M}}{\partial x}\right)\times\left(\frac{\partial\vec{M}}{\partial y}\right)\right\}\mathrm{d}A = \frac{n}{2}p \tag{2.173}$$

and remarkably this complicated integral reduces to $\frac{n}{2}p$. The similarity of both expressions (G and q_t) is easily recognized. Manipulating G_{xy} mathematically in that manner, that the expression for q_t can be applied, G_{xy} reads

$$G_{xy} = \frac{4\pi\mu_0 M_\mathrm{s}}{\gamma_0}\left(\int_{z=0}^{t}\mathrm{d}z\right)\left(\frac{1}{4\pi M_\mathrm{s}^3}\int_A \vec{M}\cdot\left\{\left(\frac{\partial\vec{M}}{\partial x}\right)\times\left(\frac{\partial\vec{M}}{\partial y}\right)\right\}\mathrm{d}A\right) \tag{2.174}$$

and it is obtained [45]:

$$G_{xy} = \frac{2\pi\mu_0 M_\mathrm{s} n p t}{\gamma_0} \tag{2.175}$$

As already mentioned, for a magnetization texture solely depending on x and y, it follows from Eq. (2.104), that G is[1]

$$G = \begin{pmatrix} 0 & G_{xy} & 0 \\ G_{yx} & 0 & 0 \\ 0 & 0 & 0 \end{pmatrix} = \begin{pmatrix} 0 & G_{xy} & 0 \\ -G_{xy} & 0 & 0 \\ 0 & 0 & 0 \end{pmatrix} \tag{2.176}$$

and contains only one single parameter, since $G_{xy} = -G_{yx}$ holds. Finally, the gyrovector has to be calculated out of the gyrotensor to compare the result obtained from two different methods. In Sec. 2.2.3.5 about the derivation of G and $\vec{G}$ it has been explained, that the mathematical connection between both is given by Eq. (2.106), yielding in the actual case[1]:

$$\vec{G} = -G_{xy}\vec{e}_z \tag{2.177}$$

Inserting the result for G_{xy} [1]

$$\vec{G} = -\frac{2\pi\mu_0 M_s npt}{\gamma_0}\vec{e}_z \tag{2.178}$$

the same result for $\vec{G}$ as before is gained.

2.3.2.7 Damping Tensor for a Vortex in a Disc

In this section the damping tensor for a vortex in a disc will be calculated, serving as a preliminary work and starting point for the calculation of Γ for a realistic VDW. On one hand side the result for the damping tensor of the VC itself has to be determined either way in the realistic VDW model and on the other hand, this section serves as a demonstration how to treat equations containing outer products. Since treating a vortex in a disc, the same symmetries appear as in the section about the gyrovector $\vec{G}$. Choosing again spherical coordinates, the general form of the damping tensor Γ is given by[1]

$$\Gamma = \frac{\alpha\mu_0 M_s}{\gamma_0}\int\limits_V \left(\left\{\vec{\nabla}\vartheta\right\}\otimes\left\{\vec{\nabla}\vartheta\right\} + \sin^2(\vartheta)\left\{\vec{\nabla}\varphi\right\}\otimes\left\{\vec{\nabla}\varphi\right\}\right)\mathrm{d}V \tag{2.179}$$

whereby the damping tensor is computed on base of the analytical model where the sine of the the polar angle ϑ is parameterized by R_0, the radius of the VC, and ρ, the actual radial position [87].

$$\sin(\vartheta) = \begin{cases} \frac{2R_0\rho}{R_0^2+\rho^2} & \text{for} \quad 0 \leqq \rho \leqq R_0 \\ 1 = \text{const.} & \text{for} \quad R_0 \leq \rho \leqq R_{\max} \end{cases} \tag{2.180}$$

This analytical expression is defined section-wise, distinguishing between the rather small region of the VC itself and the rest of the disc. With exception of the VC, the magnetization lies in-plane, expressed by $\vartheta = \frac{\pi}{2}$ or $\sin(\vartheta) = 1$ =const., respectively. The only region where the polar angle of magnetization is changing in dependence of ρ is within the VC. There it changes from pointing out of plane ($\vartheta = 0$) at the center of the VC (at ρ) to $\vartheta = \frac{\pi}{2}$ at $\rho = R_0$. It should be mentioned, that the azimuthal angle φ is parametrized by the same function $\varphi = n\beta + c\frac{\pi}{2}$ as in the previous section. Dealing with a section-wise defined function requires a section-wise calculation of the damping tensor Γ. For this task the distinction between the contribution to Γ form the VC $\Gamma_{\rho\gg R_0}$ and the rest of the disc $\Gamma_{\rho\gg R_0}$ is done. In both sections the calculations based on Eq. (2.179) have to be carried out, but based on the considerations concerning ϑ those have been done in the frame of the analytic model, it is possible to neglect at least some terms, simplifying the mathematical task. Within the VC, the full expression

for Γ has to be calculated, but in the area outside the VC up to the edge of the disc, the integral reduces to the part containing only the spatial gradients for φ. With ϑ being constant outside the VC results in $\vec{\nabla}\vartheta = 0$ and additionally the term $\sin(\vartheta)$ can be set to 1 [1].

$$\begin{aligned}\Gamma =&\Gamma_{\rho\leqq R_0} + \Gamma_{\rho\gg R_0}\\ =&\frac{\alpha\mu_0 M_\mathrm{s} t}{\gamma_0}\int_{\rho=0}^{R_0}\int_{\beta=0}^{2\pi}\left(\left\{\vec{\nabla}\vartheta\right\}\otimes\left\{\vec{\nabla}\vartheta\right\} + \sin^2(\vartheta)\left\{\vec{\nabla}\varphi\right\}\otimes\left\{\vec{\nabla}\varphi\right\}\right)\rho\mathrm{d}\rho\mathrm{d}\beta +\\ &\frac{\alpha\mu_0 M_\mathrm{s} t}{\gamma_0}\int_{\rho=R_0}^{R_\mathrm{max}}\int_{\beta=0}^{2\pi}\left\{\vec{\nabla}\varphi\right\}\otimes\left\{\vec{\nabla}\varphi\right\}\rho\mathrm{d}\rho\mathrm{d}\beta\end{aligned} \tag{2.181}$$

Exploiting the discussed symmetries of φ and ϑ, it yields for the outer product between the spatial gradients[1]

$$\left\{\vec{\nabla}\vartheta\right\}\otimes\left\{\vec{\nabla}\vartheta\right\} = \left\{\frac{\partial\vartheta}{\partial\rho}\right\}^2\vec{e}_\rho\otimes\vec{e}_\rho \tag{2.182}$$

and[1]

$$\left\{\vec{\nabla}\varphi\right\}\otimes\left\{\vec{\nabla}\varphi\right\} = \frac{n^2}{\rho^2}\vec{e}_\beta\otimes\vec{e}_\beta \qquad , \tag{2.183}$$

respectively. In the expression for $\left\{\vec{\nabla}\varphi\right\}\otimes\left\{\vec{\nabla}\varphi\right\}$ the fact that the partial derivative of φ with respect to β is given by the winding number n has been applied. Plugging this into the formula for the full value of Γ is leading to[1]:

$$\begin{aligned}\Gamma =&\Gamma_{\rho\leqq R_0} + \Gamma_{\rho\gg R_0}\\ =&\frac{\alpha\mu_0 M_\mathrm{s} t}{\gamma_0}\int_{\rho=0}^{R_0}\int_{\beta=0}^{2\pi}\left(\left\{\frac{\partial\vartheta}{\partial\rho}\right\}^2\vec{e}_\rho\otimes\vec{e}_\rho + \sin^2(\vartheta)\frac{n^2}{\rho^2}\vec{e}_\beta\otimes\vec{e}_\beta\right)\rho\mathrm{d}\rho\mathrm{d}\beta +\\ &\frac{\alpha\mu_0 M_\mathrm{s} t}{\gamma_0}\int_{\rho=R_0}^{R_\mathrm{max}}\int_{\beta=0}^{2\pi}\frac{n^2}{\rho^2}\vec{e}_\beta\otimes\vec{e}_\beta\,\rho\mathrm{d}\rho\mathrm{d}\beta\end{aligned} \tag{2.184}$$

For a further evaluation of the damping tensor Γ, the integration over variables ρ and β has to be performed. It has to be kept in mind, that on one hand the polar angle ϑ is a measure of the radius ρ and on the other hand, that the unit vectors $\vec{e}_\rho$ and $\vec{e}_\beta$ depend on the angle β. So, all quantities appearing in both terms of Γ have to be expressed by the variables in which the integration is done[1].

$$\begin{aligned}\Gamma =&\Gamma_{\rho\leqq R_0}+\Gamma_{\rho\gg R_0}\\ =&\frac{\alpha\mu_0 M_\mathrm{s} t}{\gamma_0}\int\limits_{\rho=0}^{R_0}\left\{\frac{\partial\vartheta}{\partial\rho}\right\}^2\rho\mathrm{d}\rho\int\limits_{\beta=0}^{2\pi}\vec{e}_\rho\otimes\vec{e}_\rho\,\mathrm{d}\beta+\\ &\frac{\alpha\mu_0 M_\mathrm{s} t n^2}{\gamma_0}\int\limits_{\rho=0}^{R_0}\frac{1}{\rho}\sin^2(\vartheta)\,\mathrm{d}\rho\int\limits_{\beta=0}^{2\pi}\vec{e}_\beta\otimes\vec{e}_\beta\,\mathrm{d}\beta+\\ &\frac{\alpha\mu_0 M_\mathrm{s} t n^2}{\gamma_0}\int\limits_{\rho=R_0}^{R_\mathrm{max}}\frac{1}{\rho}\,\mathrm{d}\rho\int\limits_{\beta=0}^{2\pi}\vec{e}_\beta\otimes\vec{e}_\beta\,\mathrm{d}\beta\end{aligned}\tag{2.185}$$

Using the dependence of $\vec{e}_\rho$ and $\vec{e}_\beta$ on β, it is found after multiplying the relations for[1]

$$\begin{aligned}\vec{e}_\rho\otimes\vec{e}_\rho=&\cos^2(\beta)\vec{e}_x\otimes\vec{e}_x+\cos(\beta)\sin(\beta)\vec{e}_x\otimes\vec{e}_y\\ &+\sin(\beta)\cos(\beta)\vec{e}_y\otimes\vec{e}_x+\sin^2(\beta)\vec{e}_y\otimes\vec{e}_y\end{aligned}\tag{2.186}$$

and[1]

$$\begin{aligned}\vec{e}_\beta\otimes\vec{e}_\beta=&\sin^2(\beta)\vec{e}_x\otimes\vec{e}_x-\sin(\beta)\cos(\beta)\vec{e}_x\otimes\vec{e}_y\\ &-\cos(\beta)\sin(\beta)\vec{e}_y\otimes\vec{e}_x+\cos^2(\beta)\vec{e}_y\otimes\vec{e}_y\end{aligned}\tag{2.187}$$

those have to be integrated. Since there are no other dependencies of Γ with respect to β, it has to be dealed with integrals of the form[1]

$$\int\limits_{\beta=0}^{2\pi}\sin^2(\beta)\,\mathrm{d}\beta=\int\limits_{\beta=0}^{2\pi}\cos^2(\beta)\,\mathrm{d}\beta=\pi\qquad\text{and}\qquad\int\limits_{\beta=0}^{2\pi}\sin(\beta)\cos(\beta)\,\mathrm{d}\beta=0\tag{2.188}$$

where only two of the possible four combinations give a value differing from 0, namely π. For both integrals the same result is obtained[1]:

$$\int\limits_{\beta=0}^{2\pi}\vec{e}_\rho\otimes\vec{e}_\rho\,\mathrm{d}\beta=\int\limits_{\beta=0}^{2\pi}\vec{e}_\beta\otimes\vec{e}_\beta\,\mathrm{d}\beta=\pi\left(\vec{e}_x\otimes\vec{e}_x+\vec{e}_y\otimes\vec{e}_y\right)\tag{2.189}$$

which is leading closer to the final result. As a last step, parts of the equations which are containing ϑ have to be considered. This is important due to the fact, that in the applied analytical description of the magnetization structure, ϑ is a function of ρ and an integration over ρ has to be performed in the end. Within the VC, ϑ can be written as[1] (see Eq. (2.180))

$$\vartheta=\arcsin\left(\frac{2R_0\rho}{R_0^2+\rho^2}\right)\tag{2.190}$$

leading to the expressions[1]:

$$\left\{\frac{\partial\vartheta}{\partial\rho}\right\}^2\rho=\frac{1}{\rho}\sin^2\left(\vartheta\right)=\frac{4R_0^2\rho}{\left(R_0^2+\rho^2\right)^2}\tag{2.191}$$

By integration over ρ, it is found for the three integrals contained in the

equation for Γ [1]

$$\int_{\rho=0}^{R_0} \left\{\frac{\partial\vartheta}{\partial\rho}\right\}^2 \rho\,\mathrm{d}\rho = 1 \qquad \text{and} \qquad \int_{\rho=R_0}^{R_{\max}} \frac{1}{\rho}\,\mathrm{d}\rho = \ln\left(\frac{R_{\max}}{R_0}\right) \quad ,$$

resulting in the final result for the damping tensor in a disc[1]:

$$\begin{aligned}\Gamma =& \Gamma_{\rho\leqq R_0} + \Gamma_{\rho\gg R_0} \\ =& \frac{\alpha\mu_0 M_\mathrm{s} t\pi}{\gamma_0}\left\{(1+n^2) + n^2\ln\left(\frac{R_{\max}}{R_0}\right)\right\}(\vec{e}_x\otimes\vec{e}_x + \vec{e}_y\otimes\vec{e}_y) \\ =& \frac{\alpha\mu_0 M_\mathrm{s} t\pi}{\gamma_0}\left\{2 + \ln\left(\frac{R_{\max}}{R_0}\right)\right\}(\vec{e}_x\otimes\vec{e}_x + \vec{e}_y\otimes\vec{e}_y)\end{aligned} \tag{2.193}$$

In general the expression for the damping dyadic Γ of a vortex in a disc can be written in a more compact way. Furthermore it is possible to put it in relation to the absolute value of the gyrovector. For the contributions $\Gamma_{\rho\leqq R_0}$ of the vortex core itself the constant C (C stands for core) can be defined according to [30] as[1]

$$C = \int_{\rho=0}^{R_0}\left(\frac{\rho}{n^2}\left\{\frac{\partial\vartheta}{\partial\rho}\right\} + \frac{1}{\rho}\sin^2(\vartheta)\right)\mathrm{d}\rho \tag{2.194}$$

and write the total expression for Γ [1]:

$$\begin{aligned}\Gamma =& \Gamma_{\rho\leqq R_0} + \Gamma_{\rho\gg R_0} \\ =& \frac{\alpha\mu_0 M_\mathrm{s} t n^2\pi}{\gamma_0}\left[C + \ln\left(\frac{R_{\max}}{R_0}\right)\right](\vec{e}_x\otimes\vec{e}_x + \vec{e}_y\otimes\vec{e}_y) \\ =& \frac{\alpha\mu_0 M_\mathrm{s} t n^2\pi}{\gamma_0}\left[\ln\left(\mathrm{e}^C\right) + \ln\left(\frac{R_{\max}}{R_0}\right)\right](\vec{e}_x\otimes\vec{e}_x + \vec{e}_y\otimes\vec{e}_y) \\ =& \frac{\alpha\mu_0 M_\mathrm{s} t n^2\pi}{\gamma_0}\ln\left(\frac{R_{\max}\mathrm{e}^C}{R_0}\right)(\vec{e}_x\otimes\vec{e}_x + \vec{e}_y\otimes\vec{e}_y)\end{aligned} \tag{2.195}$$

To gain deeper insight into the ratio of the appearing viscous and gyroforces the prefactor for Γ will be expressed in terms of the absolute value $|\vec{G}| = G_\mathrm{c}$ of the gyrovectror $\vec{G}$. It yields[1]:

$$\Gamma = \frac{\alpha n}{2p} G_\mathrm{c}\ln\left(\frac{R_{\max}\mathrm{e}^C}{R_0}\right)(\vec{e}_x\otimes\vec{e}_x + \vec{e}_y\otimes\vec{e}_y) \tag{2.196}$$

2.3.2.8 Damping Tensor for a Vortex Domain Wall

In the previous section the damping tensor for a vortex in a disc, which can serve as a rough approximation for a VDW has been calculated. However, a VDW is a magnetic texture with a rich internal structure, as for example the VC, straight and parabolic Néel walls and regions with curling magnetization. All these regions have the property of a non-vanishing spatial gradient of the

magnetization, and due to this reasons, they have to be taken into account for Γ as well!

Aiming to calculate the damping tensor of a VW, it has to be turned to the more realistic analytical model by Youk et. al [59]. This model contains the later mentioned substructures, whereby the VDW is represented as follows: The VW contains three topological defects, namely the VC residuing in the bulk and two HAVs located at the edge of the stripe. From the two HAVs emanate at 45° in both directions straight Néel walls, whereby the straight wall segments who are pointing away from the DW make a transition to parabolic Néel walls at a certain point. This point is given by the $Y-$position of the VC and changes when the VC is moving. The two straight walls which are pointing inside the VDW form together one diagonal Néel wall across the stripe on which the VC is located. When the VC starts to move sidewards due to the action of the gyroforce, in the frame of Youk's model the VC is moving along the diagonal straight Néel wall, and in this sense, its motion is predetermined by the connection line between the two HAVs. Imagine the VDW divided into four quadrants, where the VC marks the meeting point of all four, then the areas with curling in-plane magnetization are found in two quadrants which are confined by the parabolic walls. All these substructures contribute significantly to the total value of the damping tensor Γ. In component wise notation the total value $\Gamma_{ij}^{\mathrm{tot}}$ is given by[1]:

$$\Gamma_{ij}^{\mathrm{tot}} = \Gamma_{ij}^{\mathrm{VC}} + \Gamma_{ij}^{\mathrm{S}} + \Gamma_{ij}^{\mathrm{P}} + \Gamma_{ij}^{\mathrm{C}} \tag{2.197}$$

At this stage it should be noted in advance, that in the later calculations the contributions of the VC are neglected, since it is small compared to the other parts of the DW. However, the value for $\Gamma^{\mathrm{VC}} = \sum_{ij} \Gamma_{ij}^{\mathrm{VC}}$ is equal to the value of the VC in a disc, namely $\Gamma_{\rho \leqq R_0}$. Γ_{ij}^{S} includes the contributions of the three different straight Néel wall segments, while in Γ_{ij}^{P} the two parabolic shaped walls are included. As mentioned, two additional areas with curling magnetization, their damping action is summed up in Γ_{ij}^{C}. For the computation of the damping tensor the formula

$$\Gamma = \alpha J \int_V \left\{\vec{\nabla}\varphi\right\} \otimes \left\{\vec{\nabla}\varphi\right\} \mathrm{d}V \qquad , \tag{2.198}$$

is used, since all substructures with exception of the VC have only in-plane magnetization. This is leading to a zero spatial gradient for ϑ. In the following a few quantities and definitons are introduced, which are very helpful in calculating the different constituents of Γ. One of these quantities is the surface tension σ of a straight Néel wall [58], given by

$$\sigma = 2A \int_{v=-\infty}^{\infty} \left(\frac{\partial \varphi}{\partial v}\right)^2 \mathrm{d}v = 2A\frac{\sqrt{2}}{\lambda} \left(\sin(\varphi_0) - \varphi_0 \cos(\varphi_0)\right) \tag{2.199}$$

and stating, that the tension is depending on the spatial gradient of φ, integrated perpendicularly accross the wall (v is the perpendicular direction). In the end it yields, that σ is basically fixed by the parameters A, λ and φ_0. A and λ are the exchange constant and exchange length, respectively, while the most important quantity is the angle φ_0 that is the total change of in-plane direction

across the wall. To be more precise, when walking on a line which is locally perpendicular on the wall, than φ_0 is the total changing rate of the in-plane angle of the magnetization an observer recognizes. For the straight segments $\varphi_0 = \frac{\pi}{4}$ is found, while for the parabolically shaped ones φ_0 is changing along the wall and it reads [45]:

$$\varphi_0 = \frac{1}{2}\arctan\left(\frac{y}{\sqrt{w(w-2y)}}\right) + \frac{\pi}{4} \tag{2.200}$$

The formula for the surface tension of a straight Néel wall can also be aplied for the calculation of Γ_{ij}^{P} by a slight modification. This modification arises naturally from the calculation, as will be demonstrated later on. Furthermore, it will prove as very helpful for the calculation of the damping contributions coming from the curling regions, to express the maximal possible length of the radius ρ in dependence on β [45].

$$\rho(\beta) = \begin{cases} \frac{w}{1+\sin(\beta)} & 0 \leqq \beta \leqq 2\pi - \beta_0 \\ \frac{w}{1-\sin(\beta)} & 2\pi - \beta_0 < \beta \leqq \frac{3\pi}{4} \end{cases} \tag{2.201}$$

Speaking about the curling magnetization, the angle φ is parameterized like before via the angle β and the circulation c, namely $\varphi = \beta + c\frac{\pi}{4}$. Starting with the straight Néel wall segments, a change the coordinate system is required in order to apply the surface tension σ for the calculation. This coordinate system is rotated by $\beta = \frac{\pi}{4}$ around the z-axis, so that one coordinate axis is parallel and one perpendicular to the Néel wall, respectively. In the new frame, the coodinates are v, u and z and the position of the VC is given by U and V. The gradient in dependence of the VC position is given by[1]

$$\vec{\nabla}\varphi = \frac{\partial\varphi}{\partial U}\vec{e}_u + \frac{\partial\varphi}{\partial V}\vec{e}_v + \frac{\partial\varphi}{\partial Z}\vec{e}_z \tag{2.202}$$

which reduces after making the usual replacement and exploiting the fact, that φ varies only in v-direction[1]:

$$\vec{\nabla}\varphi = \frac{\partial\varphi}{\partial V}\vec{e}_v = -\frac{\partial\varphi}{\partial v}\vec{e}_v \tag{2.203}$$

The expression for Γ^{S} is found to be[1]

$$\Gamma^{\mathrm{S}} = \alpha J \int_{z=0}^{t} \mathrm{d}z \int_{u=0}^{2\sqrt{2}w} \mathrm{d}u \int_{v=-\infty}^{\infty} \left(\frac{\partial\varphi}{\partial v}\right)^2 \mathrm{d}v \, (\vec{e}_v \otimes \vec{e}_v) \tag{2.204}$$

and one identifies the integration over the variable v as the surface tension σ. Integrating over thickness t the length w of all three Néel wall segments, which is equal to $2\sqrt{2}w$ [45],

$$\Gamma^{\mathrm{S}} = \frac{4\alpha J t w}{\lambda} \left\{\sin(\varphi_0) - \varphi_0\cos(\varphi_0)\right\} (\vec{e}_v \otimes \vec{e}_v) \tag{2.205}$$

is obtained for Γ^{S} in the rotated coordinate system. Being interested in the representation of the damping tensor in Carthesian coordinates, a coordinate transformation has to be performed. This will be done by setting $\vec{e}_v =$

$-\sin(\varphi)\vec{e}_x + \cos(\varphi)\vec{e}_y$ [45].

$$\Gamma^{\mathrm{S}} = \frac{0,304\alpha J t w}{\lambda}\left\{\vec{e}_x \otimes \vec{e}_x - \vec{e}_x \otimes \vec{e}_y - \vec{e}_y \otimes \vec{e}_x + \vec{e}_y \otimes \vec{e}_y\right\} \tag{2.206}$$

As next subsystem of the VDW the parabolic Néel walls are going to be considered. Basically Γ^{P} is calculated in the same way than the straight walls. But due to the curved shaped of the walls, there are slight complications. In contradiction to the previous computation, the angle φ_0 and the angle of rotation β of the coordinate system are changing along the wall. In the parameterization that will be chosen, both angles are functions of the y-coordinate. Nevertheless, it is possible to calculate the damping tensor under the use of the surface tension σ. Considering an infinitesimal section $\mathrm{d}u$ of the parabolic wall, the curvature can be neglected and the small part with length $\mathrm{d}u$ regarded as straight. At this point it is possible to tackle the calculation. At a certain point[1]

$$\Gamma^{\mathrm{P}} = \alpha J \int_{z=0}^{t} \mathrm{d}z \int_{u=0}^{l(u)} \mathrm{d}u \int_{v=-\infty}^{\infty} \left(\frac{\partial \varphi}{\partial v}\right)^2 \mathrm{d}v \, (\vec{e}_v \otimes \vec{e}_v) \tag{2.207}$$

locally holds true. By carring out the integration over z and replacing the integral over v by the surface tension σ one obtains[1]:

$$\Gamma^{\mathrm{P}} = \frac{\sqrt{2}\alpha J t}{\lambda} \int_{u=0}^{l(u)} \mathrm{d}u \left\{\sin(\varphi_0) - \varphi_0 \cos(\varphi_0)\right\} (\vec{e}_v \otimes \vec{e}_v) \tag{2.208}$$

As mentioned, the angle φ_0 and β are depending on the spatial coordinate y. It is convenient to perform a coordinate transformation to y by substituting $\mathrm{d}u = \cos(\varphi_0)\mathrm{d}y$ and replacing $\vec{e}_v$ by the linear combination of the basis vectors $\vec{e}_x$ and $\vec{e}_y$. Ending up with the equation[1]

$$\begin{aligned}\Gamma^{\mathrm{P}} = \frac{\sqrt{2}\alpha J t}{\lambda} \int_{y=0}^{-\frac{w}{2}} \mathrm{d}y \cos(\varphi_0) \left\{\sin(\varphi_0) - \varphi_0 \cos(\varphi_0)\right\} \\ \left\{-\sin(\varphi_0)\vec{e}_x + \cos(\varphi_0)\vec{e}_y\right\} \otimes \left\{-\sin(\varphi_0)\vec{e}_x + \cos(\varphi_0)\vec{e}_y\right\}\end{aligned} \tag{2.209}$$

for Γ^{P}, it yields by inserting the y-dependent expression for φ_0 and integrating numerically [45]

$$\Gamma^{\mathrm{P}} = \frac{\alpha J t w}{\lambda}\left\{0.057\vec{e}_x \otimes \vec{e}_x + 0.069c\vec{e}_x \otimes \vec{e}_y + 0.069c\vec{e}_y \otimes \vec{e}_x + 0.083\vec{e}_y \otimes \vec{e}_y\right\} \tag{2.210}$$

as result for the parabolic Néel wall. As last contribution to the damping of the VDW the calculation for Γ^{C} has to be performed. Spherical coordinates are the convenient choice in this case. Utilizing the usual replacement rule for the spatial derivatives and exploiting the fact, that φ depends only on β [1],

$$\vec{\nabla}\varphi = -\frac{1}{\rho}\frac{\partial \varphi}{\partial \beta}\vec{e}_\beta \tag{2.211}$$

is obtained,yielding the equation [1]

$$\Gamma^{\mathrm{C}} = \alpha J \int\limits_{z=0}^{t} \mathrm{d}z \int\limits_{\beta=\frac{3\pi}{4}}^{0} \mathrm{d}\beta \int\limits_{\rho=r_0}^{\rho(\beta)} \mathrm{d}\rho \frac{1}{\rho} \left(\frac{\partial \varphi}{\partial \beta} \right) \{\vec{e}_\beta \otimes \vec{e}_\beta\} \tag{2.212}$$

for the damping originating from the curling in-plane magnetization. As before, the integration over z can be carried out independently in the other two integrals. Since the radius ρ depends on β, in a first step the integration over ρ has to be performed. As shown before, the upper limit for the integration depends on β and is defined section-wise. Due to this, the integral needs to be splitted up into two parts. Both integrals yield a natural logarithm as function. For the calculation of the integral over β, the unit vectors $\vec{e}_\beta$ have to be by $\vec{e}_\beta$ [1].

$$\begin{aligned} \Gamma^{\mathrm{C}} = \alpha J t \int\limits_{\beta=\frac{3\pi}{4}}^{2\pi-\beta_0} \mathrm{d}\beta \, \{\vec{e}_\beta \otimes \vec{e}_\beta\} \int\limits_{\rho=r_0}^{\frac{w}{1-\sin(\beta)}} \mathrm{d}\rho \frac{1}{\rho} \\ + \alpha J t \int\limits_{\beta=2\pi-\beta_0}^{2\pi} \mathrm{d}\beta \, \{\vec{e}_\beta \otimes \vec{e}_\beta\} \int\limits_{\rho=r_0}^{\frac{w}{1+\sin(\beta)}} \mathrm{d}\rho \frac{1}{\rho} \end{aligned} \tag{2.213}$$

Both integrals yield a natural logarithm as function. For the calculation of the integral over β, the unit vectors $\vec{e}_\beta$ have to be replaced by $\vec{e}_\beta = \cos(\beta)\vec{e}_x + \sin(\beta)\vec{e}_y$. This yields[1]

$$\begin{aligned} \Gamma^{\mathrm{C}} = \alpha J t \int\limits_{\beta=\frac{3\pi}{4}}^{2\pi-\beta_0} \mathrm{d}\beta \ln\left(\frac{\frac{w}{r_0}}{1-\sin(\beta)} \right) \{\cos(\beta)\vec{e}_x + \sin(\beta)\vec{e}_y\} \otimes \{\cos(\beta)\vec{e}_x + \sin(\beta)\vec{e}_y\} \\ + \alpha J t \int\limits_{\beta=2\pi-\beta_0}^{2\pi} \mathrm{d}\beta \ln\left(\frac{\frac{w}{r_0}}{1+\sin(\beta)} \right) \{\cos(\beta)\vec{e}_x + \sin(\beta)\vec{e}_y\} \otimes \{\cos(\beta)\vec{e}_x + \sin(\beta)\vec{e}_y\} \end{aligned} \tag{2.214}$$

as equation which is integrated numerically, resulting in the contribution of the curling magnetization to the total Γ as follows [45]:

$$\begin{aligned} \Gamma^{\mathrm{C}} = & \alpha J t \left(\frac{\pi}{4} \ln\left(\frac{w}{r_0} \right) - 0.398 \right) (\vec{e}_x \otimes \vec{e}_x) \\ & - \alpha c J t \left(\frac{1}{2} \ln\left(\frac{w}{r_0} \right) - 0.133 \right) (\vec{e}_x \otimes \vec{e}_y) \\ & - \alpha c J t \left(\frac{1}{2} \ln\left(\frac{w}{r_0} \right) - 0.133 \right) (\vec{e}_y \otimes \vec{e}_x) \\ & + \alpha J t \left(\frac{\pi}{4} \ln\left(\frac{w}{r_0} \right) - 0.010 \right) (\vec{e}_y \otimes \vec{e}_y) \end{aligned} \tag{2.215}$$

Summing up all contributions to Γ originating from the different substructures within the VDW (neglecting as mentioned the contribution of the VC) it holds [45]:

$$\begin{aligned}\Gamma^{\mathrm{C}} = &\alpha Jt\left(0.418\frac{w}{\lambda}\frac{\pi}{2}\ln\left(\frac{w}{r_0}\right) - 0.797\right)(\vec{e}_x \otimes \vec{e}_x)\\ &+ \alpha cJt\left(0.442\frac{w}{\lambda} - \ln\left(\frac{w}{r_0}\right) + 0.265\right)(\vec{e}_x \otimes \vec{e}_y)\\ &+ \alpha cJt\left(0.442\frac{w}{\lambda} - \ln\left(\frac{w}{r_0}\right) + 0.265\right)(\vec{e}_y \otimes \vec{e}_x)\\ &+ \alpha Jt\left(0.470\frac{w}{\lambda} + \frac{\pi}{2}\ln\left(\frac{w}{r_0}\right) - 0.020\right)(\vec{e}_y \otimes \vec{e}_y)\end{aligned} \tag{2.216}$$

This result serves as basis for the theoretical predictions later on. In the preceeding sections the values for the force $\vec{F}^{\mathrm{f}}$ acting on a VDW and as well the damping tensor Γ and gyrovector $\vec{G}$ are computed. Based on this preliminary work, the theoretical considerations arrive at the point how to solve the one- and two-dimensional force equations. As already explained, due to the exchange interaction the magnetization profile can be regarded as fixed in z-direction, and solely the magnetic texture in the x-y-plane has to be regarded. Thereby, the solution for the one-dimensional case yields a very important result concerning steady-state motion and serves in addition as help for the determination of the two dimensional equation of motion.

2.3.2.9 Equation of Motion in the One-Dimensional Case

In the one-dimensional case, only the X-coordinate of the VC is considered and the differential equation describing the motion reduces to the form[1]:

$$F_X - \Gamma_{XX}\dot{X} = 0 \tag{2.217}$$

One recognizes that the expression for the gyroforce is missing. This can be understood from both, a more abstract mathematical view and a physical interpretation. Starting with the mathematical consideration, it has been shown in Sec. 2.2.3.5 that the gyrotensor is connected to the generalized Kronecker symbol, which can be expressed by a determinant. However, this definition holds true only for dimensions larger than 1 and is, by this, not defined for the one-dimensional case. This makes sense since the generalized Kronecker symbol defines a permutation, and it is useless to do a permutation in one dimension. The more physical point of view, the gyrovector always yields a force perpendicular to the velocity vector of the VC. Moving solely in x-direction, the force would act in the transverse direction and force the VC out of the equilibrium position to the stripe edges. Although having no y-direction included in the equations, there is no way the gyroforce can act on the VC and push it sidewards. Inserting the force in longitudinal direction due to the external applied field[1],

$$QH - \Gamma_{XX}\dot{X} = 0 \tag{2.218}$$

is obtained as equation of motion which is easily solved by resolving with respect of $\dot{X}$ [47]

$$\dot{X} = \frac{QH}{\Gamma_{XX}} \tag{2.219}$$

This result yields the steady-state velocity of the VDW and holds also true

for the two dimensional motion. Why this is the case can be understood by considering the physical situation under steady-state motion. Allowing the VC to move in both directions, namely x and y, at the beginning, the VC starts to move along the stripe and is pushed sidewards. After reaching its longitudinal equilibrium position under the action of an external field, the dissipation rate is solely given by the dissipation due to friction. This friction is determined by the damping tensor Γ, and since in the steady-state motion the DW is assumed to move along one spatial direction (here x is chosen), only Γ_{XX} counts. The gyrotropic force can be neglected because of being in the new transversal equilibrium position, the gyroforce is balanced by the restoring forced of the potential $U(Y)$. This is another way to understand, why the one-dimensional Thiele equation results in a physical meaningful solution, and, as will be shown in the next section, it is the limiting case for the two-dimensional equation of motion. Additionally, it has to be mentioned that the result obtained is equal to the famous steady-state solution found by Walker and Schryer [29]. In order to demonstrate this, the concrete expressions for Q and Γ_{XX} are inserted, and the equation yields[1]:

$$\dot{X} = \frac{2\mu_0 wtM_\mathrm{s}H}{\alpha\frac{\mu_0 M_\mathrm{s}}{\gamma_0}\int\limits_V \left(\frac{\partial\vec{m}}{\partial x}\right)\left(\frac{\partial\vec{m}}{\partial x}\right)\mathrm{d}V} \tag{2.220}$$

Manipulating the equation mathematically to bring it to the form[1]

$$\dot{X} = \frac{\gamma_0 H}{\alpha}\underbrace{\left(\frac{1}{2wt}\int\limits_V \left(\frac{\partial\vec{m}}{\partial x}\right)\left(\frac{\partial\vec{m}}{\partial x}\right)\mathrm{d}V\right)^{-1}}_{=\Delta_\mathrm{T}} = \frac{\gamma_0\Delta_\mathrm{T}H}{\alpha} = v_\mathrm{st} \tag{2.221}$$

one identifies the Thiele domain wall width Δ_T.

2.3.2.10 Equation of Motion in the Two-Dimensional Case

Making the transition to the two-dimensional model for the motion of a VDW, the longitudinal position Y of the VC has to be included in addition to the transversal position X. This opens a new spatial degree of freedom and allows the VC to move sidewards to the edges of the stripe, which captures the motion of the VDW way much better. A short time after the external field is applied and in the oscillatory motion above the Walker field, an improved theoretical description is achieved; especially for the non-steady-state motion. The two-dimensional system of equation that arises in this case reads in general[1]

$$\begin{pmatrix}F_X\\F_Y\end{pmatrix} - \begin{pmatrix}\Gamma_{XX} & \Gamma_{XY}\\ \Gamma_{YX} & \Gamma_{YY}\end{pmatrix}\begin{pmatrix}\dot{X}\\\dot{Y}\end{pmatrix} + pG_\mathrm{c}\begin{pmatrix}0 & 1\\-1 & 0\end{pmatrix}\begin{pmatrix}\dot{X}\\\dot{Y}\end{pmatrix} = 0 \tag{2.222}$$

where the two-dimensional version $\epsilon_{2\times2}$ of the Levi-Civita tensor was used. Aiming to describe the motion of the VC, the equations have to be resolved regarding the time derivatives of X and Y in order to obtain the equations of motion. To do this, the explicit expressions for the forces in longitudinal and transversal directions are inserted, and the vector $\vec{F}^\mathrm{f}$ is inserted to the right

side of the equation. Combining the matrices for Γ and G to a single matrix, it yields[47]

$$\begin{pmatrix} \Gamma_{XX} & \Gamma_{XY} + pG_\mathrm{c} \\ \Gamma_{YX} - pG_\mathrm{c} & \Gamma_{YY} \end{pmatrix} \begin{pmatrix} \dot{X} \\ \dot{Y} \end{pmatrix} = \begin{pmatrix} QH \\ rcQH - kY \end{pmatrix} \tag{2.223}$$

as equation system which can be resolved easily by multiplying both sides of the equation with the inverse matrix. The inverse matrix contains the determinant $\det(\Gamma + pG_\mathrm{c}\epsilon_{2\times 2})$ of the original matrix in the prefactor. It can be shown by using the dentiy $p^2 = 1$ that this determinant is equal to[1]

$$\det(\Gamma + pG_\mathrm{c}\epsilon_{2\times 2}) = \det\Gamma + G_\mathrm{c}^2 \tag{2.224}$$

which results, in the end, in the following system of equations of motion for the position of the VC[1]:

$$\begin{pmatrix} \dot{X} \\ \dot{Y} \end{pmatrix} = \frac{1}{\det\Gamma + G_\mathrm{c}^2} \begin{pmatrix} \Gamma_{YY} & -(\Gamma_{XY} + pG_\mathrm{c}) \\ -(\Gamma_{YX} - pG_\mathrm{c}) & \Gamma_{XX} \end{pmatrix} \begin{pmatrix} QH \\ rcQH - kY \end{pmatrix} \tag{2.225}$$

Basically, this is the two-dimensional system of equation which describes the VDM under the action of an external field for low and intermediate fields in a sufficient accurate way. However, it is possible to manipulate the equations for $\dot{X}$ and $\dot{Y}$ in order to get a deeper insight in the behavior of the motion. For this task it is helpful when one has already an idea which kind of behavior the system shows. In a first step, a closer look will be taken on the equation for the transversal position Y. After multiplying the inverse matrix with the vector containing the forces, the formula describing the time evolution of Y is found to be[1]:

$$\dot{Y} = \frac{1}{\det\Gamma + G_\mathrm{c}^2} \left(-QH\Gamma_{YX} - QHpG_\mathrm{c} + rcQH\Gamma_{XX} - kY\Gamma_{XX}\right) \tag{2.226}$$

From the considerations in the previous sections, it is known that the gyrotropic force acts perpendicular to the motion of the VC and the DW, respectively. This induced motion in Y-direction continues until the VC reaches a transversal position where the forces, due to the Y-dependent potential $U(Y)$, are balanced. This special value for the transversal coordinate, the equilibrium position, was labeled Y_eq. Reaching this position is accompanied by steady-state motion in x-direction and zero velocity in the transversal one. To conclude it, having $Y = Y_\mathrm{eq}$ leads to $\dot{Y} = 0$, and the equation for the velocity in y-direction is to be expected to have the form $\dot{Y} \propto Y - Y_\mathrm{eq}$. Placing the prefactor $k\Gamma_{XX}$ of Y in front of the brackets, it results in[1]

$$\dot{Y} = -\frac{k\Gamma_{XX}}{\det\Gamma + G_\mathrm{c}^2} \left(\frac{QH\Gamma_{YX}}{k\Gamma_{XX}} + \frac{QHpG_\mathrm{c}}{k\Gamma_{XX}} - \frac{rcQH\Gamma_{XX}}{k\Gamma_{XX}} + Y\right) \tag{2.227}$$

and the first three terms in brackets are identified as $-Y_\mathrm{eq}$. The equilibrium position itself depends on the polarity p, and as it will become clear soon, on

the circulation c as well. Why Y_{eq} depends on p can be easily understood by considering the expression of the gyrovector $\vec{G}$. Changing the polarity means changing the value of $\vec{G}$, and thus the direction of the gyroforce as well which leads to an equilibrium position close to the lower or upper edge of the stripe. Originating from the Zeeman barrier caused by the curling magnetization of the vortex, the circulation c modifies Y_{eq} slightly. To highlight the dependence of Y_{eq} on the key parameter of a VDW, the expression for the equilibrium position will be reformulated. After some algebra, the three terms contained in the formula for Y_{eq} can be combined to [45, 47]

$$Y_{\mathrm{eq}} = \frac{QHG_{\mathrm{c}}}{k\Gamma_{XX}} \{cg - p\} \tag{2.228}$$

where the abbreviation g is introduced for the term [45, 47]

$$g = \frac{r\Gamma_{XX} - c\Gamma_{XY}}{G_{\mathrm{c}}} \ll 1 \tag{2.229}$$

which yields a small value $g \ll 1$. Despite the small magnitude of g, the dependence of the transversal equilibrium position of the VC on the circulation c should not be neglected because it gives rise to significant different behavior of VW with different chirality χ above the Walker breakdown. Combining all results, the equation [45, 47]

$$\dot{Y} = -\frac{k\Gamma_{XX}}{\mathrm{det}\Gamma + G_{\mathrm{c}}^2} (Y - Y_{\mathrm{eq}}) \tag{2.230}$$

is obtained for X. The equation exhibits the expected form and reproduces the behavior of vanishing velocity in y-direction in the limiting case of steady-state motion. In the same way the equation for $\dot{Y}$is approached, and the consideration of $\dot{X}$ is started with a discussion what kind of motion has to be expected. Based on the considerations of the one-dimensional case and the transversal motion, the equation for $\dot{X}$ has to yield in the limit of steady-state motion the velocity v_{st}. Additionally, the steady-state motion is coinciding, as mentioned before, with the condition $Y = Y_{\mathrm{eq}}$. This leads to the assumption that the expression for $\dot{X}$ has to contain, in some way, a term which is proportional to $Y - Y_{\mathrm{eq}}$. The equation of motion for the longitudinal coordinate of the VC is given by[1]

$$\dot{X} = \frac{1}{\mathrm{det}\Gamma + G_{\mathrm{c}}^2} \left(\Gamma_{YY} QH + k \left(\Gamma_{XY} - pG_{\mathrm{c}} \right) \left(Y - \frac{rcQH}{k} \right) \right) \tag{2.231}$$

and starting the reformulation of the equation by recovering the term $Y - Y_{\mathrm{eq}}$. The only term in Eq. (2.231) which contains the quantity Y is the last bracket. From this term Y_{eq} has to arise. For this purpose the fraction $\frac{rcQH}{k}$ is expanded with Γ_{XX}, and in addition, adding and subtracting the required terms to get Y_{eq} is necessary; hence, it yields[1]

$$\dot{X} = \frac{1}{\det\Gamma + G_c^2}\left(\Gamma_{YY}QH + k\left(\Gamma_{XY} - pG_c\right)\left(Y - Y_{eq} - \frac{QH\Gamma_{YX}}{k\Gamma_{XX}} - \frac{QHpG_c}{k\Gamma_{XX}}\right)\right) \tag{2.232}$$

as intermediate result for the final version of the equation of motion for X. After working out the dependency on Y_{eq}, the convergence of velocity $\dot{X}$ to v_{st} in the limiting case $Y, \to Y_{eq}$ should be highlighted. Collecting all terms which are not connected to $Y - Y_{eq}$ and expanding them in a convenient way to get the expression $\frac{QH}{\Gamma_{XX}}$ [1],

$$\dot{X} = \frac{1}{\det\Gamma + G_c^2}\left(\frac{QH}{\Gamma_{XX}}\left\{\det\Gamma + G_c^2\right\} + k\left(\Gamma_{XY} - pG_c\right)\left(Y - Y_{eq}\right)\right) \tag{2.233}$$

is gained, and as final result for $\dot{X}$ the equation [45]

$$\dot{X} = \frac{QH}{\Gamma_{XX}} + \frac{k\left(\Gamma_{XY} - pG_c\right)}{\det\Gamma + G_c^2}\left(Y - Y_{eq}\right) \tag{2.234}$$

is obtained. This equation indeed fulfills the required properties. It depends on the equilibrium position Y_{eq} and yields in the steady-state motion the velocity v_{st}.

2.3.3 Solution for the Equation of Motion of a Vortex Domain Wall in the Framework of the Collective Coordinate Approach

The corresponding equations of motion for the one- and two-dimensional case are solved in the following sections. The solutions are required to compare the theoretical predicted values for DWM with the results obtained in experimental measurements. Solving, in a first step, the one-dimensional case and considering the result from the point of view of modes, the quantity of DW mobility μ will be introduced. Subsequently, the discussion turns to the two-dimensional case and derivates from the equations of $\dot{Y}$ and $\dot{Y}$ do not contain only the solutions themselves but also important results concerning the critical velocity V_c, critical field H_c and critical transversal displacement Y_{crit}. Similar to the one-dimensional case, the results are considered from the point of view of modes, yielding a good criterium to assess the number of collective coordinates which have to be included in the model. The next section will start with the solution of the one-dimensional equation of motion.

2.3.3.1 Solution for the Equation of Motion in the One-Dimensional Case

The one-dimensional solution for the VC $X(t)$ is calculated by the method of separation of variables and integration. By setting $t_0 = 0$ and $X_0 = X(t_0) = 0$ it is found to be[1]:

$$X(t) = \frac{QH}{\Gamma_{XX}}t \tag{2.235}$$

Considering this result in the frame of modes, the motion in x-direction in one dimension can be written as[1]

$$X(t) = \frac{QH}{\Gamma_{XX}} t = \frac{QH}{\Gamma_{XX}} t e^{-\frac{t}{\tau_0}} \tag{2.236}$$

with a characteristic decay time $\tau_0 = \infty$ [45, 47]. Please note that the velocity v_{st} holds true for the field regime below the critical Walker field. From this result, it can be concluded that the dominant mode in the steady-state motion regime is given by the translational one in longitudinal direction. This mode has the largest decay time of all modes and has to be taken into account in all considered cases. Another important quantity, which is a key number for DWM, is the DW mobility μ. It is defined as the derivative of the velocity $\dot{X}$ with respect to the externally applied field H [45].

$$\mu = \frac{\mathrm{d}\dot{X}}{\mathrm{d}H} \tag{2.237}$$

In the linear regime below the Walker breakdown, μ will further be denoted as μ_{LF}, the low field mobility [45, 47]. For this quantity

$$\mu_{\mathrm{LF}} = \frac{Q}{\Gamma_{XX}} \tag{2.238}$$

is obtained as result [45, 47]. This considerations of the one-dimensional case will be helpful for the investigation of the two-dimensonal case in the subsequent section.

2.3.3.2 Solution for the Equation of Motion in the Two-Dimensional Case

Turning to the solution of the two-dimensional model, it will become clear that the extension to the y-direction yields a very powerful and realistic description of the DWM. Having an additional degree of freedom for the DWM, the system of equations is capable to describe the translational motion after the field is applied and also to describe the oscillatory motion above the Walker breakdown. Resulting from this fact, the second spatial degree of freedom gives rise to the existence of critical values for field, velocity and transversal displacement up to where the linear regime is valid. These quantities will be derived now because they can be deduced from the two-dimensional force equation and the application of some physical based assumption without solving the exact equations.

Starting to determine the critical velocity V_{c}, the linear regime breaks down, and the oscillatory motion of the VC across the stripe sets in. The following assumption is used: In linear regime the forces due to the dissipation dyadic are comparably small with respect to the gyrotropic force. As a rough approximation, frictional forces can be neglected that lead to $\dot{Y} = 0$ in direct consequence because the critical velocity is connected to Y_{eq}; in this situation the transversal velocity is zero. For the system of equations[1]

$$\begin{pmatrix} 0 & pG_{\mathrm{c}} \\ -pG_{\mathrm{c}} & 0 \end{pmatrix} \begin{pmatrix} \dot{X} \\ 0 \end{pmatrix} = \begin{pmatrix} QH \\ rcQH - kY \end{pmatrix} \tag{2.239}$$

is found, yielding the condition for the equilibrium position[1]:

$$-pG_{\mathrm{c}}V = kY_{\mathrm{eq}} \tag{2.240}$$

Here, V is set to be equal to $\dot{X}$, and because the absolute value for the critical velocity is of interest, the term $-p$ is omitted. The critical velocity, which is equal to the maximum velocity, the VC can reach within the stripe is determined by $Y_{\mathrm{eq}} = \frac{w}{2}$. Resolving with respect to V, the critical velocity V_{c} is given by [45]:

$$V_{\mathrm{c}} \approx \frac{kw}{2G_{\mathrm{c}}} \tag{2.241}$$

The condition for V_{c} obtained from the force equation allows another physical interpretation. Eq. (2.240) states nothing else that the equilibrium position and, as a consequence of this, the connected velocity V, is governed by the balance of gyrotropic force and restoring force due to the deflection of the VC out of the middle of the stripe. This implies that the linear regime breaks down, and the VC collides with one of the edges, when both forces cannot balance each other for values of Y_{eq} within the stripe. Based on the result for V_{c}, it is possible to estimate a value for the critical field H_{c}. On one hand, V_{c} is given by Eq. (2.241), and on the other hand, it can be expressed via the steady-state velocity Eq. (2.219) and setting $H = H_{\mathrm{c}}$[1].

$$V_{\mathrm{c}} = \frac{QH_{\mathrm{c}}}{\Gamma_{XX}} \tag{2.242}$$

Equating both expressions and resolving with respect to H_{c}, the critical field

$$H_{\mathrm{c}} = \frac{kw\Gamma_{XX}}{2QG_{\mathrm{c}}} = \frac{\Gamma_{XX}}{Q}V_{\mathrm{c}} \tag{2.243}$$

is found as an estimate [45, 47]. Instead of considering the extremal case of $Y_{\mathrm{eq}} = \frac{w}{2}$, an arbitrary equilibrium position within the stripe, the critical transversal displacement Y_{crit}, is found by inserting H_{c} into formula Eq. (2.240) [47].

$$Y_{\mathrm{eq}} = Y_{\mathrm{crit}} = \frac{QH_{\mathrm{c}}G_{\mathrm{c}}}{k\Gamma_{XX}}\left(cg - p\right) = \left(cg - p\right)\frac{G_{\mathrm{c}}V_{\mathrm{c}}}{k} \tag{2.244}$$

This is a very important result which will be useful later on. Additionally, it is worth to mention that Y_{crit} does not depend solely on the parameters c and p (resulting in different behavior for different chiralities) but ,additionally, on the stripe width w. The dependence on w enters the equation via the factor g, which is itself a function of the stripe diameter because the contained components of the damping dyadic (Γ_{XX}, Γ_{XY}) depend on w.

Advancing to the solution of the equation of motion for the spatial coordinates of the VC, it will be started with the corresponding equation for Y. This is, due to the dependency of Eq. (2.230), solely on Y. The equation determining the time evolution of X depends on Y, and aiming to find $X(t)$, $Y(t)$, it has to be calculated first and inserted into the equation for $\dot{X}$. Solving the differential equation for Y with separation of variables and setting $t_0 = 0$ and $Y_0 = Y(t_0) = 0$, it yields [45, 47]:

$$Y(t) = Y_{\mathrm{eq}} \left(1 + e^{-\frac{k\Gamma_{XX}}{\det\Gamma + G_{\mathrm{c}}^2} t}\right) \tag{2.245}$$

This result incorporates the expectation that the VC approaches the equilibrium position Y_{eq} for sufficiently large times t. What is sufficiently large is determined by the prefactor to t in the exponent of the exponential function. This prefactor serves as time constant for the decaying motion denoted in the following as τ_1, and at the same time, it is the characteristic time for the mode in y-direction. The time constant reads [45, 47]

$$\tau_1 = \frac{\det\Gamma + G_{\mathrm{c}}^2}{k\Gamma_{XX}} \tag{2.246}$$

and is the second largest characteristic time in the physical system. For short pulse times $t_{\mathrm{p}} < \tau_1$, where the sidewards motion is as dominant as the longitudinal motion, the mode in y-direction has to be taken into account to get a convenient theoretical prediction of the DW displacement. Plugging the general expression for Y_{eq} into Eq. (2.245), the transversal displacement of the VC[1]

$$Y(t, H, w, c, p) = \frac{(c \cdot g(w) - p)\, G_{\mathrm{c}} Q H}{k\Gamma_{XX}} \left(1 + e^{-\frac{t}{\tau_1}}\right) \tag{2.247}$$

that depends on five parameters in total is found. As mentioned before, in the two-dimensional model it is possible to estimate the time T_{trans} that is needed by the VC in the oscillatory regime to cross the stripe in transversal direction. Striving to determining this time, the same ansatz as for the calculation of the critical velocity is used. In contradiction to the later mentioned case, the velocity $\dot{X}$ along the stripe can be neglected in the oscillatory motion. Setting $\dot{X}$ to zero results in[1]

$$\begin{pmatrix} 0 & pG_{\mathrm{c}} \\ -pG_{\mathrm{c}} & 0 \end{pmatrix} \begin{pmatrix} 0 \\ \dot{Y} \end{pmatrix} = \begin{pmatrix} QH \\ rcQH - kY \end{pmatrix} \tag{2.248}$$

as system of equations, which yields for the velocity $\dot{Y}$ [45]:

$$\dot{Y} = \frac{QH}{pG_{\mathrm{c}}} \tag{2.249}$$

This equation implies that the velocity is constant and the transversal velocity can be noted as $\dot{Y} = \frac{w}{T_{\mathrm{trans}}}$ [45]. Equating both expressions and resolving them with respect to T_{trans}, it is obtained [45]:

$$T_{\mathrm{trans}} = \frac{w}{|\dot{Y}|} = \frac{pG_{\mathrm{c}} w}{QH} \tag{2.250}$$

Inserting the concrete expression for the magnetic charge of the DW Q and the gyrotropic constant G_{c}, the result for T_{trans} reduces to a remarkably simple form [45].

$$T_{\mathrm{trans}} = \frac{\pi}{\mu_0 \gamma H} = \frac{\pi}{\gamma_0 H} \tag{2.251}$$

It yields that the transition time T_{trans} depends only on the externally applied

field H. Regarding modes, T_{trans} can serve as characteristic time as well. As explained in the introduction of the CCA, the criteria which defines modes as particular soft have to be taken into account, and they can be a characteristic time itself or some other time scale. For the oscillatory regime above the Walker field, this time scale is given by the time the VC needs to cross the stripe. At field barely above H_{c}, T_{trans} is smaller than τ_1 but larger than τ_2, the characteristic time connected with the motion of the HAVs. However, T_{trans} depends on the external field H and by increasing the field strength, the translational time can become shorter than τ_2. In this case the motion of the HAVs which are confined at the edges has to be included in the model.

Until proceeding to solve the differential equation for X, a last discussion of the dependence of the equilibrium position Y_{eq} (with special attention regarding the chirality of the VDW) will be done. As demonstrated, VDWs with different chiralities have slightly modified Y_{eq}. The critical displacement out of the middle of the strip is for a VDW with $\chi = 1$ smaller than for walls with $\chi = -1$. As long as it is in the linear regime below H_{c}, it makes no difference in the general behavior of the VW. However, the different critical transversal displacements are leading to different critical Walker fields H_{c} for both chiralities, which have important consequences on the kind of polarity reversal process of the VC. It turns out that the critical displacement for walls with $\chi = -1$ lies always outside the stripe, which implies that the critical transversal displacement is not given by Y_{eq} but by $\frac{w}{2}$. Aiming to calculate the chirality dependent critical field, both chiralities have to be distinguished. It yields[1]

$$Y_{\mathrm{eq}} = Y(t, H, w, c, p) \qquad \text{and} \qquad \frac{w}{2} = Y(t, H, w, c, p) \tag{2.252}$$

for $\chi = 1$ and $\chi = -1$, respectively. Resolving with respect to H_{c} [1]

$$H_{\mathrm{c},\chi=1} = \frac{\Gamma_{XX} V_{\mathrm{c}}}{Q} \frac{1}{1 + e^{-\frac{k\Gamma_{XX}}{\det\Gamma + G_{\mathrm{c}}^2} t}} \tag{2.253}$$

is obtained and[1]

$$H_{\mathrm{c},\chi=-1} = \frac{wk\Gamma_{XX}}{2\left(c \cdot g(w) - p\right) G_{\mathrm{c}} Q} \frac{1}{1 + e^{-\frac{k\Gamma_{XX}}{\det\Gamma + G_{\mathrm{c}}^2} t}} \tag{2.254}$$

for the critical fields. These expressions are still time dependent. In order to remove the time dependency and get the lower limit for $H_{\mathrm{c},\chi=1}$ and $H_{\mathrm{c},\chi=-1}$, the limit $t \to \infty$ is taken yielding[1]

$$\lim_{t\to\infty} H_{\mathrm{c},\chi=1} = \frac{\Gamma_{XX} V_{\mathrm{c}}}{Q} \tag{2.255}$$

and[1]

$$\lim_{t\to\infty} H_{\mathrm{c},\chi=-1} = \frac{wk\Gamma_{XX}}{2\left(c \cdot g(w) - p\right) G_{\mathrm{c}} Q} \tag{2.256}$$

as result. To complete the considerations, the differential equation for $\dot{X}$ will be solved as a last task. Inserting the solution $Y(t)$, the equation for the

longitudinal velocity $\dot{X}$ reads[1]

$$\dot{X} = \frac{QH}{\Gamma_{XX}} + Y_{\mathrm{eq}} \frac{k\left(\Gamma_{XY} - pG_{\mathrm{c}}\right)}{\det\Gamma + G_{\mathrm{c}}^2} e^{-\frac{k\Gamma_{XX}}{\det\Gamma + G_{\mathrm{c}}^2}t} \tag{2.257}$$

from these the modified low field mobility μ_{LF} can be directly computed[1].

$$\mu_{\mathrm{LF}} = \frac{\mathrm{d}\dot{X}}{\mathrm{d}H} = \frac{Q}{\Gamma_{XX}} \left(1 + (cg - p)\, G_{\mathrm{c}} \frac{\left(\Gamma_{XY} - pG_{\mathrm{c}}\right)}{\det\Gamma + G_{\mathrm{c}}^2} e^{-\frac{k\Gamma_{XX}}{\det\Gamma + G_{\mathrm{c}}^2}t}\right) \tag{2.258}$$

In the two-dimensional model the mobility is now time dependent. Its limit value for $t \to \infty$ approaches[1]

$$\lim_{t\to\infty} \mu_{\mathrm{LF}} = \frac{Q}{\Gamma_{XX}} \tag{2.259}$$

which is the same result obtained in the one-dimensional case. This is expected because t approaching in ∞ is equal to the case of steady-state motion which can be described in a one-dimensional model. Finally, the solution of $X(t)$ (with $t_0 = 0$ and $X_0 = X(t_0) = 0$) is obtained[1]:

$$X(t) = \frac{QH}{\Gamma_{XX}} t - (cg - p) \frac{G_{\mathrm{c}}\left(\Gamma_{XY} - pG_{\mathrm{c}}\right)}{k\Gamma_{XX}} \left(e^{-\frac{k\Gamma_{XX}}{\det\Gamma + G_{\mathrm{c}}^2}t} - 1\right) \tag{2.260}$$

2.4 Ferromagnetic Resonance

The measurement technique of ferromagnetic resonance (FMR), with all its different technical realizations (e.g. VSM, TR-MOKE), established as important tool to access experimentally material parameters of thin film layers [37, 38] in the last decades. Especially, due to its property of being destruction free, FMR has become a standard method to characterize ferromagnetic layers and determining, for example, the Gilbert damping parameter α or magnetic anisotropies. Since FMR is used in this thesis to determine the damping parameter α, both, on full-film and in a patterned stripe geometry, the mathematics behind this method should be explained in the following. In a first step, basic considerations about an appropriate coordinate transformation are done. This preliminary work will make it easier to solve the equations originating from the LLG equation. In Sec. 2.4.2 the solution for the resonance conditions and the dynamic susceptibility in a general fashion is obtained. These results can be applied for the determination of α in full-film FMR and TR-MOKE measurements.

The idea behind FMR is to immerse a magnetic sample into a strong external magnetic field $\vec{H}$, thus, in the static case the magnetization $\vec{M}$ of the sample aligns itself along the direction of the external field. Exciting additionally the magnetization by a rf-field $\vec{h}_{\mathrm{rf}}$ which exhibits components perpendicular to $\vec{H}$ and alternates with angular frequency ω, the magnetization starts to precess around its equilibrium position with the same angular frequency. The magnitude of precession depends on ω and $\vec{H}$, and similar to the oscillations of a

driven harmonic oscillator, the magnetic system has a resonance frequency that depends on $\vec{H}$. Setting the external field to a fixed value, it is possible to record a resonance or absorption spectra respectively by sweeping the angular frequency ω of the rf-field. Available rf-generators are not capable to sweep the frequency continuously. This limits to certain discrete values where one can probe the magnitude of excitation of $\vec{M}$. Due to this restriction, another way is chosen to record a quasi continuous FMR spectra. Since the mentioned resonance frequency of the system is a function of the external field, there is the opportunity to set a fixed excitation frequency and sweep instead the resonance frequency of the system by altering the external field. This approach to FMR is commonly applied and used in this thesis. Based on these considerations, it will be turned to the mathematical description of FMR now. The mathematical treatment of the LLG eq. in the case of FMR can be found in several classic publications [88–91], PhD Thesises [92–94] and textbooks [38, 95]. The self done calculations presented in Sec. 2.4.1 and 2.4.2 are following the later mentioned references. Especially, the used notation is adopted partially from [92–94].

In a first step it will be discussed in Sec. 2.4.1 how to solve the LLG eq. in the case of FMR. Finally, the theoretical discussion evolve to the solution in a full-film and stripe geometry (Sec. 2.4.2).

2.4.1 Considerations Regarding the Coordinate System: How to Solve the Landau-Lifshitz-Gilbert Equation in the Case of Ferromagnetic Resonance

As already mentioned in the introduction to FMR, the selection of the appropriate coordinate system is important because it simplifies the mathematical task of solving the LLG equation for the case of FMR. Assuming a strong external magnetic field $\vec{H}_{\mathrm{ext}}$ arbitrary aligned in space, the magnetization vector $\vec{M}$ adapts to the direction of the external field. Additionally, a strong external field enables to adopt the macrospin approximation, which is beneficial for the determination of an analytic solution. From the considerations of the LLG it is known that the length of the magnetization $\vec{M}$ and the saturation magnetization M_{s} respectively is preserved, and $\vec{M}$ starts to precess around its equilibrium position as soon as it is deflected out of the latter one. During this precessional motion caused, for instance, by a high frequency rf-field $\vec{h}_{\mathrm{rf}}$, the tip of the magnetization vector starts to describe a curve on a surface of a sphere. Assuming arbitrary spatial orientated vectors $\vec{M}$ and $\vec{h}_{\mathrm{rf}}$, the precession is arbitrary aligned as well, describing a motion that exhibits components in all three lateral directions. However, by a suitable coordinate transformation and the application of a small angle approximation, the three dimensional motion can be reduced to a two dimensional one. For this aim it is convenient to express all vectors in spherical coordinates. Parameterizing the external field $\vec{H}_{\mathrm{ext}}$ by the coordinates ϑ and φ, the magnetization vector points in the same direction in the static case, and one reads[1]

$$\vec{M} = \begin{pmatrix} M_x \\ M_y \\ M_z \end{pmatrix} = \begin{pmatrix} M_\mathrm{s} \sin(\vartheta)\cos(\varphi) \\ M_\mathrm{s} \sin(\vartheta)\sin(\varphi) \\ M_\mathrm{s} \cos(\vartheta) \end{pmatrix} \tag{2.261}$$

for $\vec{M}$. In realistic cases, the rf-driving field is much weaker than the external field and the magnetization of the sample. Resulting from this fact, the opening angle of the precession cone is very small allowing a small angle approximation to apply in that frame; the motion of $\vec{M}$ does not happen on the surface of a sphere but on a two dimensional flat plane perpendicular to the equilibrium position. Performing a transformation of coordinates which rotates the original coordinate system in such a way that the new x-axis is parallel to the equilibrium position; then the precessional motion of $\vec{M}$ takes place in the new y-z-plane. The new coordinates will be denoted in the following by u, v and w, corresponding to the rotated x, y and z. Furthermore, the terms lab system - when dealing with quantities expressed by the old coordinates (x,y,z) - and designation local system, when considering quantities parametrized by u, v and w, have to be introduced. The transformation from the lab into the local coordinate system can be achieved from a mathematical point of view by the application of rotation matrices. In this case an arbitrary vector $\vec{v}_\mathrm{lab}$ has to be transformed into its representation $\vec{v}_\mathrm{loc}$ in new coordinates; the rotation matrices $D(\varphi)$ and D_ϑ [39] have to be applied to $\vec{v}_\mathrm{lab}$ [46].

$$D(\varphi) = \begin{pmatrix} \cos(\varphi) & \sin(\varphi) & 0 \\ -\sin(\varphi) & \cos(\varphi) & 0 \\ 0 & 0 & 1 \end{pmatrix} \qquad D(\vartheta) = \begin{pmatrix} \sin(\vartheta) & 0 & \cos(\vartheta) \\ 0 & 1 & 0 \\ -\cos(\vartheta) & 0 & \sin(\vartheta) \end{pmatrix} \tag{2.262}$$

$D(\varphi)$ describes a counterclockwise rotation of the old coordinate system around the z-axis by an angle φ, while D_ϑ rotates the system again counterclockwise by an angle ϑ around the y-axis. Thereby, the order of the performed transformation is important because rotation matrices do not commute. In the actual case, $D(\varphi)$ is first applied and subsequently $D(\vartheta)$. Both can be combined by matrix multiplication to a rotation matrix $D(\vartheta,\varphi)$ which describes the full coordinate transformation and rotation, respectively. For $D(\vartheta,\varphi)$ it yields[1] [46]

$$D(\vartheta,\varphi) = \begin{pmatrix} \sin(\vartheta)\cos(\varphi) & \sin(\vartheta)\sin(\varphi) & \cos(\vartheta) \\ -\sin(\varphi) & \cos(\varphi) & 0 \\ -\cos(\vartheta)\cos(\varphi) & -\cos(\vartheta)\sin(\varphi) & \sin(\varphi) \end{pmatrix} \tag{2.263}$$

by computing $D(\vartheta,\varphi) = D(\vartheta)D(\varphi)$ [46]. The transformation rule for a vector in the lab system, then, is given by the equation [46, 96]

$$\vec{v}_\mathrm{loc}(u,v,w) = D(\vartheta,\varphi)\vec{v}_\mathrm{lab}(x,y,z) \tag{2.264}$$

which allows to calculate the representation of the vector in the local system. Writing the vector in the lab system in the most general way as $\vec{v}_\mathrm{lab} = (x,y,z)$, it is obtained for $\vec{v}_\mathrm{loc} = (u,v,w)$ [1]:

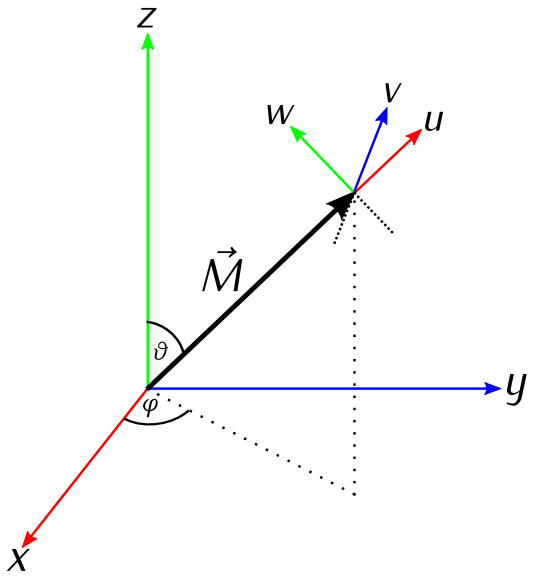

Figure 2.6. Both coordinate systems used for the mathematical treatment of the LLG equation in the case of ferromagnetic resonance (FMR). The lab coordinate system is spanned by the coordinate axes x, y and z, while the local coordinates system is given by the axes u, v and w. In the lab system, the vector of the magnetization $\vec{M}$ is characterized by its length $|\vec{M}| = M_\mathrm{s}$, the angles ϑ and φ. The connection between the systems is given by both angles because the local system is originating from the lab system by rotations of the lab system by ϑ and φ.

$$\vec{v}_\mathrm{loc} = \begin{pmatrix} u \\ v \\ w \end{pmatrix} = \begin{pmatrix} x\sin(\vartheta)\cos(\varphi) + y\sin(\vartheta)\sin(\varphi) + z\cos(\vartheta) \\ -x\sin(\varphi) + y\cos(\varphi) \\ -x\cos(\vartheta)\cos(\varphi) - y\cos(\vartheta)\sin(\varphi) + z\sin(\varphi) \end{pmatrix} \tag{2.265}$$

If the back-transformation of a vector has to be performed from the local to the lab system, the inverse matrix of $D(\vartheta, \varphi)$ has to be applied to the vector $\vec{v}_\mathrm{loc}$. This inverse matrix $D(\vartheta, \varphi)^{-1}$ is easily calculated when exploiting some mathematical properties of rotation matrices. From an more abstract point of view, rotation matrices are orthogonal matrices; for them it holds that their inverse is equal to the transposed matrix. Since products of orthogonal matrices are orthogonal as well, the inverse of $D(\vartheta, \varphi)$ is given by $D(\vartheta, \varphi)^{\mathrm{T}}$ [1] [40, 96].

$$D^{-1}(\vartheta, \varphi) = D^{\mathrm{T}}(\vartheta, \varphi) = \begin{pmatrix} \sin(\vartheta)\cos(\varphi) & -\sin(\varphi) & -\cos(\vartheta)\cos(\varphi) \\ \sin(\vartheta)\sin(\varphi) & \cos(\varphi) & -\cos(\vartheta)\sin(\varphi) \\ \cos(\vartheta) & 0 & \sin(\varphi) \end{pmatrix} \tag{2.266}$$

As transformation rule[1]

$$\vec{v}_\mathrm{lab}(x, y, z) = D^{-1}(\vartheta, \varphi)\vec{v}_\mathrm{loc}(u, v, w) = D^{\mathrm{T}}(\vartheta, \varphi)\vec{v}_\mathrm{loc}(u, v, w) \tag{2.267}$$

is obtained and it is found for the representation of a vector $\vec{v}_\mathrm{loc} = (u, v, w)$ in the lab system[1]:

$$\vec{v}_{\mathrm{lab}}(x,y,z) = \begin{pmatrix} x \\ y \\ z \end{pmatrix} = \begin{pmatrix} u\sin(\vartheta)\cos(\varphi) - v\sin(\varphi) - w\cos(\vartheta)\cos(\varphi) \\ u\sin(\vartheta)\sin(\varphi) + v\cos(\varphi) - w\cos(\vartheta)\sin(\varphi) \\ u\cos(\vartheta) + w\sin(\varphi) \end{pmatrix} \tag{2.268}$$

Furthermore, it yields for this type of matrices that all columns and rows for themselves build a set of orthogonal basis vectors. In the actual case they are even orthonormalized. Resulting from this fact, it is possible to read off directly the basis vectors $\hat{u}$, $\hat{v}$ and $\hat{w}$ of the local system[1].

$$\hat{u} = \begin{pmatrix} \sin(\vartheta)\cos(\varphi) \\ \sin(\vartheta)\sin(\varphi) \\ \cos(\vartheta) \end{pmatrix} \qquad \hat{v} = \begin{pmatrix} \sin(\varphi) \\ \cos(\varphi) \\ 0 \end{pmatrix} \qquad \hat{w} = \begin{pmatrix} -\cos(\vartheta)\cos(\varphi) \\ -\cos(\vartheta)\sin(\varphi) \\ \sin(\varphi) \end{pmatrix} \tag{2.269}$$

Comparing this to the unit vectors in spherical coordinates, namely $\vec{e}_r$, $\vec{e}_r$ and $\vec{e}_r$, it yields[1]

$$\hat{u} = \vec{e}_r \qquad , \qquad \hat{v} = \vec{e}_\varphi \qquad \text{and} \qquad \hat{w} = -\vec{e}_\vartheta \tag{2.270}$$

for the relation between both orthonormalized bases. For the further treatment of the LLG equation, an arbitrary vector $\vec{V}_{\mathrm{lab}}$, which is not coinciding with the equilibrium position of $\vec{M}$ and given by[1]

$$\vec{V}_{\mathrm{lab}} = V_0 \begin{pmatrix} \sin(\vartheta^V)\cos(\varphi^V) \\ \sin(\vartheta^V)\sin(\varphi^V) \\ \cos(\vartheta^V) \end{pmatrix} \tag{2.271}$$

in the lab system, has to be transformed into the local system. In the local coordinate system $\vec{V}_{\mathrm{loc}}$ reads[1]

$$\vec{V}_{\mathrm{loc}} = \begin{pmatrix} u \\ v \\ w \end{pmatrix} = V_0 \begin{pmatrix} \frac{1}{2}\left\{\cos(\vartheta_-^V)\cos(\varphi_-^V) - \cos(\vartheta_+^V)\cos(\varphi_-^V)\right\} + \cos(\vartheta_-^V) + \cos(\vartheta_+^V) \\ -\sin(\vartheta^V)\sin(\varphi_-^V) \\ \frac{1}{2}\left\{\sin(\vartheta_+^V)\cos(\varphi_-^V) - \sin(\vartheta_-^V)\cos(\varphi_-^V) - \sin(\varphi_-^V) - \sin(\varphi_+^V)\right\} \end{pmatrix} \tag{2.272}$$

where the abbreviations[1]

$$\begin{aligned} \vartheta_+^V &= \vartheta + \vartheta^V & \vartheta_-^V &= \vartheta - \vartheta^V \\ \varphi_+^V &= \varphi + \varphi^V & \varphi_-^V &= \varphi - \varphi^V \end{aligned} \tag{2.273}$$

are introduced. These abbreviations originate from the application of addition theorems for trigonometric functions. To proceed further, it has to be thought about the task how to achieve the prospective to solve the LLG equation in the case of FMR. Beside different common methods for solving a differential equation, the inserting of a suitable ansatz into the equation is often utilized and be applied in the following: Inserting a convenient ansatz into a differential equation transforms the mathematical problem into an easier soluble algebraic equation. Aiming to find the solution for the time evolution of the magnetization, the next task is to find the expedient ansatz $\vec{M}(t)$. For this purpose the

equilibrium position of $\vec{M}$ is considered, which is equivalent to the static situation where the magnetization is aligned parallel to the strong external field. In the lab coordinate system, $\vec{M}_{\mathrm{lab}}$ can be expressed as[1]

$$\vec{M}_{\mathrm{lab}} = M_{\mathrm{s}} \begin{pmatrix} \sin(\vartheta)\cos(\varphi) \\ \sin(\vartheta)\sin(\varphi) \\ \cos(\vartheta) \end{pmatrix} \tag{2.274}$$

and can be transformed by the application of the transformation rule Eq. (2.267). Carrying out the calculation $\vec{M}_{\mathrm{lab}}$, it reads[1]

$$\vec{M}_{\mathrm{lab}} = M_{\mathrm{s}} \begin{pmatrix} \sin^2(\vartheta)\cos^2(\varphi) + \sin^2(\vartheta)\sin^2(\varphi) + \cos^2(\vartheta) \\ -\sin(\vartheta)\sin(\varphi)\cos(\varphi) + \sin(\vartheta)\sin(\varphi)\cos(\varphi) \\ -\sin(\vartheta)\cos(\vartheta)\cos^2(\varphi) - \sin(\vartheta)\cos(\vartheta)\sin^2(\varphi) + \sin(\vartheta)\cos(\vartheta) \end{pmatrix} \tag{2.275}$$

this reduces by collecting all terms into[1]:

$$\vec{M}_{\mathrm{lab}} = \begin{pmatrix} M_{\mathrm{s}} \\ 0 \\ 0 \end{pmatrix} \tag{2.276}$$

This implies that due to the choice of the coordinate transformation, the magnetization vector in the static case is parallel to the u-axis which, of course, should be achieved by the transformation. Being expressed in the local system, $\vec{M}_{\mathrm{loc}}$ is the starting point to construct a possible ansatz for $\vec{M}(t)$. As it was explained, applying an additional external hf-field $\vec{h}_{\mathrm{rf}}$, which alternates with angular frequency ω, causes the magnetization to precess with the same angular frequency around its equilibrium position. In the frame of the earlier mentioned approximation, which relies on small cone angles, it is assumed that the curve described due to the precession of $\vec{M}(t)$ is located in the v-w-plane. Since the time-dependent magnetization components in v- and w-direction are very small, the change of the length of the magnetization pointing along the u-axis can be neglected. Consequently, M_u is chosen to be equal to M_{s}. The time dependent components are $m_v(t) = m_v e^{\mathrm{i}\omega t}$ and $m_w(t) = m_w e^{\mathrm{i}\omega t}$, and thereby, the ansatz for $\vec{M}_{\mathrm{loc}}(t)$ is given by[1]:

$$\vec{M}(t)(u,v,w) = \begin{pmatrix} M_{\mathrm{s}} \\ m_v e^{\mathrm{i}\omega t} \\ m_w e^{\mathrm{i}\omega t} \end{pmatrix} \tag{2.277}$$

Since the LLG equation contains additionally the total time derivative of $\vec{M}$, $\dot{\vec{M}}(t)$ has to be computed in order to solve the differential equation. Resulting straight forward from Eq. (2.277), it yields for $\dot{\vec{M}}(t)$ [1]:

$$\frac{\mathrm{d}\vec{M}}{\mathrm{d}t}(t)(u,v,w) = \begin{pmatrix} 0 \\ \mathrm{i}\omega m_v e^{\mathrm{i}\omega t} \\ \mathrm{i}\omega m_w e^{\mathrm{i}\omega t} \end{pmatrix} \tag{2.278}$$

This result will be later inserted into the LLG. Striving for the solution of the LLG equation, the expression for the effective field $\vec{H}_{\mathrm{eff}}$ needs to be known

in addition. The effective field is determined by the energy terms appearing in the physical system one can investigate. Dealing with $Ni_{80}Fe_{20}$ that is known to be free of crystalline anisotropies, only the contributions of the Zeeman Energy E_{Zee} and the demagnetization Energy E_{dem} originating from dipolar interactions are considered. In total the effective field $\vec{H}_{\mathrm{eff}}$ is composed out of three terms [1]:

$$\vec{H}_{\mathrm{eff}} = \vec{H}_{\mathrm{dem}} + \vec{H}_{\mathrm{Zee}} + \vec{h}_{\mathrm{rf}}(t) \tag{2.279}$$

Before determining the exact form of the effective field, the geometry for the situation of FMR is discretized by setting the external magnetic field $\vec{H}_{\mathrm{ext}}$ lying in the x-y-plane and pointing along the y-axis. In this special geometry, the direction of the magnetization in equilibrium position is given by the angles $\varphi = \frac{\pi}{2}$ and $\vartheta = \frac{\pi}{2}$. Now the effective field has to be transformed into the local coordinate system, which is done in two steps: First, by applying the transformation matrix $D(\vartheta, \varphi)$ which reads for the given angles as[1]

$$D(\vartheta, \varphi) = \begin{pmatrix} 0 & 1 & 0 \\ -1 & 0 & 0 \\ 0 & 0 & 1 \end{pmatrix} \tag{2.280}$$

to the certain components adding up to $\vec{H}_{\mathrm{eff}}$. After rotating the coordinate system for the demagnetization field $\vec{H}_{\mathrm{dem}}$, the Zeeman field $\vec{H}_{\mathrm{Zee}}$ and the rf-field $\vec{h}_{\mathrm{rf}}$ [1] are obtained:

$$\vec{H}_{\mathrm{dem}}(x, y, z) = - \begin{pmatrix} N_x M_x \\ N_y M_y \\ N_z M_z \end{pmatrix} \tag{2.281}$$

$$\vec{H}_{\mathrm{Zee}}(x, y, z) = \begin{pmatrix} 0 \\ H \\ 0 \end{pmatrix} \tag{2.282}$$

$$\vec{h}_{\mathrm{rf}}(x, y, z) = \begin{pmatrix} h_y \\ -h_x \\ h_z \end{pmatrix} e^{\mathrm{i}\omega t} \tag{2.283}$$

This is only one half of the transformation. Taking a closer look on $\vec{H}_{\mathrm{dem}}$ and $\vec{H}_{\mathrm{Zee}}$, it can be recognized that both expressions still contain quantities from the lab system, or in other words, both fields still depend on the magnetization components of the old coordinate system, namely M_x, M_y and M_z. To fully transform the fields into the local system, latter mentioned components of $\vec{M}$ have to be expressed in terms of M_u, M_v and M_w. The second part of the transformation is the connection between both representations of the magnetization that can be calculated by performing the back transformation from the local to the lab system. Finding the connection[1]

$$\begin{pmatrix} M_x \\ M_y \\ M_z \end{pmatrix} = \begin{pmatrix} 0 & 1 & 0 \\ -1 & 0 & 0 \\ 0 & 0 & 1 \end{pmatrix} \begin{pmatrix} M_u \\ M_v \\ M_w \end{pmatrix} = \begin{pmatrix} -M_v \\ M_u \\ M_w \end{pmatrix} \tag{2.284}$$

The fields contained in $\vec{H}_{\mathrm{eff}}$ read in terms of the magnetization components

in the local system as[1]:

$$\vec{H}_{\mathrm{dem}}(u,v,w) = D(\vartheta,\varphi)\vec{H}_{\mathrm{dem}}(x,y,z) = \begin{pmatrix} -N_y M_y \\ N_x M_x \\ -N_z M_z \end{pmatrix} = -\begin{pmatrix} N_y M_u \\ N_x M_v \\ N_z M_w \end{pmatrix} \tag{2.285}$$

$$\vec{H}_{\mathrm{Zee}}(u,v,w) = D(\vartheta,\varphi)\vec{H}_{\mathrm{Zee}}(x,y,z) = \begin{pmatrix} H \\ 0 \\ 0 \end{pmatrix} \tag{2.286}$$

$$\vec{h}_{\mathrm{rf}}(u,v,w) = D(\vartheta,\varphi)\vec{h}_{\mathrm{rf}}(x,y,z) = \begin{pmatrix} h_u \\ h_v \\ h_w \end{pmatrix} e^{\mathrm{i}\omega t} \tag{2.287}$$

forming the total effective field[1]

$$\vec{H}_{\mathrm{eff}}(u,v,w) = \begin{pmatrix} -N_y M_u + H + h_u e^{\mathrm{i}\omega t} \\ -N_x M_v + h_v e^{\mathrm{i}\omega t} \\ -N_z M_w + h_w e^{\mathrm{i}\omega t} \end{pmatrix} \tag{2.288}$$

which will be inserted into the LLG equation later on. Before tackling the task of solving the LLG equation, the preliminary considerations of the torque acting on the magnetization in the static case have to be carried out. Defined as the time changing rate of the magnetization, the torque $\vec{T}$ that originates from the LLG equation, is given by the formula[1] [32]:

$$\vec{T} = -\gamma_0 \vec{M}_{\mathrm{stat}}(u,v,w) \times \vec{H}_{\mathrm{eff,stat}}(u,v,w) \tag{2.289}$$

Aligned parallel to the y-axis in equilibrium position, the static magnetization $\vec{M}_{\mathrm{stat}}(x,y,z)$ is given in the lab system by[1]

$$\vec{M}_{\mathrm{stat}}(x,y,z) = \begin{pmatrix} 0 \\ M_{\mathrm{s}} \\ 0 \end{pmatrix} \tag{2.290}$$

and after transformation into the local system[1]

$$\vec{M}_{\mathrm{stat}}(u,v,w) = D(\vartheta,\varphi)\vec{M}_{\mathrm{stat}}(x,y,z) = \begin{pmatrix} M_{\mathrm{s}} \\ 0 \\ 0 \end{pmatrix} \tag{2.291}$$

is obtained for $\vec{M}_{\mathrm{stat}}(u,v,w)$. As $\vec{T} = \frac{\mathrm{d}\vec{M}}{\mathrm{d}t} = 0$ in the static case, the damping term vanishes and the precessional term has to be zero as well. Writing it with the magnetization and the effective field for this situation, one obtains[1]:

$$\vec{T} = \begin{pmatrix} M_{\mathrm{s}} \\ 0 \\ 0 \end{pmatrix} \times \begin{pmatrix} -N_y M_{\mathrm{s}} + H \\ 0 \\ 0 \end{pmatrix} = \begin{pmatrix} 0 \\ 0 \\ 0 \end{pmatrix} \tag{2.292}$$

This result implies that, indeed, the torque vanishes in the geometric situation chosen in the considered case. If, for example, a physical system is considered where the cross product between $\vec{M}_{\mathrm{stat}}(u,v,w)$ and $\vec{H}_{\mathrm{eff,stat}}(u,v,w)$ is not identi-

cal zero on both sides, then the originating equation has to be used to eliminate certain terms in the solution of the LLG equation. The actual solution is found by inserting the ansatz for $\vec{M}(t)$ and the resulting time evolution $\frac{\mathrm{d}\vec{M}}{\mathrm{d}t}$ into the LLG eq., as well as the full expression for the effective field $\vec{H}_{\mathrm{eff}}$. As starting point[1]

$$\begin{aligned}\begin{pmatrix} 0 \\ \mathrm{i}\omega m_v e^{\mathrm{i}\omega t} \\ \mathrm{i}\omega m_w e^{\mathrm{i}\omega t} \end{pmatrix} = -\gamma_0 \begin{pmatrix} M_\mathrm{s} \\ m_v e^{\mathrm{i}\omega t} \\ m_w e^{\mathrm{i}\omega t} \end{pmatrix} \times \begin{pmatrix} -N_y M_u + H + h_u e^{\mathrm{i}\omega t} \\ -N_x M_v + h_v e^{\mathrm{i}\omega t} \\ -N_z M_w + h_w e^{\mathrm{i}\omega t} \end{pmatrix} \\ + \frac{\alpha}{M_\mathrm{s}} \begin{pmatrix} M_\mathrm{s} \\ m_v e^{\mathrm{i}\omega t} \\ m_w e^{\mathrm{i}\omega t} \end{pmatrix} \times \begin{pmatrix} 0 \\ \mathrm{i}\omega m_v e^{\mathrm{i}\omega t} \\ \mathrm{i}\omega m_w e^{\mathrm{i}\omega t} \end{pmatrix}\end{aligned} \tag{2.293}$$

is given, and after carring out the cross products and neglecting higher orders of $e^{\mathrm{i}\omega t}$ [1]

$$\begin{pmatrix} 0 \\ \mathrm{i}\omega m_v e^{\mathrm{i}\omega t} \\ \mathrm{i}\omega m_w e^{\mathrm{i}\omega t} \end{pmatrix} = -\gamma_0 \begin{pmatrix} 0 \\ \{(N_z - N_y)M_\mathrm{s} + H\} m_w - M_\mathrm{s} h_w \\ \{(N_y - N_x)M_\mathrm{s} - H\} m_v - M_\mathrm{s} h_v \end{pmatrix} + \begin{pmatrix} 0 \\ -\mathrm{i}\alpha\omega m_w \\ \mathrm{i}\alpha\omega m_v \end{pmatrix} \tag{2.294}$$

is obtained as system of equations. At this stage an advantage of the coordinate transformation and the selection of the applied ansatz becomes clear.Being identical zero, the first line of the system of equations vanishes and the mathematical problem reduces to a two dimensional system. This is expected because the ansatz was chosen in such a manner that the dynamics of $\vec{M}$ occurs only in the v-w-plane. Introducing the abbreviations $\mathfrak{B}$ and $\mathfrak{H}$, defined as[1]

$$\mathfrak{B} = (N_z - N_y)M_\mathrm{s} + H \qquad \text{and} \qquad \mathfrak{H} = (N_x - N_y)M_\mathrm{s} + H \tag{2.295}$$

respectively, it yields[1]

$$\begin{pmatrix} 0 \\ \mathrm{i}\omega m_v e^{\mathrm{i}\omega t} \\ \mathrm{i}\omega m_w e^{\mathrm{i}\omega t} \end{pmatrix} = -\gamma_0 \begin{pmatrix} 0 \\ \mathfrak{B} m_w - M_\mathrm{s} h_w \\ -\mathfrak{H} m_v - M_\mathrm{s} h_v \end{pmatrix} + \begin{pmatrix} 0 \\ -\mathrm{i}\alpha\omega m_w \\ \mathrm{i}\alpha\omega m_v \end{pmatrix} \tag{2.296}$$

for the two dimensional system. The introduced fields $\mathfrak{B}$ and $\mathfrak{H}$ are the induction-like and field-like terms. With the objective to find an expression for the response of the magnetization $\vec{m}$ on an external field $\vec{h}$, the equation to $\vec{m} = \chi\vec{h}$ have to be re-arranged. Here, χ is the dynamic susceptibility of the system. In order to resolve the system of equations with respect to $\vec{m}$, all terms containing m_v or m_w are collected at the left hand side[1]

$$\begin{pmatrix} \mathrm{i}\omega m_v + \mathrm{i}\alpha m_w + \gamma_0 \mathfrak{B} m_w \\ -\mathrm{i}\alpha\omega m_v + \gamma_0 \mathfrak{H} m_v + \mathrm{i}\omega m_w \end{pmatrix} = -\gamma_0 M_\mathrm{s} \begin{pmatrix} -h_w \\ h_v \end{pmatrix} \tag{2.297}$$

and written in matrix notation. This matrix notation is helpful in resolving the equation to the desired form[1].

$$\begin{pmatrix} \mathrm{i}\frac{\omega}{\gamma_0} & \mathfrak{B} + \mathrm{i}\alpha\frac{\omega}{\gamma_0} \\ \mathfrak{H} + \mathrm{i}\alpha\frac{\omega}{\gamma_0} & -\mathrm{i}\frac{\omega}{\gamma_0} \end{pmatrix} \begin{pmatrix} m_v \\ m_w \end{pmatrix} = M_\mathrm{s} \begin{pmatrix} h_w \\ h_v \end{pmatrix} \tag{2.298}$$

Resolving with respect to $\vec{m}$, the matrix contained in Eq. (2.298) is defined in a first step as χ'^{-1}, and its inverse χ' is calculated. The reason why the matrix has been denoted as χ'^{-1} and not as χ^{-1} is that the matrix on the left hand side of the equation is not the inverse of the susceptibility matrix but, at least, proportional to it. Thereby, the proportional factor is given by $\frac{1}{M_\mathrm{s}}$ and the matrix χ'^{-1} is found to be[1]

$$\chi' = \frac{1}{\mathrm{det}\chi'^{-1}} \begin{pmatrix} -\mathrm{i}\frac{\omega}{\gamma_0} & -(\mathfrak{B} + \mathrm{i}\alpha\frac{\omega}{\gamma_0}) \\ -(\mathfrak{H} + \mathrm{i}\alpha\frac{\omega}{\gamma_0}) & \mathrm{i}\frac{\omega}{\gamma_0} \end{pmatrix} \tag{2.299}$$

which leads to the equation[1]

$$\begin{aligned} \begin{pmatrix} m_v \\ m_w \end{pmatrix} &= \frac{M_\mathrm{s}}{\mathrm{det}\chi^{-1}} \begin{pmatrix} -\mathrm{i}\frac{\omega}{\gamma_0} & -(\mathfrak{B} + \mathrm{i}\alpha\frac{\omega}{\gamma_0}) \\ -(\mathfrak{H} + \mathrm{i}\alpha\frac{\omega}{\gamma_0}) & \mathrm{i}\frac{\omega}{\gamma_0} \end{pmatrix} \begin{pmatrix} h_w \\ h_v \end{pmatrix} \\ &= \begin{pmatrix} \chi_{vw} & \chi_{vv} \\ \chi_{ww} & \chi_{wv} \end{pmatrix} \begin{pmatrix} h_w \\ h_v \end{pmatrix} \end{aligned} \tag{2.300}$$

Here, the term $M_\mathrm{s}\chi'$ is defined as the susceptibility matrix χ because this is an agreement with the definition $\vec{m} = \chi\vec{h}$. At this stage, the task of calculating the response of the magnetization on an external field, the dynamic susceptibility of the system, is done; but an important fact can be concluded from Eq. (2.300) about the resonance point of the system. The resonance of an oscillation system is always accompanied by a maximum in amplitude of the oscillation. Looking at the concrete form of the susceptibility matrix χ, it can be seen that the terms reach their maximum when the denominator of the prefactor $\frac{M_\mathrm{s}}{\mathrm{det}(\chi'^{-1})}$ becomes minimal. In this case, the smaller value for $\mathrm{det}(\chi'^{-1})$ is given by zero, leading to the resonance condition for FMR as $\mathrm{det}(\chi'^{-1} = 0)$. Calculation of the denominator N leads to the mathematical expression[1]

$$\mathrm{det}\chi^{-1} = N = \left(\frac{\omega}{\gamma_0}\right)^2 - \left(\mathfrak{H} + \mathrm{i}\alpha\frac{\omega}{\gamma_0}\right)\left(\mathfrak{B} + \mathrm{i}\alpha\frac{\omega}{\gamma_0}\right) \tag{2.301}$$

which is still a complex function. Since striving for experimentally accessible predictions, the absolute value of the denominator needs to be computed by multiplying N with its complex conjugated value N^* yielding the square value of N. Equating this result with zero, the general resonance condition in the case of FMR is obtained[1].

$$|N|^2 = NN^* = \left\{\left(\frac{\omega}{\gamma_0}\right)^2 - \mathfrak{H}\mathfrak{B}\right\} = 0 \tag{2.302}$$

This relation holds true in general, and it does not matter which physical system is considered and how many different interactions are included. Being solely interested in the resonance condition for the system under consideration, only the corresponding induction and field like terms $\mathfrak{B}$ and $\mathfrak{H}$ have to be calculated. In the actual experiments, the angular resonance frequency is of interest; this

angular frequency can directly be calculated from Eq. (2.302). An important relation also follows from the following equation [88, 89]:

$$\left(\frac{\omega}{\gamma_0}\right)^2 = \mathfrak{H}\mathfrak{B} \tag{2.303}$$

This expression will be used in the next section when deriving the shape of the resonance curve.

2.4.2 Solutions for Ferromagnetic Resonance in the Full-Film and Stripe Geometry

In the previous section the dynamic susceptibility of the magnetization under the action of an external rf-field and the general resonance condition for FMR have been computed. In the following, the concrete formulas for the resonance frequency ω in the stripe and full-film geometry are computed, proceeded by the determination of the line shape of the resonance curve. Starting with the resonance frequency, it is obtained by inserting the concrete expressions of $\mathfrak{B}$ and $\mathfrak{H}$ into Eq. (2.303)

$$\omega = \gamma_0 \sqrt{\{(N_x - N_y)M_\mathrm{s} + H\}\,\{(N_z - N_y)M_\mathrm{s} + H\}} \tag{2.304}$$

which applies to the situation when measuring FMR on patterned magnetic stripes. Eq. (2.304) is the so called Kittel formula for the resonance condition in the case fo FMR [88, 89, 95]. This result can be adopted to the full film geometry by setting the demagnetizing factors $N_x = N_y = 0$ and $N_z = 1$. It yields[1]:

$$\omega = \gamma_0 \sqrt{H(H + M_\mathrm{s})} \tag{2.305}$$

Measuring ω as function of the external field H, it is possible to access experimentally the quantity γ_0 by fitting the measurement data with respect to the obtained equations Eq. (2.304) and (2.305). It should be mentioned that it is, of course, possible to do the fitting routine with 5 free variables, namely γ_0, M_s, N_x, N_y and N_z. However, this will result very likely in wrong values for the later mentioned quantities. A better way to approximate the determination of γ_0 is to do the measurement of ω as function of H and additionally determine M_s by SQUID. The demagnetizing factors can be calculated analytically in good approximation, yielding very accurate values for γ_0.

Another important material parameter of magnetic materials is the Gilbert damping parameter α, which is a measure for the dissipation rate of energy in the magnetic system (see Sec. 2.1). As will be seen now, α is accessible via FMR measurements or, to be more precise, by fitting the obtained resonance curve with the theoretical predicted line shape. The question what the shape of this resonance curve is arises. Considering the resonance curve, it has to be clarified what is detected in the TR-MOKE experiments. In the polar MOKE configuration utilized for the time resolved measurements of the magnetization dynamics, the component of the dynamic magnetization which is pointing perpendicular to the plane of the magnetic film at a certain time is detected, namely $m_w(t)$. Thereby, $m_w(t)$ is given by the corresponding dynamic susceptibility χ_{ww} times

the component of the rf-field in w-direction. Having[1]

$$m_w(t) = \chi_{ww} h_w e^{\mathrm{i}\omega t} \tag{2.306}$$

with the dynamic susceptibility χ_{ww} given by[1]:

$$\chi_{ww} = M_\mathrm{s} \frac{(\mathfrak{H} + \mathrm{i}\alpha\frac{\omega}{\gamma_0})}{(\mathfrak{H} + \mathrm{i}\alpha\frac{\omega}{\gamma_0})(\mathfrak{B} + \mathrm{i}\alpha\frac{\omega}{\gamma_0}) - \left(\frac{\omega}{\gamma_0}\right)^2} \tag{2.307}$$

Basically, the line shape in dependence of α and the angular frequency ω is determined. However, it is still a complex function and it has to be converted into a real value function to be applied to the experimental data. Furthermore, it is convenient to express the terms $\mathfrak{H}$ and $\mathfrak{B}$ by a Taylor series in H around the resonance point. As it will become clear soon, this is helpful to reduce the rather complicated line shape to an expression which is very familiar. The Taylor expansion [39, 40] for the induction and field like terms are given by[1]

$$\mathfrak{H} = \mathfrak{H}|_{H=H_\mathrm{r}} + \frac{1}{1!}\frac{\mathrm{d}\mathfrak{H}}{\mathrm{d}H}\bigg|_{H=H_\mathrm{r}} (H - H_\mathrm{r}) = \mathfrak{H}_\mathrm{r} + \delta H \tag{2.308}$$

and[1]

$$\mathfrak{B} = \mathfrak{B}|_{H=H_\mathrm{r}} + \frac{1}{1!}\frac{\mathrm{d}\mathfrak{B}}{\mathrm{d}H}\bigg|_{H=H_\mathrm{r}} (H - H_\mathrm{r}) = \mathfrak{B}_\mathrm{r} + \delta H \tag{2.309}$$

where $\mathfrak{H}_\mathrm{r}$ and $\mathfrak{B}_\mathrm{r}$ are the corresponding fields at the resonance points. The Taylor expansion is often used to approximate a complicated function by a simpler one; however, it is worth to note that in the actual case it returns the exact function back. The reason is that both fields have the form H plus a constant factor. Being linear in the external field H, a Taylor series up to the second term reproduces exactly the original function. Defining $H - H_\mathrm{r}$ as δH and plugging the expressions for both fields into the formula for χ_{ww}, it yields[1]

$$\chi_{ww} = M_\mathrm{s} \frac{(\mathfrak{H}_\mathrm{r} + \delta H + \mathrm{i}\alpha\frac{\omega}{\gamma_0})}{(\mathfrak{H}_\mathrm{r} + \delta H + \mathrm{i}\alpha\frac{\omega}{\gamma_0})(\mathfrak{B}_\mathrm{r} + \delta H + \mathrm{i}\alpha\frac{\omega}{\gamma_0}) - \left(\frac{\omega}{\gamma_0}\right)^2} \tag{2.310}$$

as function for the dynamic susceptibility. This looks now even more complicated than before; but multiplying out both brackets in the denominator and using the identity Eq. (2.303), it is possible to convert χ_{ww} into the form[1]

$$\chi_{ww} = M_\mathrm{s} \frac{(\mathfrak{H}_\mathrm{r} + \delta H + \mathrm{i}\alpha\frac{\omega}{\gamma_0})}{(\mathfrak{H}_\mathrm{r} + \mathfrak{B}_\mathrm{r})(\delta H + \mathrm{i}\alpha\frac{\omega}{\gamma_0})} \tag{2.311}$$

which is still complex. The conversion into a real value function can be achieved by expanding in a first step the fraction contained in χ_{ww} with the complex conjugate of the denominator. This yields[1]

$$\chi_{ww} = M_\mathrm{s} \frac{(\mathfrak{H}_\mathrm{r} + \delta H + \mathrm{i}\alpha\frac{\omega}{\gamma_0})(\delta H - \mathrm{i}\alpha\frac{\omega}{\gamma_0})}{(\mathfrak{H}_\mathrm{r} + \mathfrak{B}_\mathrm{r})(\delta H + \mathrm{i}\alpha\frac{\omega}{\gamma_0})(\delta H - \mathrm{i}\alpha\frac{\omega}{\gamma_0})} \tag{2.312}$$

and after multiplying the brackets and additionally neglecting higher order terms in α, one obtains[1]

$$\chi_{ww} = M_\mathrm{s}\frac{\mathfrak{H}_\mathrm{r}}{\mathfrak{H}_\mathrm{r}+\mathfrak{B}_\mathrm{r}}\frac{\delta H - \mathrm{i}\alpha\frac{\omega}{\gamma_0}}{(\delta H)^2+(\alpha\frac{\omega}{\gamma_0})^2} \tag{2.313}$$

for the dynamic susceptibility.

The considerations arrived at a stage where it becomes obvious which concrete shape of the resonance curve is to be expected. Looking at Eq. (2.313), it is recognizable that this is the line shape of a Lorentzian curve. Such Lorentzian line shapes appear always in the mathematical description of harmonic driven oscillators, and by knowing this fact, it is possible to get a feeling why the functions $\mathfrak{H}$ and $\mathfrak{B}$ have been expanded around the resonance points. For example, the resonance curve of a harmonic driven oscillator known from classical mechanics is not perfectly Lorentzian. However, considering the line shape in a more or less narrow range around the resonance point, it can be approximated very well by this kind of function. Please note that strictly spoken, the formula obtained is a mixture of a symmetric and antisymmetric Lorentzian function. Omitting, for now, the complex prefactor i in front of ΔH and splitting it up in two parts, the symmetric Lorentzian is given by the function with δH in the numerator. The antisymmetric one is given by the function where ΔH is found in the numerator. Such Lorentzian functions are characterized by three parameters, namely, the amplitude A, the position of the resonance and the full half width of the curve. In the considered case, the resonance position is contained in δH and the term $\frac{\omega}{\gamma_0}$ can be identified as full half width. Defining the full half width as ΔH[1],

$$\Delta H = \alpha\frac{\omega}{\gamma_0} \tag{2.314}$$

is found, leading to the expression[1]:

$$\chi_{ww} = M_\mathrm{s}\frac{\mathfrak{H}_\mathrm{r}}{\mathfrak{H}_\mathrm{r}+\mathfrak{B}_\mathrm{r}}\frac{\delta H - \mathrm{i}\Delta H}{(\delta H)^2+(\Delta H)^2} \tag{2.315}$$

This is a very important result within the considerations. As mentioned above, it is the aim to derive an expression of the resonance curve which allows to determine the Gilbert damping parameter α. As it was seen, the full width at half maximum H is directly proportional to α and ω. Since γ_0 is just a constant factor in this equation, it is possible to determine α by measuring FMR for different angular frequencies ω of the driving field and fitting the obtained resonance curve to the experimental data. Following from this is that the resulting full widths at half maximum ΔH is fitted in dependence on ω, and from the slope of the linear curve, α is calculated. As mentioned, the resonance curve obtained theoretically has to be given as real value function. In a first step denominator is converted into a real value function by expanding the fraction by the complex conjugate of the denominator. Being still complex valued, χ_{ww} has to be transformed mathematically. For this purpose χ_{ww} is inserted into the expression for $m_{ww}(t)$ [1].

$$m_{ww}(t) = M_\mathrm{s}\frac{\mathfrak{H}_\mathrm{r}}{\mathfrak{H}_\mathrm{r}+\mathfrak{B}_\mathrm{r}}\frac{\delta H - \mathrm{i}\Delta H}{(\delta H)^2+(\Delta H)^2}h_w e^{\mathrm{i}\omega t} \tag{2.316}$$

By the use of the identity for the complex exponential function $e^{\mathrm{i}\omega t} = \cos(\omega t) + \sin(\omega t)$, multiplying and taken only the real part of the function $m_{ww}(t)$, namely $\mathrm{Re}\{m_{ww}(t)\}$, it yields[1]:

$$\begin{aligned}\mathrm{Re}\{m_{ww}(t)\} &= M_\mathrm{s} h_w \frac{\mathfrak{H}_\mathrm{r}}{\mathfrak{H}_\mathrm{r} + \mathfrak{B}_\mathrm{r}} \frac{1}{(\delta H)^2 + (\Delta H)^2} \{\delta H \cos \omega t) + \Delta H \sin(\omega t)\} \\ &= \frac{A}{(\delta H)^2 + (\Delta H)^2} \{\delta H \cos(\omega t) + \Delta H \sin(\omega t)\}\end{aligned} \tag{2.317}$$

As described in the section about the experimental method of TR-MOKE (see Sec. 3.3), the resonance curve at certain times t_n is measured. This time can be also expressed by the phase angle with respect to the probing laser pulse and the precession of the dynamic magnetization. It can be written mathematically as[1]

$$\omega t = \omega t_n = \varphi_n \qquad \text{and} \qquad \varphi_n = 2\pi n m + \Theta \tag{2.318}$$

which leads to the formula for the angle φ_n[1]:

$$\varphi_n = \frac{2\pi}{\omega} n m + \frac{\Theta}{\omega} \tag{2.319}$$

Here, n stands for the number of periods of the precessing magnetization, whereby m is the ratio between the frequency of the exciting rf-field and the repetition rate of the laser pulses - for the technical details see Sec. 3.3. Inserting this expression into Eq. (2.317), it becomes[1]

$$\mathrm{Re}\{m_{ww}(t)\} = \frac{A}{(\delta H)^2 + (\Delta H)^2} \{\delta H \cos(\Theta) + \Delta H \sin(\Theta)\} \tag{2.320}$$

and it is found that the resonance curve is a mixture between the a symmetric and antisymmetric Lorentzian function, whereby the portion between both parts is determined by the mixture angle Θ. Please note that the prefactor in front of the fraction in formula Eq. (2.317) was labeled as A, the amplitude of the Lorentzian function. The function $\mathrm{Re}\{m_{ww}(t)\}$ serves in the experiments as fitting function for the experimental FMR data obtained.

2.5 Magneto-Optical Kerr Effect

The magneto-optical Kerr effect (MOKE) belongs to the magneto-optical effects; these effects also include physical phenomena, for instance, the Faraday effect or linear (MLD) and cirular magnetic dichroism (MXCD). All of them have in common that in reflection (Kerr effect) or transmission (Faraday effect) of linearly polarized light and through a magnetized material respectively, a rotation of the polarization plane appears [97]. Especially the MOKE has gained a lot of importance in the recent decades because it is a very powerful destruction free method for the investigation of thin film magnetic samples [97]. In general it is distinguished between three different geometric configurations for the MOKE,

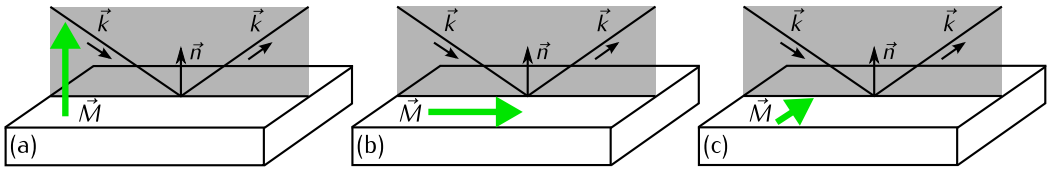

Figure 2.7. Three possible configurations for the Kerr effect. The green arrows represents the direction of the magnetization $\vec{M}$, $\vec{k}$ the wave vector of the incident light and $\vec{n}$ the surface normal of the sample. Both last mentioned vectors ($\vec{k}$ and $\vec{n}$) span the plane of incidence which is marked with the bright gray surface. Which type of Kerr effect occurs depends on the relative direction of the magnetization compared to the plane of incidence. (a) sketches the situation for the polar MOKE, (b) longitudinal MOKE and (c) transversal MOKE.

which are characterized by the direction of the magnetization in the sample regarding the plane of incidence of incoming polarized light (see Fig. 2.7). These three configurations are the polar, longitudinal and transversal MOKE [37, 97], whereby the polar MOKE exhibits the biggest effect concerning the rotation of the plane of polarization. In the longitudinal and transversal geometry, effects are obtained which are one and two times smaller in the order of magnitude compared to the polar MOKE [98]. The classification of the three effects in basis of the present geometry (direction of magnetization with respect to the plane of incidence of light) is as follows: The polar MOKE appears when the vector of magnetization $\vec{M}$ is pointing perpendicular to the sample plane, and thereby, it is parallel to the plane of incidence. In the case of longitudinal and transversal MOKE, it has the direction of magnetization $\vec{M}$ lying in the sample plane and being parallel or perpendicular respectively to the plane of incidence of the incoming polarized light [37, 97].

All these three effects have in common, as already mentioned at the beginning of this section, that in reflection a rotation of the polarization plane by an angle θ_K is obtained, and in addition, an ellipticity of light η_K is induced. These key quantities which describe the MOKE can be combined to one physical quantity, the complex Kerr rotation angle Φ_K, which is defined as $\Phi_\mathrm{K} = \theta_\mathrm{K} + \mathrm{i}\eta_\mathrm{K}$ [37]. In this thesis two measurement setups are applied which rely on the MOKE. Thereby, the TR-MOKE setup utilizes the polar MOKE geometry, whereas for the detection of DWM in the WF-MOKE, the longitudinal MOKE is exploited. In the subsequent two sections the quantum mechanical origin of the MOKE (Sec. 2.5.1) will be explained. The effect on linearly polarized light will be discussed in the frame of classical optics (Sec. 2.5.2); but first, the MOKE is considered from the quantum mechanics point of view.

2.5.1 Quantum Mechanical Origin of the Magneto-Optical Kerr Effect

The quantum mechanical origin of the MOKE lies in the spin dependent splitting of the band structure of magnetic materials [97] which leads to different absorption coefficients for left and right circular light. In quantum mechanics, light is described by massless particles called photons. These photons carry an angular momentum of $\pm\hbar$, which is the quantum mechanical analogon for left

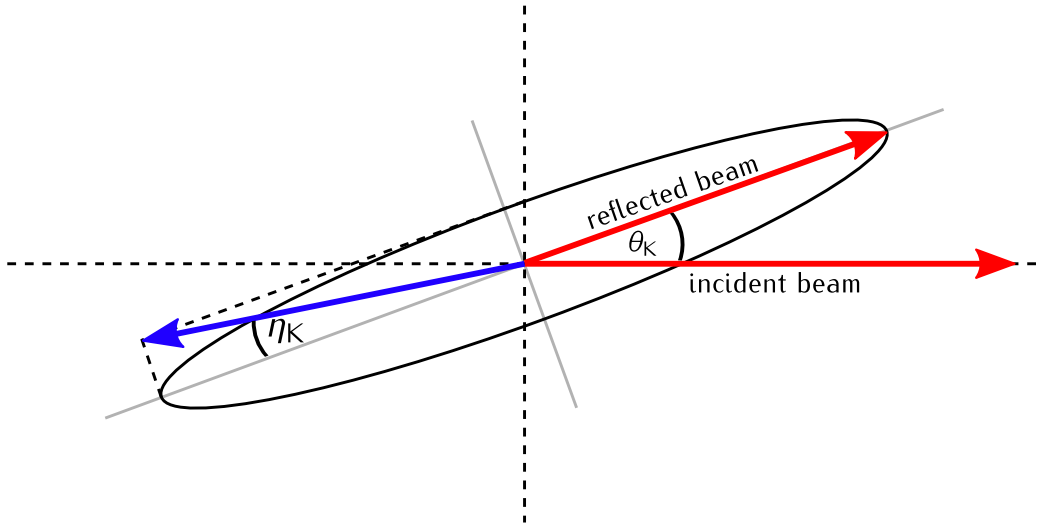

Figure 2.8. Elliptically polarized light as it is obtained after reflection of an initially linear polarized light from a magnetized sample. In this sketch the two key quantities θ_K and η_K are drawn. Both quantify the effect of the Kerr rotation and are combined in the complex Kerr rotation angle Φ_K.

$(+\hbar)$ and right $(-\hbar)$ circular polarized light [38]. For the appearance of a MOKE signal, different absorption coefficients for photons with both values of angular momentum are required. Absorption of light is described in quantum mechanics via the absorption of photons by electrons. Due to later mentioned process, the electrons gain energy and change from a state in the valence band into an unoccupied state in the conduction band above the Fermi level. Hence it is possible, these transitions have to fulfill certain selection rules, which are given by:

$$\Delta l = \pm 1 \qquad \text{and} \qquad \Delta m = \pm 1 \qquad , \tag{2.321}$$

This rule implies that absorption processes of photons are accompanied by the change of the azimuthal quantum number l and magnetic quantum number m. These changes in quantum number bears the fact that the angular momentum of the photon given by $\pm\hbar$ is transferred to the electron [38]. Additionally, the energy $E_{\text{Phot}} = \hbar\omega$ of the photon has to be large enough for the band gap to be overcome because only these have sufficiently large transition probabilities. Furthermore, the states in the valence and conduction bands have to be split up spin dependently [97]. In a ferromagnetic material, transitions between $d_{xz}^{\uparrow\downarrow}$ or $d_{yz}^{\uparrow\downarrow}$ that change to the $p_z^{\uparrow\downarrow}$ orbital satisfy this condition. Exchange interaction causes a spin dependent split-up between orbitals with spin-up and spin-down, respectively. This is leads to a lowering in energy for the orbitals $d_{xz}^{\uparrow}$ as well as $d_{yz}^{\uparrow}$, and it results in a gain in energy for the $d_{xz}^{\downarrow}$ and $d_{yz}^{\downarrow}$ ones. The degeneration of the orbitals is removed due to the spin-orbit coupling, which causes, additionally, a small energetically splitting between the d_{xz} and d_{yz} orbitals [99]. In total, this leads to different transition probabilities for transitions with an exchange of angular momentum with $\pm\hbar$. The macroscopic effect on linear polarized light that is caused by the different transition probabilities will be explained in the next section with methods of classical optics.

2.5.2 Magneto-Optical Kerr Effect in the Frame of Classical Optics

In this section the macroscopic effect on linear polarized light which is reflected from an magnetized surface will be explained. As demonstrated in the previous section, there are different transition probabilities for photons exhibiting positive and negative angular momentum, respectively. This unequal transition probabilities reflect themselves in different microscopical absorption and reflection coefficients. Linear polarized light can be decomposed in two equal parts of left and right circular polarized light, which is the classical analogon for photons with positive and negative angular momentum. In the following, the considerations are restricted to the electrical field of the electromagnetic wave because the effect on the magnetic field is the same. Applying vector notation, the decomposition of linear polarized light reads [98]:

$$\vec{E} = E_0 \begin{pmatrix} 1 \\ 0 \end{pmatrix} e^{\mathrm{i}(kz-\omega t)} = \frac{E_0}{2} \left[\begin{pmatrix} 1 \\ \mathrm{i} \end{pmatrix} + \begin{pmatrix} 1 \\ -\mathrm{i} \end{pmatrix} \right] e^{\mathrm{i}(kz-\omega t)} \tag{2.322}$$

Considering the part of the light which is reflected from the magnetized surface, different reflection coefficients for left (r_+) and right (r_-) circular polarized components have to be taken into account. The reflected part of the electromagnetic field $\vec{E}_\mathrm{r}$ then is given by[1]:

$$\vec{E}_\mathrm{r} = \frac{E_0}{2} \left[r_+ \begin{pmatrix} 1 \\ \mathrm{i} \end{pmatrix} + r_- \begin{pmatrix} 1 \\ -\mathrm{i} \end{pmatrix} \right] e^{\mathrm{i}(kz-\omega t)} = \frac{E_0}{2} r_+ \begin{pmatrix} r_+ + r_- \\ \mathrm{i}(r_+ - r_-) \end{pmatrix} e^{\mathrm{i}(kz-\omega t)} \tag{2.323}$$

Recombining it even further, it becomes obvious that different coefficients r_+ and r_- lead to a phase shift ϵ between the x- and y-components of the electric field, which is nothing else than the expression for elliptic polarized light in classical optics [98].

$$\vec{E}_\mathrm{r} = \begin{pmatrix} E_x \\ E_y e^{i\epsilon} \end{pmatrix} e^{\mathrm{i}(kz-\omega t)} \tag{2.324}$$

Regarding the representation of this complex valued vector in the plane of complex numbers, it describes an ellipse; these major principal axis and the axis for real numbers confine an angle θ_K, given by[1]

$$\tan(2\theta_\mathrm{K}) = 2\frac{E_x E_y}{E_x^2 + E_y^2} \cos(\epsilon) \tag{2.325}$$

and named as Kerr angle. Another key number describing the reflected light is the so called Kerr ellipticity η_K that can be calculated from the rotation between E_y and E_x [98].

$$\tan(\eta_\mathrm{K}) = \frac{E_y}{E_x} \tag{2.326}$$

Chapter 3

Experimental Techniques and Data Evaluation

Ch. 3 is dedicated to the experimental techniques and methods of data evaluation applied in this thesis. Starting with the explanation of the sample design (Sec. 3.1), it will be continued with the depiction of the utilized measurement methods for sample characterization and DWM measurements. These methods are presented in Sec. 3.2-3.5. The last two parts of this chapter explain how the experimental and simulational data were evaluated (Sec. 3.6 and Sec. 3.7).

3.1 Sample Design

Regarding the sample fabrication, the samples are designed as follows to match the experimental requirements. On top of a GaAs substrate a coplanar waveguide (CPW) made of 150 nm Au is fabricated by sputter deposition for the application of electrical pulses in the nanosecond range, wherein the dimensions of the CPW have been adjusted to match 50 Ω in- and output resistance. Subsequently, $Ni_{80}Fe_{20}$ nanostripes of various widths w (0,45 - 1,20 μm) and 20 nm thickness t are added by thermal evaporation. To protect the $Ni_{80}Fe_{20}$ layer from oxidation, 3 nm of Al are evaporated on top and beneath. These magnetic nanostructures are placed on top of the signal line of the CPW. CPW and nanostripes are electrically decoupled by 150 nm of crosslinked polymethyl methacrylate (crosslinked PMMA). This crosslinked PMMA also exhibits an extreme flat surface which provides a perfect underlayer for the subsequently added nanostripes and ensures a high DW mobility. The magnetic structures under investigation consist of an elliptical nucleation pad at one extremity, while on the other side the strips terminate as a tip to favor domain wall (DW) annihilation. DWs can be nucleated and moved by applying electrical pulses across the CPW, providing Oersted fields along the X-direction around the waveguide. Additionally, a 5 mm × 5 mm blank piece of GaAs substrate was placed next to the main sample during the evaporation process of the Al/$Ni_{80}Fe_{20}$/Al layer for the magnetic structures. The sample was coated similarly to the main sample by a

dielectric layer of Al_2O_3 in an ALD process to protect it from dirt and oxidation. This sample is used later on to characterize the magnetic layer in SQUID (determining the saturation magnetization M_s) and full-film FMR (measuring the Gilbert damping parameter α). A third piece of GaAs, half coated by PMMA, served as reference sample for the thickness of the Al_2O_3 layer (determined by AFM measurements) after the lift-off process.

In the following the design of the samples used in the studies is described and explained in more detail. Aiming to investigate field-driven DWM in $Ni_{80}Fe_{20}$ stripes, several problems appear in both, from a technical and a physical point of view. Moreover, the experimental requirements are illuminated which set automatically, as an immediate consequence, the goals which have to be achieved by the sample design. Based on this list, the arising problems are discussed below and then explained how they can be avoided by process engineering and appropriate sample design. Summarizing these considerations, the actual sample fabrication and design are depicted at the end of this section. Starting with the requirements, the samples have to fulfill four measurements of field-driven DWM. There are basically three points:

- Create, move freely and annihilate VDWs
- Apply homogeneous short-time in-plane field pulses
- Enable optical detection of the DWM

This sounds very simple, but in fact difficulties are encountered in many ways and a tremendous amount of fabrication process and sample design has to be done. For the application of short-time field pulses in the nanosecond range a coplanar waveguide (CPW) is used, which enables the application of short current pulses; they create the desired in-plane magnetic field on the top of the CPW. The applied current pulses are rectangularly shaped and exhibit very short rising and falling times (<0.5 ns) at their flanks; this results in a rich frequency spectrum with components even in the high GHz frequency range. For the achievement of undisturbed signal transmission, all frequency components of the pulse have to be transmitted with the same attenuation in the ideal case. The CPW design utilized in this work is given in the following way: It consists of three metallic stripes made out of Au and exhibits a rectangular cross section. The middle line is denoted as signal line, while the two adjacent metallic stripes are called ground lines. These ground lines are separated by a gap from the signal line (see Fig. 3.1). Such kind of CPW design has proven as suitable for experiments with high frequency signals [100–102] and field-driven DWM [22]. For an almost lossless transmission of the applied signals, these CPWs can be matched to the desired impedance by adjusting the width and broadness of the gap between signal and ground line using commercial available programs (e.g. TXLINE).

Another advantage of CDWs comes across due to the large aspect ration of width to thickness of the signal line. This large aspect ratio causes a surrounding magnetic field where the field lines patterning the rectangular shape of the signal line. This creates the experimentally needed homogeneous in-plane driving field

for the measurements of DWM. As result, the second point of the requirements is fulfilled.

An optical detection (TR-MOKE and WF-MOKE) can be ensured by placing the magnetic structures on top of the signal line and by capping these by an optically transparent layer of Al_2O_3. By placing the structures on top of the signal line, an electrical decoupling of both has to be ensured. This task can be achieved by a thin dieletric layer made of Al_2O_3. In the actual case, a different material, namely crosslinked Poly(methyl methacrylate) (crosslined PMMA or CPMMA), is utilized. These advantages will be explained later in more detail. The magnetic structures itself are made out of $Ni_{80}Fe_{20}$ (Permalloy), a prototypical material for experiments concerning DWM in different geometries, for example, rings [83] or stripes [22, 103, 104].

In order to create, move and subsequently annihilate VDWs by the application of a magnetic field pulse, the magnetic structures are patterned as stripes attached at one end to large elliptical pads, and on the other end the stripes terminate as a tip (see Fig. 3.1). The reason for choosing this design will be explained now by starting with the consideration of the elliptical nucleation pads.

Nucleation of a DW into a nanostripe can be achieved for instance by the Oersted field of a metallic nanowire traveling perpendicularly across the magnetic strip [105] or via rectangular nucleation pads [103, 104, 106]. Since striving for a controlled nucleation and injection of VDWs into a stripe, it has been demonstrated in both, by experiment and micromagnetic simulations, that elliptical pads are more suitable [107]. This design has been used successfully in recent experimental works, e.g. [108] or [22]. Depending on geometric parameters, for instance, layer thickness and the dimensions of major and minor axis of the ellipse, the magnetic groundstate can be a one- or two-vortex state [107, 109, 110]. Attaching the stripe parallel to the major axis to the ellipse enables the nucleating a VDW into the stripe by applying an external magnetic field of the order of magnitude of a few ten Oersted [107]. Such design even enables the control of the circulation c of the VDW nucleated [107], which is not necessary in the actual case because it aims at equal distribution of both chiralities. As demonstrated in [107], the circulation c of the nucleated VDW is predetermined by the circulation of the vortex state in the nucleation pad. The dimensions of the elliptical pad chosen for the samples favors a two vortex state where both circulations are always present. In this way, the sample design guarantees the presence of VDWs with both types of circulation in a certain single measurement which includes serveral stripes in the actual used sample geometry. An equal distribution of VDWs with both chiralities χ is, averaged over a large number of single measurements, given by the energetic degeneration of the four ground states of VDWs in a stripe. Even when possible to predict the circulation of the VDW, the polarity of the emerging VDW is not controllable; but due to the fact that all four possible ground states are energetically degenerate, it can be assumed to have an equal distribution of both chiralities and all four different configurations of VDWs on average.

However, since the position of the stripe has an influence on the field needed to nucleate a new VDW into the stripe, it is crucial where exactly the strips are

attached to the ellipse. Placing the stripe along the symmetry axes of the ellipse results in very low nucleation fields, which brings along the difficulty that every field pulse that is applied to move the DW along the stripe, is accompanied by the nucleation of a new VDW. This is not desired and one way to avoid this is to lower the symmetry of the sample geometry by offsetting the stripe with respect to the principal axis of the nucleation pad [107]. The farther the stripe is from the principal axis, the higher the field becomes for the injection of a new DW. It is possible by this method to keep separate the field ranges for the DWM and DW nucleation in the experiments.

After nucleation of the DW and a subsequent motion along the stripe, the VDW has to be annihilated in the end. For this purpose, the ends of the stripes are formed as triangular tips. These kind of sample geometries are suitable for DW annihilation as has been proven by experimental studies [107, 111] and by micromagnetic simulations [107]. Taking a look at the list of requirements, almost everything has been fullfilled and discussed with exception that the DW has to be able to move freely along the stripe.

In order to ensure this finesse experimentally, a tremendous optimization effort has to be done for the samples. For example, aiming to determine the damping parameter α via DWM, all external influences have to be avoided as good as possible in order to get close to the intrinsic values. It was proven in several works that grains and edge roughness can act as pinning sides for the topological defects (VC, HAVs) the VDW is consisting of. Concerning edge roughness, basically the HAVs which are located at the edges, are affected. Already small defects at the edges can affect sensitively the pinning field for the DW, as it was proven in many experimental [20, 103–105, 108, 112–115] and simulational studies [20, 103, 114–116] about artificial defects (notches) at stripe edges. A lot of effort has been taken into sample fabrication to reduce edge roughness to the lowest possible measure. Double resist methods for electron beam lithography was utilized in combination with dose test series in order to find the optimal dose for the lithography process. The double resist, which creates an undercut in the development process, ensures a clean and smooth lift off process after thermal evaporation of the stripes. Additionally, the position of the sample in the evaporation chamber was controlled to avoid misalignment and evaporate with an oblique angle of incidence which results in defective edges and flanks.

Further influencing factors known for greatly affecting DWM are grains, impurities and surface roughness. This was demonstrated in experimental works [117], theory and micromagnetic studies [118–124]. In order to ensure an unimpeded DWM, it is expedient to reduce the effects of later mentioned disturbances on DWM to the smallest possible measure by an improved sample fabrication process. Since grains are naturally given by the polycristalline nature of the used ferromagnetic material ($Ni_{80}Fe_{20}$), it has to be dealt with. Nevertheless, one influencing factor which enhances the surface roughness of the stripes can be canceled out by sample optimization. The ferromagnetic structures are patterned onto the CPW signal line made out of a thick Au layer deposited by sputtering technique. Such sputter deposited gold surfaces exhibit a large surface roughness. These irregularities are additionally impressed on the $Ni_{80}Fe_{20}$

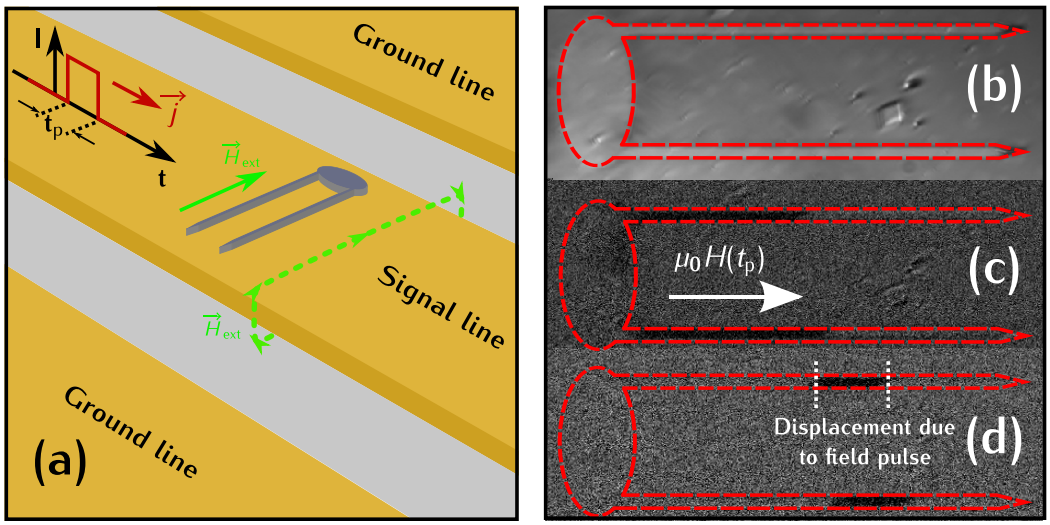

Figure 3.1. (a) Sample design. (b-d) presentation of the measuring principle (details can be found in the text).

strips. As previously mentioned, an additional layer between the CPW and the structures on top is required for an electrical decoupling. Utilizing Al_2O_3, which is a common material for this type of application, does not solve the problem regarding the roughness of the stripes. Even depositing more than 100 nm of Al_2O_3 as dielectric spacer, the surface roughness is still mediated unchanged by the Al_2O_3 layer. However, this task can be solved by changing to a different material. The material of choice is crosslinked PMMA (CPMMA), basically a layer of PMMA resist which is crosslinked by irradiation of a very high electron beam dose. Coating the sample with PMMA, the resist covering the sample exhibits an extremely flat surface. Crosslinking the PMMA resist at the desired locations by electron beam lithography shrinks the thickness of the PMMA, but the CPMMA retains its flat surface, even when there is a very rough layer present underneath. These CPMMA layers can be utilized as dielectric spacer [125] and have already been used e.g. as micromechanical elements [126]. In the actual case it serves as a perfect seed layer for the stripe/pad geometry.

To avoid impurities in the bulk of the $Ni_{80}Fe_{20}$ layer itself, the thermal evaporation process and the layer stack of the ferromagnetic sample were optimized. Proceeding to the thermal evaporation process of the layer stack, Cr was evaporated for a few minutes before the actual layer. Cr acts as a getter material for oxygen which enhances the vacuum in the evaporation chamber, and results in a better quality of the ferromagnetic layer. Subsequently, a $Al/Ni_{80}Fe_{20}/Al$ trilayer is deposited where the thin Al layer underneath and on top of the $Ni_{80}Fe_{20}$ layer serves as protection from dirt and oxidation. After liftoff, the whole sample is coated by 90 nm Al_2O_3 to protect it from oxidation and the immersion oil used in the wide-field MOKE measurements. Thereby, the layer thickness of the Al_2O_3 coating is optimized for a high reflectivity in light with wavelength $\lambda = 450$ nm, which is the wavelength provided by the LED used in experiments WF-MOKE setup. The dielectric coating was done by atomic layer deposition (ALD) in a commercially available tool.

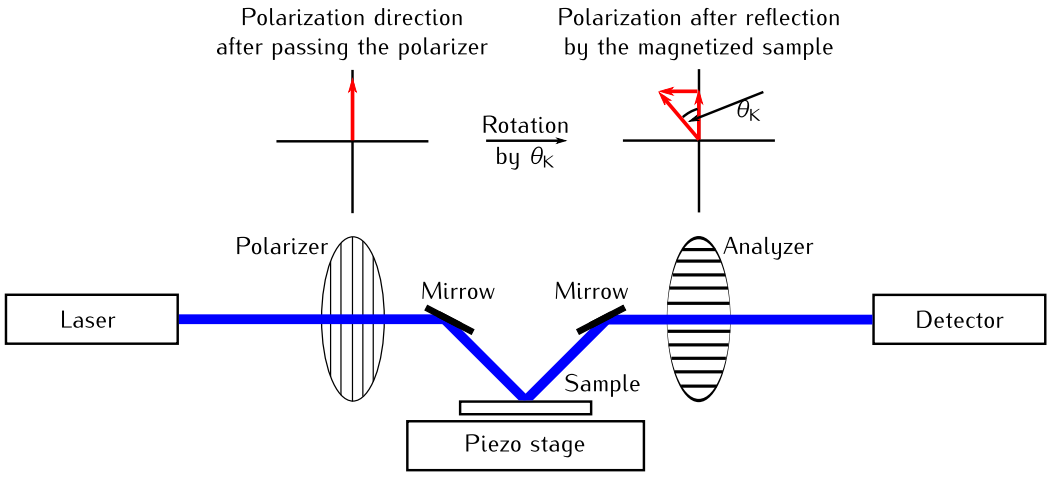

Figure 3.2. Illustration of the basic measurement principle of a setup utilizing the MOKE for the determination of the magnetization in a sample.

3.2 Superconducting Quantum Interference Device

In order to determine the saturation magnetization M_s of the magnetic layer, a superconducting quantum interference device (SQUID) is utilized. A SQUID belongs to the group of inductive measurement techniques for the determination of the saturation magnetization and, to be more precise, it is the superconducting variant of the vibrating sample magnetometer (VSM) [50]. Utilizing a superconducting ring that contains a weak link like a Josephson junction, it acts like a very sensitive quantum interferometer [37]. Passing a sample through the ring, the persistent current induced in the ring is proportional to the magnetization [37] measured by counting the changing number of magnetic flux quanta via the Josephson junction [38]. This is a very high sensitive method to measure magnetic moments up to the order of approximately $\approx 10^{-12}$ Am^2. The saturation magnetization can be calculated by dividing the total magnetic moment by the magnetic volume V of the sample [37]. For more details about the working principles of a SQUID it is referred to the references [37, 38, 50].

3.3 Time-Resolved Kerr Microscopy

To access the Gilbert damping parameter α directly on the patterned magnetic structures on the sample, time-resolved Kerr microscopy (TR-MOKE) is applied for the FMR measurements. It should be noted that the information concerning the TR-MOKE setup is taken from [93, 127]. The TR-MOKE technique enables the performing of a destruction free FMR measurement with high spatial resolution of about 230 nm, which is convenient when dealing with structures exhibiting dimensions in the micrometer or nanometer range. Basically, there are three requirements a measurement setup has to fulfill for being capable to perform such a measurement:

- Apply an external magnetic field, bipolar tunable over a range of a few 100 mT.

- Apply a high frequency excitation field in the GHz frequency range.
- A pulsed laser system which can be synchronized with the exciting microwave field to enable a stroboscopic measurement of the dynamic magnetic susceptibility.

Basically, a MOKE setup, not especially a TR-MOKE setup, consists out of four components:

- Light source, in the actual case of a TR-MOKE a laser.
- Polarizer
- Analyzer
- Detector

As mentioned, a laser serves as light source and provides monochromatic light. Regarding a pure (not time-resolved) MOKE setup, the laser does not have to be necessarily pulsed. This light is passing through a polarization filter serving as polarizer and setting the plane of polarization for the incoming light to a fixed direction, and it goes onto the magnetic sample, whereby the reflected light gains, due to the magneto-optical Kerr effect, a rotation of the polarization plane (plus an ellipticity). The light is guided to a second polarizer; this forward direction is adjusted in such a way that in the absence of a Kerr rotation the whole intensity of the reflected laser beam is absorbed and no light can pass through. In other words, the second polarizer provides the function of an analyzer. At the presence of a rotation of the polarizaton plane, a particular small amount of the beam intensity can pass the analyzer and enters a detector. This detector converts the light signal into an electrical one. However, the setup used in this thesis proves as a little bit more complicated and complex because a few additional technical elements are implemented into the measurement setup. This will be explained in the following.

One of the additional special requirements is the desired high spatial resolution. In order to achieve high resolution, the laser light is coupled into a microscope and focused onto the sample. As light source serves a frequency doubled Titan Saphire laser (TiSa laser) with a wavelength of $\lambda = 800$ nm (output power $P = 1 - 2$ W) which is pumped by a green Nd.YAG laser (output power $P = 10$ W). After frequency doubling by a barium borate crystal (BBO) light with reduced intensity but a wavelength of $\lambda = 400$ nm is obtained. With a numerical apperture $NA = 0.9$ given by the microscope itself and a wavelength of $\lambda = 400$ nm, the spatial resolution is obtained as [98]:

$$\frac{\lambda}{2NA} = 230\,\mathrm{nm} \tag{3.1}$$

In the advanced measurement setup of the TR-MOKE, the light passes a telescope (for adjusting the beam width and beam divergence) and a periscope (redirecting the beam). As described previously, a polarizer is passed by the beam to set a fixed polarization direction of the incoming light being subsequent

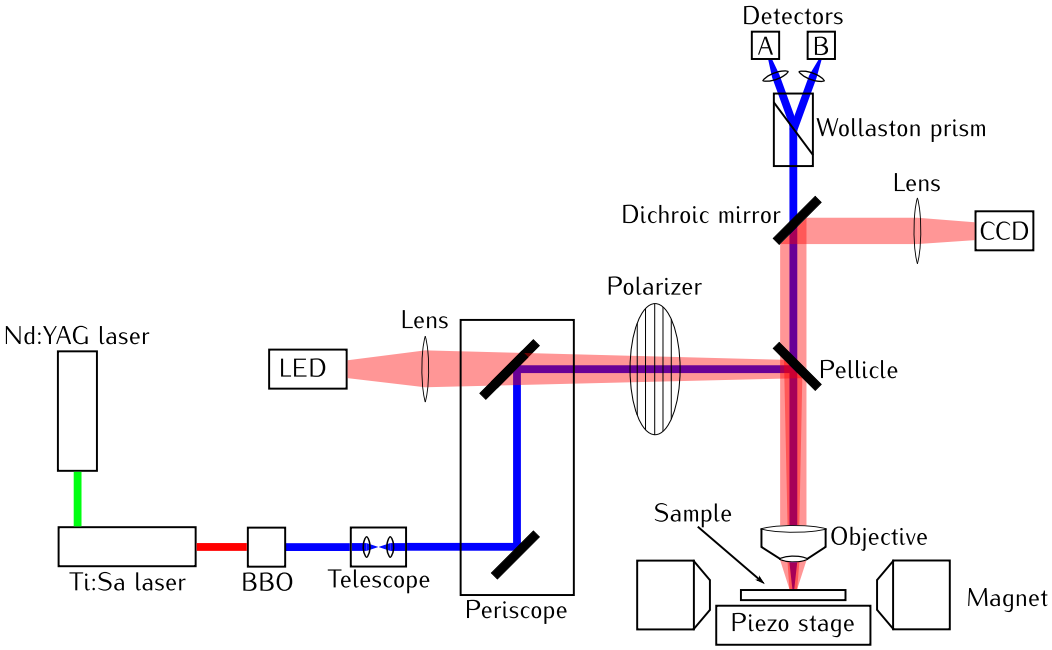

Figure 3.3. Schematic representation for the basic optical setup of the TR-MOKE setup. It contains all optical, electronic and mechanical elements of the setup which are required to achieve the stroboscopic optical measurements of the dynamic magnetization.

redirected by a pellicle beam splitter. The sample itself is mounted onto a piezoelectric sample holder (piezo stage) which enables to adjust the position of the sample in the setup. The electrical positioning is realized by computer control, whereby it is possible to control the x-, y- and z-position of the sample with an accuracy of a few nm. Reflected light coming from the sample passes again the pellicle beam splitter and enters a Wollaston prism which divides the light in two perpendicular polarization components. The intensity of both partial beams is converted into voltages U_A and U_B by two electronic detectors A and B. These signals are converted into a sum and a differential signal by adding up and subtracting both voltages from each other electronically. The sum signal is given by $U_A + U_B$ and the corresponding differential signal reads $U_A - U_B$. For the measurements the Wollaston prism is adjusted in such a manner that U_A and U_B are equal in the case of absent Kerr rotation. Hence, the differential signal $U_A - U_B$ becomes zero. A magnetized sample exhibiting a perpendicular magnetization component causes a Kerr rotation due to the polar magneto-optical Kerr effect. In turn, this leads to a finite differential signal that allows to deduce the Kerr angle and z-component of the magnetization. As it can be proven very easily, the ratio A_{Kerr} between differential and sum signal is connected to the Kerr angle θ_{K} by the relation:

$$A_{\mathrm{Kerr}} = \frac{U_A - U_B}{U_A + U_B} = \tan(2\theta_{\mathrm{K}}) \tag{3.2}$$

Assuming small angles θ_{K}, which is indeed a valid assumption since θ_{K} is in the range of $10^{-3\circ}$, the small-angle approximation can be applied. This approximation enables the replacement of $\tan(2\theta_{\mathrm{K}})$ by $2\theta_{\mathrm{K}}$ which yields :

$$A_{\mathrm{Kerr}} = \frac{U_A - U_B}{U_A + U_B} \approx \theta_{\mathrm{K}} \propto M_{\mathrm{s}} \tag{3.3}$$

Since the Kerr rotation θ_{K} is proportional to M_z, it is possible to have direct access to the magnetization component in z-direction via the direct proportionality between A_{Kerr} and θ_{K}. Regarding the Kerr signal A_{Kerr} it should be noted that the measurement of the differential signal $U_A - U_B$ is basically sufficient, but including the sum signal $U_A + U_B$ makes the experimentally determined quantity A_{Kerr} insensitive to small fluctuations of the beam intensity. For sample positioning, the already mentioned piezo stage is utilized for two different tasks. On the one hand, the piezo stage is used for scanning the topography of the sample by measuring the intensity of the reflected laser beam. Since the intensity of the back coming light is proportional to the topography and the surface texture, it allows to image the surface. On the other hand, the piezo stage is applied for the stabilization at a certain point on the sample during the measurement. In order to do this, light with the wavelength $\lambda = 670$ nm is provided by a LED and is additionally coupled into the beam path. This light is detected by a digital camera and analyzed via computer. The corresponding stabilization software detects contemporaneous deviations from the chosen position and corrects it via piezo stage instantaneously. An additional light source like the red LED influences the sum and differential signal detected. This issue can be avoided by inserting a dichroic mirror into the beam path of the microscope right before the beam enters the Wollaston prism. A dichroic mirror exhibits a wavelength dependent reflectivity which allows to decouple the red and blue light. The blue light is transmitted through the mirror, while the red one is reflected to the side where it is detected by the digital camera. Up to this stage, the capability of the described setup is limited to static MOKE measurements with high spatial resolution (approximately 230 nm). Aiming to determine the dynamic susceptibility, further technical expenditure is required to achieve both, high lateral and high time resolution. The required components, which have to be implemented into the experimental setup, will be explained in the following.

In the configuration of the TR-MOKE as used in this work, the polar MOKE is utilized to detect the magnetization component perpendicular to the surface of the sample. This implies that the dynamic susceptibility of m_z is measured at fixed times t_n. These times t_n are given by the period $T_{\mathrm{rf}} = \frac{1}{f_{\mathrm{rf}}}$ of the driving field, a phase angle Θ and the integer values n and m. For the time t_n it yields:

$$t_n = nmT_{\mathrm{rf}} + T_\varphi = nm\frac{2\pi}{\omega} + \frac{\Theta}{\omega} \qquad \text{with} \qquad 0 < \Theta < 2\pi \tag{3.4}$$

The technical limits which need to be fulfilled are naturally given by the type of measurement itself. Typical FMR measurements are conducted at external fields in the range of a few tens of mT up to a few T. At this field strength, the ferromagnetic resonance frequency is matched at frequencies in the GHz regime. Since the precession frequency of the magnetization is equal to the one of the exciting rf-field, the rf-field has to be operated in the same frequency range. Speaking about a sampling of the time dependent magnetization, the probing pulses have to be much shorter than the period time T_{rf}. These short laser

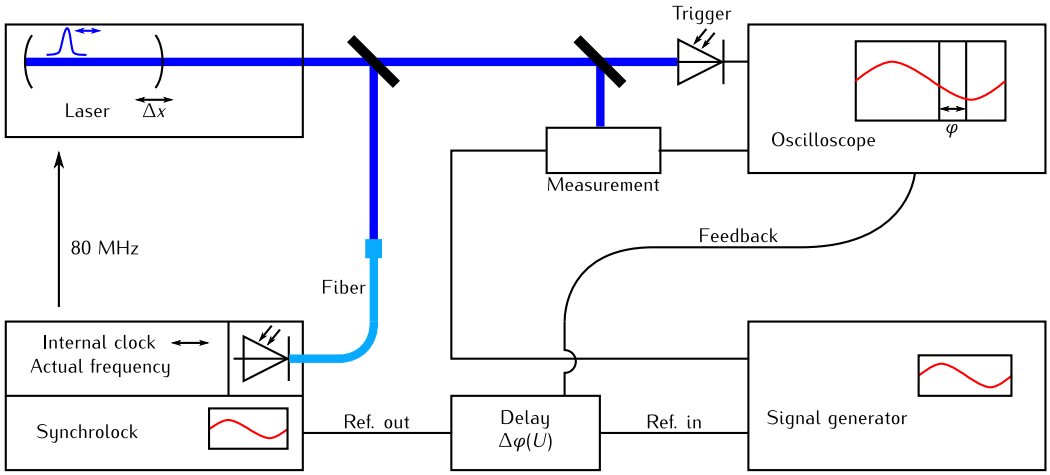

Figure 3.4. Schematic representation of the electronic components and their mutual regulation used in the TR-MOKE setup to achieve phase adjustment and stabilization.

pulses are delivered by a Ti:Sa laser operated in mode locking. It is pulsing with a repetition rate of $f_{\mathrm{Laser}} = 80$ MHz and pulse widths of $T_{\mathrm{Pulse}} = 200$ fs. As illustrative example, taking a typical excitation frequency $f_{\mathrm{rf}} = 10$ GHz,

$$T_{\mathrm{rf}} = 500\, T_{\mathrm{Pulse}} \tag{3.5}$$

is obtained for the ratio between T_{rf} and T_{Pulse}. This result clarifies that it is indeed valid to speak about a sampling of the magnetization at a certain time t_n. Additionally, a factor $m = \frac{f_{\mathrm{rf}}}{f_{\mathrm{Laser}}} = 125$ is obtained from the values chosen in this example. Here, m states that the magnetization is probed every 125 periods by a laser pulse. Striving to measure the z-component of the magnetization $\vec{M}$, it is important to probe at times when m_z reaches its maximum value. This is technically realized by a synchrolock which is implemented in the setup. The synchrolock serves as a controller and stabilizer for the phase φ between the rf-signal and the laser pulses. Aiming to achieve such phase control, the synchrolock has to fulfill two different tasks. It is crucial not solely to control the phase between rf-signal and laser pulses, but, in addition, to keep the repetition rate of the laser pulses constant at 80 MHz as well. The repetition rate is measured by a fast photo diode whose signal is fed into the synchrolock. The synchrolock has an internal clock which provides a reference signal at a frequency of 10 MHz. In the event the repetition rate deviates from the desired value, and the length of the laser resonator is adjusted by the synchrolock via the control of a piezo mirror in the Ti:Sa laser. The second task, namely the adjustment and stabilization of the phase, is done in the following manner. The mentioned 10 MHz reference signal provided by the synchrolock is fed into the rf-generator which provides a high-frequency signal. Between both devices a line stretcher is interposed which controls the phase between synchrolock and rf-generator. The phase control is achieved by the application of a DC voltage to the line stretcher which is supplied from the synchrolock.

The rf-signal itself is displayed after the transmission through the sample on an oscilloscope. The oscilloscope itself is triggered by the signal of the fast photo diode which measures the laser pulses. Determining the actual phase of the rf-signal with respect to the laser pulses is done digitally by reading out the

oscilloscope and fitting the signal by a program. If it is necessary, the computer sends a signal to the line stretcher, and the phase is adjusted. The control of the phase reaches a very high accuracy. For example, assuming a rf-signal with frequency of 10 GHz, the precision of the phase is better than 3°. The Kerr signal obtained in the MOKE measurements is usually on the order of magnitude of μV. Such weak signals are very often detected by a lock-in amplifier, which needs a modulation of the signal, which has to be detected, for the operation. For the actual measurements, the signal modulation is realized by feeding it through an additional modulator which switches the original rf-signal on and off in the kHz range. The modulator itself is triggered by the same signal that was used for the triggering of the lock-in amplifier. A CPW is used for the excitation of the magnetization by the rf-signal. It provides a convenient possibility to apply homogeneous in- and out-of plane fields to magnetic structures. Homogeneous in and out-of plane fields are accessible by placing the magnetic sample on top of the signal line or in the gap between signal and ground lines, respectively.

For reasons arising from the way the DWM is measured, the magnetic samples are structured on top of the signal line, which sets the experiments naturally to the usage of the in-plane field for the rf-excitation of the magnetization. The properties of the CPW, e.g. impedance and conductivity, are determined by certain key numbers. These key parameters are the geometric dimensions (width of the signal line and width of the gap between signal and ground line), the material the CPW is made of (Au) and the dielectric constant of the substrate (GaAs). These parameters can be put in commercially available simulation tools, for example, TXLINE, which has been used in this work to match the impedance to 50 Ω. The magnetic field strength originating from an applied electrical current can be calculated by applying Biot-Savart law. This is done by dividing the cross section of the signal line in infinitesimally small areas $\mathrm{d}A$, where a corresponding infinitesimal current $\mathrm{d}I$ is flowing through. This infinitesimal current gives rise to an infinitesimal magnetic field $\mathrm{d}B$ in the distance r. The complete field created by the signal line is obtained by integrating over the contributions of all $\mathrm{d}A$. For the calculation of the in-plane field on top of the signal line, it is sufficient to regard solely the current carried by the signal line. Speaking about the field in the gap between signal and ground line, it is something completely different. For this case the contributions of both, ground and signal line, have to be regarded. The infinitesimal field $\mathrm{d}B$ created by $\mathrm{d}I$ is given by [36, 38]:

$$\mathrm{d}B(r) = \frac{\mu_0}{2\pi}\frac{1}{r}\mathrm{d}I \tag{3.6}$$

Replacing $\mathrm{d}I$ by $j\mathrm{d}A$ and a subsequent integration yields an analytical expression for the in-plane-field, which can be found in Sec. A4. Here, a constant current density j was assumed, which is a justified approximation for rf-signal in the low GHz range. For higher excitation frequencies the skin effect, which causes an inhomogeneous current density distribution over the cross section of the signal and ground lines, has to be included. Additionally, it should be mentioned that this formula is valid for the calculation of the magnetic field created by the short time field pulses in the DWM measurements. For conducting FMR measurements, an external static magnetic field is required. This is provided by an electromagnet. The sample is placed in the gap between the pole pieces,

whereby the field is measured by a Hall probe attached to one of the pole pieces. In order to ensure that the field measured by the Hall probe is the same as given at the position of the sample itself, the field is calibrated with 2,2-diphenyl-1-picrylhydrazyl (DPPH). DPPH is a free radical whose g-factor is very precisely known and given by $g_{\mathrm{DPPH}} = 2,0036$. The method utilized for the calibration is electron parametric resonance (EPR) [38] and very closely related to the method of FMR. The calibration is done in the following way: A sample of DPPH is placed on top of a waveguide at the very same position where the sample will be placed later. At a fixed excitation frequency, the external field is swept, and the losses of the transmitted microwave power are measured. The line shape can be fitted by the formula [38]

$$B_{r,\mathrm{ESR}} = \frac{2}{g_{\mathrm{DPPH}}}\frac{m_e}{e}2\pi f \qquad \rightarrow \qquad \omega_{r,\mathrm{ESR}} = \frac{g_{\mathrm{DPPH}}}{2}\frac{e}{m_e}B \tag{3.7}$$

and the calculated resonance field is compared with the field measured by the Hall probe. Conducting this measurement for different excitation frequencies enables the calibration of the field of the Hall probe very accurately. For more information about the working principle of a TR-MOKE setup, it is referred to [93].

3.4 Full-Film Ferromagnetic Resonance

The full-film FMR characterization of the magnetic layer under consideration was done with a conventional FMR setup. Such a setup is very similar to the FMR setup described in Sec. 3.3 and relies on the same basic measurement principle. The requirements for FMR and the technical realization are the same. An external field is created by an electromagnet, whereby the sample holder is placed inbetween the pole pieces and a Hall probe detects the applied magnetic field. Differences arise in the measurement of the FMR. The sample, in the concerning case a large (5 mm $\times$ 5 mm) piece of GaAs substrate with one side fully coated by the magnetic layer (Al/$Ni_{80}Fe_{20}$/Al), is glued face down to the waveguide. A rf-signal is applied to the waveguide, causing the rf-excitation of the magnetization. Contradicting to the measurement method of TR-MOKE, the magnetization component is not directly accessed. Instead, the absorbtion of microwave power by the exctited ferromagnetic resonance in the sample is detected. The transmitted microwave power is converted by a Schottky diode into an electrical signal which is very weak and a lock-in amplifier is applied to measure this signal. For the detection of the signal by the lock-in amplifier a signal modulation is neccessary. In the specific realization of the utilized FMR setup this has been done by the attachment of small modulation coils to the pole pieces. These modulation coils create a weak AC magnetic field of magnitude < 1 mT and frequencies in the Hz upto kHz range. This field superimposes with the rf-signal, enabeling the detection by the lock-in amplifier. For further details about this measurement aparatus it is refered to the references [93, 94].

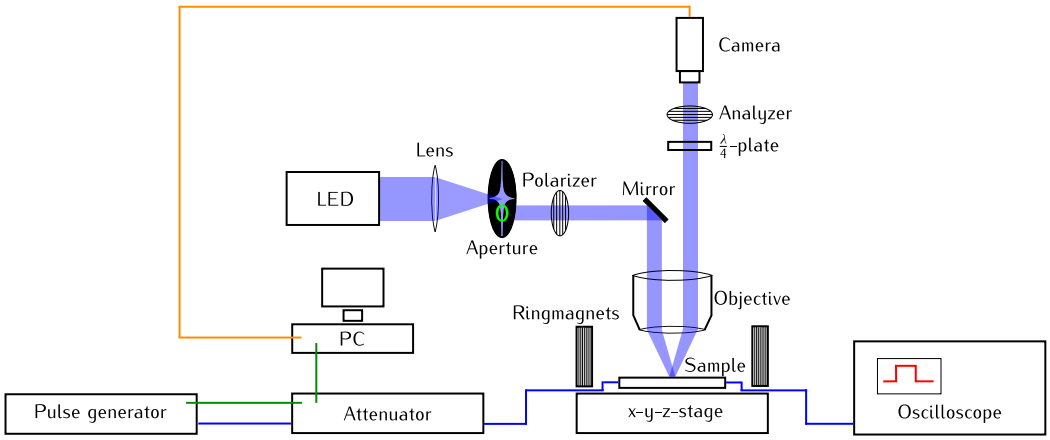

Figure 3.5. The upper row of the pictures depicts the generation of the live Kerr image while the lower part of this figure explains the optical measurement process in general.

3.5 Wide-Field Kerr Microscopy

For the detection of the DWM, a Wide-Field MOKE (WF-MOKE) has been utilized for the detection of the DW shift due to an external applied field. In the realization of the WF-MOKE as it has been used in this thesis[2] [128], it relies on the longitudinal MOKE. Basically, it consists out of the same basic optical elements (light source, analyzer, polarizer, detector) as the TR-MOKE setup. In this paragraph the optical setup of the WF-MOKE is explained in a first step, proceeding to the devices involved for the automatized application of short time bibolar field pulses to the sample. All information regarding the optical setup of a WF-MOKE are taken from [50]. As previously mentioned, the WF-MOKE applies the same basic measurement principle as the TR-MOKE. A solid state diode serves as light source providing blue light with wavelength of $\lambda = 450$ nm and optical output power $P = 2$ W. A polarizer fixes the polarization of the light coming from the LED to a fixed direction, and the light is reflected to the sample by a mirror. Before hitting the sample, the light travels through the objective that focuses the radiation onto the sample. Here, an objective with magnification of 100 $\times$ and numerical aperture of $N = 1.25$ has been used. Objectives exhibiting a numerical aperture higher than 1 require an immersion oil between sample and objective, which enhances the spatial resolution of the microscope. In the case under consideration ($\lambda = 450$ nm, $N = 1.25$), it yields a spatial resolution down to 225 nm. Light being reflected from the sample gains a rotation of the polarization plane and an additional elliptizity due to the longitudinal MOKE. This light travels again through the objective lens and passes a second polarizator serving as analyzer for the light.

As for the TR-MOKE setup, analyzer and polarizer are adjusted in that way that only light, which has undergone a Kerr rotation, will pass the analyzer by a certain propotion. Behind the analyzer a digital camera is placed which captures the light coming from the sample. The camera is additionally connected to a

[2] I like to thank Benedikt Boehm who worked on the topic of VDW motion for his master thesis and built up the WF-MOKE setup.

computer where the image is displayed. Since the longitudinal Kerr effect utilized for the WF-MOKE measurement is fairly weak, additional technical effort has to be done. Adjusting the microscope to the longitudinal geometry and optimal Kerr contrast, an aperture is inserted in the optical path between the LED and the polarizer. In order to explain why an aperture is helpful in achieving this, lets consider the back focal plane of the objective. Assuming analyzer and polarizer are optimal adjusted for light coming straight from the LED and not with some incident angle (this geometric situation corresponds to measurements using the polar MOKE), the diffraction image in the back focal plane looks like shown in Fig. 3.5. The zone of maximal extinction is cross-like-shaped in k-space (k-space corresponds to the image in the back focal plane) and by inserting an aperture, it is possible to cut out certain k-vectors for the measurement. The longitudinal MOKE geometry can be adjusted by closing the aperture almost completely and by moving the aperture off center. Doing this, the only light coming from the LED with an incident angle is hitting the sample, and the microscope can be adjusted to the longitudinal MOKE geometry. Furthermore, the aperture is helpful to enhance the Kerr contrast of the microscope. For best Kerr contrast the illumination path should neither be too large or too small. Large illumination paths lead to losses in contrast due to high background intensity of the reflected light. Small apertures can cause disturbing diffraction images at edges. Thus, the aperture can help to adjust it to optimal conditions. It should be mentioned that it is very important that the diaphragm is effectively uniform for the whole field of observation. Being not the case, it leads to a nonuniform Kerr contrast or, in the worst scenario, even to a contrast inversion in the observed image. Aiming to avoid this, an extra adjustable lens is inserted into the beam path between diaphragm and polarizer. This lens enables it to place the optical position of the aperture, which should not be confused with the physical one, into the back focal plane; in this way a homogeneous contrast over the whole observation field is ensured. Negative affects on the Kerr contrast also arise from the ellipticity gained by the light due to the Kerr effect. This ellipticity can be removed by inserting a $\frac{\lambda}{4}$-plate right before the analyzator. The sample itself is mounted on a stage that can be adjusted in all lateral directions for choosing the measurement area (x- and y-direction) and focus on the magnetic structures (z-direction). Very close besides the sample, two small ring magnets are mounted to generate alternating magnetic fields in order to optimize the imaging contrast.

For the creation of the short-time electrical field pulses, a pulse generator providing field pulses with a maximal pulse duration of 100 ns and different attenuations is applied. The maximum output voltage is 45 V (corresponding to 0 dB attenuation) and it is possible to apply bibolar voltage pulses (switch between positive and negative voltage). Striving for reliable statistic values in the measurements, a large number of single measurements are necessary, which can only be managed by automatization. For this aim the pulse generator was modified and an additional attenuator, controllable by computer, was built. In the setup used in this work, the pulse generator is operated at full output voltage supplying solely the bipolar voltage pulses in the ns range. The attenuation itself is managed by the electronically controllable attenuator which is interposed between pulse generator and the sample itself. An oscilloscope is arranged after

the sample to record the transmitted voltage pulses. With this setup it is possible to move DWs and capture optically their displacement. The Kerr contrast pictures taken are digitally contrast-enhanced and saved on the hard drive of the computer. For a detailed explanation of the measurement sequence and the way the pictures are obtained, it is referred to the following section (Sec. 3.6).

3.6 Evaluation of Measurement Data

In Fig. 3.6 the generation of the live Kerr image and the general measurement principle is illustrated. The upper row in the graphic explains the basic idea behind the digital contrast enhancement for the creation of the Kerr contrast picture. The wide-field MOKE used in the measurements utilizes the longitudinal configuration of the magneto-optical Kerr effect for detection of the configuration of the magnetic domains in the stripes. The change in intensity due to the change of the magnetic state in the sample is fairly weak compared to the total intensity of the picture. To visualize the change, digital contrast enhancement, which works in two steps, is utilized. First, a picture is taken which serves as a reference or background image. As next step the live image is taken with a constant frame rate by the digital camera and the background image is subtracted continuously. In this case, no field pulse is applied, no change in the magnetic state occurs and the picture appears gray. Applying a field pulse and shifting the domains, a shift (equal to the change of the magnetic state in the sample) is seen as black or white stripes. Additionally, the camera software offers the possibility to average over a certain amount of pictures and to use digital contrast enhancement before saving the pictures.

The general measurement sequence, which is done for every new measurement, is shown in the middle and lower part of Fig. 3.6. Before every new measurement (which means taking a picture), new domains are initialized to ensure an equal distribution for all four possible configurations of VDWs each time. In the first step the stripes are saturated completely in one direction by a strong field pulse with a magnitude of $\mu_0 H \approx 11$ mT (Fig. 3.6(a)). Subsequently, the direction of the applied field is reversed by reversing the current direction through the CPW. New domains are nucleated with a field magnitude $\mu_0 H \approx 5 - 9$ mT and a pulse duration t_p which is the same time range as used in the measurement itself (Fig. 3.6(b)). In the next step the measurement is performed. The field magnitude is changed to the value at which the measurement should be conducted ($\mu_0 H > 1$ mT) while the field direction remains the same. After this a new background image is recorded and the field pulse is applied. The picture is digitally enhanced as explained before and the picture is saved. In the last two steps a strong field pulse with $\mu_0 H \approx 11$ mT (Fig. 3.6(d)) saturates the stripes completely in one direction, and after reversing the field direction, the stripes are saturated in the opposite direction (Fig. 3.6(d)). This magnetic configuration is the starting point for a new measurement. Recorded displacements, which are visible in the saved pictures (Fig. 3.6(c)), are evaluated digitally. The evaluation of an amount of pictures in the range of $N \approx 5000$ for each measurement at a certain field provides sufficient statistics about the displacement distribution.

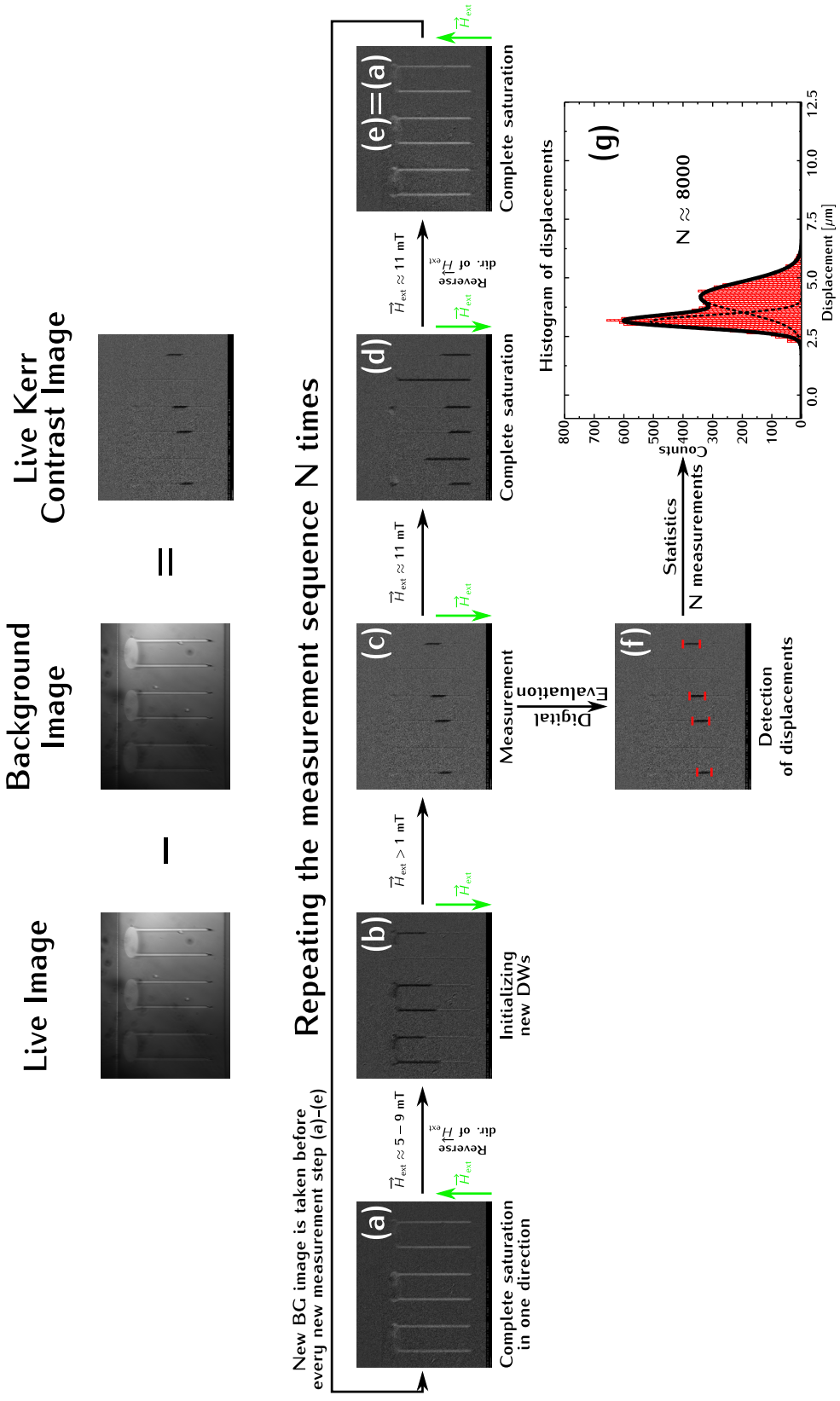

Figure 3.6. The sketch depicts the general way how the optical measurement of DWM is conducted. The upper row illustrates the digital image substraction, which results in the differential image. The middle line clarifies the five different steps which are required to obtain one measurement. The lower row gives an example for the digital displacement evaluation which results after a sufficient number of measurements in a reliable statistics.

3.7 Evaluation of Simulation Data

The evaluation and processing of data obtained from micromagnetic simulation was performed in the programming language Python. A self-written program[3] converted the original data which is provided by the simulation tool MUMAX3 as file format ".ovf" into arrays, making the further data processing easier. The processing of the raw data or the calculation of derivated quantities is a task which reduces, in principle, to slicing and dicing arrays or calculating the time and spatial derivatives of the magnetization. Derivatives with respect to time and spatial coordinates are calculated via the numerical method of a five-point stencil, which is a common way to determine derivatives of functions on a grid.

Fig. 31 presents a schematic representation of how the time derivative $\mathrm{d}\vec{m}(t)/\mathrm{dt}$ was calculated by using a five-point stencil (upper part of Fig. 31). Based on this result the gyrofield h_{gyro} and Zeeman energy $E_{\mathrm{gyro,z}}$ were calculated.

[3] I like to thank Johannes Stigloher for writing and sharing the ovf-converter which is the basis for further evaluation of simulation data.

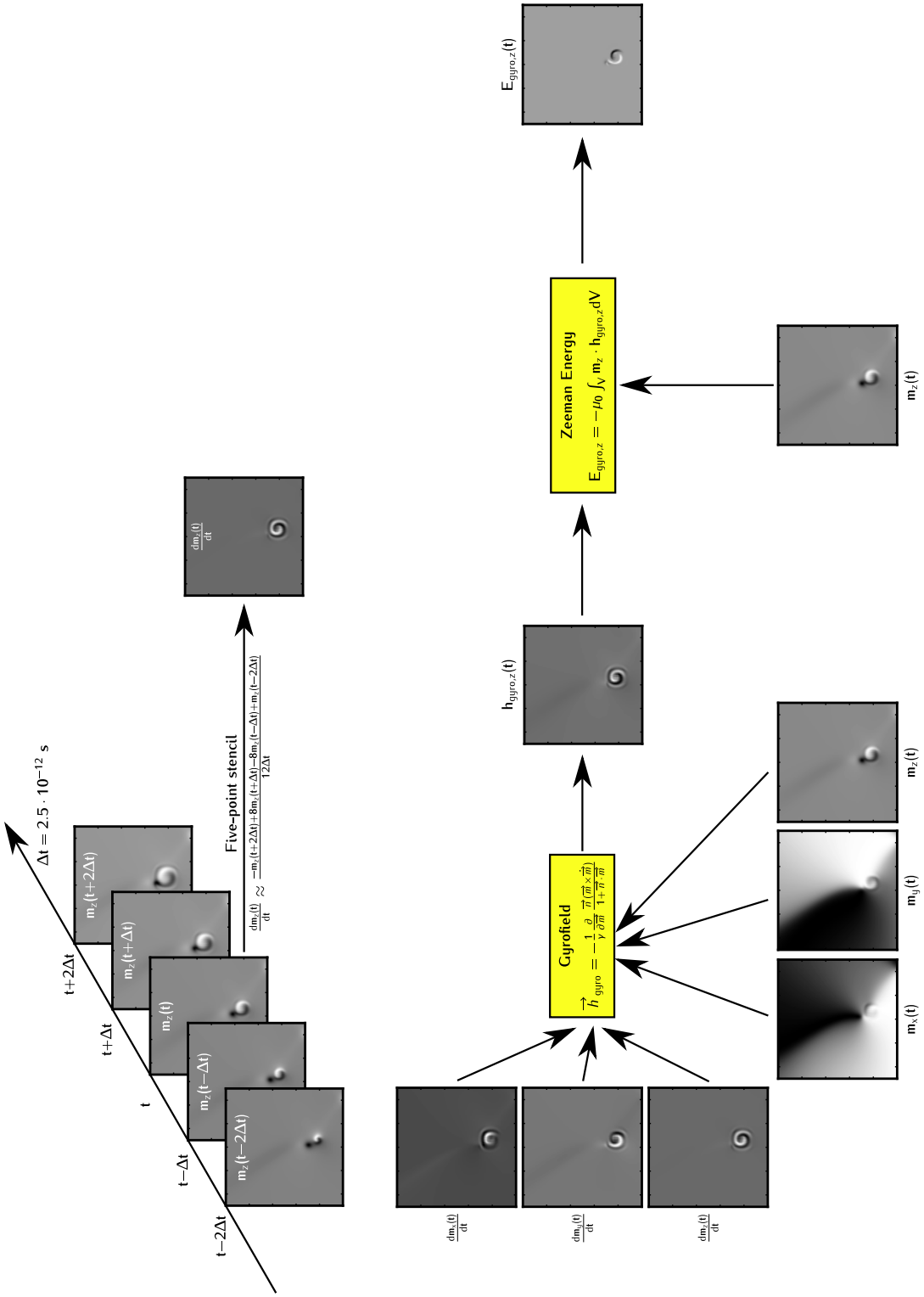

Figure 3.7. In this diagram a schematic representation is given how the time derivative of $\vec{m}(t)$ was calculated by using a five-point stencil. Based on this method, h_{gyro} and $E_{\mathrm{Zee,z}}$ were computed, respectively.

Chapter 4

Experimental Results and Simulations

In Ch. 4 the experimental and stimulational results are presented. In Sec. 4.1 the outcomes of the sample characterization are presented. They are important for checking the quality of the sample and for applying the gained material parameters as input parameters for the simulations. Carrying on to Sec. 4.2, a new chirality-dependent effect on the VDW is evidenced experimentally and explained by both, analytical calculations and micromagnetic simulations.

4.1 Sample Characterization

In this section the experimental results of the sample characterization are presented. Starting with the results of the saturation magnetization M_s found in SQUID measurements (Sec. 4.1.1) it is proceeded to the FMR characterization. Values for the gyromagnetic ratio γ_0 and Gilbert damping constant α were extracted from the experimental data obtained in full-film (Sec. 4.1.2) and TR-MOKE FMR (Sec. 4.1.3) measurements. Characterization from the point of view of DWM was done in to different ways: On the one hand, the depinning probabilities of VDWs for stripes with $w = 450$ nm and $w = 880$ nm were taken (Sec. 4.1.4). In Sec. 4.1.5 the v-H-curve for VDWs in 880-nm-wide stripes is measured, which enables the determination of the low field mobility μ_LF and the critical field $\mu_0 H_\mathrm{c}$.

4.1.1 Superconducting Quantum Interference Device Measurements: Determining the Saturation Magnetization

The magnetic layer Al/$Ni_{80}Fe_{20}$/Al deposited by thermal evaporation exhibits a saturation magnetization $\mu_0 M_\mathrm{s}$ of

$$\mu_0 M_\mathrm{s} = (0.917 \pm 0.053)\,T \qquad \pm 5.78\% \tag{4.1}$$

where the error comes mainly from the uncertainties in the volume V of the sample. For the error estimation, a uncertainty of 0.1 mm is assumed for both, the length and width of the 5×5 mm^2 GaAs piece where the $Ni_{80}Fe_{20}$ is deposited. Concerning the $Ni_{80}Fe_{20}$ layer thickness, an error of 1 nm is assumed. This obtained result is in very good agreement with literature values [38], and the value of $\mu_0 M_s = 0.92\,\mathrm{T}$ is used for the material parameter M_s in the micromagnetic simulations. The measurements have been taken by SQUID magnetometry[4] (see Sec. 3.2) measured with a piece of the full film sample produced together with the main sample.

4.1.2 Full-Film Ferromagnetic Resonance Measurements: Determining the Magnetic Damping Parameter

In order to check the quality of the magnetic layer and determine the Gilbert damping parameter α, which is needed as parameter for the micromagnetic simulations and analytical calculations, full film FMR measurements[5] are performed. Basically, three parameters can be extracted from the FMR results. The Kittel formula (in the full film geometry) contains γ_0 and M_s as free parameter, while from the slope of the linewidth in dependence of the exciting rf-field the parameter α can be extracted. However, leaving the saturation magnetization and γ_0 free, leads to inaccurate results. It is common to determine the saturation magnetization M_s by SQUID measurements and fix the parameter M_s to this value. Using the value $\mu_0 M_s = 0.917$ T found in the SQUID measurement and fitting the resonance field H_0 in dependence of the exciting rf-field, it is obtained by using Eq. (2.305)

$$\gamma_0 = (194.83 \pm 0.12) \cdot 10^9 \,\frac{1}{\mathrm{Ts}} \qquad \pm 0.06\% \tag{4.2}$$

as result for γ_0. Expressing this result in $\frac{\mathrm{GHz}}{\mathrm{T}}$ (dividing γ_0 by 2π), it results in:

$$\frac{\gamma_0}{2\pi} = (31.01 \pm 0.02)\,\frac{\mathrm{GHz}}{\mathrm{T}} \qquad \pm 0.06\% \tag{4.3}$$

It should be mentioned that the obtained small errors for γ_0 and the resulting quantities ($\frac{\gamma_0}{2\pi}$, α) are the pure mathematical errors emerging from the fitting. The real value for the error has to be set larger because from a physical point of view, the fitting function Eq. (2.304) is depending strongly on two physical quantities; those values are not exactly known. On the one hand Eq. (2.304) depends on the value of the demagnetizing factor N_y which is, in general, spatial inhomogeneous. In this work the analytic expression given in [129] is used for the estimation of the demagnetizing factors, which is an average of the value of the demagnetizing factor over the corresponding spatial direction of the stripe. Since the demagnetizing factors are functions of the spatial dimensions, the uncertainties of the values of length, width and thickness enters the calculation as well. On the other hand, other kinds of anisotropies are not included. Even

[4] I want to thank Helmut Körner for conducting the SQUID measurement.

[5] I want to thank Robert Islinger and Markus Härtinger for conducting the full-film FMR measurements.

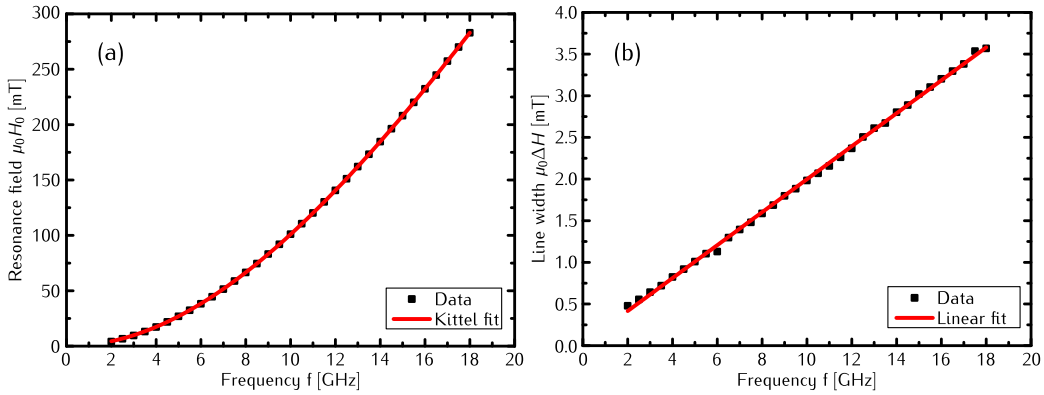

Figure 4.1. Results for the full film FMR measurement of the magnetic layers used in the DW experiments. In diagram (a) the resonance field H_0 in dependence of the exciting rf-field is plotted. From this slope the constant γ_0 can be extracted by fitting the experimental data with Eq. (2.305), the Kittel-fit. Graphic (b) displays the full width at half maximum ΔH of the fitted Lorentzian lineshape in dependence of the frequency. The linear slope yields the magnetic damping parameter α via Eq. (2.314).

a small in-plane anisotropy causes strong changes of the determined value of γ_0. For the calculation of α based on Eq. (2.314) the linear slope of the full width at half maximum ΔH in dependence of f needs to be determined. The experimental data yield a slope of

$$m = \frac{\mu_0 \Delta H}{f} = (1.98 \pm 0.01) \cdot 10^{-4} \frac{\mathrm{T}}{\mathrm{GHz}} \qquad \pm 0.51\% \tag{4.4}$$

or in Ts:

$$m = \frac{\mu_0 \Delta H}{2\pi f} = \frac{\mu_0 \Delta H}{\omega} = (0.325 \pm 0.002) \cdot 10^{-4}\,\mathrm{Ts} \qquad \pm 0.62\% \tag{4.5}$$

Using γ_0 and the linear slope m, the Gilbert damping parameter α is calculated as

$$\alpha = 0.00614 \pm 0.00003 \qquad \pm 0,49\% \qquad , \tag{4.6}$$

stating a good quality of the sample.

4.1.3 Ferromagnetic Resonance Measurements with Time-Resolved Kerr Microscopy: Determining the Magnetic Damping Parameter

To check whether the magnetic layers have changed during the structuration process or not, spatially resolved TR-MOKE measurements on different parts of the sample are performed. Determination of the material parameters γ_0 and α have been done on the ellipse part and on the stripe part of the magnetic structure on the sample where the DWM measurement is taken place. The results for the ellipse are displayed in Fig. 4.2. Since the thickness t of the magnetic layer is small compared to the lateral dimensions of the ellipse, it can

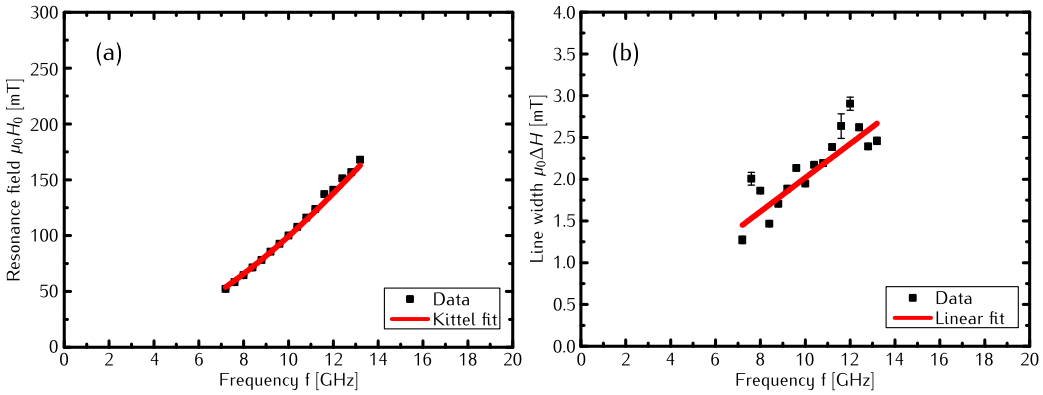

Figure 4.2. Results for TR-MOKE FMR measurement on the ellipse part of the structured sample used in the DW experiments. In diagram (a) the resonance field H_0 in dependence of the exciting rf-field is plotted. From this slope the constant γ_0 can be extracted by fitting the experimental data with Eq. (2.305), the Kittel-fit. Graphic (b) displays the full width at half maximum ΔH of the fitted Lorentzian lineshape in dependence of the frequency. The linear slope allows one to calculate the magnetic damping parameter α via Eq. (2.314).

be regarded approximately as full-film measurement (in the case no additional modes are present). Hence, Eq. (2.305) can be applied to fit the resonance field in dependence on the frequency of the exciting rf-field. As before, the value for the saturation magnetization is fixed to the value M_s to $\mu_0 M_\mathrm{s} = 0.917$ T in both cases.

For γ_0 it yields

$$\gamma_0 = (197.67 \pm 0.56) \cdot 10^9 \, \frac{1}{\mathrm{Ts}} \qquad \pm 0.28\% \tag{4.7}$$

or expressed in $\frac{\mathrm{GHz}}{\mathrm{T}}$:

$$\frac{\gamma_0}{2\pi} = (31.46 \pm 0.09) \, \frac{\mathrm{GHz}}{\mathrm{T}} \qquad \pm 0.29\% \tag{4.8}$$

The slope resulting from fitting linearly the full width at half maximum ΔH of the resonance curve yields

$$m = \frac{\mu_0 \Delta H}{f} = (2.03 \pm 0.32) \cdot 10^{-4} \, \frac{\mathrm{T}}{\mathrm{GHz}} \qquad \pm 15.76\% \tag{4.9}$$

and by performing the usual conversion to $\frac{\mathrm{GHz}}{\mathrm{T}}$ by dividing through 2π

$$m = \frac{\mu_0 \Delta H}{2\pi f} = \frac{\mu_0 \Delta H}{\omega} = (0.323 \pm 0.051) \cdot 10^{-4} \, \mathrm{Ts} \qquad \pm 15.79\% \tag{4.10}$$

is obtained. Using the results for γ_0, the slope calculates

$$\alpha = 0.0064 \pm 0.0010 \qquad \pm 15,63\% \qquad , \tag{4.11}$$

for the Gilbert damping parameter α on the ellipse part. It should be mentioned that the bigger scattering of the values for ΔH originates from the fact that in the ellipse part more modes are present in the resonance spectra. This

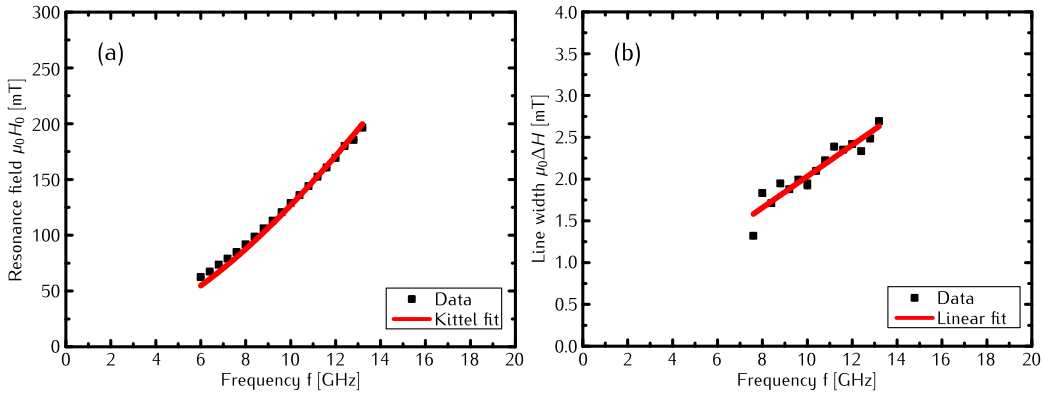

Figure 4.3. Results for TR-MOKE FMR measurement on the stripe part of the structurized sample used in the DW experiments. In diagram (a) the resonance field H_0 in dependence of the exciting rf-field is plotted. From this slope the constant γ_0 can be extracted by fitting the experimental data with Eq. (2.304), the Kittel-fit. Graphic (b) displays the full width at half maximum ΔH of the fitted Lorentzian lineshape in dependence of the frequency. The linear slope allows one to calculate the magnetic damping parameter α via Eq. (2.314).

requires a fitting with multiple Lorentzian lineshapes[6] making the results more inaccurate. This multiple peak fitting is a nontrivial task and was carried out and described, for example, in [22] to investigate differences in the determined values for the Gilbert damping parameter α found with two different measurement methods, namely TR-MOKE and DWM.

Proceeding to the TR-MOKE results taken on the stripe part of the magnetic structures, it has to be mentioned that in this case the assumption of a full film measurement is not valid any longer. Here, Eq. (2.304) has to be applied for the approximation of the experimental data for the resonance field. In order to apply this formula, the required demagnetization factors are calculated with the analytical formula given in [129]. Approximating the stripes as a rectangle with spatial dimensions of 35 μm in length (x-direction), 880 nm wide (z-direction) and 20 nm thick (z-direction), yields $N_x = 0.0009$, $N_y = 0.0331$ and $N_z = 0.9610$. As before, γ_0 and the slope m is determined and α is calculated. The results for γ_0 are

$$\gamma_0 = (187.08 \pm 0.85) \cdot 10^9 \, \frac{1}{\mathrm{Ts}} \qquad \pm 0.45\% \tag{4.12}$$

and by conversion:

$$\frac{\gamma_0}{2\pi} = (29.78 \pm 0.14) \, \frac{\mathrm{GHz}}{\mathrm{T}} \qquad \pm 0.47\% \tag{4.13}$$

The slope results by linear fitting of the experimental data in

$$m = \frac{\mu_0 \Delta H}{f} = (1.87 \pm 0.18) \cdot 10^{-4} \, \frac{\mathrm{T}}{\mathrm{GHz}} \qquad \pm 9.63\% \tag{4.14}$$

or again by converting to Ts

[6] I want to thank Hans Bauer and Martin Decker for programming and improving a program which enables the FMR data to fit with multiple Lorentzian lineshapes.

$$m = \frac{\mu_0 \Delta H}{2\pi f} = \frac{\mu_0 \Delta H}{\omega} = (0.298 \pm 0.028) \cdot 10^{-4}\,\mathrm{Ts} \qquad \pm 9.40\% \tag{4.15}$$

which leads to a value of

$$\alpha = 0.0056 \pm 0.0005 \qquad \pm 8,93\% \qquad , \tag{4.16}$$

for the Gilbert damping constant α on the stripe part of the magnetic structures. Summing up the results, equal values for the magnetic damping and slightly differing values for γ_0 are found. The scattering values for γ_0 can be addressed to the lack of data points at low excitation frequencies on the stripe and ellipse part. The value of γ_0 is mostly given by the curvature of the fitting function at low frequencies.

4.1.4 Depinning Probabilities in the Relevant Field Range and the Depinning Field

For the characterization of the fabricated stripes where the DWM measurements are performed, the pinning probabilities are measured in dependence of the external field $\mu_0 H$ on stripes with width $w = 450$ nm and $w = 880$ nm. This is important to estimate the effect and influence of the pinning field, which can have hindering effects on DWM. The experimental results are shown in Fig. 4.4. Assuming the underlying pinning field H_P to be normal distributed, the data of the depinning probability P_depin is approximated with the cumulative distribution function [130]

$$P_\mathrm{depin} = 0.5A\,(1 + \mathrm{erf}(H)) \tag{4.17}$$

where $\mathrm{erf}(H)$ is the error-function

$$\mathrm{erf}(H) = \frac{2}{\sqrt{\pi}} \int_{H'=0}^{H} \mathrm{e}^{-\tau^2} \mathrm{d}\tau \tag{4.18}$$

containing the parameter $\tau = \frac{1}{\sqrt{2}\sigma_\mathrm{P}}(H' - H_\mathrm{P})$ [40, 130]. Here, H_P is the average value of the pinning field and σ_P its full width at half maximum which is equal to the error of the parameter H_P. For the errors of the experimental data the calculated uncertainties of the external field (see Sec. A4) are used and an error of $\pm 2\%$ in P_depin is assumed. Fitting the data with fixed parameter $A = 100$, one yields for stripes with $w = 450$ nm

$$\begin{aligned} \mu_0 H_\mathrm{P} &= (1.52 \pm 0.08)\,\mathrm{mT} \qquad (\pm 5.26\%) \\ \mu_0 \sigma_\mathrm{P} &= (0.32 \pm 0.05)\,\mathrm{mT} \qquad (\pm 15.63\%) \end{aligned} \tag{4.19}$$

and for $w = 880$ nm

$$\begin{aligned} \mu_0 H_\mathrm{P} &= (0.91 \pm 0.05)\,\mathrm{mT} \qquad (\pm 5.50\%) \\ \mu_0 \sigma_\mathrm{P} &= (0.17 \pm 0.01)\,\mathrm{mT} \qquad (\pm 5.88\%) \end{aligned} \tag{4.20}$$

as result. Considering the depinning probabilities P_depin with respect to the

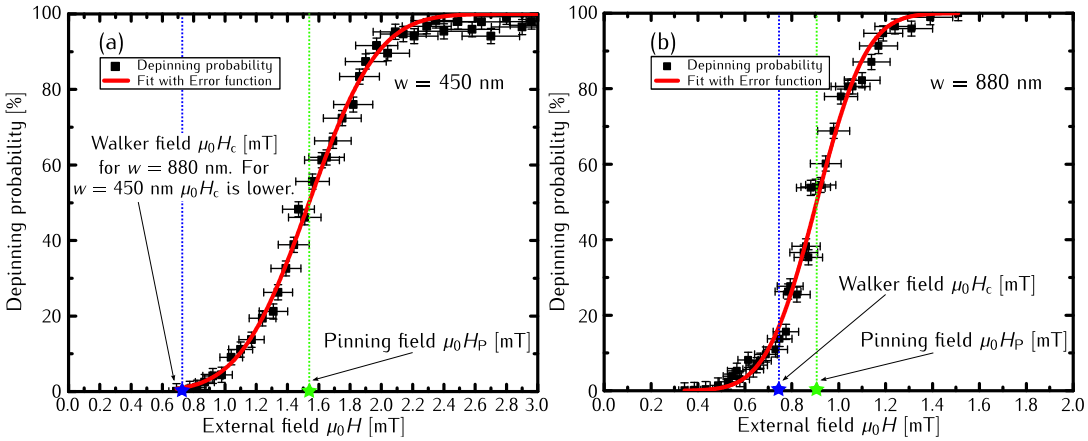

Figure 4.4. Depinning probability for DW in stripes with width $w = 450$ nm (a) and $w = 880$ nm (b). The dashed green line marks the average value of the corresponding pinning field H_P. In diagram (b) the dashed blue line indicates the critical field H_c where the Walker breakdown occurs. The critical field H_c is below the value of $H_c = (0.74 \pm 0.07)$ mT for stripes with $w = 880$ nm. Based on the knowledge that the critical field for stripes with $w = 450$ nm is smaller and comparing it with the corresponding depinning probabilities at small stripes indicates that measurements in the linear regime are not possible. As a result, the exact value for the Walker field on small stripes cannot be measured.

critical field H_c (see Sec. 4.1.5), it is found for $w = 880$ nm that below H_c in the linear mobility regime the depinning probabilities P_{depin} are smaller than 20%. This is sufficient enough for measuring the DWM in the linear regime, but indicates that the pinning potential has an influence on the overall motion of the DW. As proven, for example, by experimental [22] and numerical studies [120], pinning and disorder can lead to an enhanced effective damping α_{eff} for DWM. In contradiction to this, $\mu_0 H = 1.0$ mT at external fields obtain a value below 5% for P_{depin} for stripes with $w = 450$ nm. For narrower stripes the critical field decreases, which indicates that H_c is below 7.4 mT, and measurements of the linear motion on stripes with $w = 450$ nm is not possible on this sample. The decreasing of the critical field H_c at smaller strip width w can be understood by considering the analytic expression for H_c (see Eq. (2.243)) and by inserting the explicit expressions for all parameters. Furthermore, the obtained results allow one to rule out the effects of pinning for the main measurements done in this thesis. The main experimental results (see Fig. 4.8) were obtained in the external fields of $\mu_0 H = 1.5$ mT. In this field strength the VDWs in stripes with $w = 880$ nm are fully depinned and can move freely along the stripe. Moving freely means that at field values of $\mu_0 H = 1.5$ mT the underlying energetic landscape seen by the VDW and caused by grains or defects can be neglected, and the motion of the VDWs is expected to be uniformly.

4.1.5 Low-Field Mobility and the Walker Field

The second characterization of the fabricated stripes concerns the low-field mobility μ_{LF} as well as the value of the critical field H_c. Two goals are pursued by this characterization. On one hand, the low field mobility μ_{LF} will be used as input parameter for the analytical model, and on the other hand, quality of

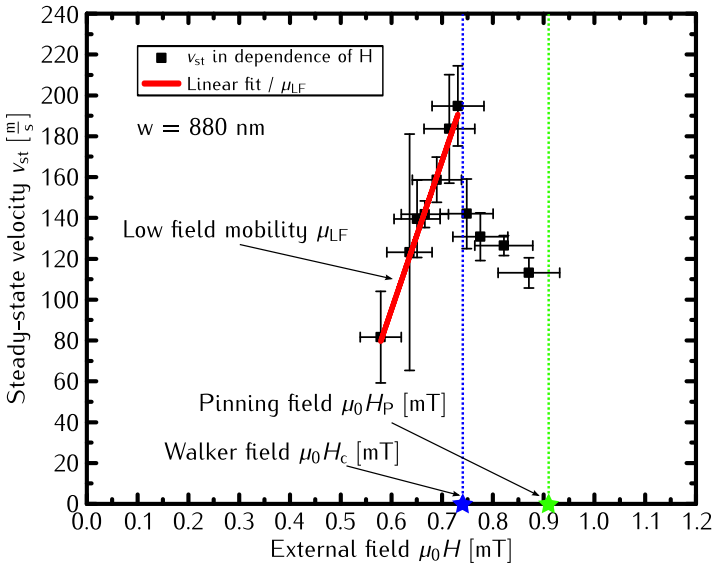

Figure 4.5. DW velocity for stripes with width $w = 880$ nm in the linear regime (steady-state motion) and above the critical field H_c. The bold line represents the linear fit in the steady-state regime, and its slope is identical with the low field DW mobility μ_{LF}. The blue and green dashed lines mark the critical field H_c and the average value of the pinning field H_P, respectively. As mentioned in Sec. 4.1.4, the linear regime is below the average value of the pinning field. This indicates that when fields are below the critical field, the DWM is hindered by the pinning due to grains and impurities.

the sample will be checked by comparing the results to other experimental and theoretical works. For this aim the displacements in dependence of the pulse time for a fixed external field is measured and fitted linearly. Doing this for different fields, it yields the DW velocity. As result the Walker field H_c is found to be

$$\mu_0 H_c = (0.74 \pm 0.07)\,\mathrm{mT} \qquad (\pm 9.46\%) \tag{4.21}$$

while fitting the velocity in below H_c linearly, the value

$$\mu_{LF} = (730.7 \pm 43.3) \cdot 10^3 \,\frac{\mathrm{m}}{\mathrm{Ts}} \qquad (\pm 5.93\%) \tag{4.22}$$

for the low field mobility μ_{LF} is obtained. Knowing both quantities is important due to the following reasons: H_c marks the border where the linear motion breaks down and an oscillatory motion of the VC sets in. Above the Walker field, it is expected to observe chirality-dependent effects. The value of the low field mobility is used to express Γ_{XX} solely by experimentally accessible quantities ($\Gamma_{XX} = Q\mu_{LF} = 2\mu_0 wtM_s\mu_{LF}$), as mentioned above. This allows one to use as much as possible experimental data as a parameter in the analytical model. The linear fit of the DW velocity in the linear regime yields the intersection with the y-axis (or V-axis, respectively) additionally:

$$V_0 = (-343.5 \pm 29.1)\,\frac{\mathrm{m}}{\mathrm{s}} \qquad (\pm 8.47\%) \tag{4.23}$$

Overall, the values found for the critical field H_c, the critical velocity V_c as

well as the low field mobility μ_{LF} are in good agreement with other results found in experimental [17, 22, 80] as well as in theoretical [45] works.

4.2 Chirality-Dependent Vortex Domain Wall Dynamics and the Double Reversal Process

In this section a chirality-dependent effect occurring for VDWs in fields above $\mu_0 H_{\mathrm{c}}$ is evidenced and elucidated. Starting in Sec. 4.2.1 with the introduction to the topic, it will be proceeded to an analytical approach of the problem (Sec. 4.2.2). Furthermore, it is tackled additionally by micromagnetic simulations (Sec. 4.2.3). Experimental evidence for this effect is given in the subsequent Sec. 4.2.4. It is found that the chirality-dependent effect is associated with a fast double reversal process (DRP) of the VC polarity p occurring for one specific chirality. This DRP is approached by different ways, descriptive (Sec. 4.2.5), as well as from the point of view of trace, energy and potential (Sec. 4.2.6 and 4.2.7). Effects of the spin wave package (SWP) originating from the V/AV annihilation are considered in Sec. 4.2.8. Investigations of the DRP in the frame of Zeeman energy originating from the gyrofield (Sec. 4.2.9) are leading to an effective potential for the VC and dip region (Sec. 4.2.10). In a last step the effects of the HAVs on the DRP are considered in Sec. 4.2.11 and the chapter is closed by the conclusion in Sec. 4.2.12.

4.2.1 Introduction

Magnetic vorticies are well-defined magnetization distributions which consist of an in-plane structure curling around an out-of-plane center named vortex core (VC) [74]. These objects have been extensively studied and play a major role in the dynamics of two kinds of magnetic prototypes: magnetic elements in the flux-closed state and magnetic racetracks with vortex domain walls (VDW); both are envisioned as promising alternatives for information technologies. One of predominant aspects of VC dynamics is its polarity reversal which has been mostly investigated in magnetic elements in the flux closed state and has been found related to a critical VC velocity [131–133]. On the other hand, in magnetic racetracks, magnetic VDWs are characterized by the magnetic global charge (head-to-head or tail-to-tail) and a set of magnetic substructures among which a vortex core has a center position (Fig. 2.4). A noticeable feature of their dynamics is the definition of the Walker breakdown (WB). The WB is connected to a critical field H_{c} (Walker field) beyond which the wall continuously changes configuration due to inability of the system to counteract the driving force (Fig. 4.9(a) and Fig. 4.5). In the case of VDWs, this constant transformation is mostly operated by nucleation and transversal displacements of the VC [85, 134]. Two scenarios are actually possible, either the initial VC collides with the edge of the nanotrack before reaching its critical velocity or, on the other hand, the VC can reach the critical velocity before being annihilated at the edges for strong driving force or wide enough stripes. In the latter case, the reversal process is similar to the one of a VC core in the magnetic vortex ground state of a disk or square, namely the creation of vortex-antivortex pair (V/AV-pair) as soon as the dynamic dip

reaches a polarity opposite to the original VC [131] (see Sec. 2.3.1). This happens at a critical velocity which is about 300 m/s for $Ni_{80}Fe_{20}$ [135]. In this section it will be evidenced that VC reversal can depend on the chirality of the VDW which leads to substantial differences in displacements just above the WB. One outcome of this study is the possibility to determine the chirality of a VDW by analyzing its total displacement. A similar result has been found in a recent study [136], where Y-shaped racetracks where utilized to sort VDWs by their chirality.

4.2.2 Chirality Dependent Vortex Domain Wall Dynamics: An Analytical Approach

Regarding a sole VC in a flux closed state, its dynamics in the approximation of the steady motion is perfectly modeled by Thiele's analytical approach [34]. Within this approach the magnetization configuration of the VC is described only by two spatial coordinates representing the position of the VC (X,Y) and two integers: the polarity p and circulation c. Furthermore, it has also been theoretically demonstrated that the dynamics of a VDW can be fairly well reproduced by this collective coordinates approach [45, 47]. In this model, it has been noticed that due to the missing mirror symmetry in a stripe with a VDW state, the motion of a VDW depends on its chirality $\chi = c \cdot p$. This behavior has also been reported in micromagnetic simulations for DW motion above the WB [123]. In this case the VC collides with the edge of the stripe and reverses its polarity which is equivalent to a monotone precession of the generalized wall angle [137]. The velocity with which it collides depends on the chirality [45]. In the following, the concept of a VC reaching the critical velocity V_c and the collective coordinate approach (CCA) for DW motion are combined. The equation of motion for the position of the VC is [34, 70]:

$$F_i - \Gamma_{ij}\dot{\xi}_j + pG\epsilon_{ij}\dot{\xi}_j = 0 \tag{4.24}$$

where F_i represents restoring and driving forces; the symmetric matrix Γ_{ij} describes viscous friction and G is the prefactor for the 2×2 antisymmetric tensor ϵ_{ij}. $\xi = (X, Y)$ are the coordinates of the VC. When considering only forces constant in time, the forces F_i without disorder are invariant under translations along the direction of the stripe axis X. It arises directly from the equation of motion for X and Y given in Ref. [45] that the VC velocity $V = \sqrt{\dot{X}_1^2 + \dot{Y}_2^2}$ is no longer a function of X, and it is directly linked to the transverse displacement Y, i.e. $V = V(Y)$. Assuming that the critical field H_c and the critical velocity V_c is the same for both chiralities, a critical transverse displacement Y_{crit} that is different for the two chiralities is found (see Eq. (2.244)).

$$Y_{crit} = (cg - p)\frac{GV_c}{k} \tag{4.25}$$

This formula was derived in detail in Sec. 2.3.3.2. Here, g is a small correction factor, and k characterizes the restoring force acting on the VC (see Sec. 2.3.2.4 and 2.3.2.5).

In Fig. 4.6 the different behavior for both chiralities concerning the critical transverse displacement Y_{crit} with respect to w, the external field magnitude

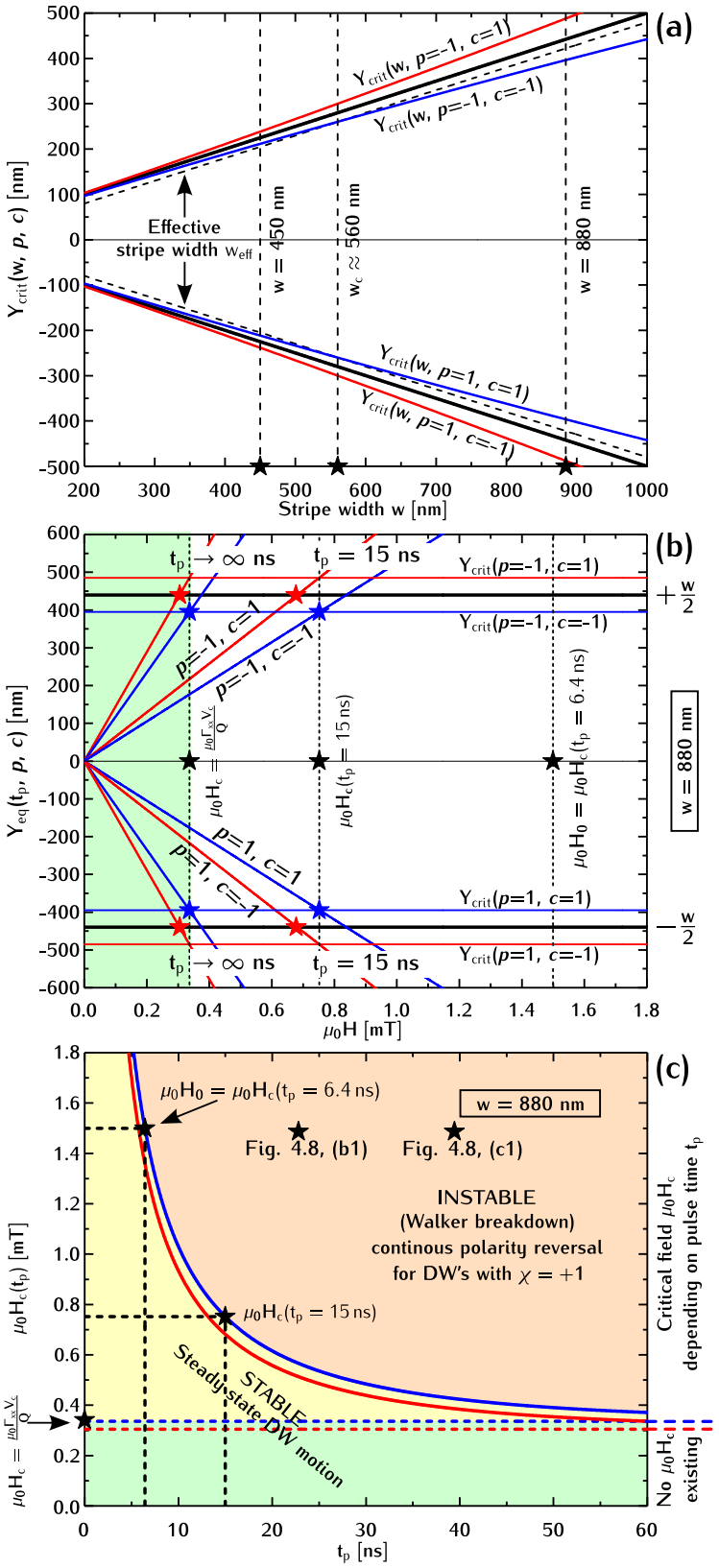

Figure 4.6. All three diagrams displayed in this figure are calculated on the basis of the model presented in Ref. [45]. (a) The critical transverse DW displacement $Y_{\mathrm{crit}}(w, p, c)$ is plotted for different stripe widths w for all four possible configurations of a VDW. (b) In the case of a 880 nm wide stripe $Y_{\mathrm{eq}}(t_{\mathrm{p}}, p, c)$ ($t_{\mathrm{p}} \to \infty$ ns and t_{p} =15 ns) in dependence of the external field $\mu_0 H$ is computed. (c) Phase diagram that shows the type of DW motion that occurs for different combination of pulse time t_{p} and applied field $\mu_0 H$.

H and pulse time t_p is shown. Fig. 4.6(a) displays the critical transverse DW displacement $Y_\mathrm{crit}(w, p, c)$ for w in the range between 200 nm and 1000 nm for all four possible configurations of a VDW (blue indicates chirality $\chi = 1$, red $\chi = -1$). The bold black lines indicate the upper and lower edges of the stripe, while the dashed black line shows the effective stripe width w_eff due to the small but finite size of the VC and the half antivortex (HAV) (VC radius $r_\mathrm{core} \approx$ 10 nm). Basically, the critical deflection out of the equilibrium position lies outside of the stripe for VDWs with $\chi = -1$ and inside for $\chi = 1$ for all w. This indicates that VDWs with $\chi = 1$ always reverse the polarity of their VC freely within the stripe independent of w. However, it is known that in narrow stripes all chiralities undergo a classical WB due to the collision of the VC with the HAV at one side of the stripe. To include this into the model, the mentioned effective stripe width $w_\mathrm{eff} = w - 4r_\mathrm{core}$ (minus $2r_\mathrm{core}$ at each edge) is introduced. Such kind of effective stripe width w_eff was used in [45] as well. Exceeding w_eff is enough to lead to a classic WB by colliding with the edge of the stripe. In addition, w_eff is setting a critical width w_c. For widths larger than $w_\mathrm{c} \approx 560$ nm, VDWs with chirality $\chi = 1$ reach the critical velocity V_c and Y_crit, respectively, before colliding with the HAV at the edge of the stripe. In Fig. 4.6(b) $Y_\mathrm{eq}(t_\mathrm{p}, p, c)$ (see Eq. (2.244)-(2.247)) is shown for two different pulse times ($t_\mathrm{p} \to \infty$ ns and t_p =15 ns) in dependence of $\mu_0 H$ for a 880 nm wide stripe. The horizontal black lines in the diagram mark again the upper and lower edge of the stripe and the critical transverse displacements $Y_\mathrm{crit}(p, c)$ which are necessary to reach the critical velocity V_c. Again, blue and red lines indicate combinations of the polarity p and circulation c which result in chirality $\chi = 1$ and $\chi = -1$, respectively. Additionally, the transverse equilibrium position in dependence of $\mu_0 H$ is plotted for all four possible configurations of the VDW for two different pulse times t_p. The intersection points (red and blue stars) between $Y_\mathrm{crit}(p, c)$ and $Y_\mathrm{eq}(t_\mathrm{p}, p, c)$ yield the critical field $\mu_0 H_\mathrm{c}(t_\mathrm{p})$ (dashed vertical line and black stars) which has to be applied for a certain pulse time to reach V_c. From the model it results that the critical fields are equal for both chiralities. A remarkable difference in $\mu_0 H_\mathrm{c}(t_\mathrm{p})$ for both chiralities results from the fact that VDWs with $\chi = -1$ are not able to leave the stripe and reach $Y_\mathrm{crit}(p, c)$. While VDWs with $\chi = 1$ always reach the critical transverse displacement which lies within the stripe; $Y_\mathrm{crit}(p, c)$ is restricted by the edge of the stripe at $\pm w/2$. This results in different critical fields for both chiralities. The difference between both critical fields increases with decreasing pulse time. From Fig. 4.6(b) it becomes clear that the critical field $\mu_0 H_\mathrm{c}$ which is necessary to reach $Y_\mathrm{crit}(p, c, t_\mathrm{p})$ depends strongly on the pulse time t_p and, in addition, on the chirality. Based on this result it is already possible to assume that different critical fields should lead to slightly different DW displacements in wide stripes ($w > w_\mathrm{c}$) when a magnetic field is applied which exceeds the critical field for a certain pulse time. To clarify the time dependence of $\mu_0 H_\mathrm{c}$ for the two chiralties, a phase diagram is shown in Fig. 4.6(c) to depict the type of DW motion which occurs for different combination of pulse time t_p and $\mu_0 H$ in a 880 nm wide stripe. Green and yellow areas mark the regions of steady-state DW motion. In the yellow ones steady-state motion only occurs for a certain pulse time below a critical field $\mu_0 H_\mathrm{c}(t_\mathrm{p})$ indicated by the blue and red line for chirality $\chi = 1$ and $\chi = -1$, respectively. In the orange area Y_crit is reached and the WB and the associated

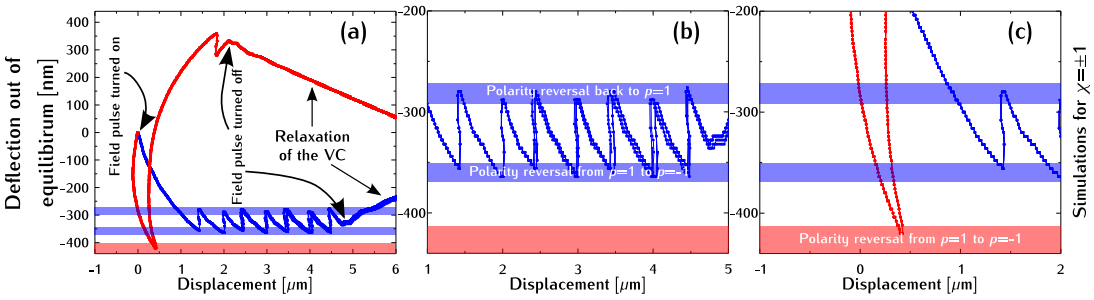

Figure 4.7. (a) Trajectories for VDWs with $\chi = 1$ (blue) and $\chi = -1$ (red) under the action of an applied field with magnitude $\mu_0 H = 15$ mT and pulse time $t_\mathrm{p} = 20$ ns. (b) Trajectories for VDWs with $\chi = 1$ (blue) in detail. (c) Trajectories for VDWs with $\chi = 1$ (red).

polarity reversals of the VC occur. All three charts show that there is a significant difference of the VDW dynamics between VDWs with chirality $\chi = 1$ and $\chi = -1$ concerning critical transverse displacement, equilibrium position, critical fields and pulse time that arises for widths larger than w_c. The same behavior for both chiralities is expected on stripes more narrow than this critical width. So far it has been found from the analytical model that different critical transverse displacements for both chiralities hold. This implies that two different polarity reversal mechanisms are involved for VDWs with $\chi = 1$ and $\chi = -1$. While VDWs with $\chi = 1$ reverse their polarity freely in wide stripes, VC of VDWs with $\chi = -1$ always collide with one HAV and get re-injected into the stripe with opposite polarity. These two different realizations of polarity reversal in wide stripes causing different behavior of the VC dynamics on a microscopic scale as for example the build up of the dip region and the creation of a vortex- anti-vortex pair which is involved in a free polarity reversal for VDWs with $\chi = 1$. These effects are not included in this simple model. In the following, micromagnetic simulations are used to investigate the influence of these effects on the VDW dynamics.

4.2.3 Chirality Dependent Vortex Domain Wall Dynamics: Micromagnetic Simulations

Mumax3 [67] is used to simulate $Ni_{80}Fe_{20}$ stripes of 20 nm thickness with 450 nm and 880 nm width under the action of a field pulse that exceeds the WB field. The material parameters used to model $Ni_{80}Fe_{20}$ are: Saturation magnetization $M_\mathrm{s} = 7.3 \cdot 10^5$ A/m with a spatial random variation of 5% to model disorder, Gilbert damping parameter $\alpha = 0.006$, exchange stiffness constant $A_\mathrm{ex} = 1.3 \cdot 10^{-11}$ J/m and the stripe width was divided into 220 cells. To include disorder, due to grains, Voronoi tessellation already implemented in mumax3 is used. The grain size is chosen to be 20 nm and M_s is varied by ±10% to mimic different heights. For a realistic simulation A_ex is reduced by 10% at the grain boundaries in order to decouple single grains from each other slightly. Two important facts, which result from the measurement technique (see Sec. 3.5), have to be taken into account in the simulations to enable a better comparison to the experimental data. First, there is a limitation to measure only effective displacements due to

the applied field pulse and the subsequent relaxation of the VC after the end of the field pulse. Thus, a sufficiently long relaxation time t_r has to be included into the simulations to enable the VC to relax to its equilibrium position in the middle of the stripe. Second, the measurements are based on statistics. To gain statistics for a certain combination of H and t_p, every simulation is repeated ten times for all 4 VDW configurations ($p = \pm 1$, $c = \pm 1$). If grains are included, a different seed for the Voronoi tessellation is set for each new run. Simulations without disorder corroborate the expected behavior: a classic WB for both chiralities in narrow (w=450 nm) stripes (Fig. 4.8(a2,a3)). In wide stripes (w= 880 nm) a VC polarity reversal appears, due to a classic WB, at the edge of the stripe for VDWs with $\chi = -1$ (Fig. 4.7 and Fig. 4.8(b3,c3)), and a free reversal process accompanied by spin wave (SW) emission for DWs with $\chi = 1$ (Fig. 4.7 and Fig. 4.8(b2,c2)) occur. In addition, the simulations show a new and unexpected feature in the dynamics of the polarity reversal for VDWs with $\chi = 1$ in wide stripes that was observed in other micromagnetic simulations as well, for instance, in Ref. [138] and closely investigated in Ref. [139]. After the first and expected polarity reversal, the VDW changes its chirality from $\chi = 1$ to $\chi = -1$ and starts moving backwards due to the changed sign of the gyrotropic force (Fig. 4.7(a,b)). Shortly after this polarity reversal, the DW switches its polarity again and changes the chirality back to $\chi = 1$. This second and unexpected reversal process is accompanied by SW emission as well, and the DW starts again to move to the edge of the stripe until the DW reaches the critical transverse displacement and a new double reversal process occurs (Fig. 4.7). In the following it will be referred to it as fast double reversal process (DRP). From simulations it was determined that the time between these two fast polarity reversals is shorter than 0.2 ns. VDWs with $\chi = 1$ exhibit an oscillatory motion near the edge of the stripe and, thus, maintain a higher average velocity in X-direction than DWs with $\chi = -1$ that undergo a classic WB. As a consequence, two different displacements for DWs with different chirality have to be expected. Only the emission of SWs causes a small deviation in the displacements for VDWs with $\chi = 1$ and two sharp different displacement distributions Fig. 4.7(b) should be detectable. Including disorder as explained above, it yields basically the same behavior as before, but the deviations between the different traces and displacements become much larger than before (Fig. 4.8(a2-c3)). In addition, there is a certain probability with every fast double reversal for the oscillating VC to be kicked out of the fast periodic polarity reversal. Repeated simulations for the same chirality $\chi = 1$ with different grains show that it depends on the seed chosen for a specific run of the simulations, whether the second polarity reversal appears or not. In other words, local disorder due to grains at the position where the second reversal would occur can prevent the VC from switching back from $\chi = -1$ to $\chi = 1$, so it can be denoted as a grain induced effect. This means that, in this case, the VC with initial chirality $\chi = 1$ does not switch back and stays in the $\chi = -1$ configuration. The VC moves backwards, crosses the equilibrium position in the middle of the stripe, and moves towards the opposite side (Fig. 4.8(b2,c2,c3)). In contrast to the prediction derived from the simple model where only one path for each chirality is possible, due to the grain induced effect, VDWs with chirality $\chi = 1$ which undergo n possibly fast polarity reversals for a certain combination of H and t_p can move on $n + 1$ paths. This has a

significant influence on the displacement distribution. At a driving field of $\mu_0 H = 1.5$ mT and pulse time $t_p = 28.8$ ns, vortices with $\chi = -1$ and those with $\chi = 1$, which are kicked out from the oscillations, form one peak at low displacements, while vortices with $\chi = 1$, which continue the oscillations till the field pulse is turned off, result in a second peak at higher displacements (Fig. 4.8(b2,b3)). The situation changes for longer pulse durations. Applying a field pulse $\mu_0 H = 1.5$ mT with $t_p = 39.4$ ns changes the situation concerning VDWs with $\chi = -1$ (Fig. 4.8(c1,c2,c3)). While VDWs with $\chi = 1$ oscillate close to the edge of the stripe and can be kicked out of the oscillations as described before (Fig. 4.8(c2)), t_p is now long enough that VDWs with initial $\chi = -1$ can also get into the oscillating state (Fig. 4.8(c3)). The longer pulse length allows the VDWs with $\chi = -1$ to switch to $\chi = 1$ crossing the stripe while moving backwards and start to oscillate at the opposite edge. Those DWs which are kicked out during the first reversals form now a peak at low displacements, while those which stay in the oscillations (or kicked out during one of the later reversals) till the field pulse is turned off result in a peak at higher displacement. DWs with initial $\chi = 1$ form a broad peak in the histogram between the previously described ones (Fig. 4.6(c2,c3)).

4.2.4 Chirality Dependent Vortex Domain Wall Dynamics: Experimental Data

In order to verify this effect experimentally, the relative displacement of VDWs driven by field pulses of varying duration t_p in the nanosecond range and varying magnitude on narrow (w=450 nm) and wide (w=880 nm) stripes are measured. The pulse time t_p is the same as chosen in the simulations. It has to be mentioned that the rise and fall times for the voltage pulses provided by the pulse generator are smaller than 0.5 ns. This is negligible compared to t_p and so it can regarded as a rectangular voltage pulse. This relative displacement caused by the applied field pulse which corresponds to the shift of the VC itself is detected by wide-field magneto-optical Kerr microscopy (wide-field MOKE). The histograms obtained in the measurements are shown in Fig. 4.8(a1-c1). While Fig. 4.8(a1) exhibits only a clear single Gaussian distribution for the displacements along the stripe, Fig. 4.8(b1) and Fig. 4.8(c1) taken on 880 nm wide stripes show two and three distributions, respectively. For a comparison between experiment and simulations, the average displacement of the simulated displacements are plotted as stars above the histograms in Fig. 4.8(a1-c1). In Fig. 4.8(a1) the black star is the average of both chiralities, while the red and blue stars in Fig. 4.8(b1) are the average displacement of both chiralities. It is possible that one should take in Fig. 4.8(b2) the average displacement of these DWs with $\chi = 1$ which are kicked out of the oscillations and the ones which stay in the oscillatory behavior till the end of the field pulse separately. In this case the average displacement of VDWs with $\chi = -1$ Fig. 4.8(b3) and these with $\chi = 1$ Fig. 4.8(b2) lie close together and form the higher peak in Fig. 4.8(b1) at lower displacements. In Fig. 4.8(c1) the blue star is the average over VDWs with $\chi = 1$ Fig. 4.8(c2), and the two red stars are the average over those with $\chi = -1$ which are kicked out of the oscillation and the ones which stay in this behavior till the end of the applied field separately. Due to a almost-twice-as-long pulse time t_p as in Fig. 4.8(b1),

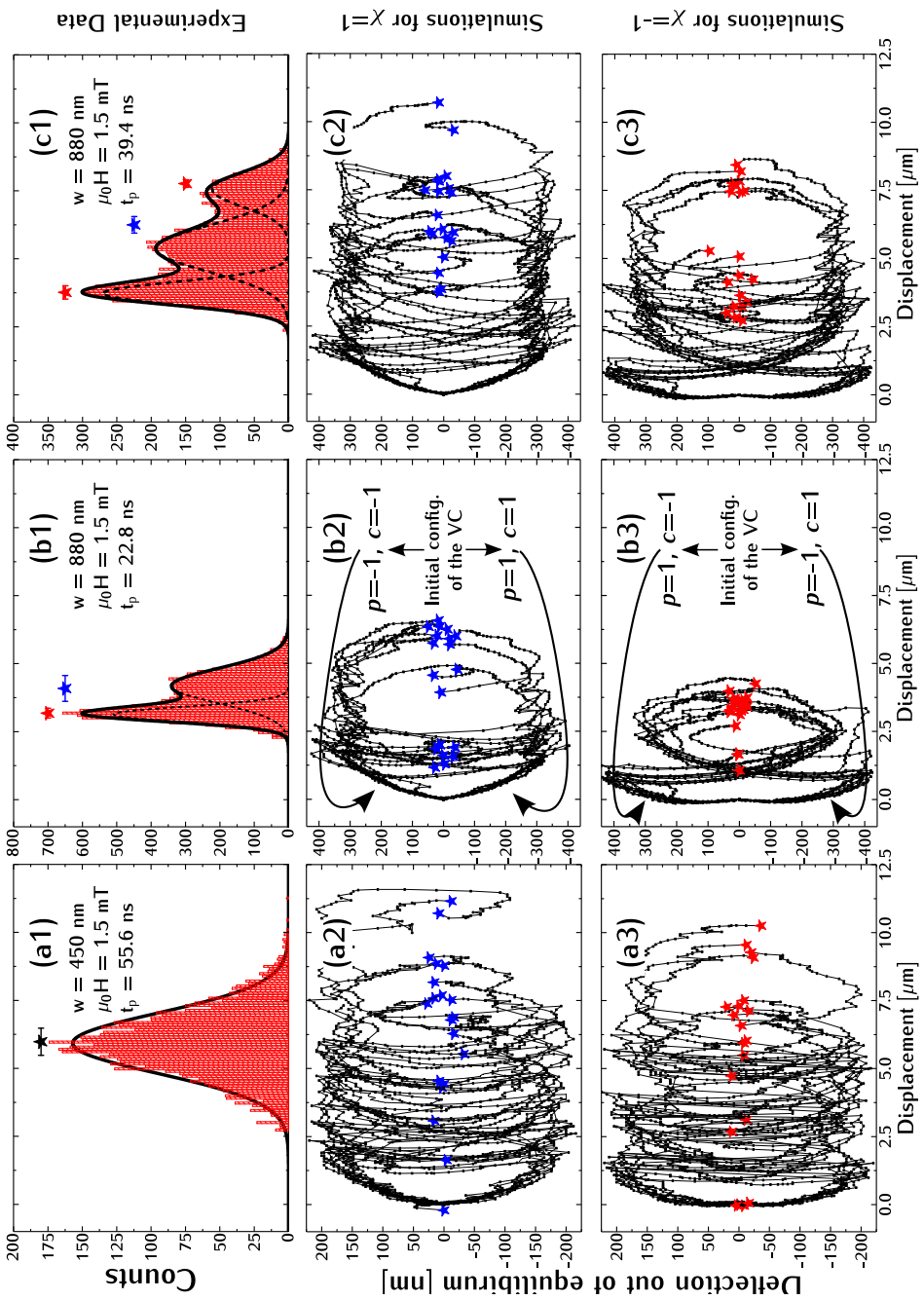

Figure 4.8. (a1-c1) Histograms of displacement measurements taken on narrow and wide stripes at $\mu_0 H = 15$ mT and different t_p. While (a1) shows only a clear single Gaussian distribution for the displacements along the stripe, (b1) and (c1) taken on 880 nm wide stripes show two and three distributions, respectively. (a2-c2) and (a3-c3) display the trajectories of VDWs with $\chi = 1$ (blue) and $\chi = -1$ (red) respectively under the action of an applied external magnetic field. The trajectories have been extracted from the micromagnetic simulations where the field magnitude and the pulse times were the same as in (a1-c1).

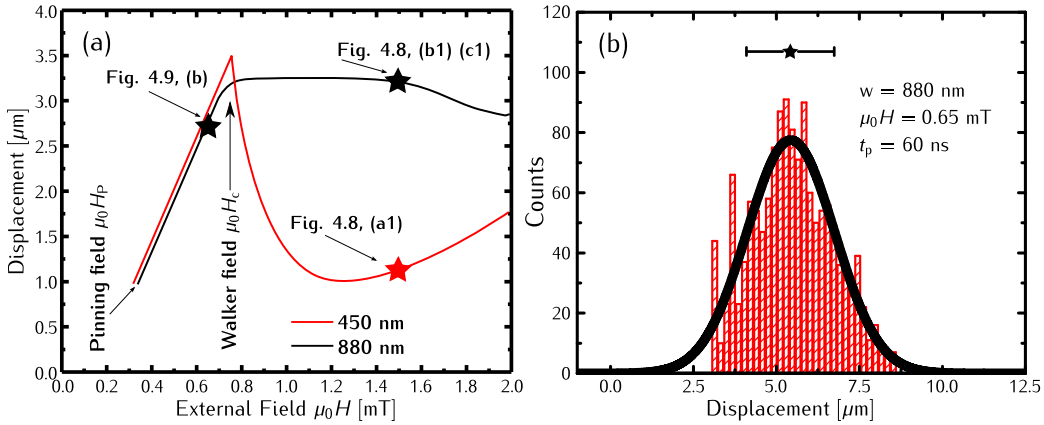

Figure 4.9. (a) Sketch of the DW displacement in dependence of the applied external field. The red curves displays the behavior for narrow stripes (w = 450 nm), while the black one depicts broad stripes (w = 880 nm). The stars mark the obtained histograms plotted in Fig. 4.8 and Fig. 4.9. (b) Histogram obtained on broad stripes (w = 880 nm) at $\mu_0 H = 0.65$ mT and pulse time $t_p = 60$ ns. The displacement show one single distribution indicating the same behavior for both chiralities at fields below H_c on broad stripes.

the peaks formed by the lower displacements in Fig. 4.8(c3) and those at higher displacements can be clearly separated. Furthermore, it has to be emphasized that the measurements were carried out on different stripes with the same width. In order to check that these multiple peaks are not there due to differences in the magnetic properties of the stripes, a look was taken at histograms obtained on every single stripe separately. Each histogram shows the same multiple peak structure as shown in Fig. 4.8(a1-c1).

4.2.5 Double Reversal Process: A Descriptive Approach

In order to understand the oscillatory behavior of the VDWs with chirality $\chi = 1$, a close look was taken at the reversal process (RP) in detail. For this aim micromagnetic simulations were performed with the same material parameters mentioned above but without grains. The initial VDW configuration was set to $p = 1$ and $c = 1$. The time steps where the magnetization is evaluated is chosen to be $\Delta t = 2.5 \cdot 10^{-12}$ s. These very short time steps are necessary to capture the magnetization dynamics during the RP from polarity $p = 1$ to $p = -1$ and back again which happens on the nanosecond time scale. In Fig. 4.10 snapshots for the z-component of the magnetization (m_z) are plotted at key moments for the double reversal process (DRP) of the VC core. The pictures show a close up of the region around the VC with an edge length of 400 nm each, wherein the lower one of each snapshot is equal to the lower stripe edge. Here a gray scale was used to represent the orientation of m_z. Black indicates areas where m_z is negative (pointing into the plane) and white ones where m_z is positive (pointing out of the plane). The starting point of each fast DR is shown in Fig. 4.10(a). It is equal to the one of a RP for VCs in a nanodiscs where the reversal and the WB is caused by the deformation of the VC due to the gyrofield [21]. Being deflected out of equilibrium in the middle of the stripe, the VC increases its

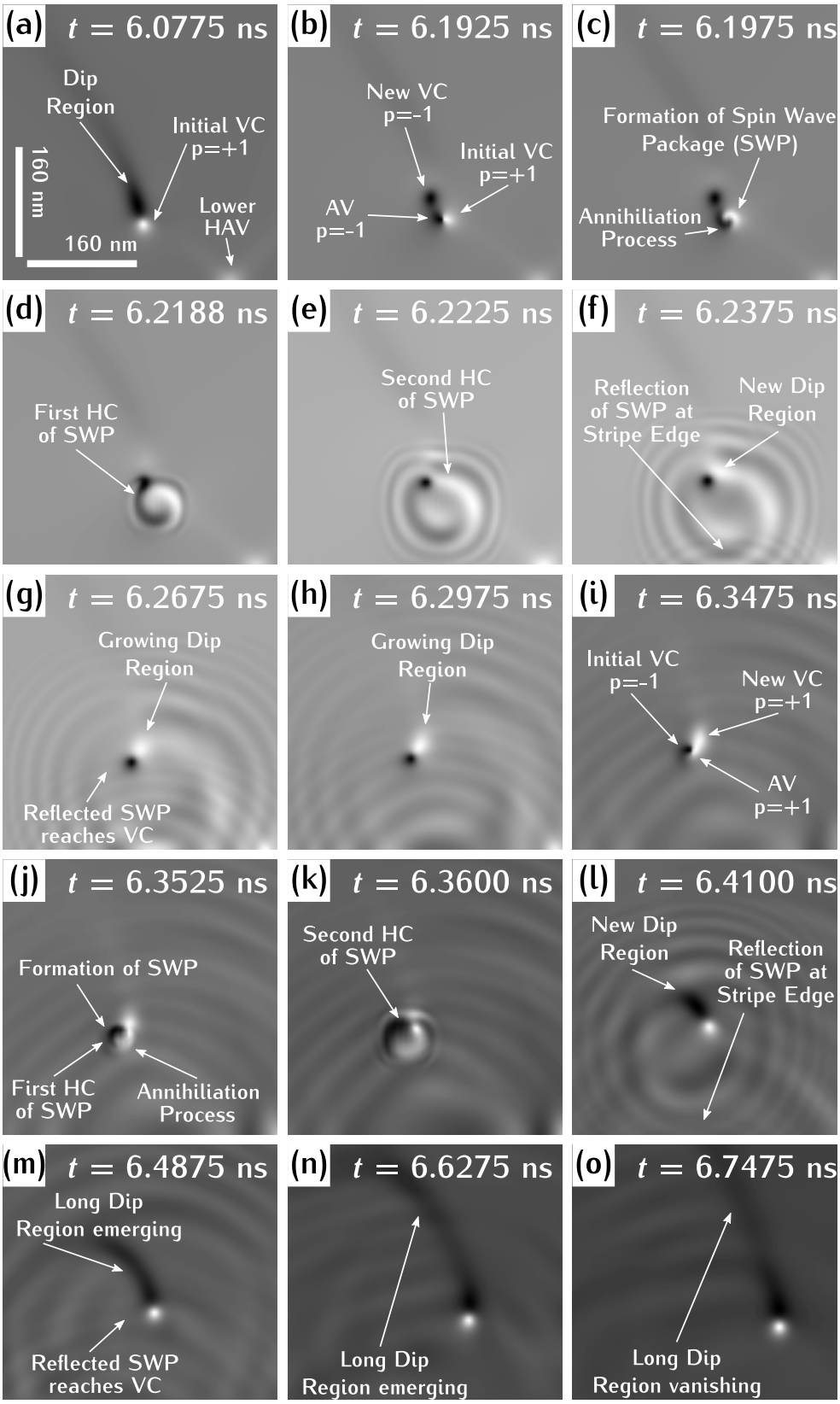

Figure 4.10. Snapshots at important time steps for the fast DRP of the VC core. The pictures show the z-component of the magnetization (m_z).

velocity and the gyrofield, a field that is caused by the dynamic magnetization, deforms the VC, and a dip region where m_z is pointing in opposite direction compared to the VC is formed close to the initial position of the VC. It has to be emphasized at this point that this dip region is bigger than the dip observed in simulations with VCs in nanodiscs [85]. This remarkable difference appears due to the special structure of the VDW itself. Within a VDW two "domain walls" (Neél type walls) exist between the connection lines of the VC and the HAVs. The magnetization at these internal DWs exhibit stronger spatial gradients than the pure curling magnetization around the VC in a nanodisc. This creates an additional strong gyrofield which superimposes with the gyrofield caused by the VC itself. Approaching the stripe edge the VC increases its velocity until it reaches the critical velocity V_c that is directly related with the critical deflection out of equilibrium Y_crit. At this point, the dip region is well established. Overall, the magnetic texture consisting of the initial VC and the dip region can be regarded as a hybridization of VCs with polarity $p = 1$ and $p = -1$. Reaching Y_crit it becomes energetically more favorable for the dip region to split up into a V and an antivortex (AV) with polarity $p = -1$ (Fig. 4.10(b)). The V with $p = -1$ is now the new VC of the VDW and it starts to move to the middle of the stripe due to the reversed gyrotropic force (not to be confused with the gyrofield) whose direction depends on the polarity. Because the topological charge of the DW in total has to be conserved, the AV is going to annihilate with the initial VC. This annihilation process starts with an anticlockwise spiral motion around each other as it can be seen in Fig. 4.10(c). This spiral motion continues and forms a spiral-like SW package (SWP) which propagates along any in-plane direction away from the annihilation point (Fig. 4.10(c-f)) and releases the energy that was stored previously in the magnetic texture of VC and AV. Shortly after the formation of the SWP, the first half-cycle (HC) of the SWP hits the VC Fig. 4.10(d) immediately followed by the second one Fig. 4.10(e). Here, during the first HC, m_z of the SWP points along the same direction as m_z of the VC, while in the second one m_z is aligned anti-parallel to the VC. Approximately 0.04 ns after the annihilation process, the SPW hits the lower edge of the stripe and becomes reflected which is depicted in Fig. 4.10(f). Furthermore, it appears that shortly after the VC was hit by the SWP, the first and the second HC of the SPW seems to be pinned to the left and right side of the VC (Fig. 4.10(e-f)). At the right side where the second HC seems to be pinned, a new dip region with opposite polarity as the current VC forms (Fig. 4.10(f)). This dip region grows while the VC is moving backwards to the middle of the stripe and the second SWP HC seems to wrap around the VC which is shown by Fig. 4.10(g) and Fig. 4.10(h). As shown in Fig. 4.10(g), approximately 0.03 ns after the SWP was reflected at the lower edge of the stripe, the reflected SWP arrives again at the VC. This immerses the VC in a constant flow of SWP oscillations (Fig. 4.10(g-h)) wherein the short wavelength components of the SWP reaches the VC at first and the one with longer wavelength later (Fig. 4.10(g-i). While traveling backwards to the middle of the stripe, the new dip region has grown so much that a second polarity reversal (PR) occurs only ≈ 0.14 ns after the first one. This unexpected PR starts in Fig. 4.10(i) with an splitting of the dip region into a V/AV-pair with polarity $p = 1$. As in the fist RP the former VC with $p = -1$ annihilates with the AV with $p = 1$ and the V with polarity $p = 1$

becomes the new VC of the VDW. This annihilation process starts this time in contrast to the first reversal with a clockwise spiral motion of V and AV around each other. This is shown in snapshot Fig. 4.10(j). Another remarkable difference which is caused by the reversed (compared to the first reversal) rotation sense of V and AV around each other is that the SWP is created closer to the new VC than in the first reversal. As a consequence the first (Fig. 4.10(j)) and second HC (Fig. 4.10(k)) of the SWP arrive a little bit earlier at the new VC than in the first reversal. While the SWP reflected at the edge is still arriving at the VC, the SWP originating from the second reversal propagates in all directions away from the annihilation point. The time it takes for the SWP to reach the lower edge of the stripe is ≈ 0.06 ns (with respect to the second reversal), and thus, it is ≈ 0.02 ns longer than in the first one. This happens because of the larger distance of the VC from the lower edge. While the SWP becomes reflected at the edge, the first HC is wrapping around the new VC and creates again a dip region with polarity $p = -1$ (Fig. 4.10(l)). Due to the reversed polarity of the new VC, the gyrotropic force changes its sign and the VC is now moving again towards the edge. During this motion the dip region becomes an extremely long tail, and in addition, the VC is again immersed in a constant flow of SWP oscillations originating from the second reversal (Fig. 4.10(m-n)). This long dip region is caused by the second SWP HC which superimposes with the internal Neèl type wall between the VC and HAV at the upper edge of the stripe. Surprisingly, this does not lead to another fast RP but to an approach of the VC to its critical transverse displacement Y_{crit} until it reaches again the critical velocity V_{c}. During this approach to Y_{crit} the long dip region vanishes (Fig. 4.10(o)) and the usual dip region solely remains (see snapshot Fig. 4.10(a)). From the description of one fast DRP different questions arise. In the following sections it has to be explained why after the expected first reversal no second one occurs and what the physical mechanism behind this behavior is. Furthermore, it has to be clarified whether the second reversal is related to the SWP and, in addition, why no fast third one occurs.

4.2.6 Double Reversal Process: Basic Considerations for Trace, Energy and Potential

In order to answer these questions the dynamics of the DRP from the energetic point of view is investigated. In Fig. 4.11 the trajecory (Fig. 4.11(a)), the total energy of the system $E_{\mathrm{Tot,DW}}$ (Fig. 4.11(b)) and the resulting potential (Fig. 4.11(c)) for the first three DRPs in the simulations is plotted. Fig. 4.11(d) - 4.11(f) shows the same potential as plotted in Fig. 4.11(c), but with the detailed energetic consideration for the first (d), second (e) and third (f) DRP, respectively. Please note: This is the same simulation run from where the first DRP was taken to depict the DRP in general (Fig. 4.10). For this very basic consideration of the DW dynamics within the DRP it will be focused on $E_{\mathrm{Tot,DW}}$ because the general internal structure of the DW is expected to be unchanged during the DRP. Under this assumption it can be expected that the observed change in $E_{\mathrm{Tot,DW}}$ is caused by the dynamics of the VC itself. This is the important part for the considerations. For details of the evaluation of $E_{\mathrm{Tot,DW}}$ see Sec. A6.

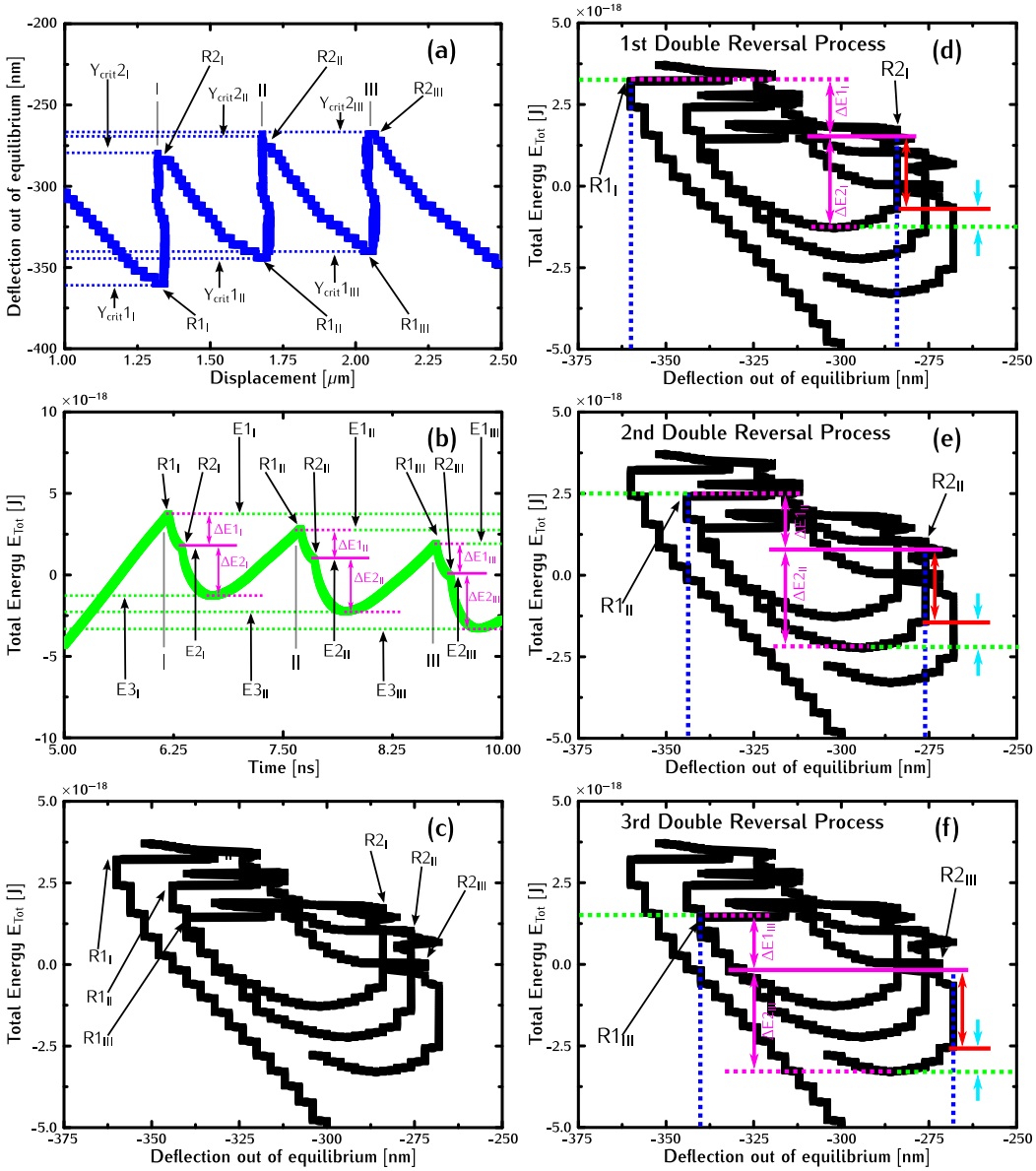

Figure 4.11. The diagrams displays the trajectories (a), the total energy of the system $E_{\mathrm{Tot,DW}}$ (b) and the resulting potential (c) for the first three DRPs in a simulation run. All quantities attributed here are labeled by 1 or 2 depending on whether they refer to the first or second reversal. In addition, a roman number is added in the subscript for each quantity to assign them to a specific DRP itself. In order to gain deeper insight into the DRP from a potential point of view, the corresponding energies are marked for the first (d), second (e) and third (f) DRP. As it becomes clear by this consideration, the released energy $\Delta E2$ is compressed out of two energy contributions. A certain amount of energy (red arrow) is the potential energy released during the second polarity reversal, while a smaller amount is dissipated afterwards during the motion of the VC to the edges (light blue arrows). This indicates that $\Delta E1$ is not showing the energy released in the first reversal but being composed out of more energy contributions as $\Delta E2$ or it comes from a completely different origin.

In Fig. 4.11(a) the trajectory exhibits the same behavior as seen in Fig. 4.7. The VC moves towards the edge of the stripe, reverses its polarity when reaching the critical transverse displacement $Y_{\text{crit}}1$ and moves backwards to the middle of the stripe. The path described by the VC during the backwards motion shows no significant motion in X-direction but a straight motion in Y-direction. After the second PR at $Y_{\text{crit}}2$ the VC is pushed again to the edge of the stripe, and the motion exhibits a displacement in X-direction as well. $E_{\text{Tot,DW}}$, which contains contributions from Zeeman energy ($E_{\text{zee,DW}}$), exchanges energy ($E_{\text{ex,DW}}$) and demagnetization energy ($E_{\text{dem,DW}}$), is given by[1]:

$$E_{\text{Tot,DW}} = E_{\text{dem,DW}} + E_{\text{ex,DW}} + E_{\text{zee,DW}} \tag{4.26}$$

Fig. 4.11(b) shows the time evolution of $E_{\text{Tot,DW}}$. Before the first DRP, the total energy of the DW increases up to a critical value, and a certain energy $\Delta E1$ is released after the first reversal. In the second reversal the system decreases its total energy again by a certain value $\Delta E2$ until it reaches a minimum in $E_{\text{Tot,DW}}$. After this minimum $E_{\text{Tot,DW}}$ grows again till the critical value is reached, a new DR occurs. A close view at the trajectories of the VC in Fig. 4.11(a) and at the total energy $E_{\text{Tot,DW}}$ in Fig. 4.11(b) reveals a specific feature of the dynamic of the fast DRP. As it can be seen, the critical displacements $Y_{\text{crit}}1$ and $Y_{\text{crit}}2$ where first and second reversal occur change with every new DRP. In the simulations, Y_{crit} is decreasing continuously within the first three reversals with $Y_{\text{crit}}1 = -350.5$ nm ($\pm 2.51\%$) and $Y_{\text{crit}}2 = -273$ nm ($\pm 2.96\%$) on average. In the same way the maximum ($E1$) and minimum ($E3$) value for $E_{\text{Tot,DW}}$ before and after a DRP, respectively, decreases continuously, as well as the energy ($E2$) where the second RP appears. While only the first three DRPs of the simulation are plotted, the simulation runs up to time of 20 ns with eight DRPs occurring in total. The trajectories and the total energy for this eight DRPs are shown in Sec. A6. It is remarkable that despite the maximum and minimum value for $E_{\text{Tot,DW}}$ changes, the values for the released energy $\Delta E1$ and $\Delta E2$ stays constant. As a consequence of this the total energy released, $\Delta E = \Delta E1 + \Delta E2$ is constant. Out of eight DRPs the average energies by $\Delta E1 = 2.01 \cdot 10^{-18}$ J ($\pm 8.46\%$), $\Delta E2 = 3.15 \cdot 10^{-18}$ J ($\pm 5.71\%$) and $\Delta E = 5.16 \cdot 10^{-18}$ J ($\pm 5.81\%$) are obtained. For a better understanding of the physical process the total potential (Fig. 4.11(c)) is additionally investigated by plotting $E_{\text{Tot,DW}}$ in dependence of the transversal displacement Y. From Fig. 4.11(c) it becomes clear that the VC describes an oscillatory motion in the potential. This bounded motion shows also the decreasing trend by shifting the potential to lower energies and lower transversal displacements within the first three DRPs.

Additionally, important quantities like critical transverse displacements ($Y_{\text{crit}}1$, $Y_{\text{crit}}2$) and energies ($\Delta E1$, $\Delta E2$) shown in Fig. 4.11(a) and Fig. 4.11(b) are marked for the first, second and third DRP in Fig. 4.11(d) - 4.11(f). Considering the second reversal (R2) and its associated released energy $\Delta E2$, it can be seen in this representation that $\Delta E2$ is composed out of two energies. These two energies are marked in red and light blue in Fig. 4.11(d) - 4.11(f), whereas the red one is the potential energy released directly during R2, and the light blue one is the contribution to $\Delta E2$ which is dissipated while the VC is already moving again towards the lower edge of the stripe. This indicates that $\Delta E1$ does not show the energy released in the first reversal, but it is composed out of more

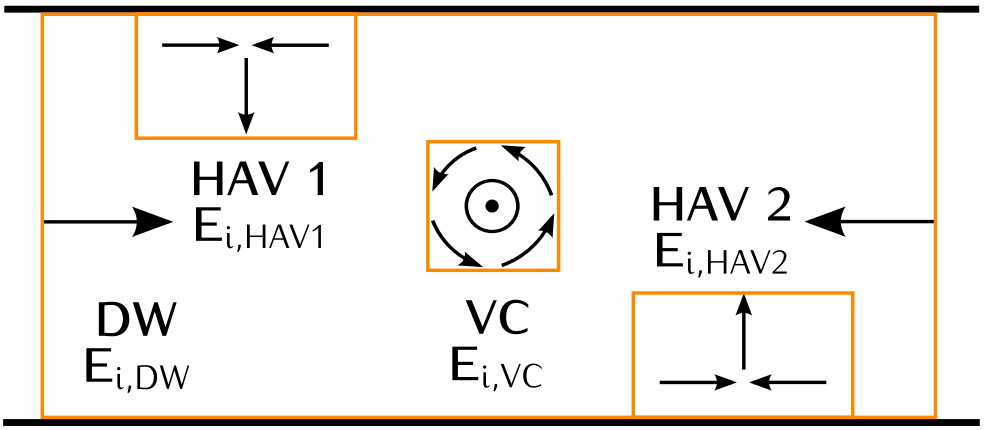

Figure 4.12. For refined investigation of the DRP and the involved energies, the DW is divided into subsystems as depicted in this sketch. These regions are naturally given by the internal DW structure itself. Defining for rectangular regions, one stretching over the total DW, one over a small region around the VC and two around the HAVs, one for each HAV at the upper and lower edge of the stripe, respectively. For the exact size of the chosen regions see Appendix A7. The associated energies are named by $E_{\mathrm{i,DW}}$, $E_{\mathrm{i,VC}}$, $E_{\mathrm{i,HAV1}}$ and $E_{\mathrm{i,HAV2}}$ where the x in the subscript stands for the specific energy that is considered. For example, the x can stand for the total energy or a single contribution, like Zeeman, exchange or demagnetization energy. Subtracting the energies $E_{\mathrm{Tot,VC}}$, $E_{\mathrm{Tot,HAV1}}$ and $E_{\mathrm{Tot,HAV2}}$ from $E_{\mathrm{Tot,DW}}$ reveals the quadratic potential E_{Pot}; the VC is moving in transversal direction (see Fig. 4.13).

energy contributions like $\Delta E2$ or it comes from a completely different origin. Especially Fig. 4.11(d) - 4.11(f) made clear that the consideration of $E_{\mathrm{Tot,DW}}$ is a good starting point for the investigation of the fast DRP, but not fully suitable and insufficient to understand the underlying physical mechanism. The tasks remaining now are to find out why the critical transverse displacements and energies are changing from one to another fast DRP and, in addition, what the contributions are to $\Delta E1$ and $\Delta E2$.

4.2.7 Double Reversal Process: A Detailed Discussion for Trace, Energy and Potential

In order to gain deeper insight, the VDW is divided into subsystems as shown in Fig. 4.12. These subsystems are naturally given by the internal structure of the VDW itself. Four rectangular regions are defined: One stretches over the total DW, one over a small region around the VC and two around the HAVs where each of them is for one HAV at the upper and lower edge of the stripe, respectively. For the exact size of these areas see Appendix A7. The associated energies are named by $E_{\mathrm{i,DW}}$, $E_{\mathrm{i,VC}}$, $E_{\mathrm{i,HAV1}}$ and $E_{\mathrm{i,HAV2}}$ where the x in the subscript stands for the specific energy that is considered,

for example, the total energy or single contributions like Zeeman, exchange or demagnetization energy. Being interested in the dynamics of the VC itself, the contributions to the VC dynamics coming from the HAVs will be regarded for now as second order effects. In the following, the potential energy E_{Pot} of the VC is defined as the total energy of the DW minus the total energy of all subsystems. To avoid confusion, it has to be pointed out that speaking about

potential means the energy in dependence of the y-coordinate of the VC. E_{Pot} is given by[1]

$$E_{\mathrm{Pot}} = E_{\mathrm{Tot,DW}} - E_{\mathrm{Tot,VC}} - E_{\mathrm{Tot,HAV1}} - E_{\mathrm{Tot,HAV2}} \tag{4.27}$$

and plotted in Fig. 4.13. E_{Pot} reveals a parabolic potential with a linear proportion which can be fitted by the function[1]

$$E_{\mathrm{Pot}} = k_{2,\mathrm{Pot}} \cdot Y^2 + k_{1,\mathrm{Pot}} \cdot Y + k_{0,\mathrm{Pot}} \tag{4.28}$$

yielding for the parameter:

$$\begin{aligned} k_{2,\mathrm{Pot}} &= (4.45575 \pm 0.00535) \cdot 10^{-5}\,\frac{\mathrm{J}}{\mathrm{m}^2} && (\pm 0.12\%) \\ k_{1,\mathrm{Pot}} &= (-2.04593 \pm 0.00102) \cdot 10^{-12}\,\frac{\mathrm{J}}{\mathrm{m}} && (\pm 0.49\%) \\ k_{0,\mathrm{Pot}} &= (1.03697 \pm 0.00031) \cdot 10^{-17}\,\mathrm{J} && (\pm 0.03\%) \end{aligned} \tag{4.29}$$

This general shape of the potential in which the VC is moving can be predicted from relative simple analytic models as shown in [45]. The quadratic part of the potential is, due to the magnetic charges, at the edges of the stripe, whereas the linear part, which causes the asymmetry of E_{Pot}, originates from the Zeeman barrier of the curling magnetization in the DW (see Fig. 2.5 and Sec. 2.3.2.4). The energy within the area of the VC $E_{\mathrm{Tot,VC}}$ has a slight linear dependence with respect to the transverse displacement and is shown in the lower part of Fig. 4.13. Because of the potential energy of the VC, the energy in the VC area can be fitted by a linear function given by[1]

$$E_{\mathrm{Tot,VC}} = k_{1,\mathrm{VC}} \cdot Y + k_{0,\mathrm{VC}} \tag{4.30}$$

which yields for the parameters:

$$\begin{aligned} k_{1,\mathrm{VC}} &= (1.12471 \pm 0.00023) \cdot 10^{-13}\,\frac{\mathrm{J}}{\mathrm{m}} && (\pm 0.02\%) \\ k_{0,\mathrm{VC}} &= (1.02895 \pm 0.00052) \cdot 10^{-18}\,\mathrm{J} && (\pm 0.05\%) \end{aligned} \tag{4.31}$$

This very small linear part of $E_{\mathrm{Tot,VC}}$ is like the linear contribution in E_{Pot} caused by the Zeeman barrier which is present in the defined region around the VC as well. For further considerations, the linear proportion of $E_{\mathrm{Tot,VC}}$ can be neglected, and its contributions to E_{Pot} regarded as a constant offset as long as no reversal of the VC occurs. Based on this subdivision, the dynamics of the fast DRP is investigated in more detail. Due to the decoupling of the energies it is possible to have a close look at the energies in the VC while the VC is moving in the potential. In Fig. 4.14 the time dependence of $E_{\mathrm{Tot,VC}}$ is plotted for the first three DRPs where now the energies released in the first and second RP appear as sharp peaks in $E_{\mathrm{Tot,VC}}$. As mentioned before, $E_{\mathrm{Tot,VC}}$ stays at a constant level (indicated by the red line in Fig. 4.14) until shortly before the first reversal occurs and the energy in the VC area rises very steeply. After reaching a maximum value, the energy decreases very fast until the second reversal of the VC occurs short time later, and $E_{\mathrm{Tot,VC}}$ rises again. This peak decays also very fast, and $E_{\mathrm{Tot,VC}}$ reaches its constant level until another fast DRP happens. Introducing for the energies released in the both of them reversals new names, $\Delta E1^*$ and

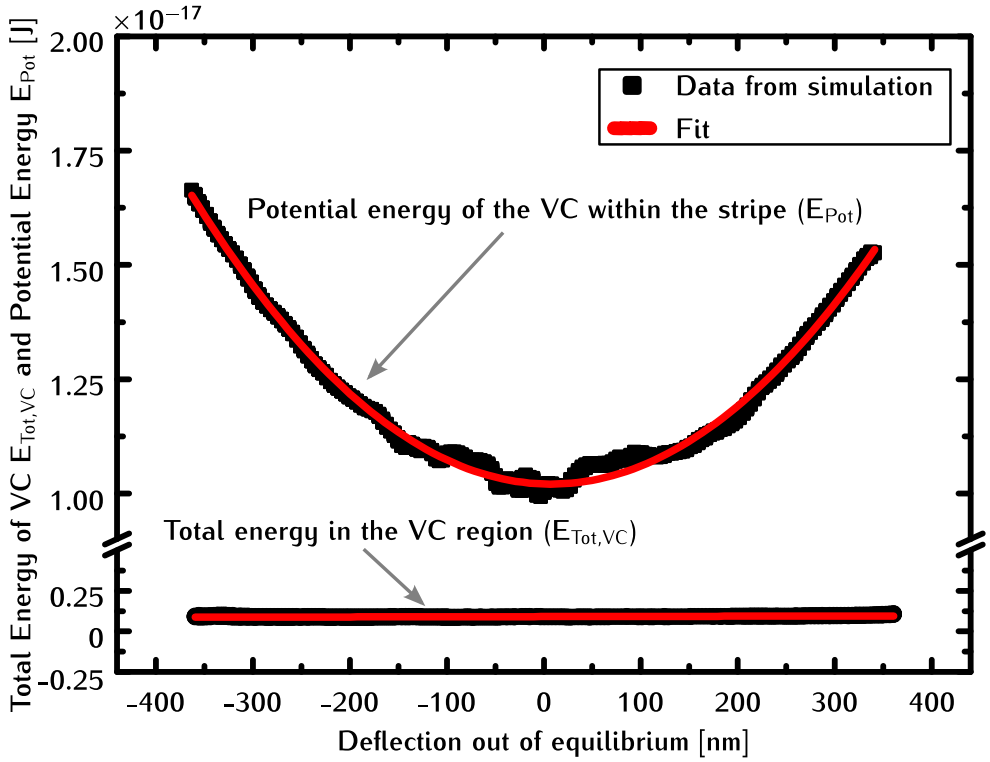

Figure 4.13. In this figure the potential energy E_{Pot} and the energy in the VC region itself ($E_{\mathrm{Tot,VC}}$) is plotted. The energies are calculated upon the devision of the DW into its substructures as described in the Fig.4.12 and in the Appendix A7. It yields the expected quadratic behavior for the potential E_{Pot}; the VC is moving in transversal direction. The quadratic part of the potential is due to the magnetic charges at the edges of the stripe, whereas the linear part, which causes the asymmetry of E_{Pot}, originates from the Zeeman barrier of the curling magnetization in the DW (see Fig. 2.5 and Sec. 2.3.2.4). The energy in the VC area $E_{\mathrm{Tot,VC}}$ has a slight dependence on the y-position. This small linear dependence arises from the Zeeman barrier because the curling magnetic texture is present in the VC area as well. Both curves obtained from the simulation date are fitted in the case of E_{Pot} by Eq. (4.28) and for $E_{\mathrm{Tot,VC}}$ by Eq. (4.30)

$\Delta E2^*$, respectively, because it is not clear whether the energy differences in Fig. 4.10(b) of $\Delta E1$ and $\Delta E2$ are the same as in Fig. 4.14 or not.

A remarkable change can be seen in $\Delta E1^*$ and $\Delta E2^*$ for different DRPs as well. In average it is obtained from eight DRPs: $\Delta E1^* = 1.15 \cdot 10^{-18}$ J ($\pm 6.96\%$), $\Delta E2^* = 0.88 \cdot 10^{-18}$ J ($\pm 3.41\%$) and for the total released energy $\Delta E1^* + \Delta E2^* = 2.03 \cdot 10^{-18}$ J ($\pm 2.96\%$). From this values, it becomes clear that there is really a difference between $\Delta E1^*$ and $\Delta E1$. First, the released energies shown in Fig. 4.14 are investigated in the frame of a VC moving in a parabolic potential. The consideration for this case is shown as an example for the first DRP in Fig. 4.14 where the bold black curve is the potential of the VC. Being interested in the DRP, the considerations concentrate on the sector of the potential ranging from -240 nm up to -380 nm in deflection out of equilibrium. Applying an external field, the VC is deflected out of equilibrium, and it moves, which is considered, from an energetic point of view along the potential line until it reaches its critical displacement. This critical displacement $Y_{\mathrm{crit}}1_{\mathrm{I}}$ for

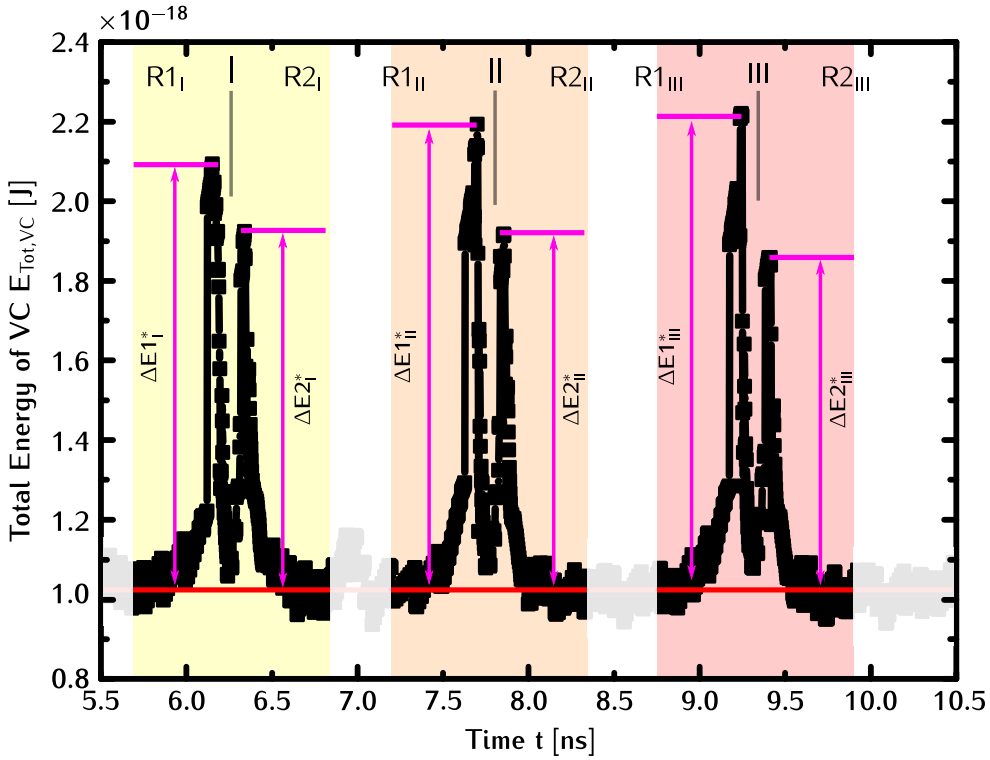

Figure 4.14. In this graph the energy in the VC area ($E_{\mathrm{Tot,VC}}$) is plotted in dependence of time t for the first three DRPs. The energies released (pink arrows) during the first and second polarity reversal appear as sharp peaks in $E_{\mathrm{Tot,VC}}$. The red line marks the constant ground level for the energy before and after the DRP. Since it turns out that the earlier mentioned energies $\Delta E1$ and $\Delta E2$ (see Fig. 4.11) are different from the released energies in the VC region, the names $\Delta E1^*$ and $\Delta E2^*$ for the later mentioned ones are introduced. The values for the energies $\Delta E1^*$ and $\Delta E2^*$ are listed in Tab. 4.1.

the reversal from polarity $p = 1$ to $p = -1$ is marked with the dashed blue line at -360 nm transverse displacement. As described previously, up to this point, the VC has been deformed by the gyrofield so much that the VC and the adjacent dip region can be regarded as a hybridization of an VC with polarity $p = 1$ and $p = -1$. In order to clarify this situation, a sketch was draw for explanation in Fig. 4.16 where one can see m_z of the magnetization in the VC region. This structure composed out of VC and dip region stretches over a rather long distance. The distance between VC and dip is labeled as $\Delta 1_{\mathrm{I}}$ and can be determined by looking at the snapshots for m_z short before and after the first RP. This was done in Fig. 4.15(a), and it yields $\Delta 1_{\mathrm{I}} = 36$ nm by marking the position of old and new VC. The importance of $\Delta 1_{\mathrm{I}}$ becomes clear when one thinks about the energy released in the first reversal. During the first reversal, the dip region splits up into a V/AV-pair and creates a new VC closer to the middle of the stripe, which means that directly after the up-splitting a VC is obtained which lies lower in energy. The position of the new VC is marked in Fig. 4.16 by a black dashed line. The intersections of the blue and black dashed line with the potential gives now the difference in potential energy which is released during the first reversal process. Labeling this energy by $\Delta E_{\mathrm{Pot}}(Y_{\mathrm{crit}}, \Delta)$ which depends on the critical displacement Y_{crit} and Δ. It can be calculated from the formula:

	DRP I	DRP II	DRP III
$\Delta E1^*$	$1.22 \cdot 10^{-18}$ J	$1.27 \cdot 10^{-18}$ J	$1.30 \cdot 10^{-18}$ J
$\Delta E2^*$	$0.98 \cdot 10^{-18}$ J	$0.97 \cdot 10^{-18}$ J	$0.90 \cdot 10^{-18}$ J

Table 4.1. In this table the released energies $\Delta E1^*$ and $\Delta E2^*$ during the first three DRPs are listed. $\Delta E1^*$ labels the energy released during polarity reversal R1, while $\Delta E2^*$ denotes the energy released during R2. For a graphic depiction of the energies in the VC region ($E_{\mathrm{Tot,VC}}$) it is referred to Fig. 4.14.

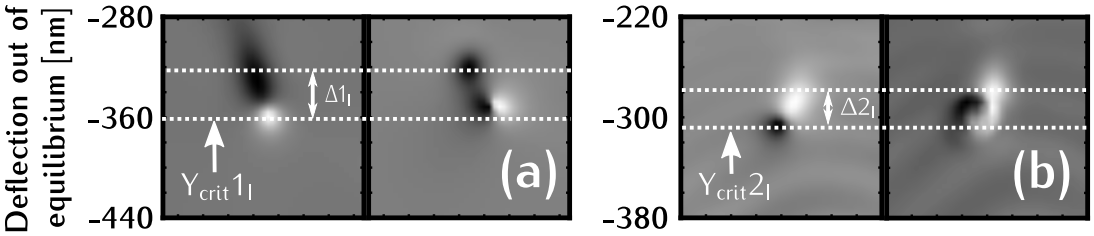

Figure 4.15. In order to investigate the released energies during the first and second polarity reversal, the distances between the initial present VC and the emerging dip region are measured upon m_z. This yields the distance $\Delta 1$ for the first and $\Delta 2$ for the second reversal during a certain DRP. Figure (a) and (b) show the distances $\Delta 1_{\mathrm{I}}$ and $\Delta 2_{\mathrm{II}}$ for the DRP I. Please note that each single snapshot shows an area of 160×160 nm^2 indicating the length of the pictures in x-direction which is 160 nm. An exact lateral position of the VC is not given because it is unimportant for the physical considerations.

$$\Delta E_{\mathrm{Pot}}(Y_{\mathrm{crit}}, \Delta) = 2k_{2,\mathrm{Pot}}\Delta \cdot Y_{\mathrm{crit}} - k_{2,\mathrm{Pot}}\Delta^2 + k_{1,\mathrm{Pot}}\Delta \tag{4.32}$$

Obtaining for the difference in potential energy $\Delta E_{\mathrm{Pot}}1_{\mathrm{I}} = 1.28 \cdot 10^{-18}$ J which is equal to the energy $\Delta E1^*_{\mathrm{I}}$ found in Fig. 4.14. This is a remarkable result because it states that the energy released in the first reversal process can be understood fully in the frame of a VC moving in the parabolic potential. This energy difference is released by the system in the annihilation process of the previous VC and the created AV, which is, in addition, the starting point for the creation of a SWP. This SWP propagates in all directions and dissipates its energy named in Fig. 4.16 as $E_{\mathrm{SWP}}1_{\mathrm{I}}$ by the well known magnetic damping mechanism. Proceeding in the description of the DRP, a VC with polarity $p = -1$ is present which moves due to the reversed gyrotropic force backwards to the middle of the stripe. This backwards motion continues until the second unexpected RP occurs and causes a further decrease in energy of approximately $0.51 \cdot 10^{-18}$ J.

At a transverse displacement of -308 nm which determines $Y_{\mathrm{crit}}2_{\mathrm{I}}$, the dip region has again developed so strong that it becomes more favorable to split up into V and AV. The basic configuration of the magnetization is shown in the lower sketch in Fig. 4.16. As for the first reversal, the distance $\Delta 2_{\mathrm{I}}$ is determined by evaluating the position of the VC short before and after the reversal process, respectively. The distance now is smaller than $\Delta 1_{\mathrm{I}}$ and determined to $\Delta 2_{\mathrm{I}} = 28$ nm. These values for $Y_{\mathrm{crit}}2_{\mathrm{I}}$ and $\Delta 2_{\mathrm{I}}$ lead to a difference in potential energy for the second reversal of $\Delta E_{\mathrm{Pot}}2_{\mathrm{I}} = 0.86 \cdot 10^{-18}$ J. Surprisingly, this time the

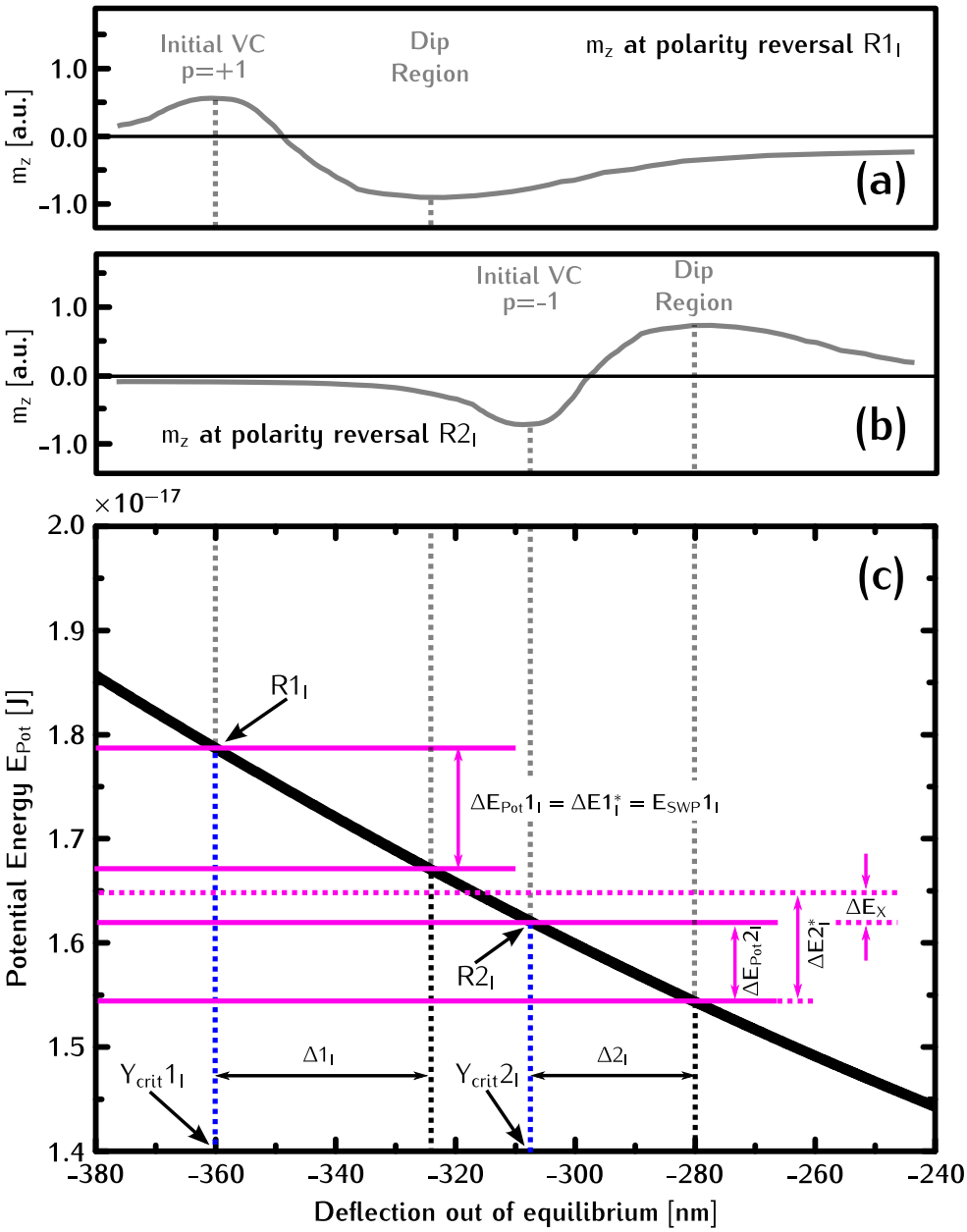

Figure 4.16. In this diagram the first DRP is considered on base of a VC which is moving in a parabolic potential. Sketches (a) and (b) depict the magnetic texture of m_z at the first and second polarity reversal (R1 and R2), respectively. Here, the case of the first DRP in the simulations is considered. In (c) the parabolic potential (black line) is plotted with the fitted parameter from the considerations done in Fig. 4.13. Additionally, the critical transverse displacements $Y_{\mathrm{crit}}1$ and $Y_{\mathrm{crit}}2$ are plotted, as well as the spatial distances $\Delta 1$ and $\Delta 2$ between dip and VC. It turns out that the released potential energy $\Delta E_{\mathrm{Pot}}1_{\mathrm{I}}$ during R1 is equal to $\Delta E1^*$. As a consequence, this must be the total energy $E_{\mathrm{SWP}}1_{\mathrm{I}}$ contained in the appearing SWP. As it can be seen by considering the second reversal, the energy $\Delta E2^*$ released during R2 is larger than the potential energy $\Delta E_{\mathrm{Pot}}2_{\mathrm{I}}$. A fact indicates that the difference ΔE_{x} between both energies has to be delivered by some additional physical mechanism.

potential energy $\Delta E_{\mathrm{Pot}}2_{\mathrm{I}}$ is smaller than the released energy $\Delta E2^*_{\mathrm{I}}$ found in Fig. 4.14. For better comparison $\Delta E2^*_{\mathrm{I}}$, ΔE_{Pot} and the difference $\Delta E_{\mathrm{X}} = 0.12 \cdot 10^{-18}$ J is marked additionally in Fig. 4.16. Now, the considerations arrive at a

very crucial point in understanding the fast DRP. It has become obvious that there is more energy involved in the second reversal from $p = -1$ to $p = 1$ than can be delivered by the difference in potential energy. Finding a mechanism that can deliver the additional energy ΔE_{X} will lead directly to the answer why there is a second polarity reversal short after the first one.

4.2.8 Double Reversal Process: Influence of the Spin Wave Package

Thinking about a mechanism that could cause the second polarity reversal and provide the additional energy ΔE_{X} , which is needed, it is obvious to suspect the SWP, which is caused by the V/AV annihilation of the first reversal. This strong SWP appearing in the direct vincinity of the created new VC could lead to some energy transfer from SWP to VC. It was found in simulations that it is possible to move transverse walls [140] and VDWs [141] by exciting SWs in a nanostripe. In [141] they determined the excitation spectra for a VDW where the frequency f for the SWs for most efficient excitation was found in the range between $10 - 40$ GHz. In order to check whether the SWP contains frequency components in the required range or not, the SWP which reaches the VC after the first reversal is recorded. In Fig. 4.17(a) the m_z in dependence of time at the position of the VC is shown. For further details how the SWP was exactly extracted from the simulation data see Sec. A8. As it can be seen, the VC is reached directly after the creation of the SWP by the first and second HC which exhibit large amplitudes of $m_z = -0.4 \cdot M_{\mathrm{s}}$ and $m_z = 0.2 \cdot M_{\mathrm{s}}$, respectively. Short time later the VC is reached by the part of the SWP that has been reflected at the lower edge of the stripe. These oscillations superimpose with the remains of the already decaying direct excitation out of SWP. These oscillations which are caused by the reflected parts of the SWP exhibit rather large amplitudes ranging for $|m_z| = 0.05 \cdot M_{\mathrm{s}}$ up to $|m_z| = 0.15 \cdot M_{\mathrm{s}}$. Aiming to estimate whether the first two strong HCs or the subsequent one can excite the VC, two regions named by SWP 1 and SWP 2 have to be defined. SWP 1 (marked by dashed orange lines in Fig. 4.17) contains the direct excitation due to the SWP and SWP 2 (indicated by the red dashed line in Fig. 4.17) and the excitation, due to the continuous flow of SWs reflected at the edge. Performing a fast Fourier transformation (FFT) for both cutouts yields that both excitations contain frequency components which are required to excite the VDW. The FFT for SWP 1 and SWP 2 is plotted in Fig. 4.17(b) and Fig. 4.17(c), respectively. Marking the important frequency range in both diagrams with a yellow area underlines the fact that both Fourier spectra contain large frequency amplitudes in this range. Comparing the amplitudes of the oscillations in the SWP with the amplitudes used for the simulations in [141] yields that in the actual case the amplitudes are up to a factor of approximately 12.3 times higher. When these findings are combined, a preliminary conclusion can be drawn: Most likely, the mechanism which can lead to the second reversal was found. The question which remains now is how this SWP excitation influences the VC exactly. For finding the answer a look has to be taken on the absolute value of the velocity v and the energy in the VC area $E_{\mathrm{Tot,VC}}$ in detail during the first DRP. For further investigation, a novel technique is applied to calculate the velocity by utilizing

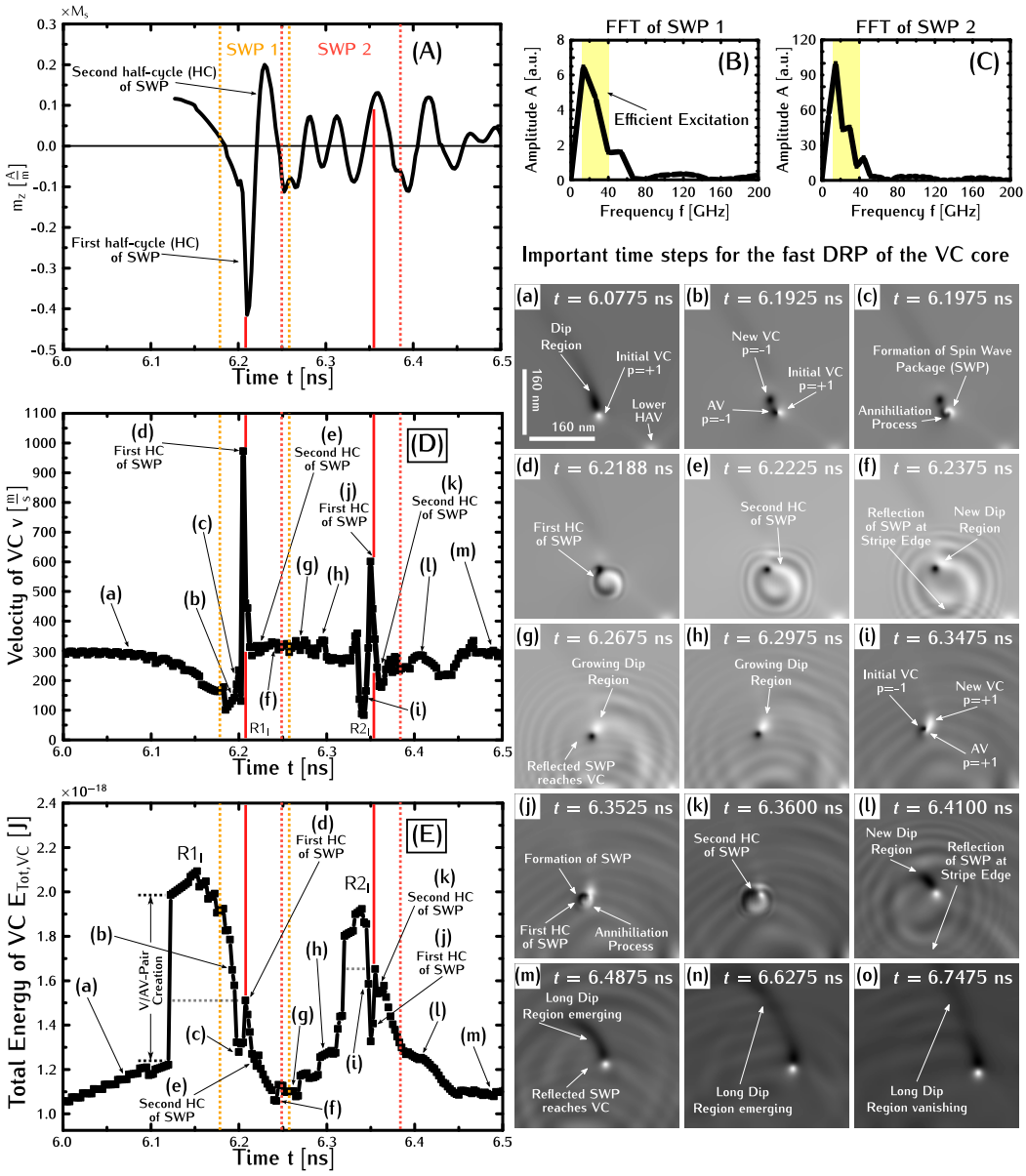

Figure 4.17. The diagrams show the effect of the SWP on the velocity and energy of the VC. In figure (A) the time evaluation of m_z of the SWP at the position of the VC is plotted. For the evaluation of the SWP please see Appendix A8. The dashed orange and red lines mark the time range in which the SWP originating in the first and second reversal process is analyzed by FFT. Red bold lines in (A) mark the time when the first half cycle of the SWP from R1 and R2 is reaching the VC. The results of the FFT analysis is presented in figure (B) and (C), whereby an efficient excitation of the VC by spin waves is possible in the frequency range marked by the light yellow boxes. In diagrams (D) and (E) the effect of the SWP on the effective velocity v of the VC (see Appendix A9) and the energy $E_{\mathrm{Tot,VC}}$ in the VC region is plotted. For better comparison the dashed and bold lines drawn in (A) are also marked in (D) and (E), as well as the important time steps of one complete reversal process shown in Fig. 4.10. The tableau given in Fig. 4.10 is inserted additionally in the actual figure to facilitate the comparison. It is easy to see that the hitting of the first HC of the SWP1 and SWP2 has a strong effect on the effective velocity and leads to an enhancement of the energy in the VC region. However, after the first reversal, the effective velocity stays high, and the energy in the VC region increases until a second reversal process appears; after the second one v is undergoing strong oscillations and the energy $E_{\mathrm{Tot,VC}}$ decreases.

the gyrofield. The gyrofield which is caused by every moving magnetic texture and, e.g., is causal for the formation of the dip region close to the VC, depends on the time derivative $\dot{\vec{m}}$. The time derivative can be written (assuming a rigid magnetic texture) as $\dot{\vec{m}} = -\vec{\mathrm{v}} \cdot \vec{\nabla}\vec{m}$. With the expression for the gyrofield $\vec{h}_{\mathrm{gyro}}$ as given in [21] one yields:

$$\vec{h}_{\mathrm{gyro}} = -\frac{1}{\gamma}\frac{\partial}{\partial \vec{m}}\frac{\vec{n}\cdot(\vec{m}\times\dot{\vec{m}})}{1+\vec{m}\cdot\vec{n}} = \frac{1}{\gamma}\frac{\partial}{\partial \vec{m}}\frac{\vec{n}\cdot(\vec{m}\times\vec{\mathrm{v}}\cdot\vec{\nabla}\vec{m})}{1+\vec{m}\cdot\vec{n}} \tag{4.33}$$

For further details about the calculation of $\dot{\vec{m}}$ and $\vec{h}_{\mathrm{gyro}}$ see Sec. A9. Knowing all quantities from simulation data, this equation is used to calculate v numerically. The advantage of this method in determining v is that the influence of an external perturbation (here the SWP) on the rigid magnetization in the VC can be investigated via the gyrofield. The reason why this method is practical in determining the velocity caused by the external perturbation can be seen by considering the expression on the right-hand side in Eq. (4.33). Regarding a certain magnetic texture immersed in the gyrofield from a perturbation, the magnetic configuration at this point can react either by changing its velocity v, the magnetic configuration (expressed by the terms $\vec{m}$ and $\vec{\nabla}\vec{m}$) or both. Since focusing on the center of the VC, which is exchange-dominated and for this reason can be regarded as rigid magnetic structure, $\vec{m}$ and $\vec{\nabla}\vec{m}$ are fixed and the VC can only react on the gyrofield by changing its velocity v [1].

$$\dot{\vec{h}}_{\mathrm{gyro}} = \frac{1}{\gamma}\frac{\partial}{\partial \vec{m}}\frac{\vec{n}\cdot(\vec{m}\times\dot{\vec{v}}\cdot\vec{\nabla}\vec{m})}{1+\vec{m}\cdot\vec{n}} \tag{4.34}$$

The results for v are shown in Fig. 4.17(d), displaying v in the time range from 6.0 ns up to 6.5 ns which is covering the first DRP. Linking these results to the description of the DRP in Sec. VII, the important time steps presented in Fig. 4.10 and in Fig. 4.17(d) are labeled additionally. Addressing it to the effect caused by SWP 1 and SWP 2 the time range where both appear are marked with dashed lines as in Fig. 4.17(a) as well. Heading towards the first RP from polarity $p = 1$ to $p = -1$, the VC is at a velocity of $\mathrm{v} = 300\frac{\mathrm{m}}{\mathrm{s}}$ (a) and then starts to decrease to a value of approximately $\mathrm{v} = 150\frac{\mathrm{m}}{\mathrm{s}}$ (b) where in the snapshots the splitting of the dip region into V and AV becomes visible. This means that the new VC with polarity $p = -1$ is not at rest but at a significant lower velocity than before. For v a slight increase is determined when the formation of the SWP (c) happens and an extremely steep increase short time later. At this point (d) the velocity rises very fast to a level of $\mathrm{v} = 1000\frac{\mathrm{m}}{\mathrm{s}}$ and decreases again. It is remarkable that the velocity, after the striking peak in v, is at the same level (approximately $300\frac{\mathrm{m}}{\mathrm{s}}$) than short before the first polarity reversal. As it becomes clear when looking at Fig. 4.10(d) and comparing it in addition with Fig. 4.17(a) by drawing a bold red line at the time when the strong peak occurs, the high velocity of the VC is caused by the first HC of the SWP. At this point, it could be guessed that the value of $\approx 1000\frac{\mathrm{m}}{\mathrm{s}}$ is simply the velocity of the SWP which is known to be in the same velocity range and its not the velocity of the VC. Here, it should be referred to the explanation of the calculation method again. As previously explained, the fixed magnetization of the VC can only react on the gyrofield of the first HC of SWP 1 by increasing its velocity to

the velocity of the SWP. Thus, the VC exhibits a velocity that could, usually, never be reached by an external applied field for a very short time. What the effect of this overcritical state from an energetic point of view is will be discussed subsequently based on Fig. 4.17(e). Proceeding the description of v, the velocity shows no significant change when the second SWP front is arriving at the VC (e), and the new dip region with polarity $p = 1$ starts to grow (f). As soon as the part of the SWP which has been reflected at the lower edge of the stripe reaches the VC (equal with SWP 2), the velocity starts to show small oscillations (g and h). These oscillations coincide with the decrease in v (after h) which is indicating the second polarity reversal. This time the decrease in velocity is more pronounced than for the first one (i). The velocity of the new created VC with polarity $p = 1$ is about 100 $\frac{\mathrm{m}}{\mathrm{s}}$ after the splitting of the dip region into V and AV. Again, a steep increase in v can be observed as soon the first HC of the SWP reaches the VC (j) (marked with the second bold red line). This time the peak velocity is as half as high (v $\approx$ 650 $\frac{\mathrm{m}}{\mathrm{s}}$) as for the first reversal. After the first HC passed the VC, v decreases again and reaches a minimum of about 200 $\frac{\mathrm{m}}{\mathrm{s}}$ shortly after the second HC (k) arrives at the VC. v rises up again slightly, but it underlays variations and stays below the critical value of v = 300 $\frac{\mathrm{m}}{\mathrm{s}}$. When the new dip region establishes (l) and the long dip region emerges, v exhibits a little bit higher values, but V_c is not reached and a fast, third reversal does not take place. So far, it has been obtained that the SWP has a strong influence on the velocity of the VC, and the interaction by SWP and VC seems to be the key in understanding the fast DRP. The energetical considerations in Fig. 4.16 have shown that more energy is released in the second polarity reversal than can be provided by the difference in potential energy. To investigate whether the interaction of the SWP with the VC can provide this additional energy ΔE_X or not, a close look has to be taken at the total energy involved in the first DRP. In Fig. 4.17(e) the same consideration for the total energy in the VC area $E_\mathrm{Tot,VC}$ is repeated as it was done in Fig. 4.17(e) for the velocity. A remarkable feature of the reversal process becomes already clear when comparing the behavior of $E_\mathrm{Tot,VC}$ and the snapshots (a) and (b) in Fig. 4.10. While approaching V_c (a), the energy in the VC area increases up to a threshold of $E_\mathrm{Tot,VC} = 1.2 \cdot 10^{-18}$ J where, then, a jump in energy occurs. This rise in energy happens due to the creation of a V/AV-pair. This means that the splitting of the dip region occurs much earlier than it can be seen in the snapshots (b). This creation of the V/AV-pair is accompanied by the starting of the decrease in velocity. Subsequent to the slitting, the V and the AV start to move away from each other what causes an additional increase in energy. As for the creation of the new V and AV, the formation of the SWP (c) and its associated release (decrease) of energy can be seen in $E_\mathrm{Tot,VC}$ much earlier than in Fig. 4.10. The most important feature in $E_\mathrm{Tot,VC}$ appears when the first HC of the SWP hits the VC. At this moment (d) where a prominent peak has already been found in v, a large peak in $E_\mathrm{Tot,VC}$ can be observed in addition. At the moment of highest velocity, the energy is peaking at $E_\mathrm{Tot,VC} \approx 1.5 \cdot 10^{-18}$ J, a value that is usually achieved when a V/AV-pair is created. For comparison see horizontal dashed gray line in Fig. 4.17(e). This incorporates the interpretation that the VC finds itself in an overcritical state at the moment when the first SWP HC is passing by. The second HC appears as a very small peak in $E_\mathrm{Tot,VC}$ (e) while the energy decreases continuously until a

minimum is reached, which coincides with the appearance of the new dip region with $p = 1$ (f). The fact that even at the minimum of $E_{\mathrm{Tot,VC}}$ between the two reversals, the energy is as high as in the state of the VC short before the first reversal (a) indicates that there was a transfer of energy from the SWP to the VC. This is supported additionally by the finding that, after the first SWP HC, the VC moves again with a velocity of approximately V_{c}. After this minimum, $E_{\mathrm{Tot,VC}}$ starts to rise undulatorily as soon as the reflected SWP arrives at the VC (g and h). $E_{\mathrm{Tot,VC}}$ increases until the critical value for the V/AV-pair creation is reached. As in the first reversal, the slitting of the dip region can be seen in the energy for the VC area earlier than in Fig. 4.10 by a sudden jump in $E_{\mathrm{Tot,VC}}$. This is followed by an additional slight increase in energy that is, due to the growing distance of the V/AV-pair, between each other. The oscillations in $E_{\mathrm{Tot,VC}}$, which have mentioned before, can be traced even in the steep jump in energy and the slight increase in $E_{\mathrm{Tot,VC}}$ after the V/AV-pair creation. When the dip region starts to split up (i) visibly and forms a SWP, due to the annihilation process, $E_{\mathrm{Tot,VC}}$ has already decreased until short time later the first HC of the SWP hits the new VC with polarity $p = 1$ (k). Once more a direct link between the first two HCs of the SWP and increase of the energy in the VC area is found. Within the first two HCs (k and j) $E_{\mathrm{Tot,VC}}$ peaks at values which can only be reached during the V/AV-pair creation process (see again dashed gray horizontal lines). This maximum in energy corresponds to a maximum velocity of $\mathrm{v} \approx 650\frac{\mathrm{m}}{\mathrm{s}}$. For better comparability between the peak in velocity and energy respectively the position is indicated by a second bold red line. After the passing-by of the two HCs, $E_{\mathrm{Tot,VC}}$ decays during the building-up of a new dip region with $p = -1$ (l) and the formation of a long dip along the internal Neèl type wall (m). As proven in the previous consideration of v, $E_{\mathrm{Tot,VC}}$ stays after the second reversal below the critical value required for another fast RP. To draw a preliminary conclusion, it is found that the interaction of the SWP with the VC sets the VC in an overcritical state which is characterized by an unusual high velocity and energy which cannot be reached by the applying of an external field. The finding of a short living overcritical state which leads to an energy transfer from SWP to VC can be seen by two facts: On the one hand, after the passing by the first HC of the SWP, the VC stays in a state of high velocity ($\mathrm{v} \approx \mathrm{V_c}$), and on the other hand, the minimum energy after the first reversal is as high as short before the first V/AV-pair creation. Unfortunately, these findings cannot explain the second and unexpected polarity reversal at all. This can be understood by the argument that although, when there is a energy transfer into the VC, there is no reason why $E_{\mathrm{Tot,VC}}$ should increase at a certain point again while the VC is moving backwards to the middle of the stripe. Assuming the VC has more energy than one would expect after the first reversal, it should loose its additional energy by classical magnetic damping mechanism. Therefore, the decay in $E_{\mathrm{Tot,VC}}$ after the first reversal should only by delayed in time and no increase in energy should occur. This argument can be understood in terms of the quadratic potential. Having a VC with an extra portion of energy causes simply a shift of the potential higher in energy but does not change the general shape and thus does not influence the basic dynamics of the system. Having a VC and the adjacent dip region short time after the first reversal process, the energy difference between VC and dip should decrease while

running backwards and no reversal should occur. Based on these arguments a physical mechanism has to be found that leads to the increase in energy which is also visible in Fig. 4.10(f-h) by a growing dip region. Based on the described behavior of $E_{\mathrm{Tot,VC}}$, it is reasonable to suspect the reflected parts of the SWP as reason for the increase in energy because $E_{\mathrm{Tot,VC}}$ starts to rise as soon as the oscillations arrive at the VC. On the other hand, simulations for driving fields higher than 1.5 mT were performed where it is obtained that the second reversal occurs before the reflected SWP reaches the VC. Hence, the interactions with the constant flow cannot be the main reason for the second reversal but maybe, at least, supportive.

4.2.9 Double Reversal Process: Considerations in the Frame of Gyrofield h_{gyro} and Zeeman Energy Caused by it

To clarify this picture, a close look is taken on the gyrofield $h_{\mathrm{gyro,z}}$ and the Zeeman energy $E_{\mathrm{gyro,z}}$ caused by the field.

In the upper part of Fig. 4.18 the calculated z-component for the gyrofield $h_{\mathrm{gyro,z}}$ has been presented. While the influence of the X and Y components of h_{gyro} can be neglected, $h_{\mathrm{gyro,z}}$ is the driving force for the dynamic processes in the system. To get an idea how to interpret the snapshots for the gyrofield and the Zeeman energy caused by it, it is explained as an example for the situation given in snapshot (a). In (a) the VC is approaching the critical velocity V_{c} and one can see at the position where the VC is located a bright and dark spot which indicates a strong positive (white) and negative (black) gyrofield. In the region where the dip region with polarity $p = -1$ forms, a less dark region can be seen. It passes into the grayish region where the internal Neél type wall is located and creates its on negative gyrofield. Why this gyrofield is causing an deformation of the VC or in general can influence the VC dynamics becomes clear when considering sketch (A) where m_z (bold black line) and the gyrofield $h_{\mathrm{gyro,z}}$ (dashed green line) are drawn. Regarding the situation immediately before the appearance of the first reversal, the initial symmetric VC has deformed into the remaining part of the VC with $p = 1$ (positive m_z) and the dip region with $p = -1$ (negative m_z). Taking this as a one-dimensional VC toy model and neglecting, for now, the dynamic changes caused by $h_{\mathrm{gyro,z}}$, a one dimensional VC moving with constant velocity v is given. From Eq. (4.33) it can be see that the shape of $h_{\mathrm{gyro,z}}$ is governed by the derivative of m with respect to the spatial coordinate. The VC area is subdivided into four regions which are determining regions where the m_z and $h_{\mathrm{gyro,z}}$ are aligned parallel or antiparallel with respect to each other. In region 1 and 3 the magnetization and the gyrofield are parallel to each other (indicated by the black and green arrows in sketch A) which means that $h_{\mathrm{gyro,z}}$ favors the directions of m_z in that regions. On the other hand, an antiparallel alignment of magnetization and field is present in regions 2 and 4. Here, the gyrofield prefers a change in the orientation of m_z which drives, for example, the creation of the dip region close to the initial VC. The consideration of the stabilizing and destabilizing action of the gyrofield on the magnetization can be considered from the energetic point of view as well. From the calculated gyrofield and the magnetic texture, the Zeeman energy $E_{\mathrm{gyro,z}}$ can be obtained

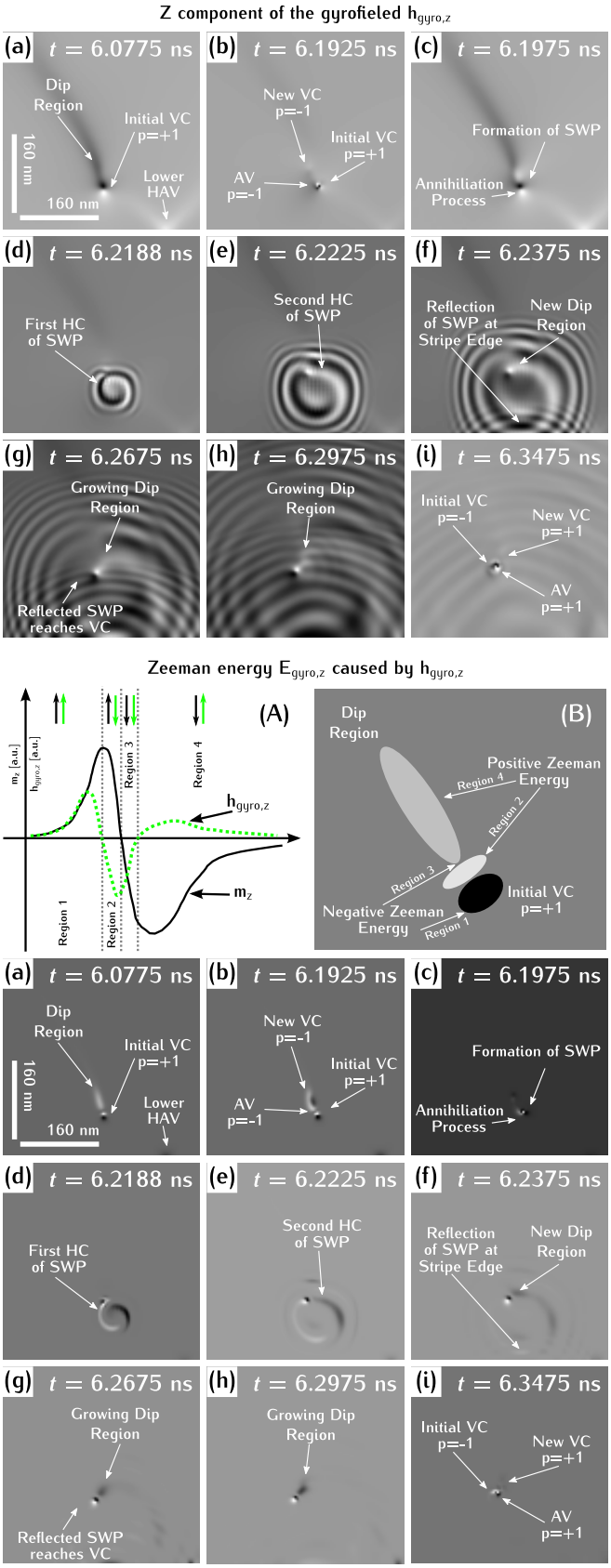

Figure 4.18. The diagrams show h_{gyro} (top) and $E_{\mathrm{gyro,z}}$ (bottom) at important time steps for the DRP. In addition, an explanation ((A) and (B)) for the result concerning $E_{\mathrm{gyro,z}}$ is given. Because of the available space, only the first nine snapshots of the important time steps are given in this figure. For the complete series of pictures covering the full DRP it is referred to Appendix A10.

from the simulation data with the expression[1] [21]:

$$E_{\mathrm{gyro,z}} = -\mu_0 \int_V m_z \cdot h_{\mathrm{gyro,z}} \mathrm{d}V \tag{4.35}$$

The results from this calculation are shown in the lower nine snapshots in Fig. 4.18. For a better understanding how to interpret the pictures showing $E_{\mathrm{gyro,z}}$ for the key steps in the RP, sketch B is drawn in Fig. 4.18. Sketch B gives, for example, the situation in snapshot Fig. 4.18(a), and it can be understood with the considerations done before. In Fig. 4.18(a) a dark and a bright spot can be seen at the position of the deformed VC. Close to the VC where the dip region establishes, a small grayish and a long white region are present. The black and gray regions correspond to negative or zero Zeeman energy while bright regions mark areas where the gyrofield causes a positive Zeeman energy, respectively. With this picture it is possible to understand the deforming action of the gyrofield on the magnetic texture of the VC. In areas where m_z and $h_{\mathrm{gyro,z}}$ are aligned parallel, a negative $E_{\mathrm{gyro,z}}$ is obtained, which means that the magnetization is in an energetic favorable state in these regions. Such areas are region 1 and 3 in sketch Fig. 4.18(B). Everywhere m_z is antiparallel, and with respect to $h_{\mathrm{gyro,z}}$ a positive Zeeman energy is found. In these areas (here region 2 and 4 in Fig. 4.18(B)) the magnetization is in an energetical unfavorable state. This is the energetic point of view why the gyrofield causes a deformation of the VC. The system wants to minimize its energy in this region and tries to align m_z parallel to $h_{\mathrm{gyro,z}}$. With this knowledge how to calculate and understand the snapshots for the gyrofield and the Zeeman energy in Fig. 4.18, the key steps of the fast DRP are revisited. Since being interested in the reason why there is an increase in $E_{\mathrm{Tot,VC}}$ short before R2, only the steps up to the point where the second reversa occurs are presented. The complete series of time steps for the DRP are shown in Sec. A10. As depicted in Fig. 4.18(a), the fast moving magnetic texture of the VC causes a strong gyrofield that deforms the structure of the VC. In time step Fig. 4.18(b) where the slitting of the dip region into the V/AV-pair appears, at the location of the new VC with $p = -1$ only a light white and grayish region can be seen. It indicates a low gyrofield and thus, a low velocity of the VC. In principle, the same situation is encountered in Fig. 4.18(c) where strong gyrofields of the forming SWP can be recognized. The interesting time steps are the subsequent ones where the first and second HC of the SWP hits the VC. As it can be seen in snapshot Fig. 4.18(d), the gyrofield which is caused by the first HC of the SWP is negative and so aligned parallel to the magnetization in the new VC. Interpreting this in terms of energy, the gyrofield of the first oscillation sets the VC in an energetically favorable state with negative $E_{\mathrm{gyro,z}}$ what can be seen as a black dot at the position of the VC in the snapshot Fig. 4.18(d) for the Zeeman energy.

To avoid confusion, the first HC of the SWP itself appears as a white half circle in the pictures for $E_{\mathrm{gyro,z}}$. This is caused by the self-interaction of the magnetization of the first HC and its own created gyrofield which results here in high $E_{\mathrm{gyro,z}}$. The effect of this energetically favorable situation is that the VC wants to stay in that state and it is dragged along with the first HC. This results in a high velocity which has already been found in Fig. 4.17(d). After the passing by of the first HC, the VC exhibits a high velocity close to V_{c} what can

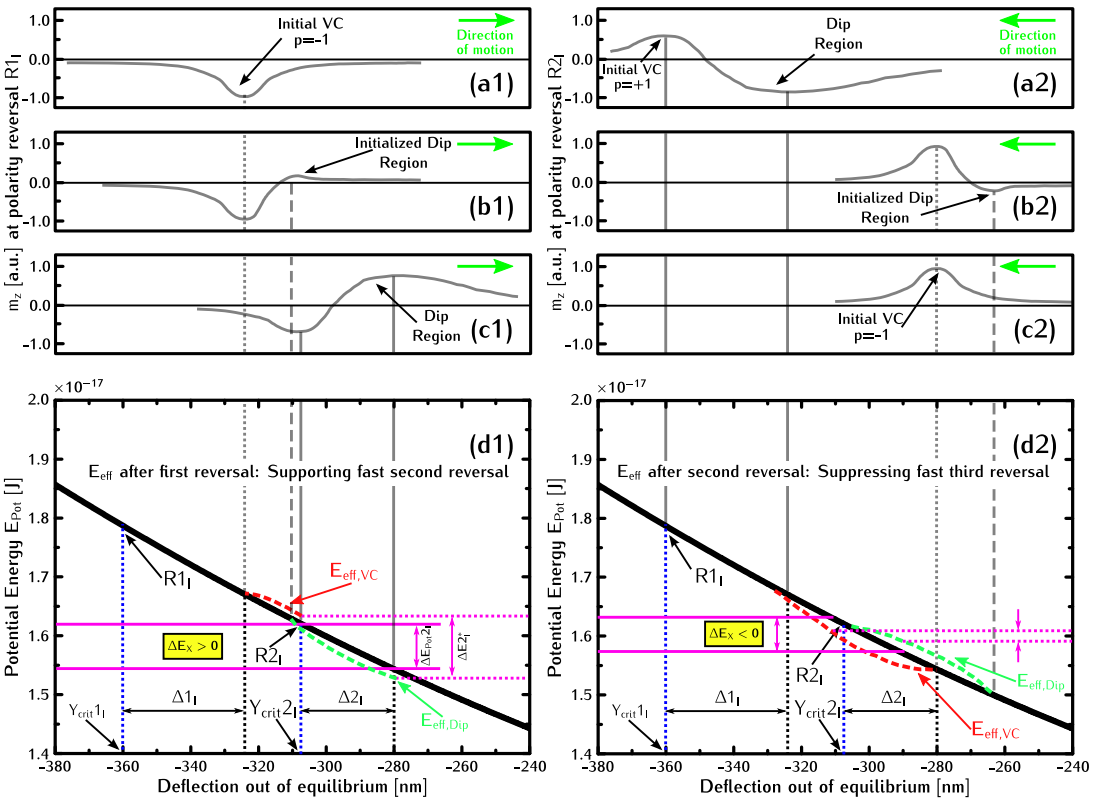

Figure 4.19. In this figure a qualitative explanation for the appearance of the fast second RP and the suppressed third one is given. (d1) illustrates the effective potential $E_{\mathrm{eff,VC}}$ and $E_{\mathrm{eff,Dip}}$ for the VC and the dip region before the second RP. This effective potential which leads to an increase (ΔE_{X} positive) of energy difference between both (VC and dip region) is caused by the SWP. (d2) gives the basic situation after the second RP. This time the effective potential which is caused by the SWP created in the second RP leads to a decrease of energy difference between VC and dip region. This negative ΔE_{X} hinders the VC from a fast third RP. For a better understanding of the mechanism, the magnetic texture of m_{z} for both situations is given at three important time steps. While (a1)-(c1) depicts the situation after R1, (a1)-(c1) clarifies the situation after R2. (a1) is the situation after the fist reversal which creates a new VC with polarity $p = -1$, while (b1) is the magnetic configuration after the hitting of the first HC of the SWP1. As it can be seen, the hitting of the SW front creates a slight dip region which will increase later on (c1) due to the energy transfer from the spiraling SWP into the magnetic texture of the VC and dip region. As can be seen in (d1), the energy transfer can be understood by an effective potential for VC and dip region, which is created by the gyrofield $h_{\mathrm{gyro,z}}$ and delivers the extra amount ΔE_{X} of energy needed for a second fast polarity reversal ($\Delta E_{\mathrm{X}} > 0$). After R2 a new VC with polarity $p = 1$ is present as depicted in (c2). Please note that the time evolution in the case of R1 is given from (a1)-(c1), while for R2 it is given by (c2)-(a2). This is also indicated by the green arrows giving the direction of the motion of the VC. After the hitting of the first HC of SWP2, a small dip region is created (b2), but here it is not enhance due to the effective field created by the SWP2. $h_{\mathrm{gyro,z}}$ favorites energetically the magnetic texture of the VC and not as before the dip region creating $\Delta E_{\mathrm{X}} < 0$. (a2) shows a large dip region as present before another reversal process. But this situation is not due to any effect of the second SWP. After R2, the SPW decays, the effective potential vanishes and both, VC as well as dip region, are moving in the same potential. The new large dip and third reversal is, then, created by the usual self-created gyrofield of the VC itself.

be seen in the pictures Fig. 4.18(e-h) for $h_{\mathrm{gyro,z}}$ and especially $E_{\mathrm{gyro,z}}$ where at the position of the VC a bright white and black dot appear close together. The discussion has arrived, now, at a very crucial point in the consideration which will lead to the understanding of the increase in $E_{\mathrm{Tot,VC}}$ short before the second PR. So far, it has been only confirmed by the investigation of $h_{\mathrm{gyro,z}}$ and $E_{\mathrm{gyro,z}}$ what has been found previously by the behavior of v and $E_{\mathrm{Tot,VC}}$ during the DRP. The first SWP HC leads to an energy transfer into the VC and accelerates it to high velocities. This sets on the starting point for the second reversal in a non trivial manner. Due to the fast moving VC after the first HC, the gyrofield caused by it begins to deform the VC again and a small dip region with $p = 1$ starts to form. This is not surprising at all and would not lead to the increase of energy in the VC area as mentioned earlier; but the subsequent second HC of the SWP creates a positive $h_{\mathrm{gyro,z}}$ which energetically favors the dip region more than the VC with $p = -1$. This second HC can be seen in Fig. 4.18(e) as white or black half circle in the pictures for $h_{\mathrm{gyro,z}}$ and $E_{\mathrm{gyro,z}}$, respectively. In the case of the first HC, as already described before, the second one causes, due to the self-interaction of its magnetization with the created gyrofield, a region of negative Zeeman energy. This has a very complicated interplay of the gyrofield created by the VC, the SWP and the magnetization of both of them, as result. The created gyrofield of the fast moving VC provides a potential which attracts the first and the second HC of the SWP at the upper and lower part of the VC, respectively. This is the reason why the two HCs are somehow attached to the VC for a short period of time what can be seen in Fig. 4.10(e-f). Especially the interplay of the gyrofield in the upper part (black dot) of the VC and the magnetization of the second HC are important for the second polarity reversal. Due to the interaction of both, the second HC is forced to travel around the VC and so it favors energetically the dip region almost from the beginning of the backwards motion until the second reversal appears. This can be seen in the snapshots for the Zeeman energy Fig. 4.18(d-h).

4.2.10 Double Reversal Process: The Effective Potential for VC and Dip Region

The consequence of this is that the dip region and the VC are subjected to different effective potentials while moving backwards to the middle of the stripe. The VC is set a little bit higher in energy and the energy of the dip is lowered. The exact shape of this time dependent effective potential is hard to estimate but a basic sketch is found in Fig. 4.19(d1). The energetic up-splitting of VC and dip region due to the Zeeman energy provides the additional energy E_{X} needed for the second reversal. The remaining question is why a third reversal does not occur. It can be answered in the same frame of different effective potentials for VC and dip region after reversal R1 and R2. After the second reversal, a SWP is created again by the annihilation process and it starts to influence the new VC with $p = 1$. First, the VC is pushed into an overcritical state by the first HC of the SWP, which can be seen by a steep increase in velocity (Fig. 4.17(d)) and energy Fig. 4.17(e) in the VC area as soon as the first HC hits the VC; but now, the effect of the second HC, which is bending around the VC, is different. Again a new dip region emerges due to the high velocity which is caused by the first HC

of the SWP. In contrast to the situation after the first reversal, the second HC does not support the dip region but the VC that can be seen in the snapshots (j-o) for $h_{\mathrm{gyro,z}}$ and $E_{\mathrm{gyro,z}}$ in Sec. A10. Lets regard the situation in the frame of a parabolic potential in combination with an effective potential again; the VC is moving in a different potential due to the SWP. After the second reversal, the polarity changes, and hence, the gyrotropic force changes its sign. The VC starts to move again to the lower edge of the stripe and the structure composed out of VC and dip increases its energy in the potential. This time the second front of the SWP has the opposite effect. $h_{\mathrm{gyro,z}}$ leads to a lower and higher effective potential for VC and dip region which decreases the energy difference between both of them (Fig. 4.19(d2)). This is suppressing the building-up of the energy difference which is necessary for the RP. The suppressing action lasts as long as the SWP is present; but since a new reversal is suppressed, the SWP vanishes slowly, and the effective potentials for VC and dip converge to the same parabolic potential. After this, the system needs some time to reach again the critical velocity V_{c} until the next fast DRP appears. At this point it turns out why the method in investigating the fast DRP by utilizing the Zeeman energy and the gyrofield is so practical. Regarding the magnetization it is possible to argue that the initialized dip region and the second SWP HC, which have the same direction of m_z, add up simply and enhance, in this way, the dip region until the second reversal occurs. This holds true for the second reversal but within this consideration there should be a third reversal as well because the SWP coming from the second reversal supports the dip formation. Taken m_z into account the magnetization of the second HC is parallel again to the magnetization in the dip region, should add up and lead to a new reversal. As it becomes clear from the simulations, this is not the case, and it can be understood when the process in terms of Zeeman energy is investigated. In the first reversal, $E_{\mathrm{gyro,z}}$ supports the formation and enhancement of the dip region, in the second one it does not.

4.2.11 Double Reversal Process: Influence of the Half Antivortices

The last remaining thing which has to be clarified is why the critical displacements and energies connected with the fast DRP change from one to another. As demonstrated in Fig. 4.11, the values for this characteristic quantities are decreasing. Interestingly this trend does not continue for all DRPs. It stops always after two or three DRPs; after these $Y_{\mathrm{crit}}1$, $Y_{\mathrm{crit}}2$, $E1$, $E2$ and $E3$ recover approximately to the starting values of the first DRP. Furthermore, it is worth mentioning that while the differences in total energy ΔE stay constant (within a certain error) the energies ΔE^* undergo significant variations. To understand this property, a close look has to be taken to the parabolic potential itself. So far, the whole discussion about the dynamics of the DRP has relied on the assumption of a time constant parabolic potential. The energy contributions of the HAVs at the upper and lower edge of the stripe have been calculated and substracted from the total energy. This was suitable to understand the basic dynamics. For the fine details, for example, understanding the changes of the mentioned quantities in time, the effects of the HAVs have to be taken into account additionally. In Fig. 4.19(a) the distance of the two HAVs in dependence

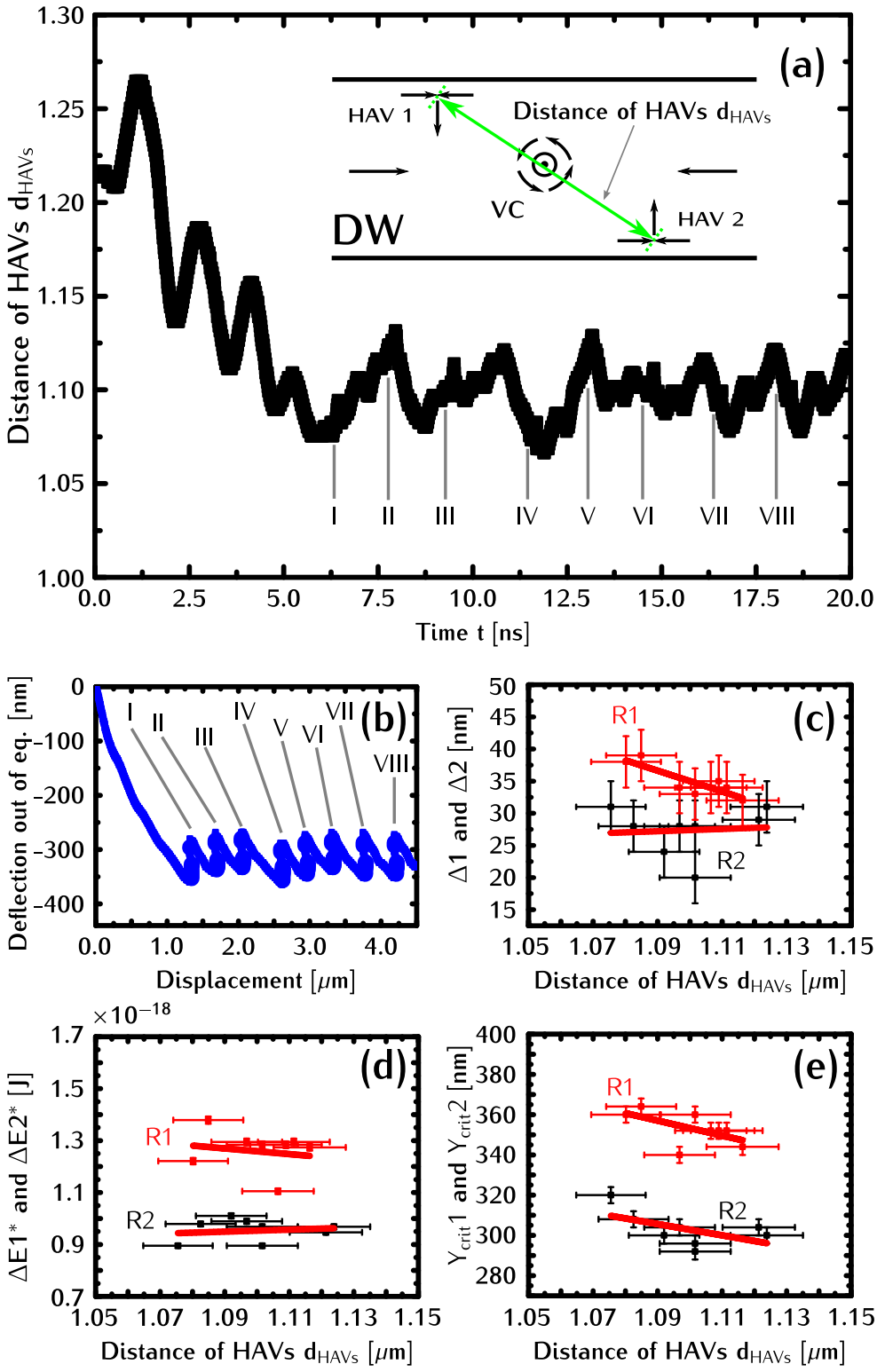

Figure 4.20. The graphs in this figure prove the connection between the time dependence of quantities characterizing the RP ($\Delta 1$,$\Delta 2$,$\Delta E1^*$,$\Delta E2^*$,$Y_{\mathrm{crit}}1$,$Y_{\mathrm{crit}}2$) and the distance of both HAVs (d_{HAVs}). (a) The variations of d_{HAVs} during time changes the form of the potential slightly. This has an influence on the trajectory (b) and also on the distance of old and new VC (c), the released energies (d) and the transverse displacements (e).

of time (Fig. 4.19(b)) has been plotted for eight DRPs. The inset in Fig. 4.19(a) shows how the distance d_{HAVs} is defined. Applying a field, d_{HAVs} starts to exhibit an undulated decrease in distance from initially $d_{\mathrm{HAVs}} = 1.22$ μm to an average value of $d_{\mathrm{HAVs}} = 1.10$ μm. This undulatory decrease appears because of the transient response of the coupled system of VC and HAVs. In this transition period, the VC and the two HAVs push and pull in a mutual influence onto each other until they reach a stable state. As it becomes clear when looking at Fig. 4.19(a), the stable state at an average distance of $d_{\mathrm{HAVs}} = 1.10$ μm is not constant at all but exhibits variations. These variations are caused by the mutual influence of the three subsystems which cause variations in the range of approximately 100 nm and can be understood by the concept of modes. d_{HAVs} is a measure to characterize the DW width, and as it can be seen in Fig. 4.19(a), the DW width undergoes oscillations. From the point of view of modes, DW oscillations are expected to occur at very high external fields H exceeding values of approximately 3.5 mT and depending on the DW model and stripe width w under consideration. For the description of the steady-state motion in the linear regime and for the oscillatory motion of the VC above the Walker breakdown, the inclusion of the X- and Y-coordinate (modes with τ_0 and τ_1, respectively) of the VC is basically sufficient. In Fig. 4.21 the decay times τ and the characteristic time T for field values between 0 and 2 mT are plotted for a stripe with $w = 880$ nm and $t = 20$ nm. Below the critical field H_{c} a one- or two-mode approximation can be chosen, depending on the goal one wants to achieve. For the prediction of the steady-state velocity, only the mode with τ_0 (red line) is necessary and the characteristic time T can be chosen between τ_0 and τ_1 (blue line). As an example, a dashed green line is drawn at 35 ns for external fields below H_{c}. In the case the transient motion of the VC in the linear regime has to be captured additionally, T has to be lower than τ_1 (bold green line). Concerning the steady-state regime, the considerations holds true for both chiralities χ. After reaching the critical value for the external field H_{c} where the steady-state motion transforms to a motion of where the VC core continuously crosses the stripe in transitional direction, the situation changes. To capture the feature of this dynamic regime accurately, a two-mode approximation has to be applied. This can be done when the X- and Y-coordinate of the VC is included. In this regime, the characteristic time T is determined by the time T_{trans} (see Eq. (2.251)), and the VC needs to cross the stripe on its way from one HAV to the opposing one. T_{trans} is indirectly proportional to the external field and is given by the green bold line in Fig. 4.21 above the Walker breakdown. Based on the CCA, the next higher mode with decay time τ_2 is the Eigenmotion of the two HAVs confined at the edges. Using the CCA, it follow that the decay time of this mode is given by [45, 47]

$$\tau_2 = \frac{4m}{\Gamma_{XY}} \tag{4.36}$$

where m is the effective mass of the HAV and Γ_{XY} the off-diagonal component of the damping tensor Γ. Taking the value for the effective mass m of the HAV estimated in [45] as $m = 1.1 \cdot 10^{-23}$ kg, it yields for stripe dimensions as used in the experiment $\tau_2 = 1.1$ ns (violet bold line in Fig. 4.21). Such low values for τ_2 lead to the fact that the Eigenmotion of the HAVs and DW oscillations respectively are only excited when T_{trans} falls below 1.1 ns. A case which can

be achieved for very high fields but not for field values slightly higher than the Walker field H_c. However, this holds true only for VDWs exhibiting a chirality $= -1$ where the VC collides with one of the HAVs and being remitted into the stripe with opposite polarity p. As proven experimentally by analytical models and micromagnetic simulations, a different behavior for VDWs with $= +1$ is present. Reaching the critical transverse displacement, the VC performs a free polarity reversal within the stripe and starts the previous described DRP with its two fast PRs. The analytical model presented in [45] yields different critical transverse displacements for both chiralities but is not able to predict the highly dynamical DRP. From the point of view of time scales, the DRP occurs at very short times. Regarding one DRP, the time between the first and second polarity reversal is approximately given by 0.25 ns, and even the time between to DRP itself is estimated as 1.25 ns. These motions exhibit short enough time scales to be able to excite the modes of the HAVs leading to DW oscillations. While T_{trans} is the fitting characteristic time T for DWs with $= -1$, the times associated with the DRP are the right measure and have to be used for T. This leads to the consequence that a precise description requires a six-mode approximation including the VC and the two HAVs as massive particles moving along the stripe and under mutual influence. In contradiction to the VC, the spatial coordinates of the HAVs are given by their X-coordinate and the out-of plane angle ϑ of the magnetization. Even when these DW oscillations are relatively small changes, they can have a modifying influence on the parabolic potential by bending the potential line slightly up and down. After the DRP set in, the excited motion of the HAVs modifies the potential seen by the VC until it becomes that distorted that a longer time is needed to reach the next DRP. During this time, the motion of the HAVs (and as a consequence the DW oscillations) decay and the parabolic potential recovers fully or at least partially until the next series of fast DRPs starts. Summing up, the DRP of the VC present in wide stripes leads to a continuous periodic start and stop of DW widths oscillations for VDWs with chirality $= +1$. In order to prove the connection between the changes of Y_{crit}, ΔE^* and the distance between the old and new VC ($\Delta 1$ and $\Delta 2$); these quantities are plotted with respect to d_{HAVs}. Fig. 4.19(c-e) shows the results. The red points belong to the first and the black points to the second RP, respectively. Referring to the first reversal (red), all quantities show a negative slope with increasing d_{HAVs}. The picture for the case of the second reversal is not that clear. While these quantities increase below the average value of d_{HAVs}, they reach a minimum at the average of d_{HAVs} and increase again. This is attributed to the fact that the first reversal is a classical one which is triggered by the reaching of a critical velocity and fully characterized by the potential itself. In contrast to this, the second reversal is mainly dominated by the influence of the SWP and the effective potential caused by it. Hence, the decreasing tendency which is also present in the slopes for the quantities belonging to the second reversal is superimposed with the effect of the effective potential.

4.2.12 Conclusion

In conclusion it has been found that the displacement of VDWs under the action of magnetic field pulses depends on the chirality of the initial state. This can be

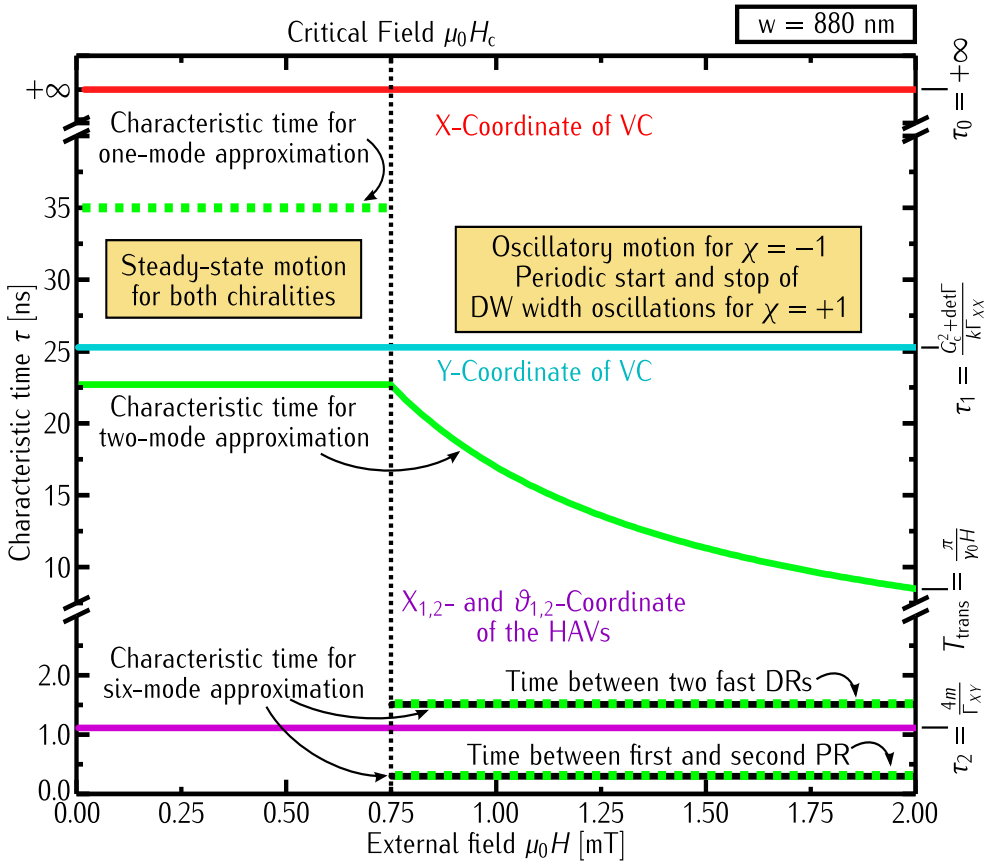

Figure 4.21. Graphic displays of decay times (τ_0-τ_2) for the three highest modes of a VDW and the characteristic times T in the different dynamic regimes in dependence on the external field $\mu_0 H$. Values have been calculated for a stripe geometry as used in the experiments with width $w = 880$ nm and thickness $t = 20$ nm. Red and blue bold lines mark the decay times for the modes of the X- and Y-coordinate (τ_0 and τ_1) of the VC, while the violet bold line gives the decay time for the mode of the HAVs (τ_2). The bold and dashed green lines mark the characteristic time T in the two different dynamic regimes, namely the steady-state and oscillatory motion below and above the critical field H_c, respectively. Additionally, the times originating from the DRP are drawn as a green/black dashed line in the diagram.

understood by the use of the Thiele equation and the concept of a critical VC velocity. Wide-field MOKE measurements show that the effect is robust enough to be observed in real samples where disorder leads to significant broadening of the displacement histograms. From the theoretical point of view, it was obtained in micromagnetic simulations with mumax3 that DWs with chirality $\chi = 1$ show an oscillatory movement which causes a higher average velocity than one could expect for applied fields above WB. This oscillatory motion is caused by a fast double reversal process (DRP) of the DW polarity. As it turns out, this DRP is triggered by the interaction of SWPs originating in the polarity reversal itself with the VC. It has turned out that the gyrofield h_{gyro} plays an important role in understanding this process. The gyrofield interacts with the magnetization and causes an effective field for the VC and the dip region which supports a second polarity reversal but suppresses a fast third one. Small variations found for key quantities like transverse displacement or energies can be attributed to a slight change of the parabolic potential in which the VC moves. This change can be explained by taking into account the influence of the HAVs on the potential. This influence occurs because of the Eigen motion of the HAVs, which is excited by the motion of the VC during the continuous appearing DRP.

Summary

To conclude this thesis, a short summary of the work done will be given. This thesis deals with the dynamics of field-driven vortex domain walls (VDWs) [56] in ferromagnetic nanostripes [49] made out of $Ni_{80}Fe_{20}$. More precisely spoken, the special dynamics of VDWs for external applied fields H exceeding the critical Walker field H_c [29] is investigated by experimental work (see Sec. 4.2.4), micromagnetic simulations [67, 68] (see Sec. 4.2.3-4.2.11) and analytical calculations (see Sec. 4.2.2 and 4.2.11).

Magnetization dynamics is governed by the Landau-Lifschitz-Gilbert equation (LLG eq.) [23–25] which can be reformulated into the Thiele equation [34], an effective force equation which is more suitable for the description of domain wall motion (DWM). The basic properties of the LLG eq. is presented in Sec. 2.1, while the reformulation into the Thiele eq. (Sec. 2.2) is explained very detailed with all intermediate steps in Sec. 2.2.1-2.2.4. Subsequently, the dynamics of VDWs is described from the theoretical point of view in Sec. 2.3 by introducing the magnetic structures under consideration (VDWs) first in Sec. 2.3.1. They are depicted by presenting the different types of magnetic DWs found to exist in ferromagnetic nanostripes [49, 53–56] and proceeding to introduce the properties of VDWs, including their specific dynamics [49] (see Sec. 2.3.1). The mathematical description of VDW dynamics is done in this thesis in the frame of the collective coordinate approach (CCA) [45, 47] (Sec. 2.3.2), a generalized version of Thiele's analysis [34]. Basic concepts and ideas (Sec. 2.3.2.1-2.3.2.4) are introduced and key quantities like the acting forces $\vec{F}^f$ (Sec. 2.3.2.5) on the DW due to the external field H, gyrovector $\vec{G}$ (Sec. 2.3.2.6) and damping tensor Γ (Sec. 2.3.2.7 and 2.3.2.8) are calculated in the frame of the CCA by using a simplified analytical VDW model [59]. The resulting equations of motion (Sec. 2.3.2.9 and 2.3.2.10) are solved in Sec. 2.3.3, whereby the results are important to understand the dynamics of the VDW for fields holding $H > H_c$ (presented in Sec. 4.2). Sec. 2.4 and Sec. 2.5 close the theoretical considerations in Ch. 2 by laying the theoretical foundations for the measurement techniques of ferromagnetic resonance (FMR) (including time-resolve MOKE) [37, 38, 93, 127] and the magneto-optical Kerr effect (MOKE) [37, 97, 98, 128]. Results which are important for the sample characterization and DWM measurements utilizing a wide-field MOKE setup [50, 128] are presented in Ch. 4.

Ch. 3 provides an overview on the experimental techniques and the applied methods of data evaluation. Sec. 3.1 explains the chosen sample design, while in Sec. 3.2-3.5 the utilized measurements techniques, followed by the description of the applied data evaluation methods (Sec. 3.6 and 3.7). Ch. 4 is dedicated to the results of the sample characterization (Sec. 4.1) and the chirality dependent VDW dynamics at fields higher than the critical field H_c (Sec. 4.2). In the sample characterization a good quality of the sample and the thin magnetic layer made out of Al/$Ni_{80}Fe_{20}$/Al was evidenced. The saturation magnetization was found in SQUID measurements (Sec. 4.1.1) to be $\mu_0 M_s = (0.917 \pm 0.053)$ T and thus, in good agreement with available literature values [38]. In order to check further the sample quality, full-film FMR (Sec. 4.1.2) and time-resolved MOKE measurements on the structurized sample (Sec. 4.1.3) were performed to obtain the Gilbert damping parameter α [24, 25]. Both measurement techniques resulted in a value of $\alpha \approx 0.006$, which is also in good agreement with literature values [38]. Additionally, the characterization was performed from the DWM point of view by two different means, namely recording depinning probabilities P_{depin} [22, 120] (Sec. 4.1.4) and the v-H-curve (Sec. 4.1.5). The depinning probabilities are important to know in order to assess a possible influence of pinning on the main experimental data (Fig. 4.8). From P_{depin} in dependence on $\mu_0 H$, a pinning field of $\mu_0 H_{\mathrm{P}} = (0.91 \pm 0.05)\,\mathrm{mT}$ and uncertainty $\mu_0 \sigma_{\mathrm{P}} = (0.17 \pm 0.01)\,\mathrm{mT}$ is estimated for stripes with width $w = 880$ nm. The mobility curve v-H allows to determine the critical field H_c for choosing the appropriate field values for the investigation of the chirality-dependent VDW dynamics. With a critical field $\mu_0 H_c = (0.74 \pm 0.07)\,\mathrm{mT}$, the result is comparable to other works [17, 22, 45, 80]. Furthermore, it yields a low field mobility μ_{LF} of $\mu_{\mathrm{LF}} = (730.7 \pm 43.3) \cdot 10^3\,\frac{\mathrm{m}}{\mathrm{Ts}}$. The determined parameters were also used as input material parameters for the micromagnetic simulations and analytic calculations.

In Sec. 4.2 the chirality-dependent dynamics for field-driven VDWs at external magnetic fields exceeding H_c is investigated. In general, different DW displacements for a certain combination of external field H and pulse time t_p are found for VDW with chirality $\chi = 1$ and $\chi = -1$. These differences are traced down to chirality-dependent critical transverse displacements Y_{crit} (Sec.4.2.2) and a fast double polarity reversal process for VDWs with $\chi = 1$ (Sec. 4.2.3-4.2.11) (also observed by simulations in [138, 139]) and evidenced by experimental recorded VDW displacements and the comparison with micromagnetic simulations (Sec. 4.2.3 and Sec. 4.2.4). Starting with an analytical approach to the chirality dependent dynamics in Sec. 4.2.2, differences in key quantities as critical transverse displacement Y_{crit} and critical fields H_c are found by solving the two dimensional equations of motion obtained from the CCA (see Sec. 2.3.2.9 and 2.3.2.10). For the investigation of the dynamics above the Walker field H_c, micromagnetic simulations are used. Simulations of perfect stripes (Sec. 4.2.3) and, more realistic, simulations including grains (Sec. 4.2.4) reveal basically the same differences in behavior for both chiralities. VDWs with $\chi = 1$ perform a continuous repeated fast double polarity reversal process (DRP), while, in contradiction, VDWs with $\chi = -1$ undergo a classic polarity reversal [49] by colliding with one of the half antivortices (HAVs) located at the edges of the stripe and re-emitted (Fig. 4.7). The only difference which arises is a grain induced effect, which can lead to a kick out of the fast DRP leading to a multiple peak

structure in the displacement histograms which was evidenced by experimental data and the comparison with simulational results (see Sec. 4.2.4 and Fig. 4.8). The DRP itself is investigated purely by micromagnetic simulations and a detailed evaluation of the gained data. Starting with a descriptive approach of the key steps in the DRP (see Sec. 4.2.5 and Fig. 4.10), the trace, the energy and the potential of the VC are examined in Sec.4.2.6 (see Fig. 4.11). Proceeding to a more accurate discussion of the the latter mentioned quantities in Sec. 4.2.7 leads to the conclusion that the energy required for the unusual fast second polarity reversal has to be delivered by some physical process. Investigating the energy in the small VC region (see Fig.4.17) delivers a hint that the spin wave package (SWP) emitted in the free reversal process of the VC [62–64] has an influence on the DRP and is, at least, supportive for the appearance of the DRP (see Sec. 4.2.8 and Fig. 4.17). By investigating the effect of the gyrofield $\vec{h}_{\mathrm{gyro}}$ [21] caused by the first SW half cycle (HC) in Sec. 4.2.8 and 4.2.9, a different effective potential for VC and dip region in the first and second reversal process (RP) of the DRP is found (Sec. 4.2.9, Fig. 4.18 and 4.19). This fact can explain why there is no third fast RP. The question why after two or three DRPs the whole system takes longer for the next DRP can be explained by the influence of the HAVs (Sec. 4.2.11) due to the activation of DW width oscillation caused by the DRP itself (see Fig. 4.20 and 4.21).

This thesis is closed by the Appendix containing additional information to different topics in this thesis, for example, the characterization of the field pulses in Sec. A4 and supportive material concerning the evaluation of the simulational data obtained in micromagnetic simulations (Sec. A5-A10).

Appendix

A1 Short Introduction into the Tensor Calculation with the Outer Product

The information concerning the mathematics presented in this and the following two sections can be found in standard textbooks about mathematics and engineering sciences. For Sec. A1-A3 they are taken from [40–42, 48, 142–145]. In this section a short introduction into tensor calculation with the outer or tensor product will be given, which is very helpful in calculating the form of the force densities. For the evaluation of these densities, a change to the component-wise notation is convenient. Doing this, Einstein summation convention will not be applied and also the explicit basis vectors connected to the single components dealing with are given in the formulas. What follows now is the introduction of the outer product $\otimes$ which is defined as the product of two vectors $\vec{A}$ and $\vec{B}$ by

$$\vec{A} \otimes \vec{B} \tag{37}$$

with

$$\vec{A} = \begin{pmatrix} A_x \\ A_y \\ A_z \end{pmatrix} \qquad \vec{B} = \begin{pmatrix} B_x \\ B_y \\ B_z \end{pmatrix} \tag{38}$$

which can be written as the matrix multiplication of the vector $\vec{A}$ and the transposed vector $\vec{B}$. This yields.

$$\begin{aligned} \vec{A} \otimes \vec{B} = \vec{A}\vec{B}^{\mathrm{T}} &= \begin{pmatrix} A_x \\ A_y \\ A_z \end{pmatrix} \begin{pmatrix} B_x & B_y & B_z \end{pmatrix} \\ &= \begin{pmatrix} A_x B_x & A_x B_y & A_x B_z \\ A_y B_x & A_y B_y & A_y B_z \\ A_z B_x & A_z B_y & A_z B_z \end{pmatrix} \end{aligned} \tag{39}$$

As it can be seen, the outer product of two vectors with m rows produces

a $m \times m$ (here $m = 3$) matrix or tensor. This is very helpful when dealing component-wise calculation because it is immediately clear which entry in a matrix or tensor a certain term is addressed to. For example, having a matrix C defined by the outer product of the vectors $\vec{A}$ and $\vec{B}$

$$C = \vec{A} \otimes \vec{B} \tag{40}$$

the component C_{ij} of the matrix C is given by:

$$\begin{aligned} C_{ij} &= (A_i \vec{e}_i) \otimes (B_j \vec{e}_j) \\ &= A_i B_j \left(\vec{e}_i \otimes \vec{e}_j\right) \\ &= A_i B_j \left(\vec{e}_i \vec{e}_j^{\mathrm{T}}\right) \end{aligned} \tag{41}$$

Here, $\vec{e}_i$ and $\vec{e}_j$ are the basis vectors for $\vec{A}$ and $\vec{B}$. These components (i, j) cover the spatial coordinates (x, y, z) or other orthonormalized coordinates; for example, choosing $\vec{e}_i = \vec{e}_x$ and $\vec{e}_j = \vec{e}_x$, the outer product addresses $A_x B_x$ of the component C_{xx} to the right entry in the matrix C.

$$C_{xx} = A_x B_x \left(\vec{e}_x \otimes \vec{e}_x\right) = \begin{pmatrix} A_x B_x & 0 & 0 \\ 0 & 0 & 0 \\ 0 & 0 & 0 \end{pmatrix} \tag{42}$$

Summing over the indices, (i, j) yield the full matrix C:

$$C = \sum_{ij} C_{ij} = \sum_{ij} A_i B_j \left(\vec{e}_i \otimes \vec{e}_j\right) \tag{43}$$

The representation of an arbitrary matrix C on the base of the outer product enables to write down two more operations in this notation. The first one is the transposing of a matrix, where the transposed matrix C^{T} is given by

$$\begin{aligned} C^{\mathrm{T}} = \sum_{ij} C_{ij}^{\mathrm{T}} &= \sum_{ij} A_i B_j \left(\vec{e}_i \otimes \vec{e}_j\right)^{\mathrm{T}} \\ &= \sum_{ij} A_j B_i \left(\vec{e}_i \otimes \vec{e}_j\right) \\ &= \sum_{ij} A_i B_j \left(\vec{e}_j \otimes \vec{e}_i\right) \end{aligned} \tag{44}$$

were the property

$$\left(\vec{e}_i \otimes \vec{e}_j\right)^{\mathrm{T}} = \left(\vec{e}_j \otimes \vec{e}_i\right) \tag{45}$$

has be used. Here, another advantage of the notation with the outer product becomes obvious. The transposition, which means nothing else than changing the row to column vector and a column to a row vector, is achieved by changing the indices (i, j) of A_i and B_j or leave them unchanged; another possibility is to change the indices of the basis vectors. The second operation that can be written in this way is the matrix multiplication with a vector. When the matrix C is applied to a vector $\vec{b}$, it results in a vector $\vec{b}'$

$$\vec{b} = \begin{pmatrix} b_x \\ b_y \\ b_z \end{pmatrix} \qquad \vec{b}' = \begin{pmatrix} b'_x \\ b'_y \\ b'_z \end{pmatrix} \tag{46}$$

by the multiplication:

$$\begin{aligned} \vec{b}' = C\vec{b} = \sum_{ijk} C_{ij} b_k \vec{e}_k &= \sum_{ijk} A_i B_j \left(\vec{e}_i \otimes \vec{e}_j\right) b_k \vec{e}_k \\ &= \sum_{ijk} A_i B_j b_k \left(\vec{e}_i \otimes \vec{e}_j\right) \cdot \vec{e}_k \end{aligned} \tag{47}$$

For further simplification, the property

$$\left(\vec{e}_i \otimes \vec{e}_j\right) \cdot \vec{e}_k = < \vec{e}_j, \vec{e}_k > \vec{e}_i = \delta_{jk} \vec{e}_i \tag{48}$$

is utilized, where $< \vec{e}_j, \vec{e}_k >$ is the scalar product of both vectors,which yields the Kronecker delta δ_{jk}. Inserting it in Eq. (47) and summing over k, it results in:

$$\begin{aligned} \vec{b}' = C\vec{b} = \sum_{ijk} C_{ij} b_k \vec{e}_k &= \sum_{ijk} A_i B_j \vec{b}_k \delta_{jk} \vec{e}_i \\ &= \sum_{ij} A_i B_j b_j \vec{e}_i \\ &= \sum_{ij} A_i B_j b_j \delta_{jj} \vec{e}_i \\ &= \sum_{ij} A_i B_j b_j \left(\vec{e}_i \otimes \vec{e}_j\right) \cdot \vec{e}_j \end{aligned} \tag{49}$$

When the summation over i is left out, the i-th component of $\vec{b}'$ is obtained

$$\vec{b}'_i = \left(C\vec{b}\right)_i = \sum_j A_i B_j b_j \left(\vec{e}_i \otimes \vec{e}_j\right) \cdot \vec{e}_j \tag{50}$$

and leads to:

$$\vec{b}' = \sum_i \vec{b}'_i \tag{51}$$

This notation is also very helpful for the component-wise representation of the Jacobian matrix and its transformed matrix. Replacing the vector $\vec{A}$ by the nabla operator,

$$\vec{\nabla} = \begin{pmatrix} \frac{\partial}{\partial x} \\ \frac{\partial}{\partial y} \\ \frac{\partial}{\partial z} \end{pmatrix} \tag{52}$$

it is easily to be checked if the transposed Jacobian matrix $J^{\mathrm{T}}_{\vec{B}}$ of a vector $\vec{B}$ is given by:

$$
\begin{aligned}
J_{\vec{B}}^{\mathrm{T}} = \vec{\nabla} \otimes \vec{B} &= \sum_{ij} \left(\vec{e}_i \frac{\partial}{\partial x_i} \right) \otimes (B_j \vec{e}_j) \\
&= \sum_{ij} \frac{\partial B_j}{\partial x_i} (\vec{e}_i \otimes \vec{e}_j)
\end{aligned}
\tag{53}
$$

The Jacobian matrix $J_{\vec{B}}$ itself can be gained by transposing $J_{\vec{B}}^{\mathrm{T}}$.

$$
\begin{aligned}
J_{\vec{B}} = \left(J_{\vec{B}}^{\mathrm{T}} \right)^{\mathrm{T}} = \left(\vec{\nabla} \otimes \vec{B} \right)^{\mathrm{T}} &= \sum_{ij} \frac{\partial B_i}{\partial x_j} (\vec{e}_i \otimes \vec{e}_j) \\
&= \sum_{ij} \frac{\partial B_j}{\partial x_i} (\vec{e}_i \otimes \vec{e}_j)^{\mathrm{T}} \\
&= \sum_{ij} \frac{\partial B_j}{\partial x_i} (\vec{e}_j \otimes \vec{e}_i)
\end{aligned}
\tag{54}
$$

Here, the component-wise representation in combination with writing down explicitly the sum symbol and the basis vectors have been already applied. Since dealing with the two forces ($\vec{f}^{\alpha}$ and $\vec{f}^{\mathrm{g}}$) in these expressions, a Jacobian and its transpose occur. Another useful property of the outer product is given by the relation

$$
\begin{aligned}
(\vec{e}_i \otimes \vec{e}_j) (\vec{e}_k \otimes \vec{e}_l) &= < \vec{e}_j, \vec{e}_k > (\vec{e}_i \otimes \vec{e}_l) \\
&= (\vec{e}_j \cdot \vec{e}_k) (\vec{e}_i \otimes \vec{e}_l) \\
&= \delta_{jk} (\vec{e}_i \otimes \vec{e}_l)
\end{aligned}
\tag{55}
$$

where $< \vec{e}_j, \vec{e}_k >$ denote the scalar or inner product of the vectors $\vec{e}_j$ and $\vec{e}_k$. In the case of ortonormalized basis vectors, the scalar product is equal to

$$
\delta_{jk} = < \vec{e}_j, \vec{e}_k > = (\vec{e}_j \cdot \vec{e}_k) \tag{56}
$$

and at the same time, it is one possible representation of the Kronecker delta δ_{jk}. Returning back to the calculation of the force densities, it is possible at base of the mathematical framework to write down the general expression for the force density $\vec{f}^{x}$ as

$$
\begin{aligned}
\vec{f}_i^{\,x} &= -\mu_0 \sum_j \frac{\partial M_j}{\partial x_i} (\vec{e}_i \otimes \vec{e}_j) H_j^x \vec{e}_j \\
&= -\mu_0 \sum_j \frac{\partial M_j}{\partial x_i} H_j^x (\vec{e}_i \otimes \vec{e}_j) \cdot \vec{e}_j \\
&= -\mu_0 \sum_j \frac{\partial M_j}{\partial x_i} (\vec{e}_i \otimes \vec{e}_j) \cdot \vec{H}_j^x
\end{aligned}
\tag{57}
$$

and as well as the total vector $\vec{f}^{x}$:

$$
\vec{f}^{\,x} = \sum_i \vec{f}_i^{\,x} = -\mu_0 \sum_{ij} \frac{\partial M_j}{\partial x_i} (\vec{e}_i \otimes \vec{e}_j) \cdot \vec{H}_j^x \tag{58}
$$

Both formulas are a suitable starting point for the further evaluation of the four different force density terms appearing in Thiele's analysis. Additionally,

this notation is very helpful for performing a coordinate transformation. When one has, for example, an expression in polar coordinates,

$$A_{\rho\phi}\vec{e}_\rho \otimes \vec{e}_\varphi \tag{59}$$

where $\vec{e}_\rho$ and $\vec{e}_\varphi$ are the basis vectors in polar coordinates, and where $A_{\rho\varphi}$ represents an arbitrary prefactor. If the transformation of this expression into the Cartesian coordinate system is desired, the basis vectors $\vec{e}_\rho$ and $\vec{e}_\varphi$ have to be expressed simply by the basis vectors in Cartesian coordinates. This is given by the relations

$$\begin{aligned} \vec{e}_\rho &= \cos(\varphi)\vec{e}_x + \sin(\varphi)\vec{e}_y \\ \vec{e}_\varphi &= -\sin(\varphi)\vec{e}_x + \cos(\varphi)\vec{e}_y \end{aligned} \tag{60}$$

and it is acquired:

$$\begin{aligned} A_{\rho\phi}\vec{e}_\rho \otimes \vec{e}_\varphi =& A_{\rho\phi}\left(\cos(\varphi)\vec{e}_x + \sin(\varphi)\vec{e}_y\right) \otimes \left(-\sin(\varphi)\vec{e}_x + \cos(\varphi)\vec{e}_y\right) \\ =& -A_{\rho\phi}\cos(\varphi)\sin(\varphi)\vec{e}_x \otimes \vec{e}_x + A_{\rho\phi}\cos^2(\varphi)\vec{e}_x \otimes \vec{e}_y \\ & - A_{\rho\phi}\sin^2(\varphi)\vec{e}_y \otimes \vec{e}_x + A_{\rho\phi}\sin(\varphi)\cos(\varphi)\vec{e}_y \otimes \vec{e}_y \end{aligned} \tag{61}$$

This is very intuitive because having a matrix in polar coordinates with one single entry and transforming it to Cartesian coordinates, which means nothing else than applying a rotation matrix, yields in general four terms in the matrix. Therefore, the notation with the outer product offers an easy way to calculate the coordinate transformation of an expression. This framework is the mathematical basis for the calculation of the force terms appearing in the Thiele equation. Nevertheless, it is necessary to have an additional close look on the generalized Kronecker Delta and the ε-Tensor to understand, among other reasons, how it is possible to calculate the Thiele equation in one or two dimensions. This will be done in the next section.

A2 Short Introduction Into the Generalized Kronecker Delta and the ϵ-Tensor

As mentioned at the end of the last section, it is essential to have a deeper knowledge about the Kronecker delta, its generalization to many arbitrary indices, and the ε-tensor. This is important because of the following three reasons: The connection of the Kronecker delta with the inner product (sometimes called scalar product or dot product) of basis vectors will provide a tool to transform the component notation of the force terms in the Thiele equation into vector notation. Furthermore, a close look on the generalization of the Kronecker delta is helpful to understand the formulation of the gyrovector $\vec{G}$ in Thiele's original work [34], and how the generalization of the Kronecker delta is connected to the ε-tensor. As it will be seen, the latter one provides a method to calculate the ε-tensor, which is well known to physicists as Levi-Civita symbol, in arbitrary dimensions, and thus,the Thiele equation is reduced to one or two dimensions. Starting with the Kronecker delta δ_{ij}, which is defined by

$$\delta_{ij} = \begin{cases} 1 & \text{for equal indices, } i = j \\ 0 & \text{for unequal indices, } i \neq j \end{cases} \tag{62}$$

and can alternatively be expressed as the inner product of two normalized basis vectors $\vec{e}_i$ and $\vec{e}_j$:

$$\delta_{ij} =< \vec{e}_i, \vec{e}_j >= (\vec{e}_i \cdot \vec{e}_j) \tag{63}$$

This relation has already been used in the previous section about the calculation with the outer product in Eq. (55). As it can easily be seen by the definition of δ_{ij} via the dot product, one has $\delta_{ij} = \delta_{ji}$, which is an important property of the Kronecker symbol. The generalization $\delta^{lm\ldots n}_{ij\ldots k}$ to M index pairs is defined as the determinant

$$\delta^{lm\ldots n}_{ij\ldots k} = \begin{vmatrix} \delta_{li} & \delta_{lj} & \cdots & \delta_{lk} \\ \delta_{mi} & \delta_{mj} & \cdots & \delta_{mk} \\ \vdots & \vdots & \ddots & \vdots \\ \delta_{ni} & \delta_{nj} & \cdots & \delta_{nk} \end{vmatrix} \tag{64}$$

where the $2M$ indices must have the the same set of values $1, \ldots, N$. Based on this definition, $\delta^{lm\ldots n}_{ij\ldots k}$ yields the values 1, -1 and 0 in the following three cases:

$$\delta^{lm\ldots n}_{ij\ldots k} = \begin{cases} 1 & \text{When all upper indices differ from each other and the sequence of the lower indices results out of an even number of permutations of the upper indices.} \\ \text{-1} & \text{When all upper indices differ from each other and the sequence of the lower indices results out of an odd number of permutations of the upper indices.} \\ 0 & \text{For all other combinations of indices} \end{cases} \tag{65}$$

Apparently, it holds $\delta^{lm\ldots n}_{ij\ldots k} = \delta^{ij\ldots k}_{lm\ldots n}$. Defining the generalization of the Kronecker Delta in this manner makes sense, which can be seen by reducing $\delta^{lm\ldots n}_{ij\ldots k}$ to one index pair; it results in $\delta^l_i = \delta_{il}$. Based on this result, it becomes clear that the name Kronecker delta is justified. This generalized Kronecker symbol has remarkably similar properties like the Levi-Civita symbol, which is well known, for example, from the component wise representation of the cross product. As it will become clear now, the generalized Kronecker delta and the Levi-Civita symbol (in arbitrary dimensions) are directly related to each other. In other words, the Levi-Civita symbol is a special case of the generalized Kronecker delta. This special group of symbols is defined as

$$\varepsilon_{ij\ldots k} = \delta^{12\ldots M}_{ij\ldots k} = \delta^{ij\ldots k}_{12\ldots M} \tag{66}$$

where the lower or upper indices of δ are fixed to $12\ldots M$. These ε are also known as a sign of permutation (permutation symbol) or Levi-Civita symbol. The corresponding Levi-Civita tensor ε is defined by the summation over all possible index combinations of $\vec{e}_i \otimes \vec{e}_j \otimes \cdots \otimes \vec{e}_k$ weighted by the permutation

symbol $\epsilon_{ij\ldots k}$.

$$\varepsilon = \sum_{ij\ldots k} \varepsilon_{ij\ldots k} \vec{e}_i \otimes \vec{e}_j \otimes \cdots \otimes \vec{e}_k \tag{67}$$

Using the definition of the Kronecker symbol, it is also possible to calculate the product of two permutation symbols $\varepsilon_{ij\ldots k}$ and $\varepsilon_{lm\ldots n}$. Beginning with

$$\begin{aligned} \varepsilon_{ij\ldots k}\varepsilon_{lm\ldots n} &= \delta^{12\ldots M}_{ij\ldots k}\delta^{12\ldots M}_{lm\ldots n} = \delta^{ij\ldots k}_{12\ldots M}\delta^{12\ldots M}_{lm\ldots n} \\ &= \begin{vmatrix} \delta_{i1} & \delta_{i2} & \cdots & \delta_{iM} \\ \delta_{j1} & \delta_{j2} & \cdots & \delta_{jM} \\ \vdots & \vdots & \ddots & \vdots \\ \delta_{k1} & \delta_{k2} & \cdots & \delta_{kM} \end{vmatrix} \begin{vmatrix} \delta_{1l} & \delta_{1m} & \cdots & \delta_{1n} \\ \delta_{2l} & \delta_{2m} & \cdots & \delta_{2n} \\ \vdots & \vdots & \ddots & \vdots \\ \delta_{Ml} & \delta_{Mm} & \cdots & \delta_{Mn} \end{vmatrix} \end{aligned} \tag{68}$$

it is obtained by exploiting the property that the product of two determinants of matrices A and B is equal to the determinant of the matrix product AB ($\det(A)\det(B) = \det(AB)$):

$$\varepsilon_{ij\ldots k}\varepsilon_{lm\ldots n} = \begin{vmatrix} \delta_{il} & \delta_{im} & \cdots & \delta_{in} \\ \delta_{jl} & \delta_{jm} & \cdots & \delta_{jn} \\ \vdots & \vdots & \ddots & \vdots \\ \delta_{kl} & \delta_{km} & \cdots & \delta_{kn} \end{vmatrix} \tag{69}$$

Based on this property, it is possible to express the product of two permutation symbols by a generalized Kronecker delta.

$$\varepsilon_{ij\ldots k}\varepsilon_{lm\ldots n} = \delta^{ij\ldots k}_{lm\ldots n} \tag{70}$$

In three dimensions (equal to three index pairs), it reduces to

$$\varepsilon_{ijk}\varepsilon_{lmn} = \delta^{ijk}_{lmn} = \delta_{lmn}{}^{ijk} \tag{71}$$

where the latter one is the notation by Thiele in [34] (of course with different letters as indices). It has been mentioned at the beginning of the section, how crucial it is to know what the ε-tensor looks like in the one- and two-dimensional case when one wants to solve the Thiele equation in less than three dimensions. Starting with the definition of ε in Eq. (67), one yields the antisymmetric tensor in the two-dimensional case ($\varepsilon_{2\times 2}$) by restricting the summation to two indices. These indices have a set of values $(1, 2)$ and by summation[1] over these values one obtains [45]:

$$\varepsilon_{2\times 2} = \sum_{ij} \varepsilon_{ij} \vec{e}_i \otimes \vec{e}_j = \sum_{ij} \left(\delta_{1i}\delta_{2j} - \delta_{1j}\delta_{2i}\right) \vec{e}_i \otimes \vec{e}_j = \begin{pmatrix} 0 & 1 \\ -1 & 0 \end{pmatrix} \tag{72}$$

For the one-dimensional case $\varepsilon_{1\times 1}$, the epsilon tensor is not defined. This can be understood by means of the permutations. The epsilon tensor describes a permutation, and in one dimension it makes no sense to define something like this. As a last step of preparation, it has to be recalled what the mathematical expression for unit vectors and the Nabla operator in the most common curvilinear coordinates is like, namely spherical and cylindrical coordinates. This will turn out to be very helpful for the calculation of the force terms in the Thiele equation.

A3 Unit Vectors and the Nabla Operator in Spherical and Cylindrical Coordinate System

As it will be clear later on, after a general evaluation of the different force terms, it is helpful for further evaluation in concrete coordinates to recall some properties of unit vectors and the Nabla operator in different coordinate systems. Due to the symmetry of vortex domain walls, it is reasonable to consider spherical and cylindrical coordinates. A vector $\vec{X}$ given in Cartesian coordinates x, y and z can be expressed in spherical ones by the radius r (radial distance), the angles ϑ (polar angle) and φ (azimuthal angle). The relation between both notation of the vector $\vec{X}$ is given by

$$\vec{X} = \begin{pmatrix} x \\ y \\ z \end{pmatrix} = \begin{pmatrix} r\sin(\vartheta)\cos(\varphi) \\ r\sin(\vartheta)\sin(\varphi) \\ r\cos(\vartheta) \end{pmatrix} \tag{73}$$

where the unit vectors connected with the new coordinates (r,ϑ,φ) can be determined by the Jacobian matrix J.

$$J = \begin{pmatrix} \frac{\partial x}{\partial r} & \frac{\partial x}{\partial \vartheta} & \frac{\partial x}{\partial \varphi} \\ \frac{\partial y}{\partial r} & \frac{\partial y}{\partial \vartheta} & \frac{\partial y}{\partial \varphi} \\ \frac{\partial z}{\partial r} & \frac{\partial z}{\partial \vartheta} & \frac{\partial z}{\partial \varphi} \end{pmatrix} = \begin{pmatrix} \sin(\vartheta)\cos(\varphi) & r\cos(\vartheta)\cos(\varphi) & -r\sin(\vartheta)\sin(\varphi) \\ \sin(\vartheta)\sin(\varphi) & r\cos(\vartheta)\sin(\varphi) & r\sin(\vartheta)\cos(\varphi) \\ \cos(\vartheta) & -r\sin(\vartheta) & 0 \end{pmatrix} \tag{74}$$

Here, the first column can be identified as a vector $\vec{r}$ which is pointing in radial direction. In the same manner, the second and third column of the Jacobian matrix are identified as the vectors $\vec{\vartheta}$ and $\vec{\varphi}$, associated with the polar and azimuthal angle.

$$\vec{r} = \begin{pmatrix} \sin(\vartheta)\cos(\varphi) \\ \sin(\vartheta)\sin(\varphi) \\ \cos(\vartheta) \end{pmatrix} \qquad \vec{\vartheta} = \begin{pmatrix} r\cos(\vartheta)\cos(\varphi) \\ r\cos(\vartheta)\sin(\varphi) \\ -r\sin(\vartheta) \end{pmatrix} \qquad \vec{\varphi} = \begin{pmatrix} -r\sin(\vartheta)\sin(\varphi) \\ r\sin(\vartheta)\cos(\varphi) \\ 0 \end{pmatrix} \tag{75}$$

Since the unit vectors in the new coordinate system are of interest, they have to be normalized by their length, which is given by the absolute value of the vector.

$$|\vec{r}| = 1 \qquad \left|\vec{\vartheta}\right| = r \qquad |\vec{\varphi}| = r\sin(\vartheta) \tag{76}$$

The unit vectors are obtained as:

$$\begin{aligned}
\vec{e}_r &= \frac{\vec{r}}{|\vec{r}|} = \begin{pmatrix} \sin(\vartheta)\cos(\varphi) \\ \sin(\vartheta)\sin(\varphi) \\ \cos(\vartheta) \end{pmatrix} \\
\vec{e}_\vartheta &= \frac{\vec{\vartheta}}{|\vec{\vartheta}|} = \begin{pmatrix} \cos(\vartheta)\cos(\varphi) \\ \cos(\vartheta)\sin(\varphi) \\ -\sin(\vartheta) \end{pmatrix} \\
\vec{e}_\varphi &= \frac{\vec{\varphi}}{|\vec{\varphi}|} = \begin{pmatrix} -\sin(\varphi) \\ \cos(\varphi) \\ 0 \end{pmatrix}
\end{aligned} \tag{77}$$

As demonstrated in Sec. A1, it is possible to calculate a transformation of coordinates with the help of the outer product by replacing the unit vectors in a certain coordinate system by their representation in terms of unit vectors in the new coordinates. As it will become clear by the example of a VDW, it is sometimes advantageous to calculate a physical quantity in spherical coordinates and then transform it back to the Cartesian system. In this case, the expression of the unit vectors in spherical coordinates in terms of Cartesian unit vectors $\vec{e}_x$, $\vec{e}_y$ and $\vec{e}_z$ can be directly obtained from the unit vectors in spherical coordinates.

$$\begin{aligned}
\vec{e}_r &= \sin(\vartheta)\cos(\varphi)\vec{e}_x + \sin(\vartheta)\sin(\varphi)\vec{e}_y + \cos(\vartheta)\vec{e}_z \\
\vec{e}_\vartheta &= \cos(\vartheta)\cos(\varphi)\vec{e}_x + \cos(\vartheta)\sin(\varphi)\vec{e}_y + -\sin(\vartheta)\vec{e}_z \\
\vec{e}_\varphi &= -\sin(\varphi)\vec{e}_x + \cos(\varphi)\vec{e}_y
\end{aligned} \tag{78}$$

Another useful relation is the connection of $\vec{e}_\vartheta$ and $\vec{e}_\varphi$ with the partial derivations of $\vec{e}_r$ with respect to the polar and azimuthal angles. Applying the partial derivations, it yields:

$$\frac{\partial \vec{e}_r}{\partial \vartheta} = \begin{pmatrix} \cos(\vartheta)\cos(\varphi) \\ \cos(\vartheta)\sin(\varphi) \\ -\sin(\vartheta) \end{pmatrix} = \vec{e}_\vartheta \qquad \frac{\partial \vec{e}_r}{\partial \varphi} = \begin{pmatrix} -\sin(\vartheta)\sin(\varphi) \\ \sin(\vartheta)\cos(\varphi) \\ 0 \end{pmatrix} = \sin(\vartheta)\vec{e}_\varphi \tag{79}$$

As it can be seen in Sec. 2.3.1, magnetic structures like vortices in discs or vortex walls in stripes exhibit a rotational symmetry, which implies that it is convenient to express the magnetization in spherical coordinates. In this case it simplifies the calculation of gradients, when the nabla operator $\vec{\nabla}$ is applied in this coordinate system. In spherical coordinates, $\vec{\nabla}$ is given by:

$$\vec{\nabla} = \vec{e}_r \frac{\partial}{\partial r} + \vec{e}_\vartheta \frac{\partial}{\partial \vartheta} + \vec{e}_\varphi \frac{1}{r\sin(\vartheta)} \frac{\partial}{\partial \varphi} \tag{80}$$

Besides spherical coordinates, polar or their extension to three dimensions, cylindrical coordinates are helpful when discussing functions with rotational symmetry; these only change in a certain plane and are constant in the spatial direction perpendicular to the plane. By virtue of this, cylindrical coordinates are discussed in the same manner as done before in the case of the spherical system. Again the starting point of the considerations is a vector $\vec{X}$ given in x, y and z that can be represented in cylindrical coordinates by the radius ρ (radial distance) and the azimuthal angle φ, which both lie in the x-y-plane.

The extension to the three dimensional case is given by the spatial direction z being perpendicular to the plane mentioned before. The representation of the vector $\vec{X}$ is given by

$$\vec{X} = \begin{pmatrix} x \\ y \\ z \end{pmatrix} = \begin{pmatrix} \rho\cos(\varphi) \\ \rho\sin(\varphi) \\ z \end{pmatrix} \tag{81}$$

where the unit vectors in the new coordinates are found (ρ,φ,z) by calculating the Jacobian matrix and by identifying the associated vectors $\vec{\rho}$, $\vec{\varphi}$ and $\vec{z}$.

$$J = \begin{pmatrix} \frac{\partial x}{\partial \rho} & \frac{\partial x}{\partial \varphi} & \frac{\partial x}{\partial z} \\ \frac{\partial y}{\partial \rho} & \frac{\partial y}{\partial \varphi} & \frac{\partial y}{\partial z} \\ \frac{\partial z}{\partial \rho} & \frac{\partial z}{\partial \varphi} & \frac{\partial z}{\partial z} \end{pmatrix} = \begin{pmatrix} \cos(\varphi) & -\rho\sin(\varphi) & 0 \\ \sin(\varphi) & \rho\cos(\varphi) & 0 \\ 0 & 0 & 1 \end{pmatrix} \tag{82}$$

$$\vec{\rho} = \begin{pmatrix} \cos(\varphi) \\ \sin(\varphi) \\ 0 \end{pmatrix} \qquad \vec{\varphi} = \begin{pmatrix} -\rho\sin(\varphi) \\ \rho\cos(\varphi) \\ 0 \end{pmatrix} \qquad \vec{z} = \begin{pmatrix} 0 \\ 0 \\ 1 \end{pmatrix} \tag{83}$$

The unit vectors are obtained by normalizing these vectors to the length of "1". Determining the absolute values of these vectors by

$$|\vec{\rho}| = 1 \qquad |\vec{\varphi}| = \rho \qquad |\vec{z}| = 1 \tag{84}$$

it is possible to calculate the unit vectors in the cylindrical coordinate system as:

$$\begin{aligned} \vec{e}_\rho &= \frac{\vec{\rho}}{|\vec{\rho}|} = \begin{pmatrix} \cos(\varphi) \\ \sin(\varphi) \\ 0 \end{pmatrix} \\ \vec{e}_\varphi &= \frac{\vec{\varphi}}{|\vec{\varphi}|} = \begin{pmatrix} -\sin(\varphi) \\ \cos(\varphi) \\ 0 \end{pmatrix} \\ \vec{e}_z &= \frac{\vec{z}}{|\vec{z}|} = \begin{pmatrix} 0 \\ 0 \\ 1 \end{pmatrix} \end{aligned} \tag{85}$$

Based on the same motivation as given before, it is helpful to know the unit vectors in spherical coordinates expressed by Cartesian unit vectors.

$$\begin{aligned} \vec{e}_\rho &= \cos(\varphi)\vec{e}_x + \sin(\varphi)\vec{e}_y \\ \vec{e}_\varphi &= -\sin(\varphi)\vec{e}_x + \cos(\varphi)\vec{e}_y \\ \vec{e}_z &= \vec{e}_z \end{aligned} \tag{86}$$

The connection of the partial derivation of $\vec{e}_\rho$ with respect to the orthogonal spatial coordinates φ and z is determined by:

$$\frac{\partial \vec{e}_\rho}{\partial \varphi} = \begin{pmatrix} -\sin(\varphi) \\ \cos(\varphi) \\ 0 \end{pmatrix} = \vec{e}_\varphi \qquad \frac{\partial \vec{e}_\rho}{\partial z} = \begin{pmatrix} 0 \\ 0 \\ 0 \end{pmatrix} \tag{87}$$

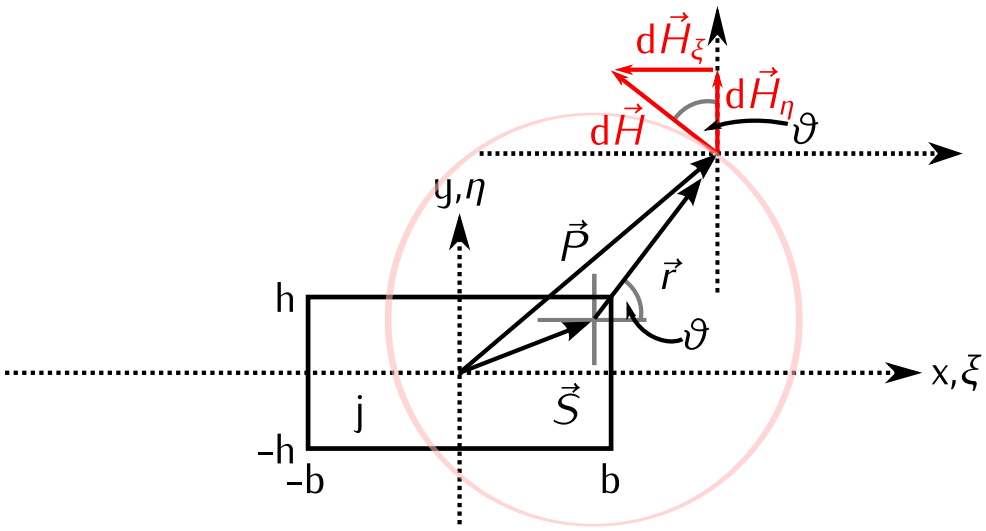

Figure 22. The sketch illustrates the quantities used for the calculation of the field H created by the CPW. The vectors $\vec{S}$ and $\vec{P}$ indicate the position of the infinitesimal area $\mathrm{d}A$ conducting a current $\mathrm{d}I$ and the point where the field has to be determined, respectively. $\vec{r}$ represents the distance between both points. The radial symmetric infinitesimal field $\mathrm{d}H$ indicated by the bright red circle is perpendicular to $\vec{r}$. Both spatial components of the field can be calculated via the enclosed angle ϑ between ϑ and the x-axis.

To conclude this section, the nabla operator is expressed in cylindrical coordinates.

$$\vec{\nabla} = \vec{e}_\rho \frac{\partial}{\partial \rho} + \vec{e}_\varphi \frac{1}{\rho} \frac{\partial}{\partial \varphi} + \vec{e}_z \frac{\partial}{\partial z} \tag{88}$$

Based on this framework, it is possible to evaluate the force terms in detail.

A4 Characterization of the Field Pulses

For the investigation of DWM, the characterization of the field pulses created by a current through the CPW is important. In this section the calculation of the magnetic field around the CPW and the calibration of the pulse times is explained. Starting with the analytic calculation of the field surrounding the signal line of the CPW, the cross section $A = 4bh$ is divided into infinitesimal small areas $\mathrm{d}A = \mathrm{d}x\mathrm{d}y$, and the infinitesimal magnetic field $\mathrm{d}H$ created in a distance r is calculated. Assuming a constant current density $j = \frac{I}{A}$ within the signal line, the infinitesimal current carried through the infinitesimal cross sectional area $\mathrm{d}A$ is given by $\mathrm{d}I = j\mathrm{d}A = j\mathrm{d}x\mathrm{d}y$. The magnetic field around a wire conducting a current I in a radial distance r is given by [36, 38]

$$H = \frac{I}{2\pi r} \tag{89}$$

which results in[1]

$$\mathrm{d}H = \frac{\mathrm{d}I}{2\pi r} = \frac{j\mathrm{d}x\mathrm{d}y}{2\pi r} \tag{90}$$

in the case of the infinitesimal current flowing through dA. In order to calculate the total field H created by the signal line of the CPW, it has to be integrated over the whole cross section area A. For this purpose two coordinate systems have to be defined. One for the characterization of the points $\vec{S}$ within the signal line (x,y) and another one to parametrize the point $\vec{P}$ outside the signal line (ξ,η) where the field has to be computed. Having[1]

$$\vec{S} = \begin{pmatrix} x \\ y \end{pmatrix} \quad , \quad \vec{P} = \begin{pmatrix} \xi \\ \eta \end{pmatrix} \quad , \quad \vec{r} = \vec{P} - \vec{S} = \begin{pmatrix} \xi - x \\ \eta - y \end{pmatrix} \tag{91}$$

it yields[1] $r = |\vec{r}| = \sqrt{(\xi - x)^2 + (\eta - y)^2}$, the absolute value of the distance vector $\vec{r}$. Inserting this result in Eq. (90), it yields

$$\mathrm{d}H = \frac{j}{2\pi} \frac{\mathrm{d}x\mathrm{d}y}{\sqrt{(\xi - x)^2 + (\eta - y)^2}} \tag{92}$$

and since being interested in the in-plane component of dH, the infinitesimal field is divided into its ξ- and η-components. These constituents of dH are given by[1]

$$\mathrm{d}H_\xi = \mathrm{d}H \sin(\vartheta) \tag{93}$$

and[1]

$$\mathrm{d}H_\eta = \mathrm{d}H \cos(\vartheta) \quad , \tag{94}$$

whereby it is convenient for the consecutive calculation of the integral over x and y to express the sine and cosine functions of ϑ in terms of the spatial coordinates (x,y,ξ,η). They read[1]

$$\sin(\vartheta) = \frac{(\eta - y)}{\sqrt{(\xi - x)^2 + (\eta - y)^2}} \tag{95}$$

and[1]

$$\cos(\vartheta) = \frac{(\xi - x)}{\sqrt{(\xi - x)^2 + (\eta - y)^2}} \tag{96}$$

respectively. Applying these expressions to Eq. (93) and (94), it yields[1]

$$\mathrm{d}H_\xi = \frac{j}{2\pi} \frac{(\eta - y)}{(\xi - x)^2 + (\eta - y)^2} \mathrm{d}x\mathrm{d}y \tag{97}$$

and[1]

$$\mathrm{d}H_\eta = \frac{j}{2\pi} \frac{(\xi - x)}{(\xi - x)^2 + (\eta - y)^2} \mathrm{d}x\mathrm{d}y \tag{98}$$

for the two spatial components of dH. Since the magnetic structures under consideration are placed on top of the signal line, only the in-plane component of the created magnetic field H_ξ has to be taken into account. As it turns out, the field on top of the signal line is very homogeneous in ξ and η-direction with exception of the most outer areas close to the edges. The expression for the

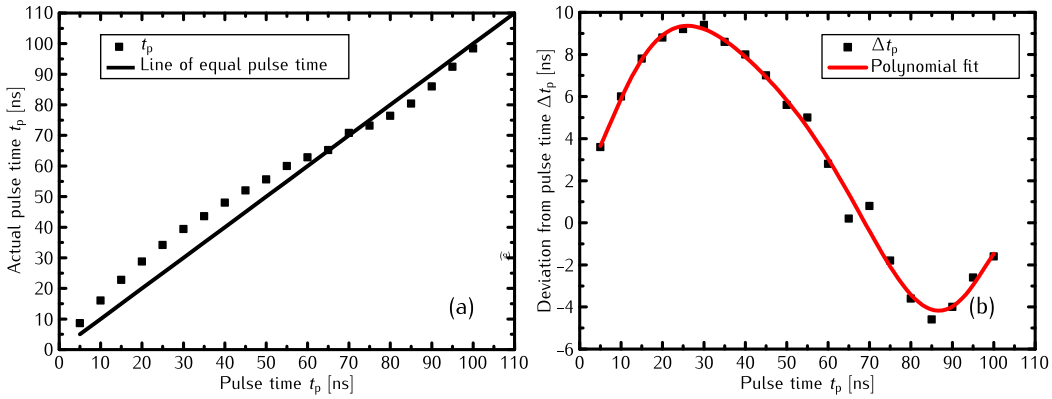

Figure 23. Figure (a) displays the actual pulse time (black dots) compared to the time adjusted on the pulse generator (solid black line). The deviation from the adjusted one (black dots) and a polynomial fit (red solid curve) is plotted in graphic (b).

magnetic in-plane field H_ξ is obtained by integration over the area A. Solving the integral[1],

$$H_\xi = \frac{j}{2\pi} \int_{x=-h}^{h} \int_{y=-b}^{b} \frac{(\eta - y)}{(\xi - x)^2 + (\eta - y)^2} \mathrm{d}x\mathrm{d}y \tag{99}$$

yields the formula that is used to calculate the field created by the short-time current pules[1].

$$\begin{aligned} H_\xi = \frac{j}{2\pi} \Bigg\{ & \frac{1}{2}(\eta - b) \ln\left(\frac{(\xi - b)^2 + (\eta - h)^2}{(\xi - b)^2 + (\eta + h)^2}\right) - \frac{1}{2}(\eta + b) \ln\left(\frac{(\xi + b)^2 + (\eta - h)^2}{(\xi + b)^2 + (\eta + h)^2}\right) \\ & + (\eta - h) \arctan\left(\frac{\xi - b}{\eta - h}\right) - (\eta + h) \arctan\left(\frac{\xi - b}{\eta + h}\right) \\ & - (\eta - h) \arctan\left(\frac{\xi + b}{\eta - h}\right) + (\eta + h) \arctan\left(\frac{\xi + b}{\eta + h}\right) \Bigg\} \end{aligned} \tag{100}$$

The pulse generator utilized in this work provides pulses with voltage V where the resulting current I is obtained via Ohm's law. The wave guide has been designed to have $R = 50\Omega$. Recording the output voltage of the pulse generator in dependence of the attenuation and fitting it with the function[1],

$$U = U_0 \cdot 10^{-\frac{x}{20-w}} \tag{101}$$

yields the parameters:

$$\begin{aligned} U_0 &= (11,33 \pm 0,02)\,\mathrm{V} \qquad (0,18\%) \\ w &= (0,26 \pm 0,02)\,\mathrm{dB} \qquad (7,69\%) \end{aligned} \tag{102}$$

By assuming an uncertainty in the attenuation of ± 0.2 dB, it is possible to calculate the current through the signal line and the magnetic field created by it. In the middle of the signal line $\xi = 0$ nm and at $\eta = 238$ nm (corresponding with the middle of the magnetic layer) the magnetic field is calculated and plotted in dependence of the attenuation in Fig. 24.

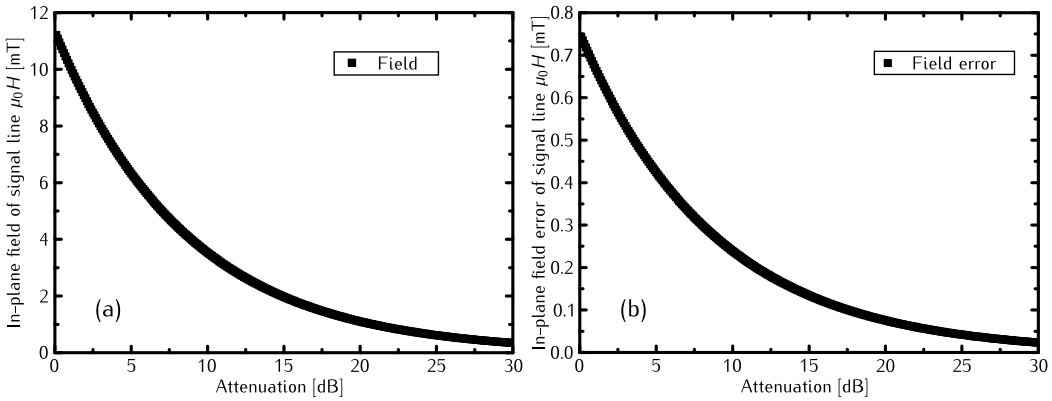

Figure 24. Graphic (a) displays the calculated field H created by the CPW in dependence of the attenuation adjusted at the pulse generator. The calculation is based on measuring the output voltage of the pulse generator (approximated by Eq. (101)) and the analytic formula for the in-plane field given by Eq. (100).

Additionally, the pulse times are characterized because the adjusted and real pulse time differ from each other. The results for t_P are shown in Fig. 23.

A5 Calculation of $U(X)$ and Average Velocity $\bar{V}$ During the Double Reversal Processes

Since being interested in the dynamics of the VC itself, which is governed mostly by the transversal motion, the part of E_Tot (equal to $U(X,Y)$) which depends on Y, namely $U(Y)$, has to be investigated. This can be done by substracting $U(X)$ from the total energy. By looking at the time dependence of E_Tot for the first eight DRPs, it can be noticed that after the onset of the oscillations, E_Tot is exhibiting a clear linear decreasing trend. This decrease is attributed to the longitudinal movement of the VDW which causes a change in Zeeman energy. This change originates from the growing and shrinking domains aligned parallel and antiparallel with respect to the external field. Doing a linear fit with the function[1]

$$E_\mathrm{Tot}(t) = m \cdot t + E_{0,\mathrm{Tot}} \tag{103}$$

in the time range where the DRPs appear, it yields a linear slope $m = -9.26 \cdot 10^{-9}\,\frac{\mathrm{J}}{\mathrm{s}}$ and an offset $E_{0,\mathrm{Tot}} = -9.81 \cdot 10^{-17}$ J. Calculating this linear decrease from the total energy, the time dependence of $E_\mathrm{Tot,DW}$ is gained and displayed in Fig. 4.11(b) and Fig. 26(b). The knowledge of the slope m enables one to calculate the average velocity in $X-$direction. As demonstrated in Appendix A, $U(X)$ is depending solely on the spatial coordinate X and, as a consequence, the changing rate in time $\frac{\mathrm{d}U(x,t)}{\mathrm{d}t}$ is determined by the average velocity in this direction (assuming Q and H being constant in time) and equal to m. In this case, it is obtained[1]

$$\left|\frac{\mathrm{d}U(x,t)}{\mathrm{d}t}\right| = QH\bar{V} \tag{104}$$

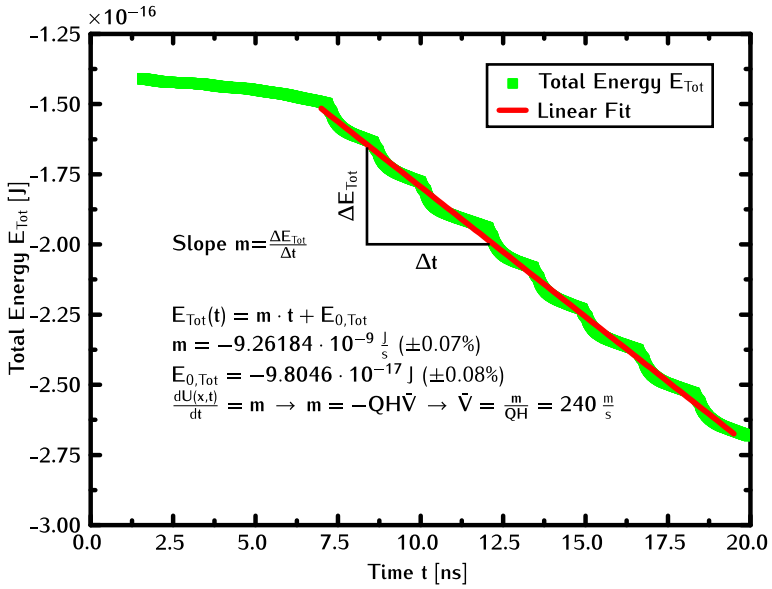

Figure 25. The graphic displays the time dependence of E_{Tot} for the first eight DRPs. It is clearly visible that after the onset of the oscillations E_{Tot} (equal to $U(X,Y)$) is exhibiting a clear linear decreasing trend which is caused by the longitudinal movement of the VDW.

yielding[1]:

$$V = \frac{m}{QH} \tag{105}$$

Using the latter, the formula returns an average velocity of $\bar{V} = 240\,\frac{\mathrm{m}}{\mathrm{s}}$.

A6 Trace and $E_{\mathrm{Tot,DW}}$ for Eight Double Reversal Processes

In the main text the behavior of trace, total energy E_{Tot} and the potential for the first three DRPs were demonstrated in Fig. 4.11. There a decreasing trend for all quantities within the first three fast DRPs are recognized. As already mentioned, this holds true only for the first three ones. To give a complete overview of the full spectra of behavior, the trace and total energy of the system covering the full simulation time of 20 ns is presented in Fig. 26. Fig. 26(a) displays the trace of the systems where consecutively after the first three DRPs a recovering of the critical transverse displacements $Y_{\mathrm{crit}}1$ and $Y_{\mathrm{crit}}2$ to the approximative value during the first DRP is observed. After the recovering, a new decreasing trend sets in. In general, it can be stated that this decrease holds on for two or three DRPs until a recovering starts. The same behavior can be found for the total energy E_{Tot} (Fig. 26(b)) of the system as well. This already indicates a connection between the critical transverse displacement at the moment of the polarity reversals within a DRP and the total energy released in this process. To get a deeper insight in the dynamic of the whole switching process, it is convenient to consider the potential. An overview of the potential from the start of the simulation up to the first three DRPs is shown in Fig. 26(c). Fig. 26(c1)

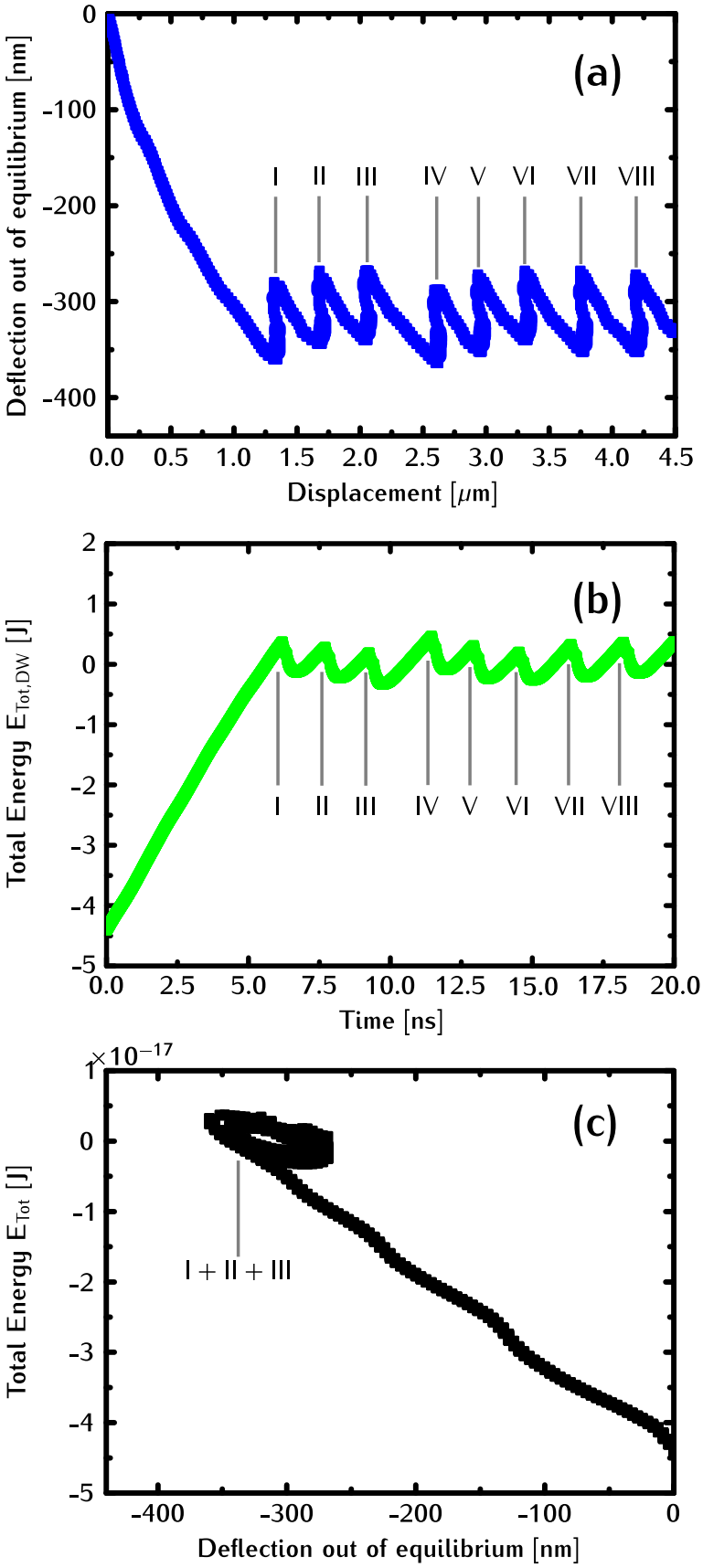

Figure 26. In this graphic an overview is given for trace (a) and total energy $E_{\mathrm{Tot,DW}}$ (b) for all eight DRPs in the simulation. (c) shows the potential from the start of the simulation up to the first three DRPs.

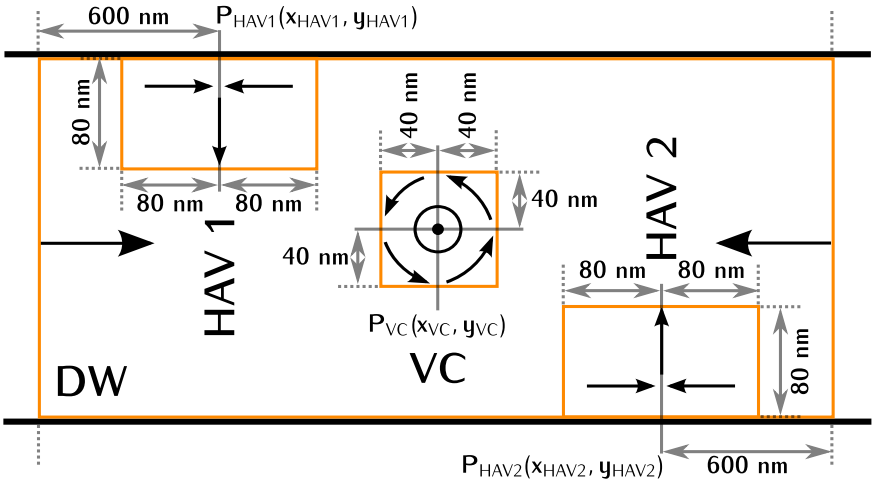

Figure 27. Schematic sketch of a VDW with polarity $p = 1$ and circulation $c = 1$ ($\chi = 1$). The orange boxes define the different regions in the DW for which the total energy was evaluated. Boxes are not drawn to scale.

illustrates very nicely that the potential calculated on base of the total energy E_{Tot} for the whole DW does not show the clear parabolic shape as presented in Fig. 4.13. This can only be revealed when the DW is divided into subsystems and the contributions of the two HAVs and the VC itself are separated.

A7 Dividing the Domain Wall in Subsystems

In Fig. 27 a schematic sketch of a VDW with polarity $p = 1$ and circulation $c = 1$ ($\chi = 1$) is presented. In this representation, orange boxes are included to define the different regions of the DW in which the total energy E_{Tot} is evaluated separately. It should be mentioned that the boxes are not drawn to scale. In total, four different regions are defined: the total region of the DW and, in addition, areas around the VC and the two HAVs at the edges. For the total DW, a rectangular box reaching from 600 nm left-hand of P_{HAV1} up to 600 nm right-hand of P_{HAV2} and in transversal direction over the complete stripe is chosen. The VC region is defined by a square with edge length of 80 nm whereby the box is always centered at the position of the VC P_{VC}. For the boxes around the two HAVs, a rectangular region reaching from 80 nm at the left side of the HAV position up to 80 nm at the right side is defined. In transversal direction, the boxes cover a region from the edges up to 80 nm into the middle of the stripe. It should be emphasized at this point that the size of the regions are chosen in that manner that the region of the VC never touches the region around the HAV2 during the oscillatory motion.

A8 Evaluation of the Spin Wave Package

In order to understand how the SWP created in the V/AV annihilation process influences the second switching of the VC, $m_z(t)$ is extracted at the position of the VC from the simulation data. The procedure how the data was obtained is depicted in Fig. 28. In a first step (Fig. 28(a)), a linescan over the z-component

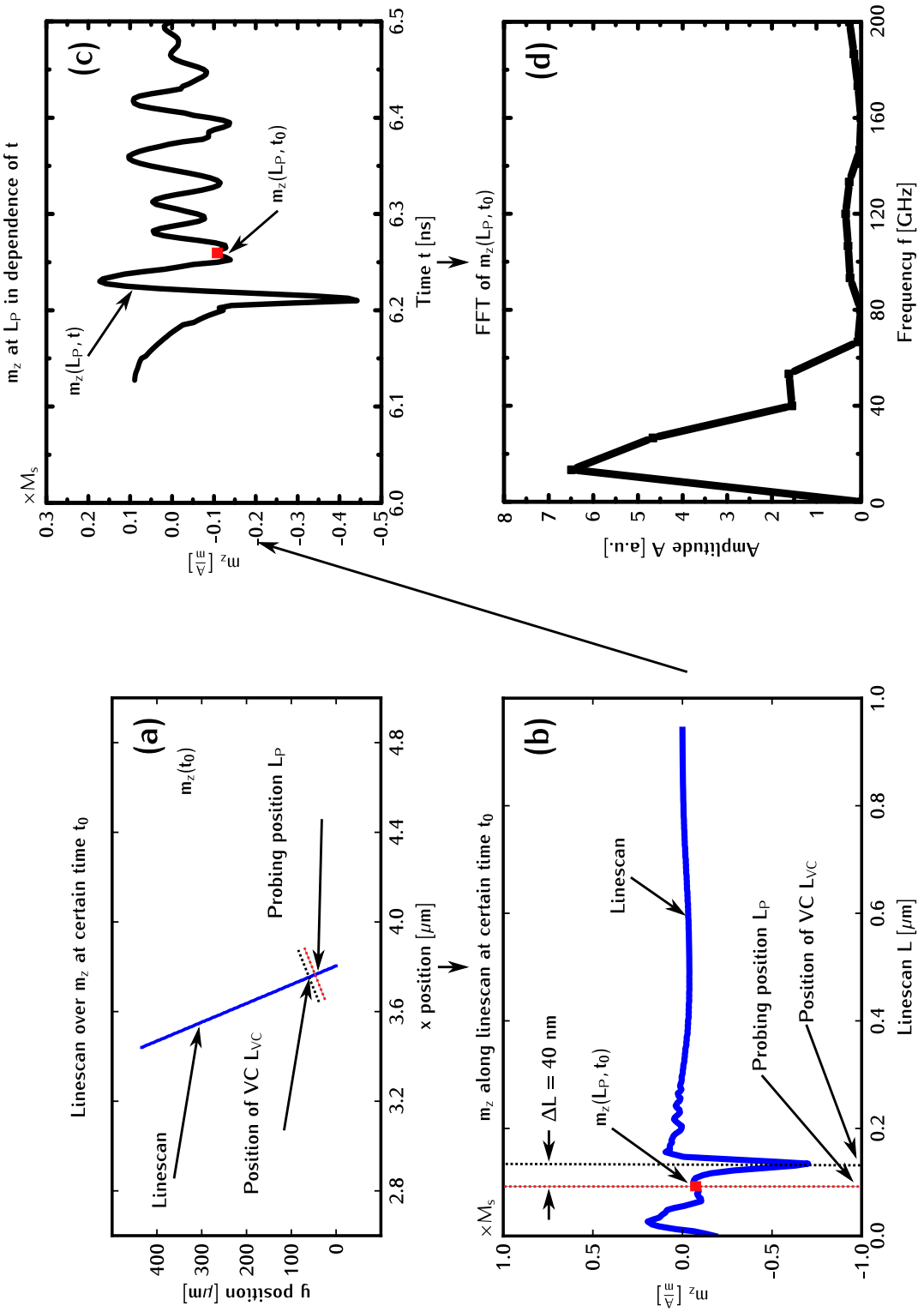

Figure 28. The graphic explains the procedure how the SWP, which excites the VC, is extracted from the simulation data and the excitation spectra is determined. (a) shows the linescan over m_z for a certain time step, while in (b) the extracted z component of the magnetization is plotted along the linescan L. In (c) $m_z(t)$ at the position of the VC is shown. A FFT of $m_z(t)$ yields the frequency spectra of the SWP (d).

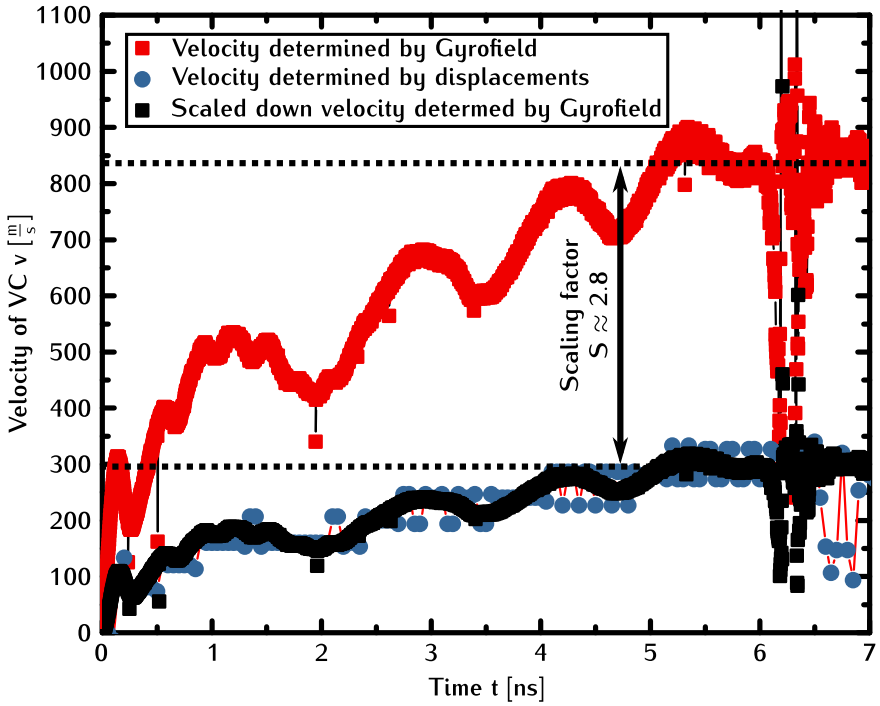

Figure 29. The three curves show the velocity determined by the gyrofield (red), the velocity found on base of the VC displacements (blue dots) and the scaled down velocity found in calculations utilizing h_{gyro} (black).

of the magnetization is performed for each time step. To define the line used for the linescan, two points are needed. Concerning the two points, one is fixed and serves as a reference point, and the other one changes in time. The reference point is determined at the time the SWP is created. The position of the VC at this time is extracted from the simulation data, and its position is projected down to the lower edge of the stripe. This point serves as the first fixed point which defines the line along $m_z(X, Y, t_0)$ that will be recorded. The second point is given at each time step by the position of the new VC. This results in a linescan that always tracks the VC. Fig. 28(b) shows the result of a linescan with length L over $m_z(X, Y, t_0)$ for the time step shown in Fig. 28(a) and yields $m_z(L, t_0)$. However, the extraction of the SWP at the exact position of the VC is difficult which is, due to the exchange dominated magnetic texture, at this point. As solution, the probing point L_{P} on the linescan is shifted by a distance $\Delta L = 40$ nm below the VC. Taking the magnetization at this point for different times, $m_z(L_{\mathrm{P}}, t)$ is obtained. This SWP excites the VC (Fig. 28(c)). Performing a fast Fourier transform (FFT) of this, SWP yields the excitation spectra of the SWP exciting the VC.

A9 Determination of the Domain Wall Velocity via Gyrofield h_{gyro}

Fig. 30 elucidates how the velocity of the VC is determined by utilizing the gyrofield h_{gyro}. In a first step, the gyrofield is determined from the simulation data by the formula [21]

$$\vec{h}_{\text{gyro}} = -\frac{1}{\gamma}\frac{\partial}{\partial \vec{m}}\frac{\vec{n}\cdot(\vec{m}\times\dot{\vec{m}})}{1+\vec{m}\cdot\vec{n}} \tag{106}$$

which can be expressed as[1]

$$\vec{h}_{\text{gyro}} = \frac{1}{\gamma}\frac{\partial}{\partial \vec{m}}\frac{\vec{n}\cdot(\vec{m}\times\vec{v}\cdot\vec{\nabla}\vec{m})}{1+\vec{m}\cdot\vec{n}} \tag{107}$$

by using the identity $\dot{\vec{m}} = -\vec{v}\cdot\vec{\nabla}\vec{m}$ [34] (see Eq. 2.69). This enables one to find something like an effective velocity with which the magnetic texture at a certain point has to move to create an equally strong gyrofield. The velocity found for the VC is shown in Fig. 30 as red curve. For comparison, the velocity of the VC is computed in a classical fashion by the time derivative of the VC position (blue graph) which yields a velocity in the steady-state of approximately 300 $\frac{\text{m}}{\text{s}}$. It becomes clear that the velocity found on the base of h_{gyro} is higher than the real velocity of the VC. Calculating the scaling factor S between the steady-state velocity of the red and blue graph (indicated by the two dashed black horizontal lines), it yields $S = 2.8$. Scaling the red curve down by this factor matches perfectly the black curve which fits the trend of the real velocity. This finding can be explained by the same simple argument as used in the explanation why the Thiele equation predicts more realistic steady-state velocities than other theoretical models. The reason for this is that the Thiele equation takes the complete magnetic structure of the DW into account by integrating and averaging over the whole DW. This yields an effective DW width Δ_{T} (Thiele width) which leads to better predictions of the steady-state velocity. At this point it becomes clear why an overestimated value for v is obtained. The calculation of the velocity uses the magnetic structure at one certain point, namely the position of the VC, and thus, cannot reproduce naturally the real value. Nevertheless, there is just a constant scaling factor S between the effective and real velocity, and the findings based on the gyrofield can be applied to investigate the interaction of the SWP with the VC.

A10 Pictures for Gyrofield and $E_{\text{gyro,z}}$ for One Complete Double Reversal Process

In Fig. 4.18 the snapshot for $h_{\text{gyro,z}}$ and the resulting Zeeman energy $E_{\text{gyro,z}}$ were given to the time where the second polarity reversal appears. For completeness, an overview for both quantities for the complete DRP is presented in Fig. 30 and 31.

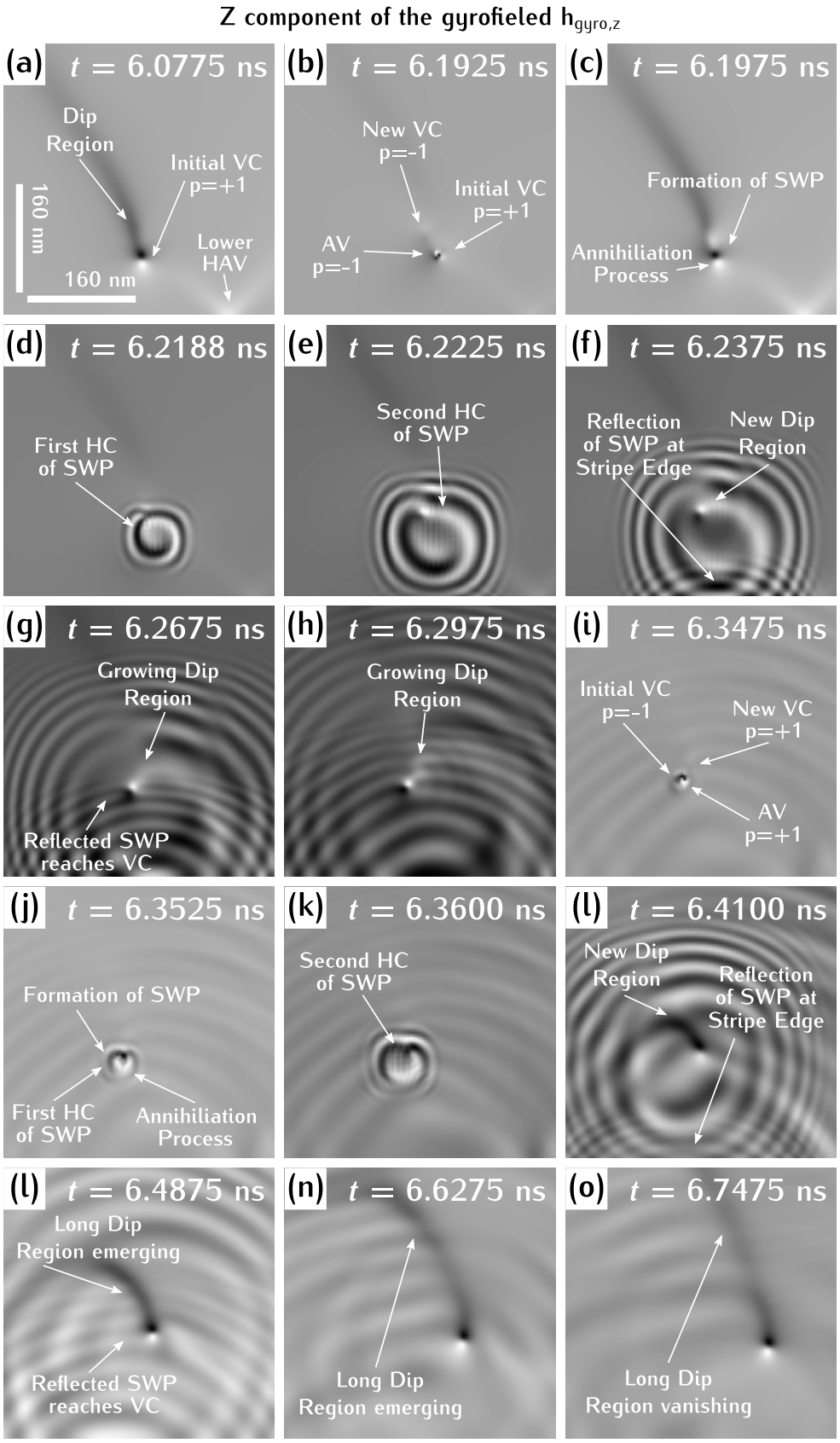

Figure 30. In this figure a complete overview for $h_{\mathrm{gyro,z}}$ for one DRP is given.

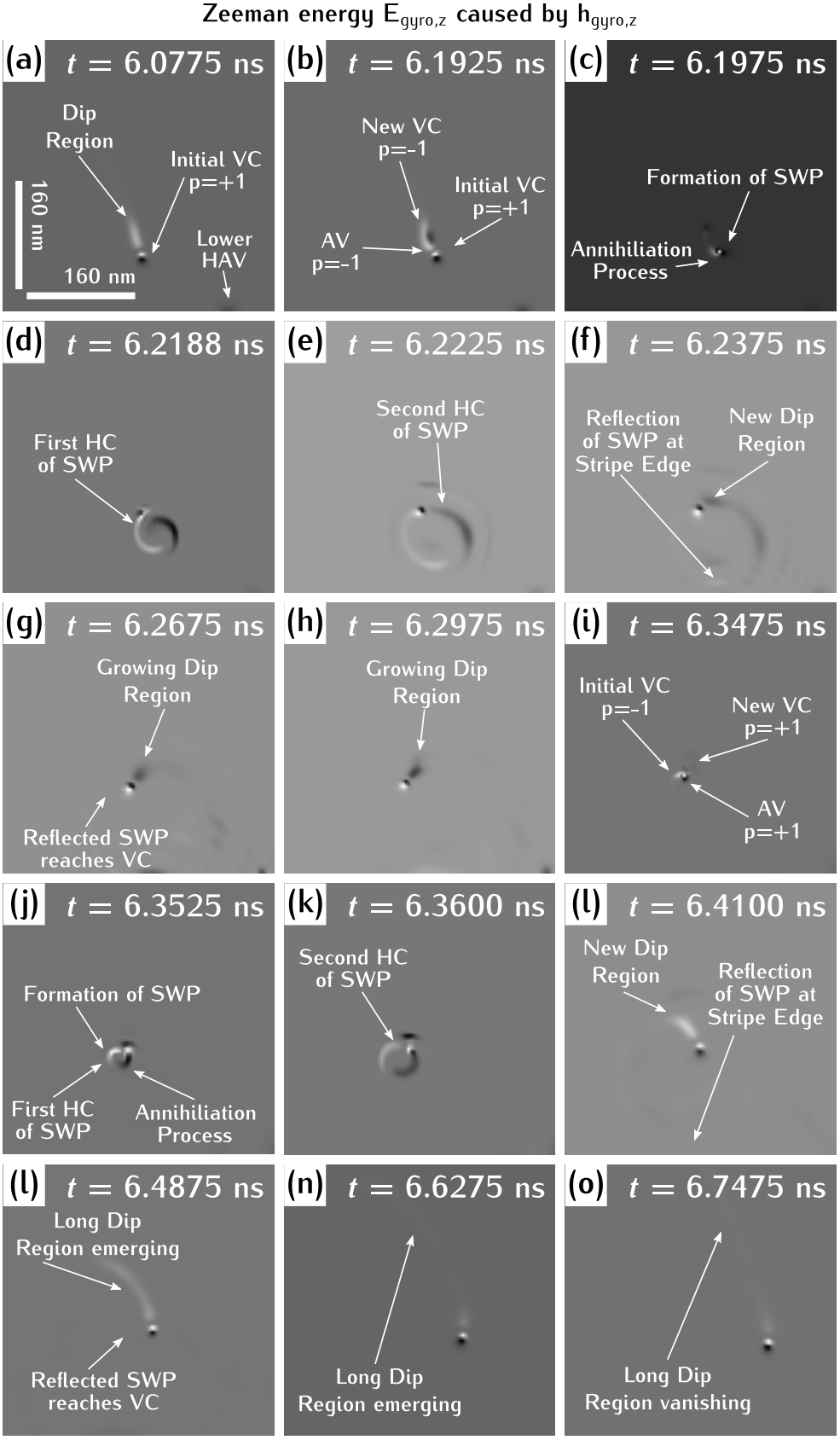

Figure 31. In this figure a complete overview for the resulting Zeeman energy $E_{\mathrm{gyro,z}}$ for one DRP is given.

Acknowledgments

Auf dem über 10 Jahre dauernden Weg von der ersten Vorlesung an der Universität bis zum Abschluss der Promotion lernt man viele Menschen kennen. Wichtig ist dabei, die Menschen zu treffen, welche zu einem passen, denn es zählt weniger, wohin man reist, sondern mit wem. Ich hatte das Glück. Im Folgenden möchte ich mich bei diesen Personen für die vielfältige Unterstützung und den Zuspruch über diese lange Zeit hinweg bedanken. Sollte ich jemanden vergessen haben, so möge er sich in meine Danksagung mit eingeschlossen fühlen. Auch stellt die Reihenfolge der Nennung keinerlei Wertung dar. Bedanken möchte ich mich bei:

- Meinem Doktorvater Prof. Dr. Christian Back, der mir die Möglichkeit gegeben hat, an seinem Lehrstuhl meine Masterarbeit und Promotion im spannenden Themenbereich der Magnetisierungsdynamik anfertigen zu dürfen. Danke Christian für die offene und kollegiale Atmosphäre an deinem Lehrstuhl sowie die Unterstützung über die letzten 7 Jahre hinweg. Du hattest immer eine offene Tür für deine Studenten bzw. Doktoranden und hast diese mit Rat und Tat unterstützt. Dies hätte ich noch viel öfter in Anspruch nehmen sollen. Bedanken möchte ich mich ich in besonderer Weise dafür, dass es für Arbeiten an deinem Lehrstuhl üblich ist, das Themengebiet in seiner Gesamtheit zu bearbeiten. Angefangen von der Planung und Mikrostrukturierung der Proben, das Durchführen der Messungen, Theorie bzw. Simulation, bis hin zur Präsentation und Veröffentlichung der Resultate konnte man alles lernen. Dies war zwar ein harter Weg, von dem ich jetzt aber profitiere. Danke!

- Prof. Georg Woltersdorf, der mir als erster das Thema der Magnetisierungsdynamik während der Betreuung meiner Masterarbeit nähergebracht hat.

- Dr. Jean-Yves Chauleau, welcher mich im ersten Jahr meiner Promotion angeleitet und in die experimentellen Techniken und theoretischen Grundlagen der Domänenwanddynamik eingearbeitet hat. Auch habe ich sehr von deinem Wissen im Bezug auf Probenherstellung profitiert und für mich vieles mitgenommen.

- Prof. Dr. Dieter Weiss für den Zugang zu den Gerätschaften und dem Reinraum an seinem Lehrstuhl. Dies hat die Probenherstellung für meine Experimente sehr erleichtert.
- Imke Gronewald vom Lst. Prof. Dr. Huber für die unkomplizierte Unterstützung bei der Probenherstellung. Dies hat den Herstellungsprozess der Proben enorm erleichtert und beschleunigt.
- Prof. Dr. Zweck, für dessen Vorlesungen ich die meisten meiner Übungsgruppen im Rahmen meiner Lehrverpflichtung abgehalten habe.
- Helmut Körner, der sich als wahrer Freund erwiesen hat und am Gelingen meiner Promotion einen großen Anteil hat. Danke für die SQUID-Messungen, die fachliche Hilfe und besonders Danke für die Fußballabende am Lehrstuhl und die außerwissenschaftlichen Unternehmungen.
- Meinen Freund und Wegbegleiter Martin Decker, mit dem ich mich gemeinsam durch Studium, Promotion und unzählige Übungsblätter gekämpft habe. Dir Martin vielen Dank dafür. Du hast einen großen Anteil daran, dass meine Masterarbeit und Promotion gelingen konnte. Auch du hast dich als wahrer Freund erwiesen und hast mir an so mancher Stelle hilfreich unter die Arme gegriffen. Vielen Dank dafür!
- Markus Härtinger für seine große Hilfe bei den Charakterisierungsmessungen an seinen FMR-Aufbauten. Auch du hast einen großen Beitrag für das Gelingen meiner Masterarbeit und Promotion geliefert. Ebenso danke für deine Mühen rund um unzählige Lehrstuhlfeiern, womit du sehr viel für die Gemeinschaft am Lehrstuhl getan hast.
- Robert Islinger, dessen Masterarbeit ich betreuen durfte und der mit seinen Messungen maßgeblich zu meiner ersten Publikation sowie Promotion beigetragen hat.
- Johannes Stigloher, der mich mit viel Programmierarbeit bezüglich der Verbesserung der Auswerteprogramme und Anpassung der Simulationssoftware MUMAX3 unterstützt hat. Auch vielen Dank für die Hilfe am TR-MOKE Aufbau.
- Hans Bauer für die Programmierung des Auswerteprogramms und die fachliche Hilfe. Auch Danke für die gemeinsamen Schwimmabende!
- Dr. Matthias Kronseder für die fachliche Expertise, besonders für das Probenwachstum an seiner MBE.
- Martin Obstbaum für seine fachliche Hilfe, besonders bei den ersten Gehversuchen in Sachen Elektronenstrahllithographie.
- Felix Schwarzuhuber für seine Mühen bei den Lorenzmikroskopiemessungen am TEM.
- Markus Hollnberger für die Hilfe bei mechanischen Arbeiten an den Messaufbauten und besonders dafür, dass du immer ein offenen Ohr für uns hattest. Ebenso Danke für die fußballerischen Fachgespräche mit dir.

- Dem ehrenwerten Lustrat, der mich für die Amtszeit 2013/14 zum Kaffeewart ernannt hat.

- Unseren Lehrstuhlsekretärinnen Claudia Zange, Magdalena Pfleger und Sylvia Hrdina, die immer hilfsbereit waren und ein offenes Ohr für uns Doktoranden hatten. Ihr habt maßgeblich zu der guten Atmosphäre am Lehrstuhl beigetragen.

- Außerdem will ich mich an dieser Stelle noch bei meinen ganzen Lehrstuhlkollegen, die ich in den 7 Jahren während Masterarbeit und Promotion kennenlernen durfte, bedanken. Allen voran möchte ich dabei Benedikt Böhm, Tassilo Heubeck, Simon Pöllath, Thomas Meier, Anatoly Shestakov, Martin Wörnle, Bernhard Endres, Martin Buchner, Bernhard Zimmermann, Michael Vogel, Stefan Günther, Tobias Grünbaum, Martin Schön, Johannes Wild, Benedikt Bauer, Alexandr Talalaevskij, Ajay Gangwar, Matthias Krause, Dirk Sindersberger, Phillip Menner, Susanne Brunner, Mirko Ribow sowie Maximilian Schmid namentlich erwähnen. Ihr alle habt zu einer großartigen Atmosphäre am Lehrstuhl beigetragen.

- Allen Studenten, die ich bei einer Bachelor- oder Studienarbeit anleiten durfte.

- Meinen Studienkollegen Christoph Pöllmann, Florian Steiner, Christian Gradl und Markus Schwemmer. Vielen Dank euch für die tolle Studienzeit und die Unterstützung beim gemeinsamen Kampf durch die Vorlesungen. Euch kann man sich als Kommilitonen nur wünschen.

- Meiner guten Freundin Bettina Preller. Danke für die Zeit mit dir und die Hilfe beim Korrekturlesen der Arbeit.

- Meinem guten Freund Christian Kirschneck, der mich seit dem Kindergarten begleitet und der mir über das Studium und besonders in der Promotion immer wieder hilfreichen Zuspruch geleistet hat.

- Meinen Arbeitskollegen bei Infineon Technologies, die mich in kürzester Zeit so gut aufgenommen haben und bei denen ich mich sehr wohl fühle.

- Zu guter Letzt meiner Familie, für die ich meine Dankbarkeit kaum in Worte fassen kann. Was sie für mich nicht nur über das Studium sondern über mein ganzes Leben hinweg getan haben, lässt sich gar nicht alles aufzählen. Auch in schwierigen Zeiten haben sie immer an mich geglaubt, mir den Rücken freigehalten und die Unterstützung zukommen lassen. Ohne sie wäre ich nicht da, wo ich heute bin. Mehr als Danke kann nicht dafür sagen. Danke!

Danke!

Abbreviations

AMR	Anisotropic Magnetoresistance
ATV	Asymmetric Transverse Wall
AV	Anti Vortex
BG	Background
Ch.	Chapter
CCA	Collective Coordinate Approach
CPMMA	Crosslinked Poly(methyl methacrylate)
CPW	Coplanar Wave Guide
DRP	Double Reversal Process
DW	Domain Wall
DWM	Domain Wall Motion
Eq.	Equation
FFT	Fast Fourier Transform
FMR	Ferromagnetic Resonance
GMR	Giant Magnetoresistance
HV	Half Vortex
HAV	Half Anti-Vortex
HC	Half Cycle
LL	Landau-Lifshitz
LLG	Landau-Lifshitz-Gilbert

MOKE	Magneto Optical Kerr Effect
PMMA	Poly(methyl methacrylate)
PR	Polarity Reversal
R	Reversal
RP	Reversal Process
Sec.	Section
SST	Spin-Momentum Transfer Torque
SW	Spin Wave
SWP	Spin Wave Package
TMR	Tunnel Magnetoresistance
TR	Time-Resolved
TV	Transverse Wall
V	Vortex
VC	Vortex Core
VDW	Vortex Domain Wall
VW	Vortex Wall
WB	Walker Breakdown
WF	Wide-Field

Publications

As First Author

- T. Weindler, H. G. Bauer, R. Islinger, B. Boehm, J.-Y. Chauleau and C. H. Back. *Magnetic Damping: Domain Wall Dynamics versus Local Ferromagnetic Resonance*. Phys. Rev. Lett. **113**, 237204 (2014).
- T. Weindler, R. Islinger, H. G. Bauer, J. Stigloher, M. M. Decker, J.-Y. Chauleau and C. H. Back. *Chirality-Dependent Vortex Domain Wall Dynamics*. In preparation.

As Co-Author

- H. S. Körner, M. A. W. Schoen, T. Mayer, M. M. Decker, J. Stigloher, T. Weindler, T. N. G. Meier, M. Kronseder and C. H. Back. *Magnetic damping in poly-crystalline Co25Fe75: Ferromagnetic resonance vs. spin wave propagation experiments*. Applied Physics Letters **111**, 132406 (2017).

Conference Contributions

- T. Weindler, H. G. Bauer, R. Islinger, B. Boehm, J.-Y. Chauleau and C. H. Back. *Magnetic Damping: Domain Wall Dynamics versus Local Ferromagnetic Resonance*. Poster presentation at the Tagung der Deutschen Physikalischen Gesellschaft, Dresden, Germany (March/April 2014).
- T. Weindler, H. G. Bauer, R. Islinger, B. Boehm, J.-Y. Chauleau and C. H. Back. *Magnetic Damping: Domain Wall Dynamics versus Local Ferromagnetic Resonance*. Poster presentation at the 3rd German-Russian-Swedish Workshop on Ordering and Dynamics in Magnetic Nanostructures, Maurach, Germany (September 2014).

Bibliography

[1] S. S. P. Parkin, M. Hayashi, and L. Thomas. *Magnetic Domain-Wall Racetrack Memory.* Science **320**, 190–194 (2008).

[2] M. Hayashi, L. Thomas, R. Moriya, C. Rettner, and S. S. P. Parkin. *Current-Controlled Magnetic Domain-Wall Nanowire Shift Register.* Science **320**, 209–211 (2008).

[3] D. Suess, A. Bachleitner-Hofmann, A. Satz, H. Weitensfelder, C. Vogler, F. Bruckner, C. Abert, K. Prügl, J. Zimmer, C. Huber, S. Luber, W. Raberg, T. Schrefl, and H. Brückl. *Topologically protected vortex structures for low-noise magnetic sensors with high linear range.* Nature Electronics **1**, 362–370 (2018).

[4] S. Parkin, X. Jiang, C. Kaiser, A. Panchula, K. Roche, and M. Samant. *Magnetically engineered spintronic sensors and memory.* Proc. IEEE **91**, 661-680 (2003).

[5] J. Slonczewski. *Current-driven excitation of magnetic multilayers.* J. Magn. Magn. Mater. **159**, L1 - L7 (1996).

[6] L. Berger. *Emission of spin waves by a magnetic multilayer traversed by a current.* Phys. Rev. B **54**, 9353–9358 (1996).

[7] G. Binasch, P. Grünberg, F. Saurenbach, and W. Zinn. *Enhanced magnetoresistance in layered magnetic structures with antiferromagnetic interlayer exchange.* Phys. Rev. B **39**, 4828–4830 (1989).

[8] M. N. Baibich, J. M. Broto, A. Fert, F. N. Van Dau, F. Petroff, P. Etienne, G. Creuzet, A. Friederich, and J. Chazelas. *Giant Magnetoresistance of (001)Fe/(001)Cr Magnetic Superlattices.* Phys. Rev. Lett. **61**, 2472–2475 (1988).

[9] T. Miyazaki and N. Tezuka. *Giant magnetic tunneling effect in Fe/Al2O3/Fe junction.* J. Magn. Magn. Mater. **139**, L231 - L234 (1995).

[10] K. C. J. Dietmayer. *Magnetische Sensoren auf Basis des AMR-Effekts (Magnetic Sensors Based on the AMR-Effect).* tm - Technisches Messen Plattform für Methoden, Systeme und Anwendungen der Messtechnik **68**, 269 (2009).

[11] M. Julliere. *Tunneling between ferromagnetic films.* Phys. Lett. A **54**, 225 - 226 (1975).

[12] S. Yuasa, T. Nagahama, A. Fukushima, Y. Suzuki, and K. Ando. *Giant room-temperature magnetoresistance in single-crystal Fe/MgO/Fe magnetic tunnel junctions.* Nat. Mater. **3**, 868 (2004).

[13] M. Noske, A. Gangwar, H. Stoll, M. Kammerer, M. Sproll, G. Dieterle, M. Weigand, M. Fähnle, G. Woltersdorf, C. H. Back, and G. Schütz. *Unidirectional sub-100-ps magnetic vortex core reversal.* Phys. Rev. B **90**, 104415 (2014).

[14] M. Helsen, A. Gangwar, J. De Clercq, A. Vansteenkiste, M. Weigand, C. H. Back, and B. Van Waeyenberge. *Non-linear radial spinwave modes in thin magnetic disks.* Appl. Phys. Lett. **106**, 032405 (2015).

[15] M. Noske, H. Stoll, M. Fähnle, A. Gangwar, G. Woltersdorf, A. Slavin, M. Weigand, G. Dieterle, J. Förster, C. H. Back, and G. Schütz. *Spin wave mediated unidirectional vortex core reversal by two orthogonal monopolar field pulses: The essential role of three-dimensional magnetization dynamics.* J. Appl. Phys. **119**, 173901 (2016).

[16] M. Noske, H. Stoll, M. Fähnle, A. Gangwar, G. Woltersdorf, A. Slavin, M. Weigand, G. Dieterle, J. Förster, C. H. Back, and G. Schütz. *Three-dimensional Character of the Magnetization Dynamics in Magnetic Vortex Structures: Hybridization of Flexure Gyromodes with Spin Waves.* Phys. Rev. Lett. **117**, 037208 (2016).

[17] G. S. D. Beach, C. Nistor, C. Knutson, M. Tsoi, and J. L. Erskine. *Dynamics of field-driven domain-wall propagation in ferromagnetic nanowires.* Nat. Mater. **4**, 741 (2005).

[18] C. Zinoni, A. Vanhaverbeke, P. Eib, G. Salis, and R. Allenspach. *Beyond the Compact Magnetic Domain Wall.* Phys. Rev. Lett. **107**, 207204 (2011).

[19] C. Garg, A. Pushp, S.-H. Yang, T. Phung, B. P. Hughes, C. Rettner, and S. S. P. Parkin. *Highly Asymmetric Chiral Domain-Wall Velocities in Y-Shaped Junctions.* Nano Lett. **18**, 1826-1830 (2018). PMID: 29420900.

[20] M. Kläui, H. Ehrke, U. Rüdiger, T. Kasama, R. E. Dunin-Borkowski, D. Backes, L. J. Heyderman, C. A. F. Vaz, J. A. C. Bland, G. Faini, E. Cambril, and W. Wernsdorfer. *Direct observation of domain-wall pinning at nanoscale constrictions.* Appl. Phys. Lett. **87**, 102509 (2005).

[21] K. Y. Guslienko, K.-S. Lee, and S.-K. Kim. *Dynamic Origin of Vortex Core Switching in Soft Magnetic Nanodots.* Phys. Rev. Lett. **100**, 027203 (2008).

[22] T. Weindler, H. G. Bauer, R. Islinger, B. Boehm, J.-Y. Chauleau, and C. H. Back. *Magnetic Damping: Domain Wall Dynamics versus Local Ferromagnetic Resonance*. Phys. Rev. Lett. **113**, 237204 (2014).

[23] L. D. Landau and E. Lifshitz. *On the theory of the dispersion of magnetic permeability in ferromagnetic bodies*. Phys. Z. Sowjet. **8**, 153 (1935).

[24] T. L. Gilbert. *Formulation, Foundations and Applications of the Phenomenological Theory of Ferromagnetism.* ILLINOIS INSTITUTE OF TECHNOLOGY., Dissertation (1956).

[25] T. L. Gilbert. *A phenomenological theory of damping in ferromagnetic materials*. IEEE Trans. Magn. **40**, 3443-3449 (2004).

[26] H. Y. Yuan, Z. Yuan, K. Xia, and X. R. Wang. *Influence of nonlocal damping on the field-driven domain wall motion*. Phys. Rev. B **94**, 064415 (2016).

[27] S. Zhang and S. S.-L. Zhang. *Generalization of the Landau-Lifshitz-Gilbert Equation for Conducting Ferromagnets*. Phys. Rev. Lett. **102**, 086601 (2009).

[28] Y. Tserkovnyak and C. H. Wong. *Theory of spin magnetohydrodynamics*. Phys. Rev. B **79**, 014402 (2009).

[29] N. L. Schryer and L. R. Walker. *The motion of 180° domain walls in uniform dc magnetic fields*. J. Appl. Phys. **45**, 5406-5421 (1974).

[30] B. Krüger. *Current-Driven Magnetization Dynamics : Analytical Modeling and Numerical Simulation*. Universität Hamburg, Dissertation (2011).

[31] F. Bloch. *Nuclear Induction*. Phys. Rev. **70**, 460–474 (1946).

[32] I. Mayergoyz, G. Bertotti, and C. Serpico. *Nonlinear Magnetization Dynamics in Nanosystems*. Elsevier Series in Electromagnetism, Elsevier Science (2009).

[33] M. Lakshmanan. *The fascinating world of the Landau-Lifshitz-Gilbert equation: an overview*. Philosophical Transactions of the Royal Society A: Mathematical, Physical and Engineering Sciences **369**, 1280–1300 (2011).

[34] A. A. Thiele. *Steady-State Motion of Magnetic Domains*. Phys. Rev. Lett. **30**, 230–233 (1973).

[35] A. A. Thiele. *Applications of the gyrocoupling vector and dissipation dyadic in the dynamics of magnetic domains*. J. Appl. Phys. **45**, 377-393 (1974).

[36] J. Jackson, K. Müller, and M. Diestelhorst. *Klassische Elektrodynamik*. De Gruyter Studium, De Gruyter (2013).

[37] S. Blundell. *Magnetism in Condensed Matter*. Oxford Master Series in Condensed Matter Physics, OUP Oxford (2001).

[38] J. Coey. *Magnetism and Magnetic Materials*. Knovel Library, Cambridge University Press (2010).

[39] F. Byron and R. Fuller. *Mathematics of Classical and Quantum Physics*. No. Bd. 1-2 in Dover books on physics and chemistry, Dover Publications (1992).

[40] L. Papula. *Mathematische Formelsammlung für Ingenieure und Naturwissenschaftler: mit Rechenbeispielen und einer ausführlichen Integraltafel*. Lothar Papula, Vieweg (2001).

[41] G. Bernacchi. *Tensors made easy*. Lulu.com (2017).

[42] J. Kurth and P. Haupt. *Continuum Mechanics and Theory of Materials*. Advanced Texts in Physics, Springer Berlin Heidelberg (2002).

[43] F. Kuypers. *Klassische Mechanik: mit über 300 Beispielen und Aufgaben mit Lösungen*. Lehrbuch Physik, John Wiley & Sons, Limited (2008).

[44] J. C. Slonczewski. *Theory of Bloch-line and Bloch-wall motion*. J. Appl. Phys. **45**, 2705-2715 (1974).

[45] D. J. Clarke, O. A. Tretiakov, G.-W. Chern, Y. B. Bazaliy, and O. Tchernyshyov. *Dynamics of a vortex domain wall in a magnetic nanostrip: Application of the collective-coordinate approach*. Phys. Rev. B **78**, 134412 (2008).

[46] H. Goldstein. *Classical Mechanics*. Pearson Education (2002).

[47] O. A. Tretiakov, D. Clarke, G.-W. Chern, Y. B. Bazaliy, and O. Tchernyshyov. *Dynamics of Domain Walls in Magnetic Nanostrips*. Phys. Rev. Lett. **100**, 127204 (2008).

[48] H. Schade and K. Neemann. *Tensoranalysis*. De Gruyter Lehrbuch, De Gruyter (2009).

[49] B. Hillebrands and A. Thiaville. *Spin Dynamics in Confined Magnetic Structures III*. Springer Berlin Heidelberg (2006).

[50] A. Hubert, R. Schäfer, and A. Rudolf Schafer. *Magnetic Domains: The Analysis of Magnetic Microstructures*. Springer (1998).

[51] F. Bloch. *Zur Theorie des Austauschproblems und der Remanenzerscheinung der Ferromagnetika*. Z. Physik **74**, 295-335 (1932).

[52] L. Néel. *Energie des parois de Bloch dans les couches minces*. Comptes Rendus Hebdomadaires Des Seances De L Academie Des Sciences **241**, 533–537 (1955).

[53] Y. Nakatani, A. Thiaville, and J. Miltat. *Head-to-head domain walls in soft nano-strips: a refined phase diagram*. J. Magn. Magn. Mater. **290-291**, 750 - 753 (2005). Proceedings of the Joint European Magnetic Symposia (JEMS' 04).

[54] V. Estévez and L. Laurson. *Head-to-head domain wall structures in wide permalloy strips*. Phys. Rev. B **91**, 054407 (2015).

[55] V. D. Nguyen, O. Fruchart, S. Pizzini, J. Vogel, J.-C. Toussaint, and N. Rougemaille. *Third type of domain wall in soft magnetic nanostrips*. Sci. Rep. **5**, 12417 (2015).

[56] R. D. McMichael and M. J. Donahue. *Head to head domain wall structures in thin magnetic strips*. IEEE Trans. Magn. **33**, 4167-4169 (1997).

[57] O. Tchernyshyov and G.-W. Chern. *Fractional Vortices and Composite Domain Walls in Flat Nanomagnets*. Phys. Rev. Lett. **95**, 197204 (2005).

[58] G.-W. Chern, H. Youk, and O. Tchernyshyov. *Topological defects in flat nanomagnets: The magnetostatic limit*. J. Appl. Phys. **99**, 08Q505 (2006).

[59] H. Youk, G.-W. Chern, K. Merit, B. Oppenheimer, and O. Tchernyshyov. *Composite domain walls in flat nanomagnets: The magnetostatic limit*. J. Appl. Phys. **99**, 08B101 (2006).

[60] R. Moser. *Boundary Vortices for Thin Ferromagnetic Films*. Arch. Ration. Mech. Anal. **174**, 267–300 (2004).

[61] M. Kurzke. *Boundary vortices in thin magnetic films*. Calculus of Variations and Partial Differential Equations **26**, 1–28 (2006).

[62] R. Hertel and C. M. Schneider. *Exchange Explosions: Magnetization Dynamics during Vortex-Antivortex Annihilation*. Phys. Rev. Lett. **97**, 177202 (2006).

[63] S.-K. Kim, Y.-S. Choi, K.-S. Lee, K. Y. Guslienko, and D.-E. Jeong. *Electric-current-driven vortex-core reversal in soft magnetic nanodots*. Appl. Phys. Lett. **91**, 082506 (2007).

[64] K.-S. Lee, K. Y. Guslienko, J.-Y. Lee, and S.-K. Kim. *Ultrafast vortex-core reversal dynamics in ferromagnetic nanodots*. Phys. Rev. B **76**, 174410 (2007).

[65] M. Kläui, C. A. F. Vaz, J. A. C. Bland, T. L. Monchesky, J. Unguris, E. Bauer, S. Cherifi, S. Heun, A. Locatelli, L. J. Heyderman, and Z. Cui. *Direct observation of spin configurations and classification of switching processes in mesoscopic ferromagnetic rings*. Phys. Rev. B **68**, 134426 (2003).

[66] M. J. Donahue and D. G. Porter. *OOMMF: Object Oriented MicroMagnetic Framework* (2016).

[67] A. Vansteenkiste and B. V. de Wiele. *MuMax: A new high-performance micromagnetic simulation tool*. J. Magn. Magn. Mater. **323**, 2585 - 2591 (2011).

[68] A. Vansteenkiste, J. Leliaert, M. Dvornik, M. Helsen, F. Garcia-Sanchez, and B. Van Waeyenberge. *The design and verification of MuMax3*. AIP Adv. **4**, 107133 (2014).

[69] J. C. Slonczewski. *Theory of domain-wall motion in magnetic films and platelets.* J. Appl. Phys. **44**, 1759-1770 (1973).

[70] D. L. Huber. *Dynamics of spin vortices in two-dimensional planar magnets.* Phys. Rev. B **26**, 3758–3765 (1982).

[71] K. Bussmann, G. A. Prinz, S.-F. Cheng, and D. Wang. *Switching of vertical giant magnetoresistance devices by current through the device.* Appl. Phys. Lett. **75**, 2476-2478 (1999).

[72] J. Raabe, R. Pulwey, R. Sattler, T. Schweinböck, J. Zweck, and D. Weiss. *Magnetization pattern of ferromagnetic nanodisks.* J. Appl. Phys. **88**, 4437-4439 (2000).

[73] T. Shinjo, T. Okuno, R. Hassdorf, †. K. Shigeto, and T. Ono. *Magnetic Vortex Core Observation in Circular Dots of Permalloy.* Science **289**, 930–932 (2000).

[74] A. Wachowiak, J. Wiebe, M. Bode, O. Pietzsch, M. Morgenstern, and R. Wiesendanger. *Direct Observation of Internal Spin Structure of Magnetic Vortex Cores.* Science **298**, 577–580 (2002).

[75] F. Q. Zhu, D. Fan, X. Zhu, J.-G. Zhu, R. C. Cammarata, and C.-L. Chien. *Ultrahigh-Density Arrays of Ferromagnetic Nanorings on Macroscopic Areas.* Adv. Mater. **16**, 2155–2159 (2004).

[76] R. Kohn, A. DeSimone, F. Otto, and S. Mueller. *Recent analytical developments in micromagnetics.* Elsevier. 269–381 (2006).

[77] O. A. Tretiakov and O. Tchernyshyov. *Vortices in thin ferromagnetic films and the skyrmion number.* Phys. Rev. B **75**, 012408 (2007).

[78] A. P. Malozemoff and J. C. Slonczewski. *Effect of Bloch Lines on Magnetic Domain-Wall Mobility.* Phys. Rev. Lett. **29**, 952–955 (1972).

[79] H. A. M. van den Berg. *Self-consistent domain theory in soft-ferromagnetic media. II. Basic domain structures in thin-film objects.* J. Appl. Phys. **60**, 1104-1113 (1986).

[80] J. Yang, C. Nistor, G. S. D. Beach, and J. L. Erskine. *Magnetic domain-wall velocity oscillations in permalloy nanowires.* Phys. Rev. B **77**, 014413 (2008).

[81] J. P. Nibarger, R. Lopusnik, Z. Celinski, and T. J. Silva. *Variation of magnetization and the Landé g factor with thickness in Ni-Fe films.* Appl. Phys. Lett. **83**, 93-95 (2003).

[82] J. M. Shaw, H. T. Nembach, T. J. Silva, and C. T. Boone. *Precise determination of the spectroscopic g-factor by use of broadband ferromagnetic resonance spectroscopy.* J. Appl. Phys. **114**, 243906 (2013).

[83] M. Kläui. *Head-to-head domain walls in magnetic nanostructures.* J. Phys.: Condens. Matter **20**, 313001 (2008).

[84] P. Tipler, G. Mosca, and D. Pelte. *Physik für Wissenschaftler und Ingenieure*. Sav Physik/Astronomie, Spektrum Akad. Verlag (2004).

[85] J.-Y. Lee, K.-S. Lee, S. Choi, K. Y. Guslienko, and S.-K. Kim. *Dynamic transformations of the internal structure of a moving domain wall in magnetic nanostripes*. Phys. Rev. B **76**, 184408 (2007).

[86] A. A. Belavin and A. M. Polyakov. *Metastable states of two-dimensional isotropic ferromagnets*. ZhETF Pisma Redaktsiiu **22**, 503 (1975).

[87] N. Usov and S. Peschany. *Magnetization curling in a fine cylindrical particle*. J. Magn. Magn. Mater. **118**, L290 - L294 (1993).

[88] C. Kittel. *On the Theory of Ferromagnetic Resonance Absorption*. Phys. Rev. **73**, 155–161 (1948).

[89] Kittel, C. *Ferromagnetic resonance*. J. Phys. Radium **12**, 291-302 (1951).

[90] J. V. Vleck. *Ferromagnetic resonance*. Physica **17**, 234 - 252 (1951).

[91] H. Suhl. *Ferromagnetic Resonance in Nickel Ferrite Between One and Two Kilomegacycles*. Phys. Rev. **97**, 555–557 (1955).

[92] G. Woltersdorf. *Spin-pumping and two-magnon scattering in magnetic multilayers*. Sinon Fraser University, Dissertation (2004).

[93] M. M. Decker. *Spin Current Induced Control of Magnetization Dynamics*. Universität Regensburg, Dissertation (2018).

[94] M. O. Härtinger. *Untersuchung magnetischer Materialien mit Methoden der Ferromagnetischen Resonanz*. Universität Regensburg, Dissertation (2017).

[95] C. Kittel and S. Hunklinger. *Einführung in die Festkörperphysik*. Oldenbourg Wissenschaftsverlag (2013).

[96] L. Papula. *Mathematik fuer Ingenieure und Naturwissenschaftler. Band 2: Ein Lehr- und Arbeitsbuch fuer das Grundstudium*. Vieweg (2001).

[97] H. Eichler. *Optik: Wellen- und Teilchenoptik*. Bergmann/Schaefer kompakt : Lehrbuch der Experimentalphysik / Klaus Lüders ; Gebhard von Oppen, De Gruyter (2004).

[98] E. Hecht. *Optics*. Pearson education, Addison-Wesley (2002).

[99] P. Bruno, Y. Suzuki, and C. Chappert. *Magneto-optical Kerr effect in a paramagnetic overlayer on a ferromagnetic substrate: A spin-polarized quantum size effect*. Phys. Rev. B **53**, 9214–9220 (1996).

[100] H. S. Körner, J. Stigloher, H. G. Bauer, H. Hata, T. Taniguchi, T. Moriyama, T. Ono, and C. H. Back. *Interfacial Dzyaloshinskii-Moriya interaction studied by time-resolved scanning Kerr microscopy*. Phys. Rev. B **92**, 220413 (2015).

[101] M. Obstbaum, M. Decker, A. K. Greitner, M. Härtinger, T. N. G. Meier, M. Kronseder, K. Chadova, S. Wimmer, D. Ködderitzsch, H. Ebert, and C. H. Back. *Tuning Spin Hall Angles by Alloying.* Phys. Rev. Lett. **117**, 167204 (2016).

[102] H. S. Körner, M. A. W. Schoen, T. Mayer, M. M. Decker, J. Stigloher, T. Weindler, T. N. G. Meier, M. Kronseder, and C. H. Back. *Magnetic damping in poly-crystalline Co25Fe75: Ferromagnetic resonance vs. spin wave propagation experiments.* Appl. Phys. Lett. **111**, 132406 (2017).

[103] L. K. Bogart, D. S. Eastwood, and D. Atkinson. *The effect of geometrical confinement and chirality on domain wall pinning behavior in planar nanowires.* J. Appl. Phys. **104**, 033904 (2008).

[104] C. C. Faulkner, M. D. Cooke, D. A. Allwood, D. Petit, D. Atkinson, and R. P. Cowburn. *Artificial domain wall nanotraps in Ni81Fe19 wires.* J. Appl. Phys. **95**, 6717-6719 (2004).

[105] A. Himeno, T. Ono, S. Nasu, K. Shigeto, K. Mibu, and T. Shinjo. *Dynamics of a magnetic domain wall in magnetic wires with an artificial neck.* J. Appl. Phys. **93**, 8430-8432 (2003).

[106] R. P. Cowburn, D. A. Allwood, G. Xiong, and M. D. Cooke. *Domain wall injection and propagation in planar Permalloy nanowires.* J. Appl. Phys. **91**, 6949-6951 (2002).

[107] D. McGrouther, S. McVitie, J. N. Chapman, and A. Gentils. *Controlled domain wall injection into ferromagnetic nanowires from an optimized pad geometry.* Appl. Phys. Lett. **91**, 022506 (2007).

[108] Y. Gao, B. You, H. L. Yang, Q. F. Zhan, Z. Li, N. Lei, W. S. Zhao, J. Wu, H. Q. Tu, J. Wang, L. J. Wei, W. Zhang, Y. B. Xu, and J. Du. *Stochastic domain wall depinning in permalloy nanowires with various types of notches.* AIP Adv. **6**, 125124 (2016).

[109] M. Pardavi-Horvath, B. G. Ng, F. J. Castaño, H. S. Körner, C. Garcia, and C. A. Ross. *Angular dependence of ferromagnetic resonance and magnetization configuration of thin film Permalloy nanoellipse arrays.* J. Appl. Phys. **110**, 053921 (2011).

[110] K. S. Buchanan, P. E. Roy, F. Y. Fradin, K. Y. Guslienko, M. Grimsditch, S. D. Bader, and V. Novosad. *Vortex dynamics in patterned ferromagnetic ellipses.* J. Appl. Phys. **99**, 08C707 (2006).

[111] K. J. Kirk, J. N. Chapman, S. McVitie, P. R. Aitchison, and C. D. W. Wilkinson. *Switching of nanoscale magnetic elements.* Appl. Phys. Lett. **75**, 3683-3685 (1999).

[112] S. Ahn, K.-W. Moon, D.-H. Kim, and S. Choe. *Geometric dependence of static and kinetic pinning of domain walls on ferromagnetic nanowires.* J. Appl. Phys. **111**, 07D309 (2012).

[113] D. Bedau, M. Kläui, M. T. Hua, S. Krzyk, U. Rüdiger, G. Faini, and L. Vila. *Quantitative Determination of the Nonlinear Pinning Potential for a Magnetic Domain Wall.* Phys. Rev. Lett. **101**, 256602 (2008).

[114] D. Petit, A.-V. Jausovec, D. Read, and R. P. Cowburn. *Domain wall pinning and potential landscapes created by constrictions and protrusions in ferromagnetic nanowires.* J. Appl. Phys. **103**, 114307 (2008).

[115] D. Petit, A.-V. Jausovec, H. T. Zeng, E. Lewis, L. O'Brien, D. Read, and R. P. Cowburn. *Mechanism for domain wall pinning and potential landscape modification by artificially patterned traps in ferromagnetic nanowires.* Phys. Rev. B **79**, 214405 (2009).

[116] S.-H. Huang and C.-H. Lai. *Domain-wall depinning by controlling its configuration at notch.* Appl. Phys. Lett. **95**, 032505 (2009).

[117] T. Y. Chen, M. J. Erickson, P. A. Crowell, and C. Leighton. *Surface Roughness Dominated Pinning Mechanism of Magnetic Vortices in Soft Ferromagnetic Films.* Phys. Rev. Lett. **109**, 097202 (2012).

[118] L. Laurson, A. Mughal, G. Durin, and S. Zapperi. *Modeling Domain Wall Dynamics in Thin Magnetic Strips With Disorder.* IEEE Trans. Magn. **46**, 262-265 (2010).

[119] J. Leliaert, B. Van de Wiele, A. Vansteenkiste, L. Laurson, G. Durin, L. Dupré, and B. Van Waeyenberge. *A numerical approach to incorporate intrinsic material defects in micromagnetic simulations.* J. Appl. Phys. **115**, 17D102 (2014).

[120] J. Leliaert, B. Van de Wiele, A. Vansteenkiste, L. Laurson, G. Durin, L. Dupré, and B. Van Waeyenberge. *Current-driven domain wall mobility in polycrystalline Permalloy nanowires: A numerical study.* J. Appl. Phys. **115**, 233903 (2014).

[121] E. Martinez. *Micromagnetic analysis of current-driven DW dynamics along rough strips with high perpendicular anisotropy at room temperature.* J. Magn. Magn. Mater. **324**, 3542 - 3547 (2012). Fifth Moscow international symposium on magnetism.

[122] E. Martinez. *The stochastic nature of the domain wall motion along high perpendicular anisotropy strips with surface roughness.* J. Phys.: Condens. Matter **24**, 024206 (2012).

[123] H. Min, R. D. McMichael, M. J. Donahue, J. Miltat, and M. D. Stiles. *Effects of Disorder and Internal Dynamics on Vortex Wall Propagation.* Phys. Rev. Lett. **104**, 217201 (2010).

[124] B. Van de Wiele, L. Laurson, and G. Durin. *Effect of disorder on transverse domain wall dynamics in magnetic nanostrips.* Phys. Rev. B **86**, 144415 (2012).

[125] W. H. Teh, C.-T. Liang, M. Graham, and C. G. Smith. *Cross-linked PMMA as a low-dimensional dielectric sacrificial layer.* Journal of Microelectromechanical Systems **12**, 641-648 (2003).

[126] W. H. Teh, J. K. Luo, M. R. Graham, A. Pavlov, and C. G. Smith. *Near-zero curvature fabrication of miniaturized micromechanical Ni switches using electron beam cross-linked PMMA.* J. Micromech. Microeng. **13**, 591 (2003).

[127] J. Stigloher. *Reflection and Refraction of Spin Waves.* Universität Regensburg, Dissertation (2018).

[128] B. Boehm. *Determination of the damping parameter: Domain wall dynamics versus ferromagnetic resonance.* Universität Regensburg, Masterarbeit (2012).

[129] A. Aharoni. *Demagnetizing factors for rectangular ferromagnetic prisms.* J. Appl. Phys. **83**, 3432-3434 (1998).

[130] L. Papula. *Mathematik für ingenieure und naturwissenschaftler.* No. Bd. 3 in Mathematik für Ingenieure und Naturwissenschaftler, Vieweg (2001).

[131] B. Van Waeyenberge, A. Puzic, H. Stoll, K. W. Chou, T. Tyliszczak, R. Hertel, M. Fähnle, H. Brückl, K. Rott, G. Reiss, I. Neudecker, D. Weiss, C. H. Back, and G. Schütz. *Magnetic vortex core reversal by excitation with short bursts of an alternating field.* Nature **444**, 461 (2006).

[132] A. Vansteenkiste, K. W. Chou, M. Weigand, M. Curcic, V. Sackmann, H. Stoll, T. Tyliszczak, G. Woltersdorf, C. H. Back, G. Schütz, and B. Van Waeyenberge. *X-ray imaging of the dynamic magnetic vortex core deformation.* Nat. Phys. **5**, 332 (2009).

[133] K. Yamada, S. Kasai, Y. Nakatani, K. Kobayashi, H. Kohno, A. Thiaville, and T. Ono. *Electrical switching of the vortex core in a magnetic disk.* Nat. Mater. **6**, 270 (2007).

[134] M. Hayashi, L. Thomas, C. Rettner, R. Moriya, and S. S. P. Parkin. *Direct observation of the coherent precession of magnetic domain walls propagating along permalloy nanowires.* Nat. Phys. **3**, 21 (2006).

[135] K.-S. Lee, S.-K. Kim, Y.-S. Yu, Y.-S. Choi, K. Y. Guslienko, H. Jung, and P. Fischer. *Universal Criterion and Phase Diagram for Switching a Magnetic Vortex Core in Soft Magnetic Nanodots.* Phys. Rev. Lett. **101**, 267206 (2008).

[136] A. Pushp, T. Phung, C. Rettner, B. P. Hughes, S.-H. Yang, L. Thomas, and S. S. P. Parkin. *Domain wall trajectory determined by its fractional topological edge defects.* Nat. Phys. **9**, 505 (2013).

[137] A. Thiaville, Y. Nakatani, F. Piéchon, J. Miltat, and T. Ono. *Transient domain wall displacement under spin-polarizedcurrent pulses.* The European Physical Journal B **60**, 15–27 (2007).

[138] V. Estévez and L. Laurson. *Magnetic domain-wall dynamics in wide permalloy strips.* Phys. Rev. B **93**, 064403 (2016).

[139] V. Estévez and L. Laurson. *Fast vortex wall motion in wide permalloy strips from double switching of the vortex core.* Phys. Rev. B **96**, 064420 (2017).

[140] X.-G. Wang, G.-H. Guo, G.-F. Zhang, Y.-Z. Nie, and Q.-L. Xia. *Spin-wave resonance reflection and spin-wave induced domain wall displacement.* J. Appl. Phys. **113**, 213904 (2013).

[141] S.-M. Seo, H.-W. Lee, H. Kohno, and K.-J. Lee. *Magnetic vortex wall motion driven by spin waves.* Appl. Phys. Lett. **98**, 012514 (2011).

[142] H. Altenbach. *Kontinuumsmechanik: Einführung in die materialunabhängigen und materialabhängigen Gleichungen.* Springer Berlin Heidelberg (2012).

[143] G. Fischer. *Lernbuch Lineare Algebra und Analytische Geometrie.* Springer Berlin Heidelberg (2017).

[144] H. Iben. *Tensorrechnung.* Mathematik für Ingenieure und Naturwissenschaftler, Ökonomen und Landwirte, Vieweg+Teubner Verlag (1999).

[145] R. Zurmühl and S. Falk. *Matrizen und ihre Anwendungen 1.* Klassiker der Technik, Springer (1997).